Cranfield University

Zsuzsanna Libor

Chemical synthesis of nanoparticles and electrohydrodynamic manipulation of nanoparticulate suspensions

School of Applied Sciences

PhD Thesis

Cranfield University
School of Applied Sciences
Department of Materials
Microsystems and Nanotechnology Centre

PhD Thesis

Zsuzsanna Libor

Chemical synthesis of nanoparticles and electrohydrodynamic manipulation of nanoparticulate suspensions

Supervisors: Dr. S.A. Wilson and Dr. Q. Zhang

September 2009

This thesis is submitted in partial fulfilment of the requirements for the Degree of PhD.

Abstract

This research concerns the study of nanoparticle synthesis methods and the influence that nanoparticles can have on the physical and electrical properties of non-polar fluids. In this study it is demonstrated that a very small volume fraction of nanoparticles can have a very large effect on the macroscopic properties of fluids. Characterization of nanoparticles and nanofluids has led to the creation of new techniques for controlled deployment of nanoparticles within larger structures. A new dielectrophoretic technique can be used for (1) uniformly sized droplet generation and manipulation with controllable droplet size, (2) oil-in-water emulsion creation in unique way, (3) recycling nanoparticles from nanoparticulate suspensions and (4) creation of core-shell structures. Different types, sizes and morphologies of nanoparticles have been made successfully by chemical synthesis and new synthesis routes have been created. A new wet chemical route has been devised to synthesise nickel nanoparticles with controllable size and different morphology including new shapes such as micro-flower and nano-stars. PZT nanoparticles have been synthesized hydrothermally with controllable size and new morphologies created such as nearly spherical nanoparticles and pellets. A novel wet chemical synthesis method was developed to produce core-shell structures of Ni- and also Fe_3O_4 - coated SiO_2, BT, and PZT particles.

The characterization of non-polar fluid-based nanofluids included a sedimentation study, studies of the fluidic properties (viscosity and surface tension) and electrical properties such as DC conductivity and dielectric permittivity. The results clearly show that the macroscopic properties of base fluids (silicone oil and perfluorinated oil) were changed even with a very low concentration (< 0.6 vol %) of nanoparticles added. The properties of nanofluids are found to depend on the properties of the base fluid and also on the properties of the dispersed nanoparticles. Importantly, the properties are demonstrated to depend on the fluid-particle interaction.

Acknowledgments

Very special thanks to my supervisors Drs Steve Wilson and Qi Zhang for their guidance and encouragement throughout the project. Without their supervision, it would have been quite impossible to complete the thesis in this manner.

I wish to thank my friends and colleagues at the Nanotechnology Centre who provided a pleasant working environment. I wish to express my gratitude to the support staff and technicians, including Mrs Enza Giaracuni, Dr Matt Kershaw and Mr Andy Stallard. Special thanks to Dr Ennio Capria for his advice in DEP technique and for his friendship.

The financial support of EPSRC is gratefully acknowledged.

I cannot end without thanking my family, for the constant support and love. Their courage and passion will always inspire me, and I hope to continue, in my own small way. I would finally like to thank my husband; he has always given me his unconditional love and support.

Table of contents

List of figures

List of tables

Nomenclature and Abbreviations

Symbol	Definition
TEM	Transmission Electron Microscopy
XRD	X-ray diffraction
AFM	Atomic Force Microscope
VSM	Vibrating Sample Magnetometer
EDX	Energy-dispersive X-ray spectroscopy
SEM	Scanning Electron Microscopy
BT	Barium titanate
PZT	Lead zirconate titanate
LbL	Layer-by-Layer
O/W	Oil-in-water
W/O	Water-in-oil
SDS	Sodium dodecyl-sulphate
DEP	Dielectrophoresis
EHD	Electrohydrodynamic
TEOS	Tetraethyl orthosilicate
PTFE	Polytetrafluoroethylene
kOe	Magnetic field strength, Oersted [kA/m]
emu/g	(Mass) Magnetization [Am^2/kg]
EtOH	Ethanol
IPA	Isopropanol
FC70	Fluorinert FC70, perfluorinated fluid
Si oil	Silicone oil, polydimethylsiloxane
PVP	Poly(vinylpyrrolidone)
PVA	Poly(vinylalcohol)

Author Publications

Journal Papers

Libor, Z. and Zhang, Q., The synthesis of nickel nanoparticles with controlled morphology and SiO_2/Ni core-shell structures, *Materials Chemistry and Physics*, 114, 2-3 (2009) 902-907

Wilson, S.A., **Libor, Z.**, Skordos, A.A. and Zhang, Q., Enhanced DC conductivity of low volume-fraction nano-particulate suspensions in silicone and perfluorinated oils, J. *Phys. D: Appl. Phys*. 42 (2009) 062003

Ansari, F., Grigoriev, P., **Libor, Z.**, Tothill, I.F. and Ramsden, J.J., DBT degradation enhancement by decorating Rhodococcus erythropolis IGST8 with magnetic Fe_3O_4 nanoparticles, *Biotechnology and Bioengineering,* 102, 5 (2009) 1505-1512

Libor, Z., Zhang, Q., Israel, C. and Mathur, N.D., Nanocoating on micro- or nano-particles, in press, *Materials Science and Technology,* 25, 11 (2009) 1307-1311

Libor, Z., Wilson, S.A. and Zhang, Q., Synthesis of magnetic and ferroelectric nanoparticles and their influence on the viscosity of non-polar liquids, submitted to *Materials Chemistry and Physics*, 2009

Wilson, S.A., **Libor, Z.**, Capria, E., Brocklehurst, P., Camillieri, A., Milsom, B., Redondo, R., Simpkins, M., Shaw, C.P. and Zhang, Q., An Electrohydrodynamic Nanoparticle Filter for Oils, submitted to *Applied Physics Letters*, 2009

Wang, W., Zhang, Q., Liu, Z., **Libor, Z.**, High efficient disaggregation of nanoparticles by the Stock Wave method, in preparation, 2009

Oral presentations

Libor, Z., Wilson, S.A., Capria, E. and Zhang, Q., Fabrication of micro-scale ceramic core-shell structures by a novel electrostatic method and their functionalization using nanoparticles, 4M Workshop, Gothenburg, Sweden, 24th October 2007

Wilson, S.A., **Libor, Z.** and Zhang, Q., Assembly of Ceramic Core-Shell Structures by Dielectrophoresis, Hanover Fair, Hanover, Germany, 18th April 2007

Libor, Z., Wilson, S.A. and Zhang, Q., Synthesis of functional nanoparticles and their manipulation by novel dielectrophoretic techniques, Cranfield Multi-Stand Conference, Cranfield, UK, 7th May 2008

Ansari, F., **Libor, Z.** and Ramsden, J.J., Fabrication and characterization of magnetic Fe_3O_4 nanoparticles Cranfield Multi-Stand Conference, Cranfield, UK, 7th May 2008

Poster presentations

Libor, Z., Wilson, S.A., Capria, E. and Zhang, Q., Fabrication of micro-scale ceramic core-shell structures by a novel electrostatic method and their functionalization using nanoparticles, Electro-Active Materials, IOP, Cranfield, 20th September 2007

Libor, Z., Wilson, S.A., Capria, E. and Zhang, Q., Fabrication of micro-scale ceramic core-shell structures by a novel electrostatic method and their functionalization using nanoparticles, Future of Manufacturing, Cranfield, 8th May 2008

Ansari, F., Horvath, R., Aref, A., **Libor, Z.** and Ramsden, J.J., Fabrication of a thin Fe_3O_4 magnetic nanofilm on silica titania for bioapplications, 7th International Conference on the Scientific and Clinical Applications of Magnetic Carriers, Vancouver, Canada at the University of British Columbia (UBC), 21st May 2008

Ansari, F., Aref, A., **Libor, Z.,** Horvath, R. and Ramsden, J.J., Adsorption kinetics of bacteria onto a thin Fe_3O_4 magnetic nanofilm, NSTI Nanotech 2008 11th Annual , Hynes Convention Center, Boston, Massachusetts, 1st June 2008

Libor, Z., Zhang, Q., Israel, C. and Mathur, N.D., Nanocoating on micro- or nano-particles, Electroceramics IX Conference, Manchester, 1st September 2008

Libor, Z. and Zhang, Q., Synthesis of nickel nano-materials and nickel nano layer coated silicon-dioxide, London Technology Network, Advances in Smart Materials Event, 21st January 2009

Libor, Z. and Zhang, Q., Synthesis of nano-materials and rheology of nanofluids, London Technology Network, Advances in Smart Materials Event, 21st January 2009

Chapter 1 Introduction

1.1 Context of the research

Nanotechnology is the design, characterization, production and application of structures and systems at nano-scale with control over their size and shape [The Royal Society, 2004]. It is a multidisciplinary technology that involves different fields of science (biology, chemistry and physics) and engineering research.

At the present time scientists can produce nanomaterials of many different shapes (from spherical nanoparticle to nanotube and nanowire) with extraordinary electric, electronic, mechanical, thermal and optical properties [Choi, S.U.S. 2009]. As an example, the optical properties of nano-size semiconductors (e.g. PbSe) can be tuned to span the optical region of the electromagnetic spectrum by varying the size of the quantum dot, because quantum size effects rule the energy of the electronic band gap [Badr, Y. et al. 2006].

Early in the study of nanotechnology scientists realised that below certain size the conventional physical and chemical rules do not apply [Preining, O. 1998]. Some of their properties dramatically change as dimensions are reduced to nano-scale. Physical property such as dynamic contact angle has changed significantly by changing the droplet size to nano-size [Sedighi, N. et al. 2008]. In some metals and semiconductors at the typical size range of 2-20 nm, the melting temperature undergoes a huge change [Wang, J. et al. 2006]. Ag and Pb nanowires of diameter 30 nm have twice as high elastic constants as the bulk Ag and Pb metals [Cuenot, S. et al. 2004]. These properties are sometimes remarkable in comparison to the bulk materials properties, and sometimes beneficial (accelerated catalysis) or harmful (increased toxicity) for the users.

Awareness of nano-structural properties could improve the understanding of many aspects of chemical and physical behaviour. For example, calcium carbonate particles have a critical size (850 nm) and particles > 850 nm are fragile and breakable, but when the size decreased to < 850 nm the particles become elastic and flexible [Wang, J. et al. 2006]. Such knowledge of the importance of the size and morphology of particles could lead to different applications.

Nanoparticles have fascinated scientists even from earlier times, for example gold nanoparticles were used by the Chinese to colour porcelain and ceramics, and in Europe for stained glass windows of cathedrals. Hence while the effects are not new it is only recently that the core understanding of the nano-scale has become of major interest. In our time, nanoparticles are class of materials with at least one dimension that is 100 nm or less. This description defines them as a sub-set of colloidal particles. The key characteristics of nanoparticles are the huge surface area to volume ratio and the small size of the particles. These two are interrelated since the large surface to volume ratio increases as the size decreases. When the particle size is reduced to nano-scale, interfacial energies become a dominant effect on most behaviour due to the increased number of atoms or molecules on the surface. For example: silver nanoparticles show antimicrobial activity, but silver metal does not; there is a change in colour of gold particles (red, blue or yellow) dependent on size. The conductance of PVA doped with PbSe nanoparticles is found to be inversely proportional to the size of the PbSe nanoparticles, which cause increased randomness in the PVA matrix [Badr, Y. et al. 2006].

Nanofluids are liquid suspensions of nanoparticles. In recent years much attention has been given to nanofluids because of their enhanced properties (heat transfer, thermal conductivity) and unique behaviour [Koo, J. et al. 2004, Keblinski, P. et al. 2008, Choi, S.U.S. 2009]. These properties indicate potential for nanofluids in industries including energy, environment, medical and electronics. Nanofluids still have potential and properties to be discovered.

1.2 Thesis objectives

The overall aim of this work is to create new methods for nanoparticle deployment and in the process of achieving that aim:

1) to study nanoparticle synthesis methods. This involves an optimised synthesis and characterization of different nanoparticles such as nickel, iron oxide, solid silicon dioxide, barium titanate and lead zirconate titanate nanoparticles, hollow silicon dioxide particles and core-shell nano- and micro-sized particles.

2) to study the influence that nanoparticles can have on the physical and electrical properties of non-polar fluids. This involves an investigation of the physical (viscosity and surface tension) and electrical (conductivity and permittivity) properties of non-polar fluid based nanofluids.

3) to use this deeper understanding to create some new techniques that can be used to:

i) redistribute nanoparticles in such a way that new synthesis routes for multifunctional nanoparticles might be possible,

ii) create core-shell structures,

iii) clean nanoparticle containing fluids,

iv) create emulsion in unique way.

To achieve this goal systematic study was needed to determine influence of nanoparticles on a new dielectrophoretic droplet generation and manipulation technique.

1.3 Thesis structure

The thesis is presented in thirteen chapters. Chapter 1 is an introduction to the rationale for this research which leads into the background and literature review in Chapter 2-4 of, respectively, nanoparticles and nanostructures, of physical properties of nanofluids and of phenomena observed under electric field and the dielectrophoretic manipulation technique, respectively.

Chapters 5 and 6 describe the experimental details of nanoparticle synthesis and characterization, the characterization of nanofluids and the set-up of the dielectrophoretic manipulation technique.

In Chapter 7 the results of experiments in nanoparticle synthesis are brought together with theory on the effect of synthesis parameters (reaction time and temperature, concentration of precursors), to show that these all affect the size and morphology of the final product. This knowledge is used to produce nanoparticles that are suitable for the next step, which is their suspension in non-polar medium. The nanoparticulate suspension characterization highlighted the importance of the type, size and the concentration of nanoparticles in the suspension. This is shown in Chapters 8 and 9 as rheological and electrical characterization, respectively.

The findings are brought together in Chapter 10 to show that the new dielectrophoretic technique could be used for droplet creation and manipulation of nanofluids, base fluid recycling from nanofluid and also for creating silicone oil based nanofluid core- polymer shell structure.

Chapter 2 Literature background of nanoparticles and core-shell structure

This chapter focuses on the nanoparticles producing techniques and their important functions in research and industries. The chapter contains an overview of nanoparticles (such as Fe_3O_4, Ni, SiO_2, BT, PZT) synthesis methods and applications which has been extended over the last few years. Chemical synthesis methods have been developed to produce nanoparticles with certain size and morphology from spherical nanoparticles through nanostars to nanocubes. This chapter also presents an overview of nanostructured core-shell particles.

2.1 Iron oxide (Fe_3O_4) nanoparticles

Magnetite is one of the first known natural magnetic minerals. The Chinese used its magnetic properties as early as the 4^{th} century. Magnetite can be found in nature, in sedimentary rocks and also in living cells, for example in bacteria, bees and pigeons. Magnetite (Fe_3O_4 or the chemical name ferrous-ferric oxide) is a black, ferromagnetic material containing both Fe(II) and Fe(III); its chemical formula may also be written as $FeO{\cdot}Fe_2O_3$. The main details of its structure were established in 1915 by Bragg and it was one of the first mineral structures to which X-ray diffraction was applied. It is stable in atmospheric conditions, but the surface of the individual particles may oxidise forming a thin layer of maghemite (γ-Fe_2O_3), which indicates that this γ-Fe_2O_3 layer helps to prevent the Fe_3O_4 from further oxidization [Cornell, R.M. et al. 1996].
Magnetic nanoparticles have received increasing attention with the rapid development of nano-science, nanotechnology and also in the fields of biotechnology and medicine. Their application in nano-biotechnology is due to their strong magnetic properties and low toxicity. Whereas conventional chemotherapy is extremely aggressive, new research shows that using magnetic iron oxide nanoparticles as vehicles for drug delivery can be very effective and with far fewer side effects. Iron oxide nanoparticles are coated with starch derivatives that have phosphate groups and a strong applied magnetic field gradient at the tumour location induces accumulation of the iron oxide nanoparticles [Laurent, S. et al. 2008].

Magnetic nanoparticles (<30 nm) will exhibit superparamagnetism, which means that they are only magnetic in a magnetic field and the magnetic field re-orientates the iron oxide crystals toward the same direction, increasing locally the amplitude of the field. Superparamagnetic iron oxide nanoparticles have been used for hyperthermia treatment. First the magnetic field has created energy, then the crystals absorb it and they can convert it into heat. Heating destroys the pathological cells [Jordan, A. et al. 1993, Laurent, S. et al. 2008]. Applications also include bio-sensing, contrast agent in magnetic resonance imaging (MRI), magnetic ink for jet printing, magnetic storage media, catalysis and ferro-fluids.

Several methods have been developed to synthesize magnetite nanoparticles: hydrothermal, sol-gel synthesis, micro-emulsions, and wet chemical (or co-precipitation) method [Laurent, S. et al. 2008]. The advantages and disadvantages of the four above-mentioned synthesis methods are summarized in Table 2.1. The first line indicates the degree of difficulty of each method with regard to of required equipment and the conditions of the synthesis. The micro-emulsion synthesis and hydrothermal method can both be used to synthesize monodispersed nanoparticles with various morphologies. The disadvantage of micro-emulsion synthesis is the requirement for a large amount of solvent which increases the cost. The hydrothermal method has only a medium yield ratio [Lu, A.H. et al. 2007].

Table 2.1 Summary of comparison of some synthesis methods of iron oxide

Synthesis methods	**Co-precipitation (wet chemical)**	**Sol-gel**	**Micro-emulsion**	**Hydrothermal**
Difficulty of synthesis	simple, ambient conditions	quite complicated	complicated ambient conditions	simple, high pressure
Reaction temp.	20-90ºC	60-80 ºC	20-50 ºC	180-230 ºC
Reaction period	minutes-hour	hours	hours	hours-day
Solvent	aqueous	organic compound	organic compound	water-ethanol
Size distribution	quite narrow	broad size distribution	relatively narrow	narrow
Shape control	quite controllable	quite controllable	controllable	controllable
Yield	<65%	<60%	<40%	<60%

For the current project first challenge was to choose a suitable synthesis method and to define the experimental conditions which lead to monodisperse nanometre size magnetite particles. The second challenge was to select a reproducible, reasonable and cheap method which can be used without complex purification. The wet chemical (or co-precipitation) method is a simplest chemical method to obtain magnetic iron oxide nanoparticles and it can produce fine, high purity nanoparticles.

The most common iron salts used in chemical co-precipitation are $FeCl_2$ and $FeCl_3$. However, several groups have selected ferric nitrate and ferrous sulphate as iron precursor. NaOH and NH_4OH are widely used as the precipitating agent. Reaction temperatures range from 20 °C to 90 °C and resultant particle size falls in the 3 nm to 55 nm range.

2.2 Nickel (Ni) nanoparticles

Nickel is an interesting material for its magnetic properties (it is ferromagnetic) and for industrial applications. Nano-scale metal materials with special morphologies have attracted intensive interest in magnetic fluid, medical diagnosis and catalysis.

Nanoparticles sometimes exhibit new properties different from the properties of bulk materials. Nickel nanoparticles have been studied extensively over the past decades due to their potential technological applications such as an inexpensive internal electrode in a multilayer ceramic capacitor (MLCC) [Abdel-Aal, E.A. et al. 2007], building blocks for single-electron devices [Puntes, V.F. et al. 2001], magnetic hyperthermia [Bettge, M. et al. 2004], rechargeable batteries [Zhang, H.T. et al. 2006], optoelectronics [Beecroft, L.L. et al. 1997] and conducting paints [Zhang, H.T. 2006].

Nickel metal nanoparticles have been less frequently studied compared to other metal nanoparticles (silver, gold and platinum) because it is quite difficult to avoid oxidation and aggregation when the size is reduced to nano-scale. In the past decade nickel nanomaterials have been synthesized with various structural and morphological forms. For example: hollow nanospheres, nanotubes, nanorods, nanobelts, sea-urchin-like and chain-like [Ma, F. et al. 2008] and hexagonal flakes [Liu, Z. et al. 2003, Zhang, H.T. et al. 2006].

The preparation of nickel metal nanoparticles is relatively difficult because they are easily oxidized. Several methods have been developed to synthesize particles with variable morphology and size, for example: chemical method [Choi, J.Y. et al. 2005], microemulsion technique [Chen, D.H. et al. 2000], polyol process [Kurihara, L.K. et al. 1995], thermal decomposition [Chen, Y. et al. 2007], hydrothermal [Ni, X. et al. 2005] and interphase reduction [Kudlash, A.N. et al. 2008].

A comparison of the five latest synthesis methods is summarized in Table 2.2. The first column refers to the difficulties or simplicity of certain methods in the means of required equipment and the conditions of the synthesis. The simplest method is the chemical synthesis method. This method can be employed on a large scale and enables the size and the shape to be controlled as well.

Table 2.2 Summary comparison of the synthesis methods of nickel nanoparticle

Synthesis methods	*Difficulty of synthesis*	*Reaction temperature*	*Reaction period*	*Size distribution*	*Shape control*
Chemical route	simple	20-80 ºC	minutes-hour	quite narrow	controllable
Thermal decomposition	quite complicated	130-290 ºC	hours	broad size distribution	controllable
Microemulsion	quite complicated	20-80 ºC	hours	quite narrow	uncontrollable
Hydrothermal	simple, high pressure	110-160 ºC	hours	broad size distribution	quite controllable
Interphase reduction	quite simple	100 ºC	hours	quite narrow	quite controllable

2.3 Barium titanate (BT) nanoparticles

Barium titanate is a ferroelectric oxide material with perovskite structure. It has been investigated due to its ferroelectric, piezoelectric properties, its high dielectric constant and its photoresistivity. Barium titanate was discovered in 1942 by E. Wainer and N. Salomon [Lee, T. et al. 2001]. Barium titanate nanoparticles have a phase

transition from ferroelectric (tetragonal) to paraelectric (cubic) at 120 ºC (Curie temperature).

Barium titanate has wide applications in the electro-ceramic industry such as multilayer ceramic capacitor (MLCCs), electro-optic devices, underwater transducers and dynamic random access memories. For most of the applications it is important to have ceramics with narrow size distribution and homogeneity.

The ferroelectric tetragonal phase has high dielectric constant (controlled by the ferroelectric domain structure and dipole-dipole interaction) that is ideal for dielectric application. The particles become less tetragonal with size reduction and eventually change to cubic phase. The exact size at which this change occurs differs slightly according to synthesis method. This has been explained by the different elastic strain energy associated with chemical impurity and crystalline defects [Kwon, S.W. et al. 2007]. As the size reduces the physical properties change [Vinothini, V. et al. 2006]. These changes are:

-lowering of melting point,

-decrease in sintering temperature,

-disappearance of ferroelectric and ferromagnetic properties,

-enhancement of electronic conductivity.

A wide variety of nanoparticles synthesis methods have been explored: solid state reaction [Buscaglia, M.T. et al. 2008], sol-gel [Lee, J.J. et al. 2006], electrophoretic deposition [Dogan, A. et al. 2006], homogeneous precipitation synthesis [Testino, A. et al. 2004], micro-emulsion method [Sakabe, Y. et al. 2005], and hydrothermal synthesis [Clark, J.I. et al. 1998]. Hydrothermal synthesis has a low cost and avoids using high temperature calcination. Synthesis conditions, such as pH, Ba/Ti ratio, reaction temperature and time have a large impact on the size and morphology of the final nanoparticles. For the synthesis of BT nanoparticles, hydrothermal method provides an opportunity of controlling the size of the particles. Its kinetics and crystallisation mechanics have been well investigated. Studies have shown that the reduction of the particle size of the starting materials causes significant size reduction of the final barium titanate powder.

2.4 Lead zirconate titanate (PZT) nanoparticles

Piezoelectric ceramics such as PZT have wide range of applications in various technologies due to its piezoelectric, ferroelectric and electro-optic properties. Below its Curie temperature (350 °C) PZT exhibits non-centro-symmertric perovskite structure with a ferroelectric tetragonal or rhombohedral phase and has spontaneous polarization. The best piezoelectric and ferroelectric properties can be obtained from the 52:48 Zr:Ti ratio ($PbZr_{0.52}Ti_{0.48}O_3$) which is in a morphotropic phase boundary of tetragonal and rhombohedra phase [Moulson, A.J. et al. 2003]. One of the important applications of PZT is in micromechanical systems. PZT used and developed in the following fields: ultrasonic transducer, i.e. medical application and inter-cardiac ultrasound scanner [Yu, H.G. et al. 2003], accelerometers, pressure sensors, i.e. micro-pumps [Polla, D.L. et al. 1996], power generators and acoustic motors. PZT is commonly used in electro-ceramics because it has a high piezoelectric coupling constant.

Several methods have been developed to produce nano-size PZT particles, such as solid-state [Moulson, A.J. et al. 2003], sol-gel [Ghasemifard, M. et al. 2009], hydrothermal [Deng, Y. et al. 2003] and electrospray [Sun, D. et al. 2005]. All of the methods have pros and cons as shown in Table 2.3.

Table 2.3 Comparison of several techniques for production of PZT nanoparticles

	Compositional control	*Morphology control*	*Calcination step*	*Cost*
Solid state	hardly controlled	hardly controlled	required	moderate
Sol-gel	controllable	hardly controlled	required	high
Hydrothermal	controllable	controllable	unnecessary	moderate
Electrospray	controllable	hardly controlled	required	high

The first column indicates the difficulties of the control over the final PZT composition, such as PZT 52/48, 70/30, 20/80; the second column the difficulty over the morphology of the obtained PZT such as cubic or spherical. The last column indicates the cost of the whole synthesis process including the required equipment,

precursors and after-treatment. The hydrothermal synthesis compares favourably in most areas. The chosen method for this project to synthesise nano-size PZT was the hydrothermal synthesis technique due to its simplicity, low temperature treatment and repeatable technique. The composition that was used in this work is $PbZr_{0.52}Ti_{0.48}O_3$ or otherwise denoted PZT 52/48.

2.5 Core-shell structure

A core-shell structure can be defined as a particle composed of a central domain (core) and an outer domain (shell) which are physically and chemically distinct. When the core is removed from the core-shell structure by dissolving or evaporating, a hollow structure results. Different types of structure are shown in Fig. 2.1.

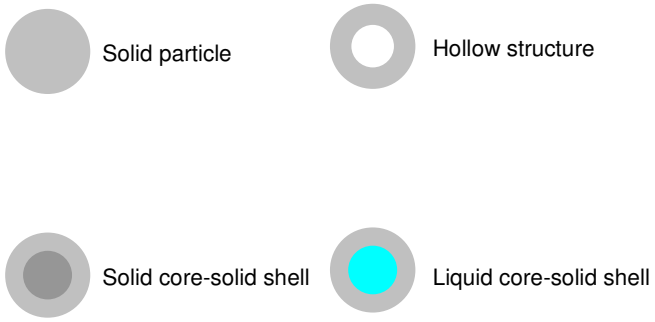

Figure 2.1 Different structures of particles (solid, hollow and core-shell)

2.5.1 Applications for core-shell structure

Hybrid materials with core-shell structure are often composed of nano- or micro-spheric core with shell of nanoparticles. Scientific and industrial interest of core-shell composite particles has increased recently because of the potential for the properties of starting core or shell material to be fine tuned, to control their magnetic, optical and electrical properties. The preparation of core-shell particles is of interest for colloid and interface sciences. Nanoparticle coating is carried out for various reasons such as

stability or functionalization. For example, some biomedical applications, such as, tagging, imaging, sensing and separation, require core-shell magnetic nanoparticles or micro-container or micro-encapsulated products. The most promising applications in the biomedical field for core-shell magnetic nanoparticles relate to the diagnosis and treatment of cancer [Pankhurst, Q.A. et al. 2003, Arruebo, M. et al. 2007].

Applications of small particles with micro- or nano-core-shell structures need to meet two basic requirements: a designable coating layer on the core particles and economical synthesis. The core-shell particles with inorganic coatings offer interesting prospects for the fabrication of a broad range of materials with different properties. From the economic and environmental points of view, an aqueous method is preferable.

2.5.2 Synthesis methods to obtain core-shell structure

A wide variety of methods have been explored and developed for the synthesis of well defined coated powders (core-shell structure), such as, heterogeneous precipitation [Villegas, M. et al. 2007], sol-gel process [Sugimoto, T. et al. 2003], hydrothermal synthesis [Yang, J. et al. 2001], homogeneous precipitation [Lee, K.R. et al. 2002], electrochemical method [Kim, S.H. et al. 2007], emulsion evaporation [Landfester, K. 2001], and spray drying [Kim, J. et al. 2002].

Other techniques to synthesize liquid core-solid shell structures are: assembly and fusion of polymer on the emulsion droplets [Dinsmore, A.D. et al. 2002], emulsification and freeze-drying [Yin, W. et al. 2008]. A novel co-axial electrohydrodynamic method has been developed by Farook et al. (2008), which can synthesise liquid filled polymer shell.

2.5.3 Synthesis methods to obtain hollow structure

The general synthesis methods that can be used to obtain hollow structure are: hard templating synthesis, soft templating synthesis and template free methods.

Hard templating synthesis methods

A, *Layer-by-layer (LbL) assembly*, Caruso et al. (1998) was the first to publish on the LbL method, where oppositely charged materials were deposited alternatively on a substrate and the core-shell reaction occurs by electrostatic interaction. The core material is removed by evaporation or dissolution.

B, *Direct chemical deposition technique*, which involves the precipitation of shell material on the template particles by chemical or physical interactions. One of the early syntheses was carried out by Matijevic (1993) who called it the controlled precipitation route. Lou et al. (2007) recently demonstrated a similar technique, called shell-by-shell template technique; he also produced SnO_2 hollow structures using it. It is based on the hydrothermal deposition of coating on silica templates.

C, *Chemical adsorption on surface layer or so called adsorption-calcinations route*. To use this technique the template particles need to be pre-treated prior to the synthesis of the hollow structure. This includes three main steps: functionalization of the template, adsorption and calcinations.

D, Stöber et al. (1968) was the pioneer of *Nanocoating from mesoporous shell* technique. The conventional hard templating synthesis is the most common and effective method but the disadvantage is a medium-low product yield.

Soft templating synthesis method

Soft template techniques use liquid or gas templates as core materials. The emulsion droplet method involves a deposition of the shell material round the interface between the two liquid phases of the emulsion. Zoldesi et al. (2005) produced hollow silica structures in an oil-in-water emulsion system by soft templating.

Template free synthesis method

Template free methods have been developed because sometimes the removal of hard or soft templates is cost-effective and could affect the quality of the hollow structure (collapse of the shell after the removal of the template). Hollow SnO_2 nanostructures are produced by a one-step template free method which includes an inside-out Ostwald ripening [Lou, X.W.D. et al. 2008]. In the early stage of reaction, solid nanoparticles or loose aggregates of precipitated nanoparticles are formed and then the nanoparticles start to crystallize from the surface layer, due to the effect of the

surrounding solution. A hollowing process accompanies the crystallisation. The molecules inside the nanoparticles have a strong tendency to dissolve, and this is the driving force for the spontaneous inside-out Ostwald ripening.

2.6 Hollow silicon dioxide particles

Silicon dioxide can be found in sand and glass and has been of interest to scientists for years. Silica is a quite unique material, has a variable morphology with a differing size range. Silica is biocompatible and has good dielectric, thermal and mechanical properties. Silicon dioxide particles can be synthesised by different methods including sol-gel, wet-chemical and hydrothermal methods. The most efficiently and economically used method is sol-gel synthesis. The sol-gel method for ceramics began in the mid 1800s [Hench, L.L. et al. 1991].

Stöber et al. in 1968 published the synthesis of silica in aqueous solution in alkaline conditions in the following main steps: through hydrolysis and condensation of a metal-organic material (e.g. tetraethyl orthosilicate, TEOS) in solvent, and the end of this reaction the gel forms and has a Si-O-Si network. The temperature, concentration and ratio of starting materials are important parameters in sol-gel synthesis, since they affect the size, morphology and size distribution of products.

From an economical point of view the synthesis and use of hollow particles is efficient. A comparison of solid and hollow particles of the same size shows that for a hollow particle with a wall thickness of 10% of its radius, it needs about 50% less material than a solid particle. Fields such as the aerospace industry welcome this lighter and lower cost material. Sol-gel is a simple and economical method to produce nano-size silica materials. Hollow silica spheres have attracted attention due to their low cost and feasible synthesis, porosity and non-toxic behaviour. Hollow silica particles are suitable for drug delivery, because the inner space can take up a large amount of drug and the mesoporous shell can be used to release it. Alternatively the outer surface can be used for biomedical purposes.

Chapter 3 Literature background of emulsion and properties of nanoparticulate suspension

A nanofluid is a suspension of nanoparticles in liquid. Nanofluids have been produced by two techniques. The one-step method synthesises and disperses the nanoparticles directly into the liquid. The two-step method separates the nanoparticles synthesis by chemical or physical methods before dispersal in the base fluid. Nowadays nanofluids are usually produced in small volumes. Generally the seven parameters that most effect the properties of nanofluids are: (1) particle concentration, (2) particle shape, (3) particle type (material), (4) particle size, (5) base fluid, (6) additives (surfactant, anti-coagulant), and (7) temperature. These parameters have effect on the nanofluids properties such as thermal and electrical conductivity [Keblinski, P. et al. 2008, Garg, J. et al. 2008, Wilson, S.A. et al. 2009], heat transfer [Jordan, A. et al. 1993, Trisaksri, V. et al. 2007] and rheological properties [Chen, H. et al. 2007].

The creation of nanofluid is connected to most of the nanotechnologies and deeper understanding of the properties of nanofluid will be helpful for further development of the area. Whereas some characteristics of nanofluids have been widely discussed there remains poor agreement in some areas and it is fair to say that greater understanding of the mechanisms involved at the atomic and molecular levels is desirable. Some characteristics of nanofluids have been widely explored such as thermal conductivity but certain properties still remain untouched (such as electrical conductivity and dielectric permittivity).

This chapter has an overview of properties such as surface tension and rheology of nanofluid and it the background of emulsions. One of the connections between nano-science and colloid science (which include the study of emulsions) is that emulsion could be stabilized by nanoparticles, which was discovered a century ago [Pickering, S.U. 1907].

3.1 Emulsions

An emulsion is a heterogeneous system, consisting of at least one immiscible liquid intimately dispersed in another in the form of droplets. Depending on the synthesis technique the size of the droplets varies between 100 nm and 0.1 mm. Such systems

possess a minimal stability, which may be promoted by such additives as surface-active agents or finely-divided solids. The two basic types of emulsion are direct (oil dispersed in water, O/W) and reversed (water dispersed in oil, W/O).

Oil-in-water (O/W)-type emulsions have been widely applied to cosmetics and toiletries due to their pleasant watery feeling when applied to skin. In order to improve cosmetic formulations, such as lotions, creams and base make-up liquid foundations, it is important to obtain fine O/W emulsions with a small amount of hydrophilic surfactant. Emulsion applications are really versatile and range from cosmetic and pharmaceutical emulsions, polishes, paints, agricultural sprays, food emulsions, medical emulsions, asphalt emulsions to textile industry [Becher, P. 1983]. Stable emulsions have been used extensively in food industries, petroleum production (drilling fluids), pharmaceutical (mainly cosmetic industry) and environmental applications.

3.1.1 Emulsion producing techniques

Liquid-liquid mixing is a well established operation in chemical engineering (and colloid science) and mixing apparatus is available with variable capacities. An efficient and convenient way to achieve such mixing is to use vertical baffles near the container walls, which deflect the fluid upwards, and to use a variable designed stirrer (rotating propeller, turbine rotor) [Sherman, P. 1968]. The problem with these techniques is that controlling the size and the size distribution of the droplets is difficult and often it ends up with poor reproducibility.

One of the new techniques is the layer-by-layer (LbL) deposition which offers a promising way to prepare emulsions using electrostatic attraction of charged biopolymers to oppositely charged droplets. In this method, an interfacial membrane that consists of multiple layers of biopolymers is prepared by adsorbing consecutive layers of oppositely charged biopolymers onto a primary emulsion prepared using a conventional homogenization technique [Moreau, L. et al. 2003].

Physical and chemical factors affect the formation of emulsions, such as choice of emulsifying agent, method of adding the two phases together and temperature. There are many properties of emulsions which technologists want to control. The most important of those properties are: concentration of the immersed phase, stability, size and distribution of droplets and viscosity of emulsions.

One of the ways to make uniformly sized emulsion is through the use of micro-fluidic technology (Fig. 3.1). The mixture of two fluids in a micro-channel is driven by volume flow rate or applied pressure. To produce solid particles via micro-fluidic droplets a further treatment is needed. This treatment could be UV photo-polymerization, solvent extraction or ionic cross linking. Methods which avoid moving parts (passive methods) can be grouped by the flow field near the pinch-off [Christopher, G.F. et al. 2007].

Other electrical or micro-fluidic methods used for emulsion production include: electro-capillary emulsification [Watanabe, A. et al. 1978], micro-porous ceramic membrane emulsifiers [Joscelyne, S.M. et al. 2000], ultrasound emulsification [Challis, R.E. et al. 2005] and coaxial jet emulsifier [Barrero, A. et al. 2007]. One of the methods is the electrospray technique which creates fine drops in high electric field. The history of electrified spraying had started with Bose in the mid 18th century who reported first electrohydrodynamic spraying, followed by Rayleigh in the late 19th century who studied the electrified drop creating field more deeply. Systematic investigation was carried out in the early 20th century by Zeleny followed by Taylor's work (1964) who took the basic understanding of the phenomena to the next level. Hayati et al. (1986) explained the mechanisms of the electrospray technique and Barrero et al. (2007) used electrohydrodynamic flow to produce droplets and emulsions.

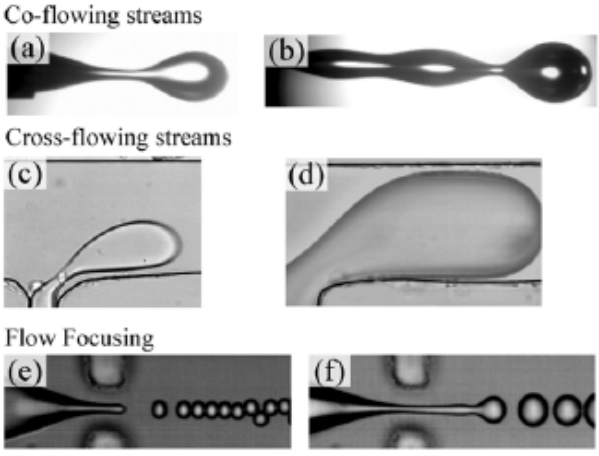

Fig 3.1 Images of different droplet break-ups: co-flowing streams dripping (a), jetting mode (b), break-up in cross-flowing streams unconfined (c), confined T-junction (d), flow focusing geometries, dripping (e) and flow focus jetting mode (f) [Christopher, G.F. et al. 2007]

3.1.2 Emulsion stabilization

The dispersion of two immiscible liquids is energetically unfavoured because emulsions have high specific surface areas and they are thermodynamically unstable. However emulsions can be stabilized in various ways, such as adding surfactant (surface active agent) or small particles. Surfactants are amphilic compounds which mean they contain hydrophilic head group and a hydrophobic tail group. The hydrophilic head group generally (excluding nonionic surfactants) ionisable and forming hydrogen bonds. Surfactants can accumulate at interfaces (is called adsorption) due to their amphilic structure which lowers the interface tension. Surfactants are divided into four groups by the hydrophilic head group [Butt, H.J. et al. 2006]:

- Anionic surfactants have a hydrophilic group which carries a negative charge, e.g. sodium dodecyl-sulphate, $C_{12}H_{25}SO_4Na$, SDS.
- Cationic surfactants have a positive charge in the hydrophilic part, e.g. cetyl ammonium bromide, $C_{16}H_{33}N\ (CH_3)_3Br$, CTAB.
- Nonionic surfactants are not charged, e.g. sorbitan monopalmitate.
- Zwitterionic surfactants have positive and negative charge; the aggregated charge is zero, e.g. N, N-dimethyldodecylamine N-oxide.

More than a century ago Pickering (1907) discovered that solid particles could stabilise emulsions. The solid particles are adsorbed at the liquid/liquid interface and created steric barriers to drop coalescence and stabilize the emulsions. To remove the particles from the interface more energy is needed than for the surfactant stabilized emulsions. Pickering discovered that if the solid particles wetted the water more than they do the oil phase, O/W emulsion is created. Stabilising the emulsion through solid particles depends on the mediums, particles size and shape, particles' wettability and the inter-particle interactions. Particles on the interface do not reduce the surface tension dramatically (while a surfactant on the interface does) [Hunter, T.N. et al. 2008]. Binks et al. (2007) investigated the O/W emulsion stabilised by solid particles and surfactant mixture. The pH of the continuous phase played an important role. Oil-in-water emulsions are more like to be obtained with hydrophilic molecules.

The stabilization of emulsion by nanoparticles is due two one of the two main mechanisms [Horozov, T.S. et al. 2006]:

-the droplet is fully covered by particles producing a layer around it and protect against coalescence by steric (mechanical) stabilization (Fig. 3.2a),

-the droplet is partly covered by particles, creating a particle bridge between the drops to avoid the coalescence of drops. The particle monolayer is a product of the strong capillary attraction due to the meniscus around the particles (Fig. 3.2b, c). This mechanism occurs at a low concentration of nanoparticles for emulsion stabilization.

The forces between nanoparticles at the aqueous-non-polar interface [Bresme, F. et al. 2007] are: (i) electrostatic interactions (Coulomb, dipole), (ii) van der Waals and repulsive interactions, (iii) capillary forces (flotation force, immersion force) and (iv) fluctuation force.

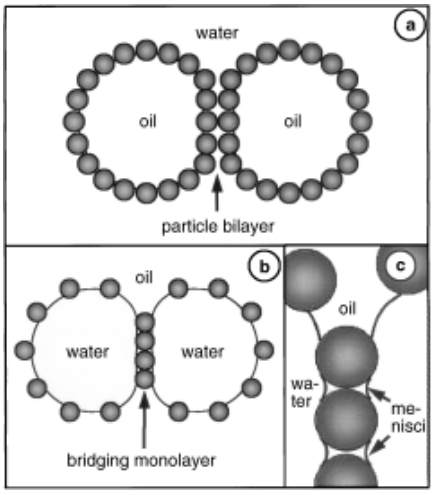

Figure 3.2 Mechanisms for the colloidal particles stabilized emulsions: steric stabilization by densely packed particle layer (a) and bridging stabilization by partly covered particle layers (b) and the menisci around the particles (c) [Horozov, T.S. et al. 2006]

The interface between the oil and the water in emulsion is a suitable place for the self-assembly of nanoparticles, driven by the reduction of interfacial energy. The hydrophilic silicon dioxide nanoparticles form a monolayer at the O/W interface under variable solution conditions [Simovic, S. et al. 2003]. Leunissen et al. (2007) proved that it is not essential for the particles to be partially wetted by both phases. Non-wetting particles are sitting adjacent but not in the interface.

Whitby et al. (2006) made the O/W emulsion stabilized by silica nanoparticles. The adsorption of nanoparticles at the O/W interface is thermodynamically positive

because O/W interfacial energy is higher than either of the particle-liquid interfacial energies. Whitby made a <0.2 vol % nanoparticles in the 2 vol % oil-in-water emulsion which was stable for weeks due to the nanoparticles' adsorption onto the drop surface.

The studies by Horozov et al. (2005 a, b) indicated that the particle-oil interface has electric charge and in the oil-particle suspension case the particles are attracted to the O/W interface. The oil-water interface in the emulsion is negatively charged due to the adsorption of hydroxyl ions (OH^-).

In the case of silica nanoparticles in liquid paraffin, the size of the particles is significant for the image-force interaction. The particle interface interaction also depends on the difference between the dielectric constants of the three phases (oil-water-nanoparticles) [Danov, K.D. et al. 2006].

Oleic acid, stabilised hematite and CdSe/ZnS quantum dots with tri-noctylphine coating were used to create magnetic and fluorescents emulsions. The results show that at low hematite concentration the nanoparticles localised at the droplet surface and at higher concentration they localised in an inner volume [Mandal, S.K. et al. 2005].

3.2 Surface- and interface tension

Adamson (1967) defined the interface tension as the unit of interfacial area created by reversible work at constant temperature (T), pressure (p) and number of molecules (n):

$$\gamma_{12} = (\partial G/\partial A)_{T,p,n} \quad (3.1)$$

where G is the Gibb's free energy of the system and *A* is the interfacial area. Interfacial tension is energy per unit area. The interface tension (γ_{12}) is a connection between two phases and surface tension (γ_1) is a special case of it when one of the phases is air.

The surface tension is a function of the entropy and enthalpy of interfacial structure per unit surface area, Δs_s and Δh_s respectively [Adamson, A.W, 1967]:

$$\gamma = \Delta h_s - T\,\Delta s_s \quad (3.2)$$

$$\Delta h_s = h_s - \Gamma_i h_i - \Gamma_2 h_2 \quad (3.3)$$

$$\Delta s_s = s_s - \Gamma_i s_i - \Gamma_2 s_2 \quad (3.4)$$

where Γ_i is the surface concentration of species *i,* h_s and s_s are the surface enthalpy and surface entropy per unit area and h_i and s_i are the partial molar enthalpy and partial molar entropy of the species *i* in the bulk phase. The bulk enthalpy and entropy is different from the surface enthalpy and entropy.

The attraction between the molecules of the fluid has various inter molecular forces as a result of which surface tension occurs. In the bulk liquid the molecular interactions are balanced by attractive forces and each molecule is bond with a characteristic binging energy. The molecular interactions are interrelated to the viscosity of the fluid. The molecular interactions are stronger when the molecules are closer together. At the surface on of the liquid phase is replaced by air which means weak interaction due to the low density of the air. The interactions of molecules with the air are minor and binding energy is reduced. Molecules at the surface have an excess surface enthalpy (energy) which is equal to the number of missing bonds multiplied by the binding energy per bond. Surface molecules have larger entropy than bulk molecules which means positive entropy of surface formation [Adamson, A.W. 1967, Alam, K. et al. 1999].

Molecules at the interface have stronger intermolecular interactions which mean lower enthalpy of interface and reduced interface tension which generally less than the surface tension of each of the phases.

Water and other polar liquids have strong intermolecular interactions which result in high surface tension but any contamination lowers the surface tension. Water has the highest surface tension due to the high degree of hydrogen bonding. Hydrocarbons have low and fluorinated fluids have very low surface tension, because the fluorine atom does not share electrons very well. This all means the chemical composition of the fluids is an important factor to determine the surface and interface tension of them.

3.2.1 Applications and measuring techniques of surface tension

The understanding of phenomena that occur at the interfaces has interested many members of both the industrial and academic communities. Surface tension is important in number of applications such as packaging, biomedicine, printing and cleaning.

Several methods were used to measure the surface tension of liquids. Figure 3.3 shows the various methods to measure surface tension. More details about the methods are in Chapter 6. The method can be static or dynamic and in either case solid particles can be involved in the fluid. The measurement of the surface and interfacial tension by a tensiometer is based on force measurement of the interaction of a probe with a surface or interface of fluids. In tensiometry the probe is hung on a balance and placed in contact with a testing liquid. Two types of probes are commonly used: DuNouy Ring and Wilhelmy Plate. Another kind of method is the pendant drop shape analysis technique which uses the shape of a drop of liquid hanging down from a syringe tip. It has a balance of forces. In all methods which are used for measuring the surface tension a great deal of care must be taken to avoid any contamination which can modify the result. Several parameters, such as temperature, time of the measurement, dust and any contamination, can have an effect on the surface tension. In the sessile and pendant drop method the size of the drop also has an influence on the result. Choosing the suitable method requires a great deal of care since each method has advantages and disadvantages.

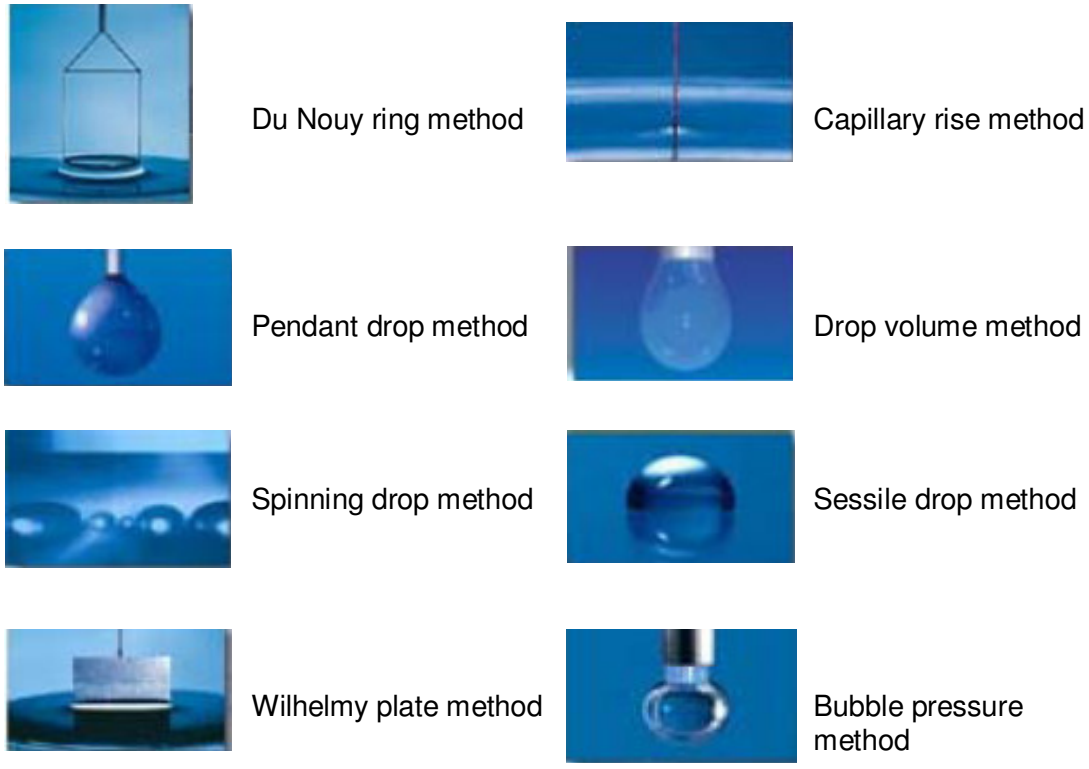

Figure 3.3 Surface tension measuring methods

3.2.2 Nanoparticles at the interface

The adsorption of colloidal particles at the interfaces between two immiscible fluids was investigated by Pickering (1907) about a century ago. Fluid interfaces are complex because electrostatic and inter-particle forces create long range deformation of the interface. Particles adsorb onto a liquid interface if the total energy is thereby reduced. The types of interaction between the particles and two immiscible fluids include van der Waals, solvation and electrostatic interactions. Electrostatic charges on the particles play an important role in their adsorption at the interface of the liquids. Vignati and Piazza (2003) suggested a mechanism of the solid stabilized emulsions and they believe that the stabilization is due to steric hindrance or surface rheology rather than the reduced interfacial tension of fluids. If small particles (submicron and nano-sized) have wettability with two fluids then it can adsorb onto the interface between them by reducing the shared area and the energy cost [Clegg, P.S. et al. 2008]. At the interface of two immiscible fluids with nanoparticles three kinds of interfaces are present: liquid-liquid, and two solid-liquid. Assembly of nanoparticles is driven by the minimization of the Helmholtz free energy.

The fluid-fluid interface offers potential for assembly of nanoparticles. Nano-size charged particles at an aqueous interface are stabilized by a repulsive Coulomb interaction. When the aqueous phase is connected with the oil phase the particles will exhibit long-ranged dipolar repulsion [Pieranski, P. 1980, Nikolaides, M.G. et al. 2002]. Nikolaides et al. (2002) measured the attractive interactions, between colloidal particles at an oil-in-water interface, due to capillary forces. Dipolar interaction causes repulsion and the interfacial distortion causes capillary attraction.

Nanoparticles in suspension/emulsion dispersed in an immiscible fluid are likely to transfer from the bulk phase to the interface dependent on their wettability. Hydrophilic particles can stabilize oil-in-water emulsions while hydrophobic particles prefer to stabilise water-in-oil emulsions. The particles are saturated at the surface and cover the interface by self-assembly.

The interactions and forces between nanoparticles at fluid interfaces are presented in Table 3.1. In the Table R means the colloid size (radius for spherical particles) and h means a distance of the next closest particle, which is $h=d-2R$ for spherical particles, d is the intercolloidal distance, *att* means attraction and *rep* means repulsion.

At the interface between particle and medium the main interactions are electrostatic and van der Waals forces. The capillary interaction which is affected by thermal fluctuations plays an important role. The last in the list are the solvation forces which are connected to molecular information of the interface. The last column in the table gives the particle size range in which the interaction can be of significance.

Table 3.1 Interactions at fluid and nanoparticle interfaces [Bresme, F. et al. 2007]

Interaction	Character	Functionality	Strength ($k_B T$)	Particle size
Capillary				
–immersion	att/rep	$\ln(R/d)$	$10 \ldots 10^5$	nm... mm
–electrostatic	att	$(R/d)^3$	$1 \ldots 10^3$	100 nm ... μm
–anisotropic	att/rep	$(R/d)^4 f(\phi)$	$1 \ldots 10^5$	μm
Electrostatic				
–dipolar	rep	$(R/d)^3$	$10 \ldots 10^5$	nm ... μm
Van der Waals	att	$(R/h) \ldots (R/d)^6$	$0.1 \ldots 1$	nm ... μm
Fluctuation force				
–fixed colloids	att	$(R/h)^{1/2} \ldots \ln \ln(d/R)$	1	nm
–free colloids	att	$(R/h)^{1/2} \ldots (R/d)^8$	1	nm
Solvation	att/rep/osc		1	nm

Vafaei et al. (2006) investigated the change of contact angle of aqueous nanofluids containing different size bismuth-telluride (average size 2.5 nm and 10.4 nm) nanoparticles. They found that both the concentration and size had an influence on the results; the contact angle increased with the concentration increase and with the size reduction.

Ravera et al. (2006) conducted an experimental investigation of the changes of the interfacial properties of liquid/air and/or liquid/liquid systems by nanoparticles with surfactant in water. They used different concentrations of silica nanoparticles with same amount of CTAB (hexadecyl-trimethyl-ammonium bromide) surfactant. They found that when they increased the concentration of the nanoparticles the starting 40 mN/m value (no SiO_2 in water/CTAB system) changed to 70 mN/m containing 0.5 wt% SiO_2. Due to the adsorption of CTAB on the particles surface in the water/CTAB/SiO_2 system increased the surface tension of the system. When they kept the nanoparticle concentration constant (1.0 wt %) and increased the surfactant concentration the surface tension remains constant.

Scientists developed different methods to control the surface wettability. These are stimuli-responsive materials which have surface free energy or morphology properties

sensitive to external environmental changes such as light irradiation, electric field, solvent and thermal treatment. The surface free energy of the substrate can be tuned, for example the surface profile can be changed from hydrophilic to hydrophobic or visa versa. One of the methods which are used to control the surface wettability is light switches. It is quick and can be targeted to individual particles (Fig. 3.4). The most studied photosensitive materials are titanium dioxide and zinc oxide. The reversible generation of photo-generated surface oxygen defects site cause the change of the surface wettability.

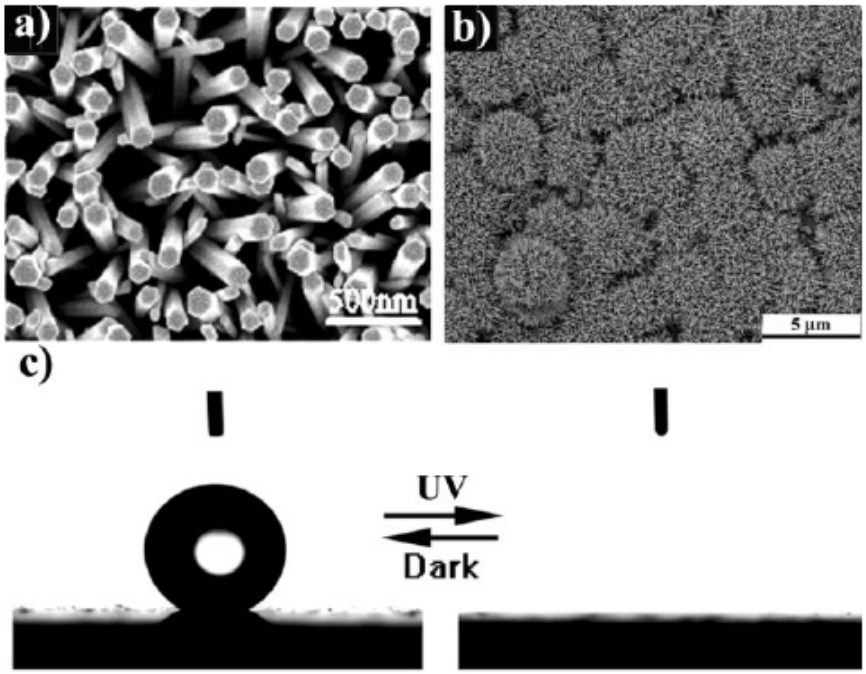

Figure 3.4 Reversible switching between hydrophobic and hydrophilic surface behaviour, ZnO nanorods (a), lotus-like TiO_2 nanorods (b) and the ZnO nanorods film before and after UV illumination (c) [Feng, X. et al. 2006]

3.2.3 Surface tension under electric field

Liquid drop under electric field changes in at least two ways:

-the shape of the drop, which is a pronounced effect and easily detectable,

-the surface tension of liquid, that is harder to detect.

One of the ways to measure the surface tension of liquid while applied field exists is the vibrating jet mode by Sato et al. (1998), because this method does not have any direct contact with the liquid surface. The surface tension of liquids is reduced by an

applied electric field [Sato, M. et al. 1997, 1998]. This reduction could be due to the macroscopic charged liquid particles repelling each other and therefore decreasing the tension force. Bateni et al. (2005) investigated the contact angle of sessile drop under electric field and found that the contact angle of polar fluids increased in electric field but there was no change for non-polar fluids.

3.3 Suspension rheology

Dispersions and suspensions have been of interest to both science and industry. Rheological science is the study of the flow and deformation of matter under applied force.

The shear stress (σ in Pa) is defined as the amount of force (F) applied to the sample per unit area (A):

$$\sigma = F / A \quad (3.5)$$

The shear rate (γ in s^{-1}) is the speed of the deformation:

$$\gamma = dy / dt \quad (3.6)$$

Viscosity (η in Pa s) is a property of suspension which is measure of its resistance to flow:

$$\eta = \sigma / \gamma \quad (3.7)$$

A viscometer is a device to measure the changes in viscosity of liquids or suspensions with varying time, shear stress or shear rate. Liquids can have Newtonian or non-Newtonian behaviour which depends on the complex interaction including hydrodynamic interaction between solid particles and the surrounding liquid, the attractive and repulsive force between the solid particles and the particle-particle interactions. The viscosity of some suspensions is dependent on the shear rate and by this dependent the rheological behaviour can be classified. Figure 3.5 shows the characteristic flow curves of Newtonian and non-Newtonian suspensions.

A Newtonian fluid has a viscosity that is independent of the shear rate and the viscosity is constant with respect of time of shearing. Shear thinning behaviour describes viscosity that decreases when the shear rate increases, and shear thickening behaviour describes viscosity that increases with the shear rate. The Bingham fluid behaviour means certain amount of force (yield value) needs to be applied to the

sample to detect the induced flow. Below this force the fluid has similar characteristic to that of a solid. Pseudoplastic behaviour means the viscosity instantaneously decreases when the shear rate increases.

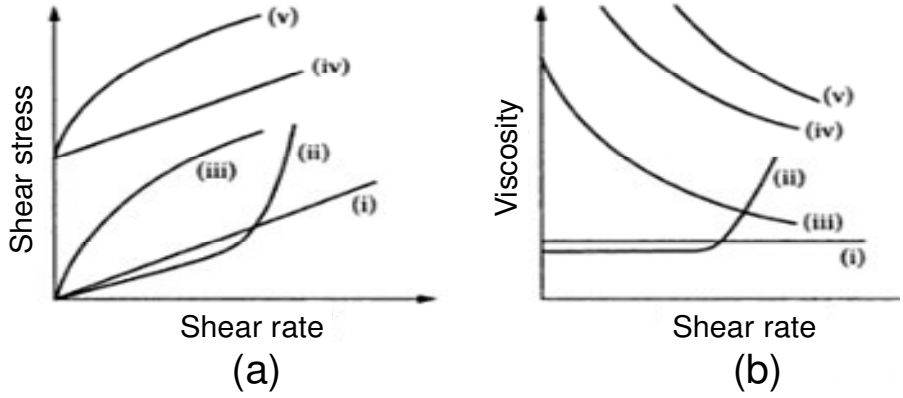

Figure 3.5 Rheological behaviour of suspensions: (i) Newtonian, (ii) shear thickening, (iii) shear thinning, (iv) Bingham plastic, and (v) pseudoplastic [Rahaman, M.N. 2006]

3.3.1 Influence of forces on viscosity

Three kinds of forces co-exist to various degrees in suspensions. Firstly, the interactions between the particles must be considered. These are controlled by the properties of the medium such as polarizability. The forces between particles can be either attractive or repulsive. Attraction can come from the van der Waals attraction between the particles or electrostatic attraction on different parts of the particles. The repulsion can come from like electrostatic charges or from entropic repulsion of the surfactant on the particles' surface. If the attraction is overcome the suspension flocculates, if the repulsion wins out a dispersed system occurs. Secondly, the Brownian motion, which is a randomising force, is strongly size dependent. Thirdly, there are also viscous forces acting on the particles. The viscous forces are proportional to the velocity difference between the particles and the surrounding medium [Barnes, H.A. et al. 1993].

Rheological measurements can give some information about aggregation in suspensions. The rheological yield values are related to the strength of the structure or of agglomerations which can be damaged by shear. The viscosity describes the volume of the fluid which aggregates at the shear rate used. Rheological data also carry information about the practical behaviour of the suspensions. In magneto rheological fluids, for example, the magnetic interaction between particles overshadows the van der Waals force and act over a greater length scale. Particle structures are formed such as chains and columns [Scholten, P.C. et al. 1990].

3.3.2 Influence of particle characteristic on the viscosity

Volume fraction

Einstein's theory of the relative viscosity (η/η_s) for small spherical particles at very low concentration ($\varphi<0.05$) is [Barnes, H.A. et al. 1993]:

$$\eta/\eta_s=1+2.5\,\varphi \qquad (3.8)$$

where η is the viscosity of the suspension,

η_s is the viscosity of the pure medium,

φ is the volume fraction of particles.

At this very low particle concentration the particle/medium interactions are important. The spherical particle has rotational motion with a same velocity as the medium flow velocity. Forces are acting on the upper and the lower hemisphere of the particle and this makes it rotate. This rotation will be resisted by viscous forces round the particle surface. As the overall flow is kept constant the stress must be increased, therefore the viscosity is increased by the added particles.

At higher particle concentrations, the effect of pairs of particles also has to be considered. If two particles are at different levels in the flow field the higher particle will overtake and pass the particle at the lower level. If the particles are too close together (less than 2r, where r is the particle diameter) the trajectories of the particles will be distorted. When they have higher concentration ($\varphi > 0.05$) the hydrodynamic forces have to be taken into account as do the near-miss trajectories and the influence of the particles' Brownian motion. At higher concentration ($\varphi > 0.625$) the increased particle concentration and the magnitude of inter-particle forces increases the chance and size of flocs i.e. the random close packing of particles and particle networks.

At high concentration the particles in the suspension are at a very low shear rate, the Brownian forces are dominating and the particles have to move around each other or bounce off. Under these conditions the viscosity will be high but constant. At slightly higher shear rates the velocity gradient induced an orientation of the particles' structure and the particles can pass each other more freely, so the viscosity is lower in this shear rate. At very high shear rates the structure is grossly orientated and the particles form layers separated by clear layers of the medium and at this point the viscosity is at its lowest value. This suspension has a shear thinning behaviour [Barnes, H.A. et al. 1993].

As the concentration of particles increases, the interaction between particles during flow which causes the viscosity changes normally increases. Krieger-Dougherty in Eq. (3.9) shows that for spherical particles the rheological properties are directly related to the volume occupied by the particles [Barnes, H.A. et al. 1993].

$$\eta_{rel}=[1-(\varphi/\varphi_m)]^{-[\eta]\,\varphi_m} \qquad (3.9)$$

where φ is the volume concentration of particles in the suspension , φ_m the maximum packing fraction, which is 63% for random close packing, $[\eta]$ is the intrinsic viscosity, or effective hydrodynamic shape factor, which is equal to 2.5 for spherical particles.

Therefore, if the viscosity of the medium and the concentration of the particles are known, and the maximum packing of the particles is determined, then the viscosity of the nanoparticle suspension can be calculated by the Krieger-Dougherty equation.

Most of the models were based on interactions between the particles and used the same viscosity of the media in the thin film around the particles as in the bulk, which is sometimes not a true depiction of the situation.

Particle size

Generally the particles size and size distribution of suspended solids have influence on the suspension viscosity due to the collision and packing [Chen, S. 2006].

Particle morphology

Generally the particles geometry has influence on the viscosity. Figure 3.6 shows the orientation and deformation of rod-like particles (a), spherical particles (b) and particles aggregation (c) under shear [Chen, S. 2006]. Particles with different morphology aggregate and de-aggregate in a different way.

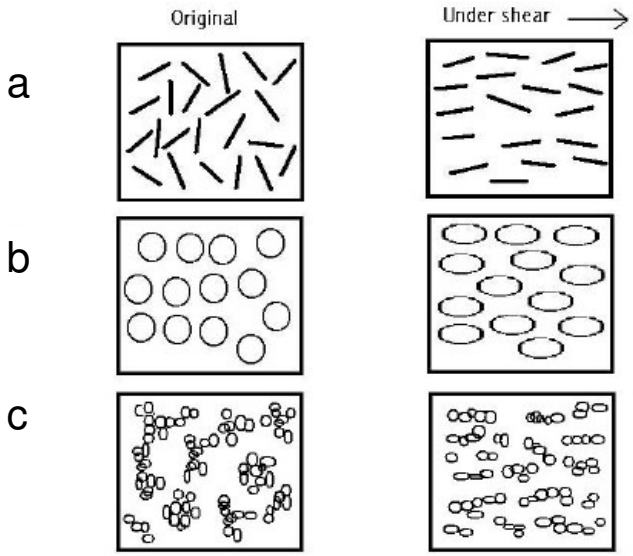

Figure 3.6 Schematic graph of deformation and structure break-up under the applied force for rod-like particles (a), spherical particles (b) and aggregations (c) [Chen, S. 2006]

3.3.3 Viscosity of nano-suspensions

The stability of a nano-suspension is governed by surface and interfacial phenomena. Nanoparticles in suspensions mostly aggregate due to the van der Waals force of attraction if they not protected from it. The van der Waals force can be reduced by introducing repulsive forces on the surface of the nanoparticles. Stability of the suspension can be achieved by the introduction of repulsive forces through electrostatic or steric stabilisation [Tripathy, S.S. et al. 2008].

$BaTiO_3$ suspension in 2-butanol-ethanol with phosphate ester surfactant has been studied by Chartier et al. (1993). They showed that in a suspension with a low solid concentration the electrostatic stabilization is dominant but that at high solid concentration steric stabilisation is dominant.

Paik et al. (1998) studied $BaTiO_3$ suspension in ethyl alcohol and fish oil. They concluded that the stability of the suspension was dependent on the solvent's polarity and the electrostatic surface potential of the $BaTiO_3$ particles. The stability of $BaTiO_3$ particles suspended in organic solvent is due to the electrostatic repulsive force.

The main portion of the rheological behaviour of a nanoparticle suspension depends on the interaction between nanoparticles. At high shear rate the large size network-structures are destroyed but when the shear rate decreases from the top value these network-structures start to re-establish [Ghasemi, E. et al. 2008].

Garg et al. (2008) investigated the viscosity of copper (particle size 200 nm) nanoparticles in ethylene glycol up to 2 vol % without surfactant and the results show that the increase of the viscosity was four times higher than predicted by the Einstein model (Eq. 3.8), but their data could fit to: $\eta/\eta_s=1+c_\eta\,\varphi$, where c_η ~11. There is a net attractive inter-particle force which gives rise to the structure of networks of particles. The rheological behaviour of a nanoparticle suspension is dependent on the solid concentration because the interaction between the nanoparticles is inversely proportional to the average separation distance. When the solid content increases the nanoparticles are get closer to each other and the van der Waals forces become dominant in comparison to the total interaction energy. The nanoparticles also form strong networks of flocs [Lopez-Esteban, S. et al. 2007].

Chen and Ding (2007) studied the rheological behaviour of titania nanoparticles in ethylene glycol with the nanoparticle concentration between 0.5 and 0.8 wt% the nanofluids were found to have Newtonian rheological behaviour. Theoretical analysis shows that the Krieger-Dougherty equation (Eq. 3.9) predicted the high shear viscosity of spherical titania nanoparticles in ethylene glycol based nanofluid. They show that the shear thinning behaviour of a nanoparticle suspension depends on the particle concentration and the base fluid's rheological character.

Hong et al. (2007) studied the rheological behaviour of the iron oxide aqueous suspension containing surfactant. They used oleate-sodium and PEG (poly-ethylene-glycol) as a surfactant and the solid loadings of the suspensions were up to 38 wt%. They found that the viscosity influenced by the temperature at low concentration of iron oxide and at higher concentration the suspension showed shear thinning behaviour.

The dependence of suspended particles size on the viscosity was studied for Al_2O_3 -(36 nm and 47 nm diameter) -water and CuO-water suspensions containing less than 4% volume fraction of nanoparticles [Nguyen, C.T. et al. 2007]. They estimated the viscosity of nanofluids using the Einstein formula but found it did not fit. Further theoretical investigation enabled the Batchelor equation (Eq. 3.10) to be established [Barnes, H.A. et al. 1993].

$\eta/\eta_s=1+2.5\ \varphi+6.5\ \varphi^2$ (3.10)

where η is the viscosity of the suspension,

η_s is the viscosity of the pure medium,

φ is the volume fraction of particles.

This equation corrects Einstein's formula and considers the effect due to the Brownian motion of spherical particles. They found that the theoretical formulas underestimated the viscosity of the nanofluids. They concluded their results as: the dynamic viscosity of nanofluid increases with the particles volume fraction and the particles size in Al_2O_3-H_2O suspension at higher concentration had effect on the viscosity [Nguyen, C.T. et al. 2007].

The rheological behaviour of nickel nanoparticle dispersion in α-terpineol with organic surfactant was examined by Tseng et al. (2006). The solid loadings went up to 28% and the shear rates were between 1 and 1000 s^{-1}. They suggested the oligomer-polyester molecules are adsorbed onto the nanoparticles' surface and formed a steric layer on it. The interparticle potential was dominated by van der Waals forces. The stability of nanoparticles in liquid medium is determined by repulsive (steric interaction in non-aqueous system) and attractive forces (such as van der Waals forces).

Hwang et al. (2005) studied the rheological behaviour of titania nanoparticles suspended in silicone oil. When the viscosity of silicone oil medium was high the suspension of titania nanoparticles showed shear thinning behaviour.

Generally the key factors which have influence on the nanoparticulate suspension's viscosity are: concentration, size, shape, size distribution, surface properties of nanoparticles and the properties of the medium.

Chapter 4 Literature background of phenomena under electric field and dielectrophoresis

As known from the late 19th century through studies by Lord Rayleigh liquids can readily interact with electric fields, which can cause them to move, form jets or break into drops. Further scientific observation made by Zeleny in the early 20th century and forty-five years ago by Taylor. Taylor (1964) studied the behaviour of various fluids under electric field and showed that the liquids even with low conductivity (< 10^{-9} S/m) would allow an electric charge to form on the drop surface. Liquids with low electrical conductivity make a fundamental difference to the physical principle governing the droplet producing process. The electrical relaxation time exceeds the hydrodynamic time and droplet generation is possible. The electric field acts on a liquid meniscus and works against the surface tension. When the applied electric field reaches a certain intensity, a cone is formed from the liquid and at higher field strengths a jet of liquid is projected from the cone tip. Repeated generation of small and uniform liquid drops [Fernández de la Mora, J. 1990] is desirable for many areas of technology.

Some nanofluids show special properties under electric field, for example electrorheological fluids are ideal mechanical–electrical interfaces because of their fast response time and their reversible rheological properties [Espin, M.J. et al. 2006].

This chapter presents an overview of electrical conductivity and dielectric permittivity of nanofluids. The final part of this chapter is dedicated to dielectrophoretic phenomena and their use in various areas of science from biology to engineering.

4.1 Phenomena under electric field

The term *electrohydrodynamics* (EHD) describes a range of phenomena. EHD in its broadest sense covers the following types of particle and fluid transport mechanisms: electrophoresis, electrorotation, electro-osmosis and dielectrophoresis.

Electrophoresis is a movement of charged particles in a stationary fluid under ac or dc uniform electric field. Electrophoresis was discovered by Reuss in the early 19th century, when he observed that clay particulates in water-based suspensions migrate under an electric field. Uncharged particulate suspension carries an electric surface

charge and electrophoresis occurs due to the specific molecular structure of the fluid at the interface of the particles. *Electrorotation* takes place when the suspended particles display angular movement under electric field. *Electro-osmosis* is a movement of the diffuse ionic layer around a fixed surface charge, the fluid moving along parallel to the fixed surface. *Dielectrophoresis* (DEP) occurs when a non-uniform ac or dc electric field exists and uncharged, polarized particles are suspended in the fluid.

4.1.1 Dielectric permittivity

James Maxwell (1831-1879) formulated the concepts of permittivity and permeability to serve as constants in his equations which described most electro-magnetic behaviour. Permittivity (ε) is a measure of the ability of a material to be polarized by an applied electric field. A given amount of material with high permittivity can store more charge than a material with lower permittivity. Permittivity, also called electric permittivity, is a constant of proportionality that exists between electric displacement and electric field intensity. This constant is equal to approximately $8.85 \cdot 10^{-12}$ F/m in free space (vacuum). In other materials it can be lot different, often substantially greater than the free-space value, which is symbolized ε_o. In applications, permittivity is often expressed in relative, rather than in absolute, terms. If ε_o represents the permittivity of free space and ε represents the permittivity of the substance in question, then the relative permittivity ε_r, is given by:

$$\varepsilon_r = \varepsilon / \varepsilon_o \qquad (4.1)$$

Relative permittivity also called dielectric constant and the complex permittivity is a function of frequency (ω). The response of materials to alternating field is characterized by a complex permittivity, which have real and imaginary parts:

$$\varepsilon(\omega) = \varepsilon`(\omega) + i\varepsilon``(\omega) \qquad (4.2)$$

where: ε`` is the imaginary part of permittivity which is related to the dissipation or loss of energy within the medium, and ε` is the real part of permittivity which is related to stored energy within the medium.

Under AC electric field the frequency of the signal comes into play and the polarization phenomena can be different at different frequencies [Maex, K. et al. 2003]. At different frequencies three polarization phenomena occur as shown in Fig.

4.1. At 10^9 Hz the maximum frequency for orientation polarization above this frequency distortion and electronic polarization occurs and in the order 10^{13} Hz resonance frequency for distortion polarization. At 10^{15} Hz the resonant frequency of the electronic polarization occurs.

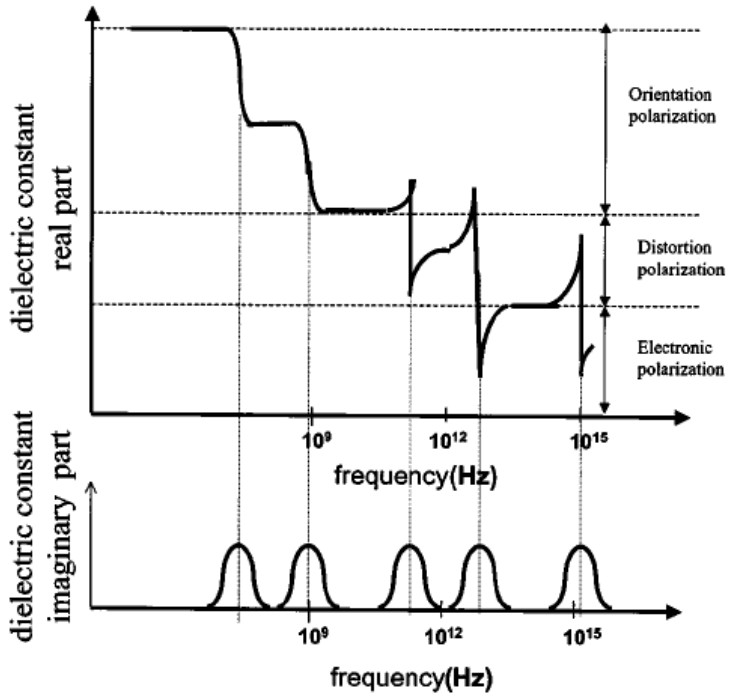

Figure 4.1 Schematic diagram of the real and imaginary parts of permittivity of fictive material [Maex, K. et al. 2003]

Saimoto et al. (1999) studied suspensions of micro and submicron-metre size silica particles in silicone oil under shear and electric field. They found that the relative permittivity of pure silicone oil was independent of the electric field strength and shear rate. The relative permittivity of suspensions containing silica particles (630 nm) and water (2 wt %) were found to decrease with an increase in the field strength (1-4 kV/mm). When silica particles (75 μm) are suspended in silicone oil and water (7 wt %) the results show that the shear rate was nearly constant at different electric field strengths (1-4 kV/mm).

Hallouet et al. (2007) investigated a composite of magnetite nanoparticles in an epoxy resin and they found that the result of their permittivity measurement could not be described by any models due to the formation of agglomerates. The ferromagnetic resonance occurs at 3 GHz and they found that it is independent of the particle concentration.

4.1.2 Electrical conductivity of nanofluids

The transport of nanofluids under electric field is important in several microfluidic applications including dielectrophoresis. The nanofluids and the discovery of their unexpected and sometimes unconventional properties require interdisciplinary expertise.

Nanoparticles tend to agglomerate if they are not prevented from doing so with functionalization or surface coatings. This leads to uncertainties in the effective particle size, particle numbers and inter-particle spacing in nanofluids. Perhaps as a consequence the overall behaviour of such fluids cannot be explained effectively by existing models based only on the volume fractions and the physical properties of the individual phases [Wen, W. et al. 2003, 2008, Gong, X. et al. 2008]. Some different models have been discussed to explain some of the unusual properties of nanofluids [Choi, S.U.S. 2009].

-*Nano-layer of liquid molecules* by Yu and Choi (2003).The ordered liquid nano-layer create a "bridge" between the nanoparticles and the base fluid. This is a static model.

-*Percolation theory*. Foygel et al. (2005) used Mont Carlo simulations to show that the percolation can start at very low concentrations (0.01 vol %).

-*Brownian motion of nanoparticles*. This is a dynamic model which closer to the reality because a nanofluid is a dynamic system even if the fluid is stationary but the nanoparticles have Brownian motion.

-*Nano-convection*. Xuan et al. (2006) develop a model with static and dynamic terms which take the nanoparticles size into account and their work shows that the nano-convection effect is stronger when the particles' size $\leq$ 30 nm. Koo et al. (2004) explain the effect of fluid dragged by nanoparticles in their theoretical model. Patel et al. (2005) use the Brownian motion, nano-convection and special specific surface area of nanoparticles to explain the behaviour of nanofluids.

One possibility for the unexpected behaviour of nanofluids is the short range particle–fluid attraction through excess fluctuations in the potential energy. The aggregates in the nanofluid under electric field are interconnected particles and the physical contact of particles in this network provides higher electrical conductivity. The agglomerates capture some fluid on the particle surface and this entrapped fluid could behave like a

solid which effectively may change the solid volume fraction. From another point of view the entrapped fluid on the surface of the particles could act as a shell around the particles providing different electrical properties than the particle had originally. The agglomeration-deagglomeration kinetics [Chakraborty, S. et al. 2008] of the solids with electrorheological style ordered chains could be the explanation of the increased electrical conductivity behaviour of nanofluids.

4.2 Dielectrophoresis

Dielectrophoresis (DEP) was first reported by H.A. Pohl at Princeton University in the early 1950s and defined as "*the translational motion of neutral matter caused by polarization effects in a non-uniform electric field*" [Pohl, H.A. et al. 1977].

If the uncharged particle with the ability to become polarized is placed in a non-uniform electric field the particle will experience a net force due to electric field gradient and move toward to the highest/lowest field intensity.

The motion is dependent on how polarized the particle becomes compared to the liquid medium. If the particle is more polarizable than the medium the particles move toward the higher electric field which called positive dielectrophoresis. If the medium is more polarizable than the particles the particles will move away from the high electric field this called negative DEP. Both variations are seen in Fig. 4.2.

Figure 4.2 (a) and (b) shows electrophoresis in a uniform electric field when the particle is more polarizable than the surrounding medium (a) and the particle less polarizable than the fluid around it (b). Figure 4.2 (c) and (d) shows positive and negative dielectrophoresis in non-uniform electric field respectively. The particle on Fig. 4.2c is more polarizable than the surrounding medium and it is moving towards the region of higher field strength; the particle that is less polarizable than the fluid (Fig. 4.2d) is moving towards a region of lower field strength.

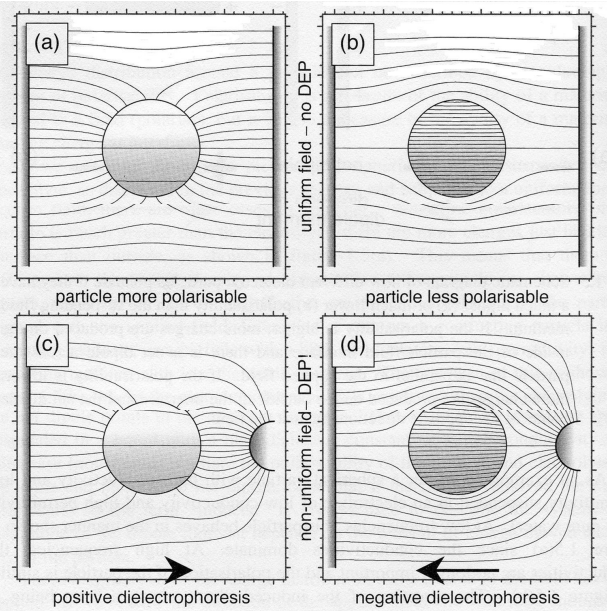

Figure 4.2 Schematic graph of electrophoresis in uniform electric field (a, b) and positive (c) and negative (d) dielectrophoresis in non-uniform electric field [Morgan, H. et al. 2003]

4.2.1 Application for dielectrophoresis

In the last decade DEP received increased interest from research and industry. State-of-the-art research involves dielectrophoretic methods in biological, medical and pharmacological fields. The main use at the moment for DEP is the manipulation of biological cells, viruses, proteins and DNA [Pethig, R. et al. 1997].

Suehiro and Pethig (1998) used a three-dimensional grid electrode to move cells by positive or negative DEP. To allow visual observation indium tin oxide electrodes were used. They also controlled the electrode size and the applied frequency in ac electric field. Cells under AC electric field behave like dielectric particles and this enables DEP to use them.

Velev and Kaler (1999) used positive and negative DEP for microscopic biosensor application. Gold nanoparticles with an active antibody were selected out from other types of particles by DEP.

One of several DEP techniques used is flow separation, whereby a fluid carries two types of biological particles, one of which duly migrates to the electrode or vessel and another of which passes through with the flow.

Particle motion can be achieved with both ac and dc non-uniform electric fields which makes DEP an important tool for manipulation, transport, trap, separation and characterization of micro- and nano-size particles in physical, chemical and biological research.

An example chemical application for the DEP manipulation of particles is given in Flores-Rodriguez, N. and Markx, G.H. (2006). They studied low concentration (0.01–1.60 w/v %) aqueous suspensions of 3 μm size barium titanate particles. The suspension showed positive dielectrophoresis over 1 kHz–20 MHz frequency range. When amphoteric molecules HEPES (N-[2-hydroxyethyl] piperazine-N-4-[2-ethanesulfonic acid] were added at low concentration (0.57 M), the suspension of BT particles showed positive DEP. However, when the concentration of ampholytes was high (0.71 M), the BT particles behaviour changed over a frequency 100 kHz and the BT particles showed negative DEP which means the particles accumulated in different position than in the previous case.

An example physical application is given by Krupke and co-workers (2003). They managed to separate semi-conducting tubes from a suspension of mixture of metallic and semiconducting single-walled carbon nanotubes. In a non-uniform AC electric field the difference between the relative dielectric constants of metallic and semi-conducting nanotubes made the separation occur. The semi-conducting nanotubes remained in the suspension while the metallic nanotubes attached to the surface of the electrodes.

4.2.2 Particle dynamics in fluids

Forces acting on particles and the surrounding fluid are:

-random or stochastic force (Brownian motion, diffusion), little control over it,

-deterministic force (gravity), more control over it,

-forces on nanoparticles: viscous drug due to fluid movement so-called electrohydrodynamic (EHD) forces, gravity, viscous (Stokes drag) forces and electrical force,

-particles suspended in a medium have a long-range attractive force such as van der Waals force or Hamaker force. The van der Waals force includes three forces (orientation or Keesom interaction force, induction or Debye force and

London dispersion force) and the extent of the total force depends on the interacting particles,

-forces on fluid are: local variation of permittivity and conductivity gradient in the charge density of the fluid cause electro-osmosis which is origin in the Coulomb force.

The two main kinds of EHD forces are: electro-osmotic force, which causes fluid pumping. This is happens above the electrode surface between the diffuse double layer and the tangential electric field. The layer around the particle forms a "shell" with its own dielectric properties. In certain situations the electro-osmotic force could be similar to or larger than the DEP force which causes fluid movement across the electrode from the edge to the centre. The insulator layer coating on the electrode can avoid the negative effect of electro-osmotic force. Mobile charge is found in the electric double layer close to the surface. The thickness of the double layer calculated and showed that it is very small compared to the size of the particle in oil. This depends on the fluid, measured as the Debye length.

The second EHD force is the electro-thermal force which causes fluid convection. A localised heating point in the medium causes local differences of conductivity and permittivity of the medium. Under DC electric field with needle and plate electrode configuration the space charge creation occur in the fluid. Close to the fluid-metal (electrode) interface charge injection occurs especially in the tip of the needle because it has the highest electric field. The injected charges have same polarity as the needle. The tip of the needle has a highest electric field and generated electric power which generates heat due to Joule effect. This heat creates a temperature gradient and makes the fluid flow. Due to this temperature: gradient viscosity, permittivity and conductivity gradients occur. Under tangential DC electric field double layer occurs on the electrode surface. The movement of ions (charges) in the fluid cause electro-osmotic flow.

EHD flow depends on the geometry of the vessel, the electrode set up, field strength and the fluid properties [Morgan, H. et al. 2003].

Particle motion under DEP is ruled by an equilibrium balance of forces: DEP force, buoyancy force, Brownian force and drag force [Morgan, H. et al. 2003, Cameron, N. et al. 2004, Thwar, P.K. et al. 2007].

$$F_{TOTAL} = F_{DEP}\,(a) + F_{BUOYANCY}\,(b) + F_{BROWNIAN}\,(c) + F_{DRAG}\,(d) \quad (4.3)$$

a; Dielectrophoretic force

$$F_{DEP} = 2\,\pi r^3 \varepsilon_m R_e\,[K(\omega)]\nabla E^2 \quad (4.4)$$

$$K(\omega) = (\varepsilon^*_m - \varepsilon^*_p)/(\varepsilon^*_p + 2\varepsilon^*_m) \quad (4.5)$$

$$\varepsilon^* = \varepsilon - j(\sigma/\omega) \quad (4.6)$$

where F_{DEP} is dielectrophoretic force, r is particles radius, $K(\omega)$ is the Clausius-Mossotti factor, $R_e\,[K(\omega)]$ is the real part of Clausius-Mossotti factor, ε^*_m and ε^*_p are complex permittivity of medium and particles respectively, ω is angular frequency, j is imaginary number and σ is conductivity. The magnitude of F_{DEP} depends on: the particle's size, the conductivity of the medium and the particle, and the electric field strength. The magnitude of the electric field and the size of the particles have the biggest impact on F_{DEP} and the relationship is $F_{DEP}\ \alpha\ E^2$ and size of the particles is $F_{DEP}\ \alpha\ r^3$. The force of DEP is related to the mediums properties this why it is important to choose a suitable medium. F_{DEP} could be higher if the difference increases between the properties (conductivity and permittivity) of the medium and the particles. The F_{DEP} is linearly related to the volume fraction of the particles ($F_{DEP}\ \alpha\ r^3$), the F_{DEP} is directly related to the permittivity of the medium ($F_{DEP}\ \alpha\ \varepsilon_m$) and F_{DEP} is related to the magnitude of the Clausius-Mossotti factor. The term $R_e\,[K(\omega)]$ is the real part of Clausius-Mossotti factor which varies between -0.5 and +1, depends on the properties of the particles and the medium. If it is positive it means positive DEP, and when it is negative it means negative DEP [Cameron, N. et al. 2004].

b; Buoyancy force

$$F_{BUOYANCY} = 4/3g\,\pi r^3(\rho_f - \rho_p) \quad (4.7)$$

where g is acceleration due to gravity, ρ_f and ρ_p are fluid and particle densities respectively.

c; Brownian motion

The Brownian motion can be studied through diffusion constant (D)

$$D = (k_B T)/(6\pi\eta r) \quad (4.8)$$

where k_B is Boltzmann constant and T is temperature.

d; Drag force

$$F_{DRAG} = 6\pi\eta r(\upsilon_f - \upsilon_p) \quad (4.9)$$

where r is particles radius, η is fluid viscosity and υ_f and υ_p are velocities of fluid and particles respectively.

4.2.3 Polarization of particles and fluids

Five different polarizations take place in a liquid under AC electric field with variable frequency: electronic, atomic, orientational, interfacial, counterion. Figure 4.3 showed the different polarization for polarizable particle under ac electric field.

Polarizations occur below the relaxation frequency and above that they disappear because they have not had enough time to establish. Electronic polarization (or atomic) occurs due to the atomic structure so can apply to any material. Under an electric field the electrons move and so they are no longer in the centre. Orientation polarization: this mechanism occurs in liquids and gases where the dipoles can rotate freely. Under an electric field aligns the dipoles and induces the polarization. Interface polarization: under an electric field bulk transport of charges occurs by surface migration.

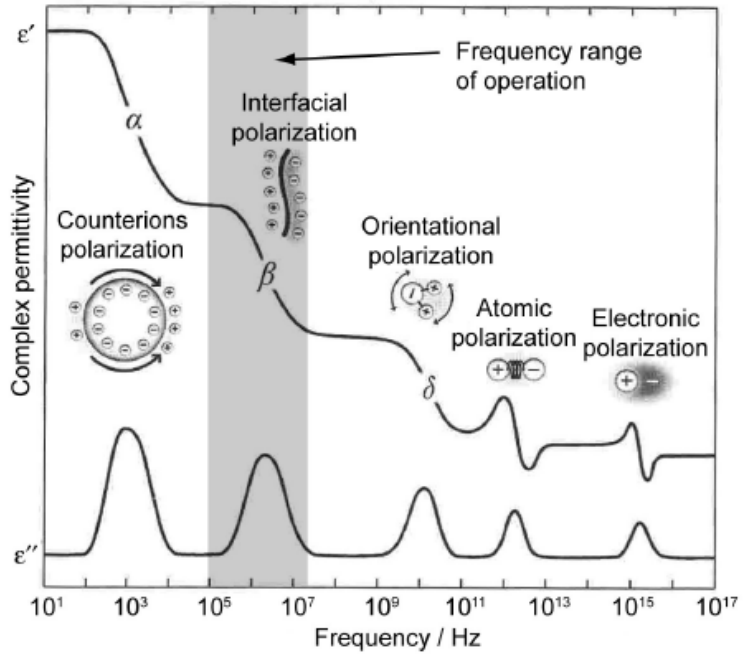

Figure 4.3 Schematic graph of the different polarization of a dielectric particle which occurs at different frequency [Demierre, N. 2008]

4.2.4 Droplet manipulation

William Gilbert in the 17th century first reported the formation of a conical meniscus when he brought an electric field (electrified piece of amber) close to a drop of water. An interface created between two immiscible fluids, one is an insulator or dielectric liquid, and another is a conducting liquid. The electrically charged interface reaches a certain level when it becomes unstable and generates a rounded shape conical phenomenon called a Taylor-cone. From this cone a steady jet can be created which can break up into charged drops or so called electrospray [Fernandez de la Mora, J. 2007]. Taylor (1964) studied the phenomenon and explained the conical shape of the meniscus with the balance of electrical and surface tensile stresses. In the Taylor-cone (semi angle 49.3º) the electrostatic forces are balanced by the surface tension of the fluid and the jet arises from the tip of the cone where the field is a maximum. A steady jet is created from the tip of the cone in a certain range of applied voltage and the jet eventually breaks up and forms charged droplets in micro-size range. Barrero et al. (2004) used this technique to produce emulsion inside the dielectric liquid bath. Figure 4.4 shows the glycerine jet in hexane and the jet could break up into drops and then the emulsion created.

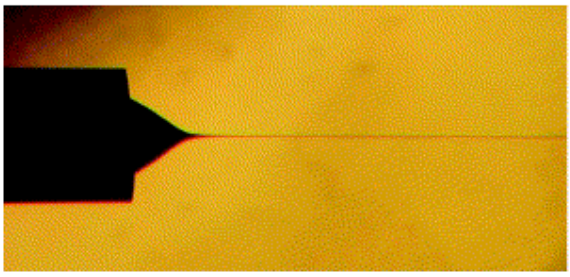

Figure 4.4 Glycerine cone jet in hexane bath [Barrero, A. et al. 2004]

The charge of the droplets has the same polarity as the needle electrode and the diameter of the droplets depends on the fluid's properties. Fernandez de la Mora (2007) showed the charge and structure of the jet also depend on the characteristics of the tip of the cone. Higuera (2003) suggested that the viscosity is irrelevant to the jet formation but the break-up of the jet involves viscosity which is present when more viscous liquid jets create bigger drops.

Dielectrophoresis is suitable for droplet creation and manipulation. Table 4.1 shows the different techniques for droplet manipulation. Each of them has pros and cons and is suitable for different applications. One of the advantages of using dielectrophoretic forces to manipulate droplets and particles is the small volume range while the disadvantage is that the liquids' properties have to form a suitable combination electrically and rheologically.

Table 4.1 Comparison of droplet manipulation techniques

	ADVANCES	DISADVANTAGES
DIELECTROPHORESIS	electronic control no surface contact	small forces strongly depend on the fluids properties interactions inside of droplet
MECHANICS/ ACOUSTICS	electronic control flexibility fast droplet transport	surface contact wetting angle hysteresis required
MICROFLUIDIC CHANNEL	high throughput	low flexibility surface contact micro structuring of channel network

Heeren et al. (2007) showed the manipulation of micro-channel nanoparticles suspended in fluids by electro-osmosis in the first part of the channel by a set of large electrode with gaps and the second part of the channel the small DEP electrode pulls the particles toward to the edges of the electrodes. The DEP is a short-range interaction which can move the particles from the surrounding area but to mobilize the suspension from further away it was necessary to use long-range interaction (electro-osmosis) to induce circulation in the micro-channel.

In two immiscible fluids, hydrodynamic force micro-flow can create a core-shell structure or coating on droplet. Ganan-Calvo et al. (1998) studied a coaxial jet flow of water with black ink and silicone oil and the flow injected through coaxial needles. The result was silicone oil covered black ink drops. Later Cohen et al. (2001) used this technique to coat micro-particles (Fig. 4.5).

Loscertales et al. (2002) produced core-shell particles via electrified coaxial jets. Capillary flow occurs when forces are stretched at the fluid interface - without it breaking - until it reaches the required dimension and by the capillary instabilities break to mono-disperse particle size. The same technique can be used to produce very thin fibres due to the early solidification of the jet which does not allow drops to be produced. This is called electrospinning.

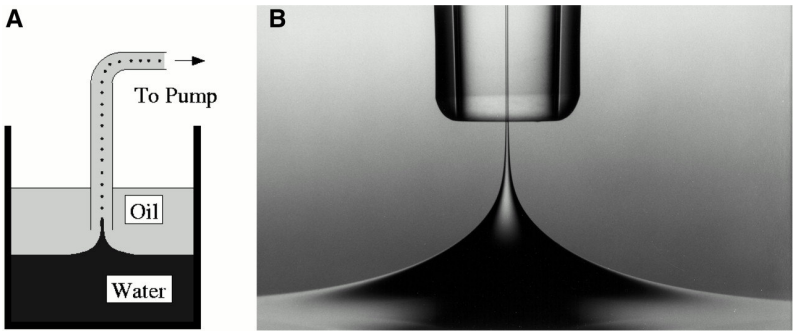

Figure 4.5 Schematic diagram of selective withdrawal apparatus (a) and creation of oil coated water jet (b) [Cohen, I. et al. 2001]

Millman et al. (2005) showed a controlled on-chip droplet micro-reactor which used a synthesis of eyeball-like particles. The movement involved assembly, encapsulation and polymerisation. The manipulation used DEP forces in non-uniform electric field.
The shape of the liquid cone is a result of the balance of pressure, surface tension, gravity, electric stress and viscosity.
The size of the droplet or capsule has a size limit for example for medicines which need to move through the intestine wall it cannot be larger than couple microns but to flow in the blood stream and be undetected by the immune system it should not be smaller than 400 nm [Barrero, A. et al. 2007]. To produce the capsules an encapsulating agent which is usually liquid (i.e. polymer) is required; the interior medicine can be solid or liquid. To make micrometric size fluid flow there are usually two options. One of them is to force the fluid through a pipe, which has some size limit and under a certain inert diameter the pipe will clog up. The second option is to use external forces, possibly surface tension, fluid dynamic forces or electrical or magnetic forces.

Chapter 5 Experimental nanoparticle synthesis and characterization

The first part of this chapter will present the experimental synthesis of different kinds of nanoparticles and review the characterization methods. The second part of this chapter concerns the electrophoretic characterization of water-based nanofluids. The final part of this chapter explains the spray drying system which is used to isolate the fragile core-shell structures made by DEP technique.

5.1 Sol-gel technique

The sol-gel process is a wet-chemical technique for the fabrication of materials (typically a metal-oxide) starting from a colloidal system, through hydrolysis of liquid precursors and condensation and network of the gel forms.

Formation of a metal oxide involves connecting the metal centres with oxo (M-O-M) or hydroxo (M-OH-M) bridges, therefore generating metal-oxo or metal-hydroxo polymers in solution. The drying process serves to remove the liquid phase from the gel thus forming a porous material. The sol-gel is a reasonably cheap and low-temperature technique that allows for the fine control on the product's chemical composition. The following equations show the general synthesis route from the colloidal solution to the final powder. Eq. 5.1 and 5.2 show the hydrolysis and condensation steps and the result is wet gel. Through the Eq. 5.3 the water condensation and the following step is the drying and calcinations step to get the metal oxide fine powder.

$$\text{M-O-R} + H_2O = \text{M-OH} + \text{R-OH (Hydrolysis)} \quad (5.1)$$

$$\text{M-OR} + \text{M-OH} = \text{M-O-M} + \text{R-OH (Alcohol condensation)} \quad (5.2)$$

$$\text{M- OH+ M-OH} = \text{M-O-M} + H_2O \text{ (Water condensation)} \quad (5.3)$$

where M is the metal and R is the alcohol group (e.g. ethoxy group).

5.1.1 Synthesis of solid silica nanoparticles

The sol-gel synthesis route described by Park et al. (2002) was chosen to make solid silica in this thesis. Figure 5.1 shows the modified synthesis route to produce silica nanoparticles with controllable size.

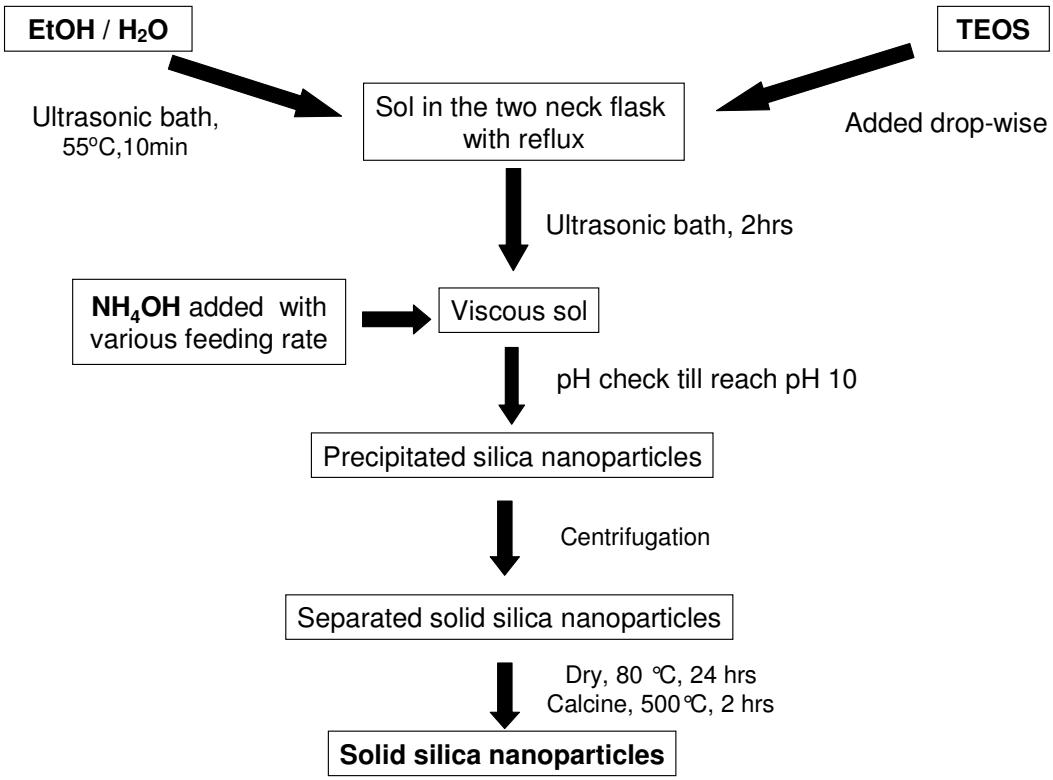

Figure 5.1 Schematic graph of synthesis route of solid silica nanoparticles

The ethanol and the distilled water were mixed in a two-neck flask in a heated ultrasonic bath. Temperature and time were closely controlled. The tetraethyl orthosilicate (TEOS) was added drop by drop into the mixture by burette and the solution was stirred in the ultrasonic bath for 2 hrs, and then the ammonium hydroxide was added with variable feeding rates (0.03-0.1 ml/min) by burette and during the whole process reflux was used. The precipitated particles were centrifuged to separate them from the fluid and then dried in an oven at 80 ^{o}C for 24 hrs, and then calcined in a furnace at 500 ^{o}C for 2 hrs. Different reaction conditions such as NH_4OH feed rate and temperature result in different sizes of the final nanoparticles.

5.1.2 Hollow SiO_2 synthesis

The process used to make hollow sphere silicon dioxide nanoparticles is a combination of sol-gel process and water-in-oil (W/O) emulsion [Li, W.J. et al. 2002, Lopez, H.J.O. 2004]. The following equations (Eq. 5.4-5.6) show the special reactions in the case of silicon dioxide synthesis by sol-gel technique.

$$n\ Si(OC_2H_5)_4 + H_2O = n\ Si(OH)_4 + 4n\ C_2H_5OH \quad (5.4)$$

$$n\ Si(OH)_4 = n\ SiO_2 + 2n\ H_2O \quad (5.5)$$

$$n\ Si(OC_2H_5)_4 + 2n\ H_2O = nSiO_2 + 4n\ C_2H_5OH \quad (5.6)$$

where n is the number of molecules.

The main synthesis process was showed in Fig. 5.2.

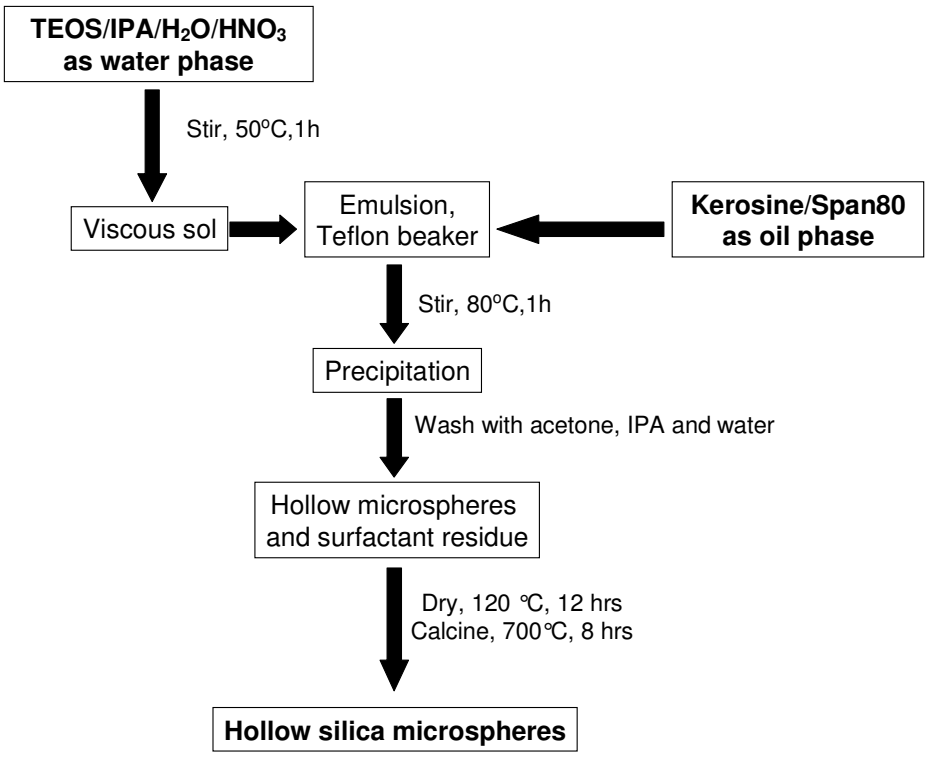

Figure 5.2 Schematic graph of synthesis route of hollow silicon dioxide particles

For the water phase: TEOS, H_2O, isopropanol (IPA) and nitric acid (HNO_3) were mixed at the molar ratio of 1: 4: 3: 0.01. The solution was vigorously stirred at 50 ^oC for 60 min. For the oil phase, kerosene and sorbitan monooleate (Span 80) were mixed at 3:1 molar ratio and mixed with the water phase in a Teflon beaker and

stirred at 80 ^{o}C for 60 min. It was then washed three times with acetone, isopropanol and water; dried in vacuum oven at 120 ^{o}C overnight, and finally the powders were calcined at 700 ^{o}C for 8 hrs in a furnace.

5.2 Hydrothermal technique

The term "hydrothermal" comes from the earth sciences (geology), where it implied a regime of high temperatures and water pressures. Typical hydrothermal research needs a moderately high temperature and high-pressure apparatus called "autoclaves". Hydrothermal synthesis involves water both as a catalyst and occasionally as a component of solid phases in the synthesis at elevated temperature (< 200°C) and pressure (> a few atmosphere). For hydrothermal experiments the requirements for starting materials are: -accurately known composition,

-as homogeneous as possible,

-as pure and as fine as possible.

The hydrothermal technique can control the particle size and shape of the produced powder through the selection of precursors and the control of the reaction time and temperature.

5.2.1 $BaTiO_3$ nanoparticles synthesis

Hydrothermal synthesis, described by Clark et al. (1999), was modified and optimised to produce the $BaTiO_3$ nanoparticles. The synthesis was carried out in an autoclave. The autoclave used in this project consists of a 45 ml PTFE liner that was surrounded by a screw top steel casing. In this study one of the aims is to produce $BaTiO_3$ nanoparticles with controlled size by hydrothermal method. The starting precursors were anatase (TiO_2) and $Ba(OH)_2{\cdot}8H_2O$. The powders obtained by hydrothermal synthesis and then washed with formic acid to dissolve any possible $BaCO_3$. Powders were finally centrifuged and dried at 100 ºC 24 hrs.

5.2.2 PZT particles synthesis

Hydrothermal synthesis described by Deng et al. (2003) was optimised and used to prepare PZT nanoparticles. The synthesis was carried out in the Teflon lined autoclave and placed in the oven at 160-200 ºC for 1-4 hrs. The starting precursors were $ZrOCl_2 \cdot 8H_2O$ (5.56 mmol), $Pb(NO_3)_2$ (8 mmol), TiO_2 (3.85 mmol), KOH (0.16 mol) and distilled water. Powders obtained were washed with distilled water and ethanol three times. Nanopowders were finally centrifuged and dried at 80 ºC for 12 hrs. PZT particles with different sizes and new morphologies were synthesised.

5.3 Wet chemical synthesis technique

Chapter 2 provided an overview of the techniques and synthesis methods used to synthesise metal and metal oxide nanoparticles. Different wet chemical synthesis methods were suitable for the synthesis of metal nickel and iron oxide nanoparticles. Chapter 5.3 contained the synthesis of nickel and iron oxide nanoparticles and core-shell particles.

5.3.1 Synthesis of iron oxide nanoparticles

Magnetite nanoparticles were synthesized by the method described by Shan et al. (2005). 23.5 g $FeCl_3 \cdot 6H_2O$ and 8.6 g $FeCl_2 \cdot 4H_2O$ were dissolved in 600 ml deionised water under N_2 with mechanical stirring at 800 rpm and 85 ^oC and then quickly added 30 ml of 7.1 M NH_4OH. 16 ml of oleic acid in 30 min was added to the suspension in drop form. The magnetic precipitate was separated by magnetic decantation and washed with deionised water. The magnetic precipitate was modified with about 4 ml of 7.1 M NH_4OH to form hydrophilic magnetic nanoparticles. Magnetite nanoparticles were monodisperse in an aqueous solution. The washed precipitates were dried in vacuum oven at 40 ºC for 12 hrs.

5.3.2 Synthesis of nickel nanoparticles

A modified wet-chemical synthesis described by Choi et al. (2005) was used to produce spherical nickel nanopowder, star-like nanoparticles and flower-like micro-particles through the control of reaction temperature and ageing time. Figure 5.3 shows a flow chart of the synthesis procedure of spherical nickel nanoparticles, nanostars and microflowers. The nickel-metal nanoparticles were prepared by the thermal decomposition of Ni-hydrazine complexes and subsequent reduction of Ni ions. Nickel acetate (0.1 mol) aqueous solution was heated up to 50 ºC and then hydrazine (0.25 mol of $N_2H_4{\cdot}H_2O$) was added to the solution with vigorous stirring. The solution was heated up to 65 ºC, which results in light violet precipitate. When the solution was cooled to 50 ºC, an aqueous solution of sodium-hydroxide (0.3 mol) was added to it. To obtain the spherical nanoparticles, the solution temperature was then increased to 55 ºC and remained at 55 ºC for 1 hr. To obtain nano-sized nickel stars, to the Ni-hydrazine complex added an aqueous solution of sodium-hydroxide (0.1 mol) and then the solution was heated to 70 ºC and remained for 3 hrs. When the solution was aged for 24 hrs at 70 ºC, the product was micro-sized nickel flower (see Figure 7.4). The precipitated particles were retrieved by centrifugation. The formed black Ni precipitate was finally washed five times with distilled water and dried at 40 ºC in the oven overnight.

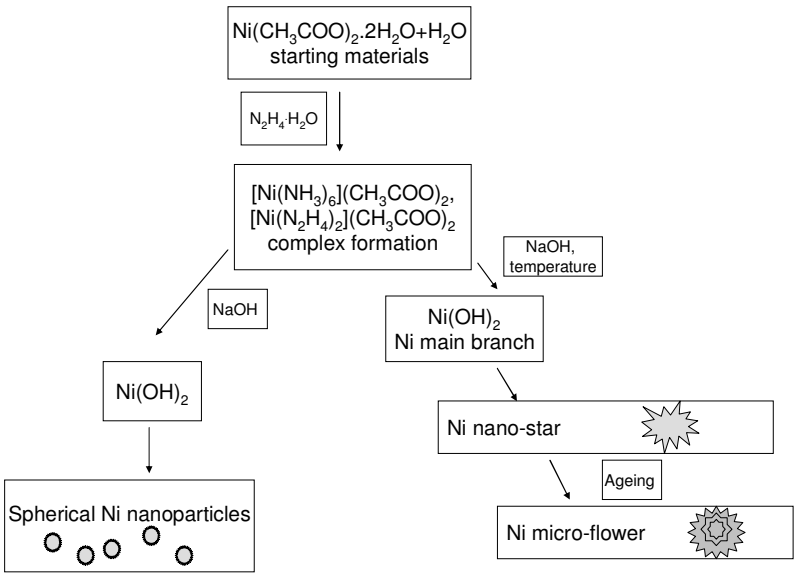

Figure 5.3 Schematic illustration of the possible formation process of the spherical nickel nanoparticles and Ni nanostar- and microflower-structures

5.3.3 Preparation of Ni- and Fe_3O_4 - coated SiO_2, BT, and PZT particles

Figure 5.4 (a) shows a flow chart of the synthesis procedure of core-shell structures. SiO_2, BT or PZT core particles were suspended in deionised water in a volumetric flask and the particle concentration was 0.1 g/l. The suspension was then placed in an ultrasonic bath for 30 min. At this point, the pH of the suspension was adjusted by adding HCl or NaOH to the value given by the measurement of zeta potential. Similarly, in another volumetric flask, Ni or Fe_3O_4 particles were suspended in deionised water. The suspension was also placed in an ultrasonic bath for 30 min and the pH of the suspension was adjusted as for the core solutions. Based on the measurements of zeta potential of particle colloids in water, core and shell particles would produce opposite surface charges at the certain pH regions. The core and shell particle colloids with such pH values were then mixed and placed to the orbital shaker for 30 min. The electrostatic force on the surfaces of the core and shell particles would make the attraction of different charged particles to each other and thus form a core-shell structure (Fig. 5.4b). The core-shell particles were dried in the oven at 40 ºC.

The core-shell nano-composites were fabricated using the immobilization of prepared magnetic Ni or Fe_3O_4 nanoparticles on the surface of SiO_2 or ferroelectric $BaTiO_3$ or $Pb(Zr,Ti)O_3$ particles by adjusting pH values in order to control their zeta potential.

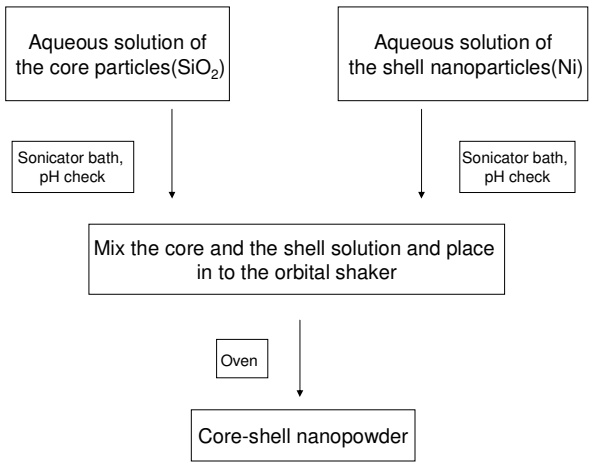

a;

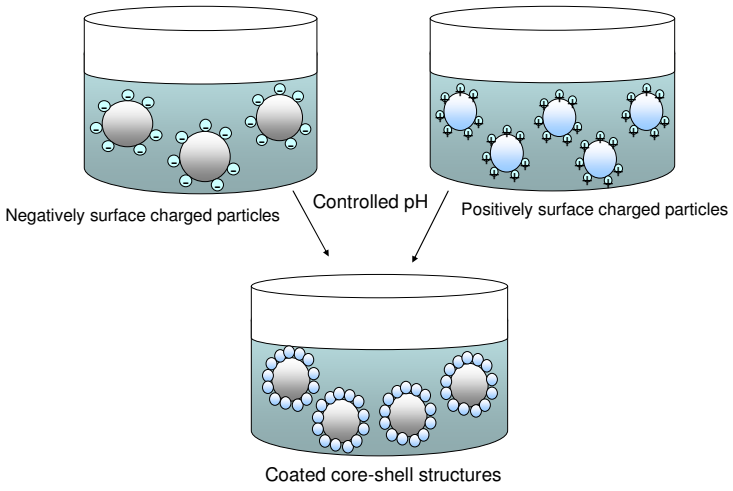

b;

Figure 5.4 Flow chart of the synthesis procedure of core-shell structures (a), the electrostatic force on the surfaces of the core (right vessel) and shell (left vessel) particles (b) they attract each other and thus form a core-shell structure

5.4 Zeta potential

Materials acquire a surface electric charge when brought into contact with polar medium, possible charging mechanisms being ionization, ion adsorption and ion dissolution. This surface charge manipulates the distribution of closest ions in the medium. Oppositely charged ions are attracted to the surface and ions of same charge are repelled from it. This motion and the thermal motion lead to the formation of an electric double layer which is made up of the charged surface and the oppositely charged ions in the medium. The electric double layer can be considered to consist of two regions: an inner region which may include adsorbed ions, and a diffuse region.

Zeta potential is a measure of the magnitude of the repulsion or attraction between particles. The measurement of zeta potential is an important parameter across a wide range of industries including ceramics, pharmaceuticals and water treatment. Zeta potential depends on the pH, concentration of particles in the solution.

The zeta potential is the electrical potential representing the difference in voltage between the surface of the diffuse layer and the medium. The zeta potential can be calculated from measurements of particle movement within an electrical field (electrophoretic mobility). Mobility is defined as the velocity of a particle per electric

field unit and is measured by applying an electric field to the dispersion of particles and measuring their average velocity. Figure 5.5 shows the inside of measurement cell. Depending on the concentration of ions, either the Smoluchowski (for high ionic strengths) or Hückel (for low ionic strengths) equation is used to obtain the zeta potential from the measured mobilities [Sherman, P. 1968, Shaw, D.J. 1999].

When two colloidal particles with same charge approach each other, their diffuse layers begin to interact and result in repulsive forces. The balance of the two opposing forces, electrostatic repulsion and van der Waals attraction, explains why some colloidal systems agglomerate while others do not. Particles with same charge have repulsive electrostatic forces which keep them apart but when the van der Waals force becomes dominant the particles will aggregate.

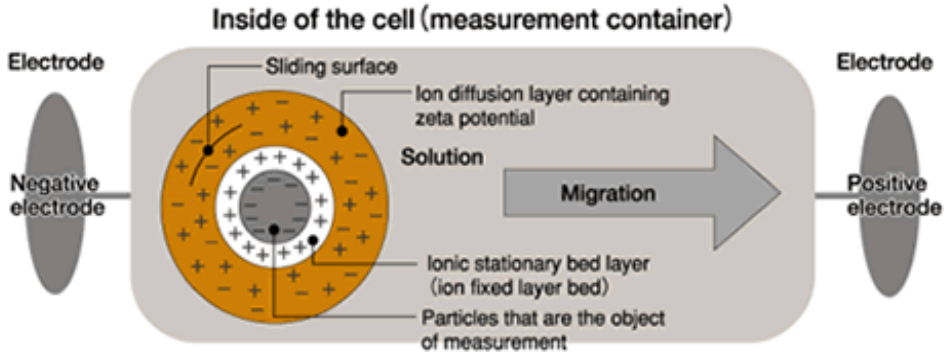

Figure 5.5 Schematic presentation of the inside of the measurement cell [Malvern].

5.5 Surface- and chemical-characterization techniques for nanoparticles

Transmission electron microscopy (TEM) was performed on a Philips CM 20 operating at 200 kV, and scanning electron microscopy (S-FEG SEM) was performed on a Philips XL30. X-ray diffraction (XRD) studies used standard XRD θ-2θ measurement in the range 2θ = 20°-90° on a Siemens D5005 diffractometer using CuKα radiation and a Goebel mirror. The crystallite size is determined from the X-ray line broadening using Scherrer formula given by $D = 0.9\ \lambda / \beta \cos \theta$, where D is the average crystallite size, λ is the X-ray wavelength used (1.5406 Å), β is the angular line width of half maximum intensity and θ is the Bragg's angle in degree. Lateral diameters of crystal grains on the film surface were made using a Digital Instruments Nanoscope IIIa Atomic Force Microscope (AFM) in intermittent contact mode. The

pH values of particles in water were measured using a Jenway 3540 pH meter. Electrophoresis measurements were performed using a Malvern Zetasizer 3000. The magnetic properties of the products were characterized using a Princeton Measurements Corporation vibrating sample magnetometer (VSM) in Cambridge University by Drs C. Israel and N.D. Mathur. The chemical composition analysis of the samples is measured by Energy-dispersive X-ray spectroscopy (EDX) which was able to identify which elements are contained in different parts of the sample. This is Philips XL30 SFEG equipment with EDX detection system. The Optical Microscopy was performed on a Nikon Optiphot (Bauner Scientific Ltd) with a 40x maximum magnification.

5.6 Spray dry technique

The silicone oil core-polymer shell produced by DEP manipulation technique and sprays dried by Büchi 190 Mini Spray Dryer (Büchi AG, Flawil, Switzerland). The spray dryer operates on the principle of nozzle spraying in parallel flow, which means the product and the air flowing in the same direction. Figure 5.6 shows the drying air flow and the principle of the system. The electrostatic force on the surfaces of the core and shell materials causes the attraction of different charged particles to each other and thus forms a core-shell structure. The oil-in-water emulsions produced by DEP contains polymer in the water phase. The spray dryer is heated to 160 °C (inlet temperature), the spraying rate was set at 3-4 ml/min, the outlet temperature was measured at around 95±5 °C and the spray airflow was set at 800 l/h.

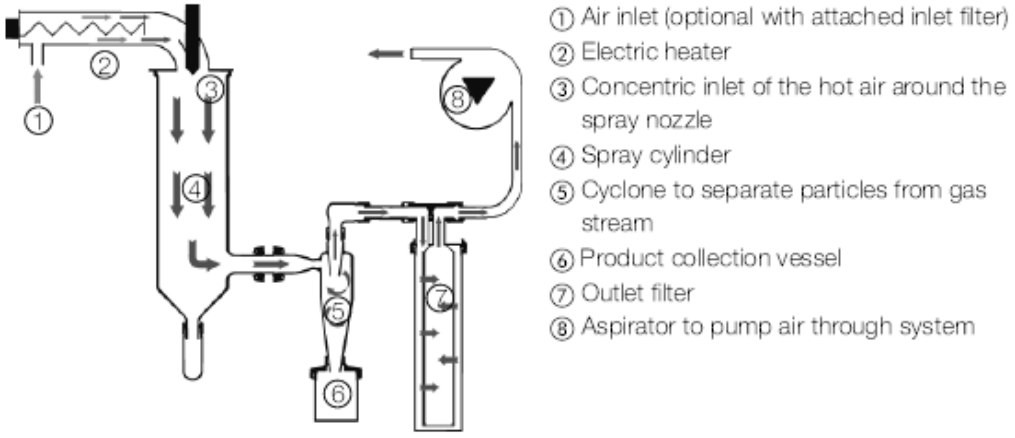

Figure 5.6 Functional principle of the drying air in spray dryer [Büchi]

Chapter 6 Experimental of nanofluid characterization

The following chapter will present experimental methods used to characterize different kinds of non-aqueous nanofluids. The first part explains the rheological characterization of nanofluids and the second part of this chapter presents the surface tension measurement of pure fluid and nanofluid by two types of measuring technique: the Wilhelmy-plate method and the pendant-drop test. The final part of this chapter explains the electric characterization of nanofluids such as electrical conductivity and permittivity measurements and dielectrophoretic manipulation technique set-up.

6.1 Rheological characterization of nanofluids

Nanofluids were prepared by dispersing a known amount of oil with nanoparticles at 10, 20 and 30 g/l concentrations and then placing the suspensions in an ultrasonic water bath for 30 min. The fluids used were silicone oil (Dow Corning 200/50cS, viscosity 50 cSt and specific gravity 0.96) and FC70 oil (viscosity 12 cSt and specific gravity 1.94). No surfactants were used in the suspension formulations. The suspensions were found to be stable and there was no observable sedimentation over a period of three hours. Rheological measurements were performed directly after the preparation of the suspensions at 25±5 °C) using a Bohlin CVO rheometer (Malvern Instruments) with cup-bob geometry (C14 cell). The measurements were based on the controlled shearing model at shear-rates ranging from 0.10-10 s^{-1}. Calibrations against standard solutions were performed on a daily basis over the course of this work to ensure measurement accuracy.

6.2 Surface tension measurement by Wilhelmy method

DST 500 Dynamic Surface Tensiometer was used to measure the surface tension of oils and nanofluids (Nima Technology Ltd). This instrument uses Wilhelmy plate to measure surface tension of liquids by the dynamic surface tension method, and the graph for the theory seen Fig. 6.1.

The whole area is cleaned with special chemical to keep dust away during the measurements. The glass container is filled up with 40 ml of oil or nanofluid and the Wilhelmy plate is dipped into it. At least 10 measurements were taken of each sample. The Wilhelmy plate hung from the balance hook is first immersed into the liquid and then carefully pulled up, by lowering the sample cup, through the surface of the liquid. The micro balance records on-line the force applied on the plate while pulling through the surface. The surface tension is the maximum force needed to detach the plate from the liquid surface. The surface of the plate is micro roughened in order to give it optimum wetting properties. The plate then pulled through the surface of the liquid until the maximum force is reached and the plate brakes away from the surface. The liquid wets the plate and increases its total mass to some maximum point which is proportional to the surface tension of the liquid.

The exact amount of nanoparticles (1 g/l to 7.5 g/l nanoparticles concentration) were weighed with an electronic scale with a tenth-milligram precision and placed into the oil. Solutions are shaken vigorously, and set in an ultrasonic bath for 30 minutes, so that they can become as homogeneous as possible.

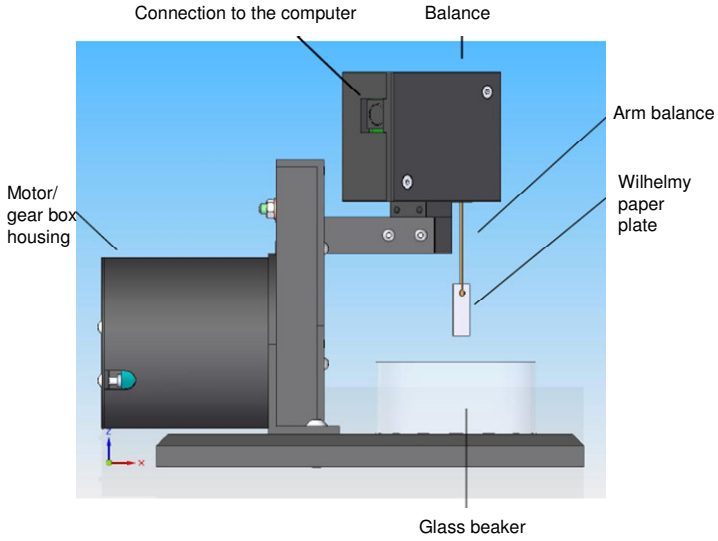

Figure 6.1 Parts and set-up of tensiometer [Nima Tech., 2006].

6.3 Surface tension measurement by pendant drop method

The pendant drops for the surface tension measurement were produced from the tip of a needle with an external diameter of 1.27 mm. The fluid was pumped slowly through

the needle by applying pressure to a syringe attached to the needle through a tube. The needle was held by stand and the experiment were recorded using a high speed Red Lake Motion Pro CMOS camera with a definition of 1280 x 1024 pixels, EX Sigma 105 mm 1:2.8 D MACRO Lens and the images was analyzed by a program written by P. Brocklehurst. After a pendant drop formation it expanded until it broke away from the end of the needle under the influence of gravity and during this move the high speed camera recorded the images, and the frames relating to a time just before the drop were used for analysis. The geometry of the drop was used to calculate the surface tension (Eq. 6.1). Figure 6.2 shows a typical image taken by the camera and used for further analysis. The surface tension of the fluid is calculated from the parameters showed on Fig. 6.2b which are the full width and the width of the drop at a distance equal to the full width of the drop above the drop's apex.

$$\gamma = (g\rho d^2_{max})/H \qquad (6.1)$$

where γ is the surface tension,

g is the gravitational acceleration,

ρ is the density of the fluid,

d_{max} is the full width

H is a shape factor, function of the ratio: $H = d_s / d_{max}$

d_s is the part width

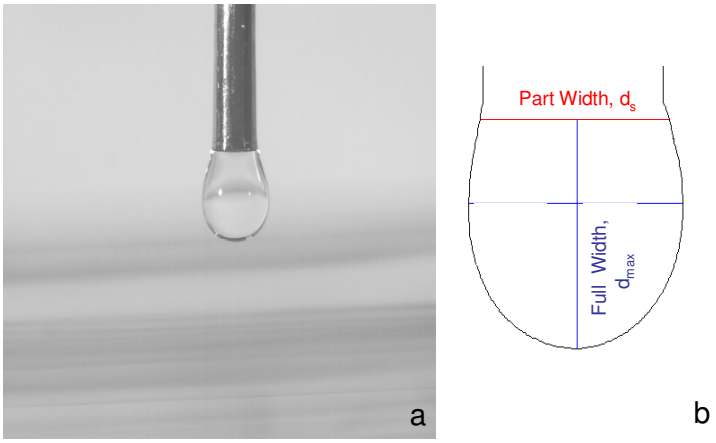

Figure 6.2 Image of pendant drop (a) by the high speed camera and the key parameters for surface tension calculation (b)

6.4 Electrical characterization of nanofluids

DC conductivity and AC permittivity measurements and the experimental set-up

In the following section the DC electrical conductivity measurement of low volume-fraction nanoparticulate suspensions in silicone and perfluorinated oils at very moderate electric field strengths will be demonstrated.

The DC electrical conductivity of base oils [silicone oil (Dow Corning 200/50cS) and perfluorinated oil (3M™ Fluorinert FC70)] and nanofluids [contains: nickel (Ni), barium titanate (BT) or iron oxide (FO) nanoparticles] was measured. The physical properties of the base fluids and the nanoparticles are shown in Table 6.1. The first part of the table shows the properties of the nanoparticles. The size of the nanoparticles measured by SEM and confirmed by XRD. The second part of the table shows the properties of the base fluids which shows they have similar electrical conductivity and relative permittivity, whilst their viscosities and specific gravity are significantly different. The third part of the table shows the mass fraction (g/l) and the volume fraction (vol %) of the nanoparticles.

Table 6.1 Physical quantities of the nanoparticles (nickel - Ni, barium titanate - BT and magnetite - FO) and two base fluids

	Mean particle diameter (nm)	Bulk density (kg/m^3)	Particle number density (m^{-3}) *	Inter-particle spacing (notional) – (nm) @ Vol. fraction (%)				
				0.05	0.1	0.2	0.4	0.6
Ni	90	8800	2.62E21	824	635	486	367	309
BT	130	5850	8.69E20	1190	918	702	530	447
FO	10	5240	1.91E24	92	71	54	41	34

Manufacturers' Data	Viscosity @ $10s^{-1}$ (Pas)	Relative permittivity	Specific gravity	Conductivity @ 1kV/m (Sm^{-1})
200/50cS silicone oil	5.0	2.60	0.973	10E-12
3M™ Fluorinert FC70	1.4	1.98	1.940	10E-12

Mass fraction (g/l)					
	2	4	10	20	30
Volume fraction (vol %)					
Ni	0.023	0.046	0.114	0.227	0.341
BT	0.034	0.068	0.171	0.341	0.512
FO	0.038	0.076	0.191	0.382	0.573

The * means the particle number density (m^{-3}) is generally calculated as follow:

-to first calculate the volume of the sphere ($4/3\ \pi r^3$) two assumptions were made: (i) all the particles are spherical and (ii) all particles are a uniform size

-the second is to calculate the mass of the materials (mass = density × volume)

-the next calculation is the number of molecules in each nanoparticle,

-then the next calculation is the number concentration of molecules in the prepared suspension: number density = Avogadro number × molar concentration, where molar concentration = (mass of solute / molecular weight of solute) ÷ volume of solvent,

-finally the number of nanoparticles in the suspension: molecules per litre/ molecules per particle = particles per litre and then to particles m^{-3}.

The nanoparticles concentrations in the base fluids were sets 2 g/l, 4 g/l, 10 g/l, 20 g/l and 30 g/l of concentration. The prepared nanofluids were placed in a temperature controlled ultrasonic bath for 30 minutes. DC current measurements were carried out using a Keithley 6517 electrometer for different applied voltages between 20 V and 100 V. The fluidic conductivity cell consisted of a 1 mm gap between concentric copper electrodes and the effective electrode area was 21.88 cm^2. The systematic error due to the measurement system was 0.05% at 20 V and 0.01% at 100 V. The current versus time profile (Fig. 6.3) showed a transient peak, due to capacitance, between 1-2 seconds after application of the voltage. Readings were therefore taken after 20 seconds representing the steady-state values. Measurements were carried out at 295 K and the cell was dried carefully in inert gas between measurements to avoid any moisture and contamination. The circuit is shown in Fig. 6.4a, where "GRN" is refers to ground. The cell was confined in the safety box and it had been coated inside with earth-linked aluminium foils because of the high sensitivity to parasite electromagnetic fields. The red object on the right size of the image (Fig. 6.4b) is a handle for the safety interlock.

AC bridge was used for measuring the permittivity of oils and nanofluids (Fig. 6.4b) and the nanofluids preparation was same as for the DC conductivity measurement.

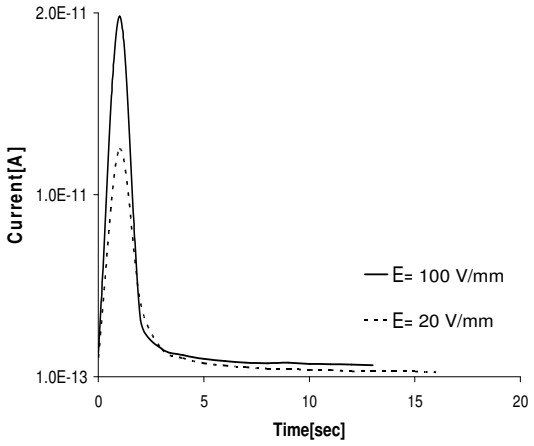

Figure 6.3 Current versus time profile of fluid at 20 V/mm and 100 V/mm

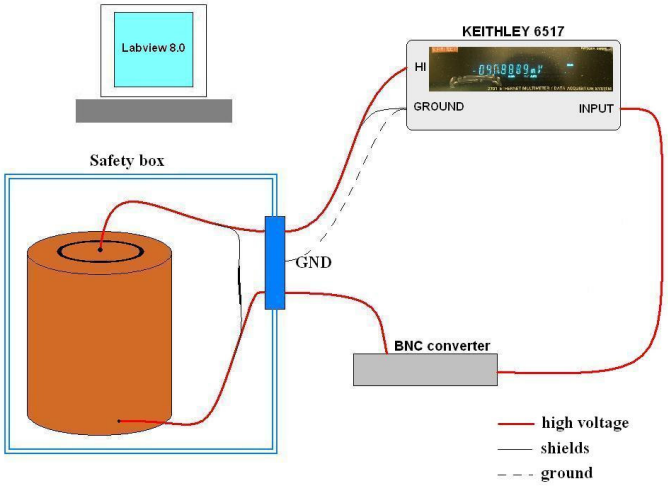

a,

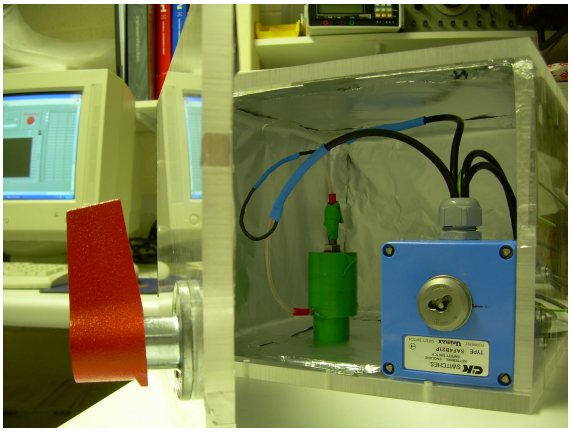

b;

Figure 6.4 Schematic images of circuit of conductivity set-up (a) and photo of the cell in the safety box (b)

6.5 Simulation of dielectrophoretic manipulation of nanofluids

Chapter 4 had a literature review and background of dielectrophoresis and it has a clear indication of the many forces, phenomenon and parameters involved in the dielectrophoretic droplet manipulation.

Maxwell 2D Student Version 9 is the software package which was used for analysing electric field in cross-sections of structures. In general the Maxwell SV uses finite element analysis (FEA) to solve two-dimensional (2D) electro-magnetic problems. During the simulation the appropriate geometry, material properties, and system of devices must be specified. The difficulty of the dielectrophoretic manipulation system is the high number of parameters involved in the simulation of the system. The simulation with Maxwell 2D was aborted because with that limited version (2D Student Version) of the simulation program could not get any useful information out.

6.6 Experimental set-up for dielectrophoretic manipulation

This section uses the equipment originally developed by Drs S.A. Wilson and E. Capria [Wilson, S.A. 1999, Capria, E. 2007]. The dielectrophoretic manipulation system (Fig. 6.5) is driven by a computer using Labview 3.1 software. The computer also controls an oscilloscope card (NI 5112), a waveform generator (NI 5401), a motion controller (NI 7344) and a video-camera acquisition card and all of them are synchronised by three National Instruments boards. The high-speed video camera (Red Lake Motion Pro) with the definition of 1280 x 1024 pixels at low speed and a recording speed between 500 and 10.000 frames per second is connected and driven to the camera acquisition card which is synchronised by a SYNC signal generated by the waveform generator. The trigger event used to synchronise all parts of the system is the waveform generation.

The light for the study is provided by optical fibre lights (Schott, KL 1500 Electronic). The camera record and show an image of the dielectric cell during the experiments. A high-speed video-camera is essential for this study, because the structuring phenomenon and the manipulation are very quick movements which could not be monitored by naked human eye. The motion controller is connected to both the motor drive and the linear transducer through a Universal motor interface (UMI 7764)

which is a 5V device. Its voltage is provided by a Thurlby PL310 DC generator. The motor is a Nanomotion piezoelectric motor HR8. Without the driving voltage the ceramic plate is at a standstill and generates holding torque on the stage [Capria, E. 2007].

Dielectric cells are used to study the jet and droplet generation from the two phase liquids system made of glass with or without the internal wall and these vessels allowing optical access. The electrode configuration was needle and plate electrodes for all the experiments. The bottom electrode is a rectangular stainless steel mirror finished electrode with variable size and placed inside or outside of the vessel depending on the experiment and the size of the vessel. The needle-like top electrode is a steel needle of 120 micron of diameter. The cell (Fig. 6.5c) is filled with two immiscible dielectric liquids. The permittivity of dielectric fluid 1 is higher than the permittivity of dielectric fluid 2.

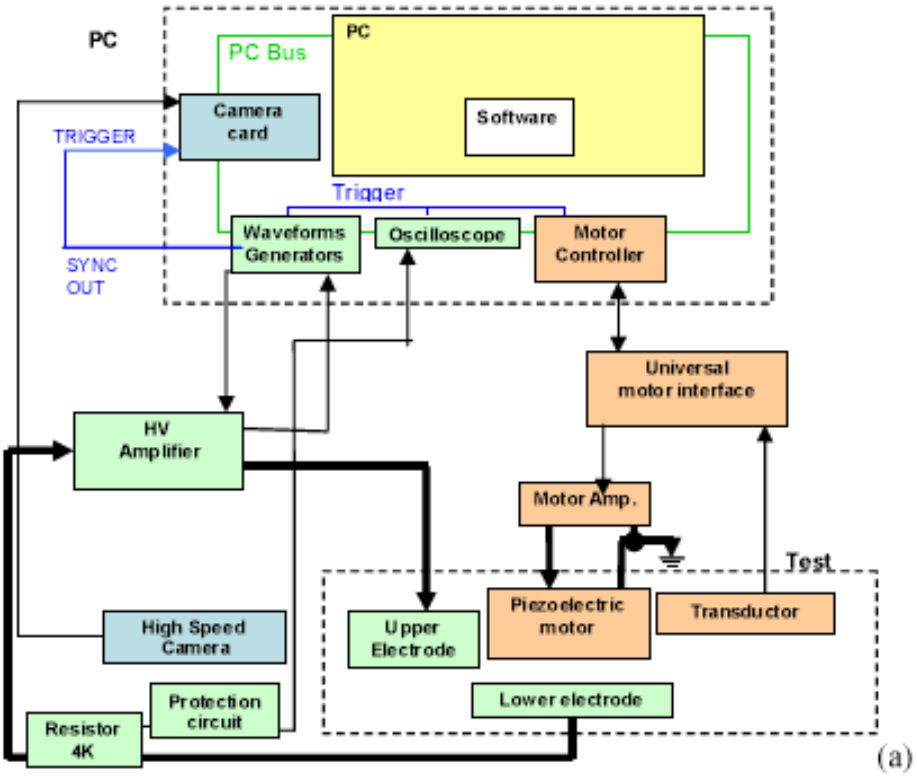

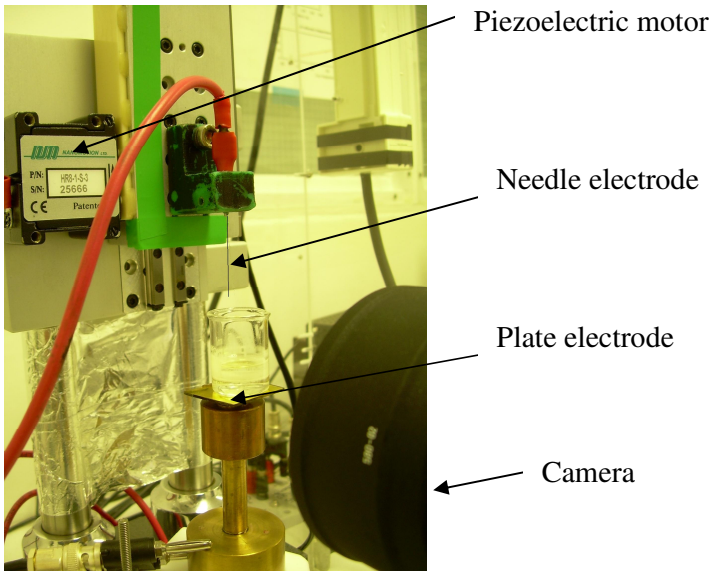

(b)

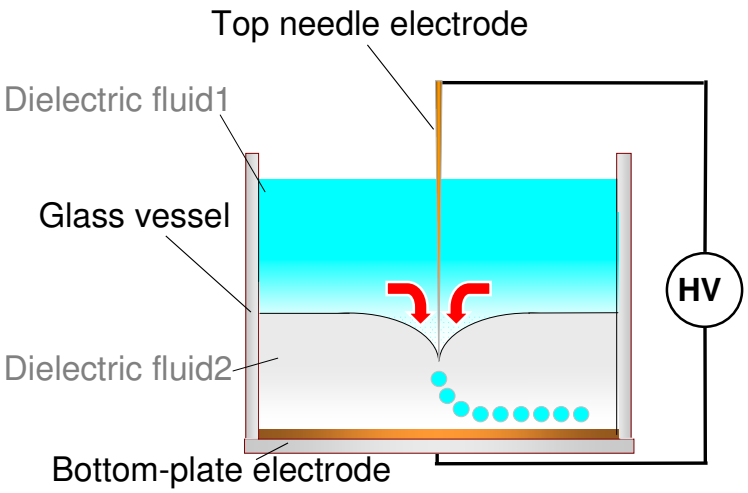

(c)

Figure 6.5 Experimental set-up for DEP rig, a block diagram (a) [Capria, E. 2007], image of the electrode configuration (b) and schematic graph of the vessel (c)

Chapter 7 Results and discussion of nanoparticles synthesis and characterization

As previous researches have shown the optical, electronic and magnetic properties of nanoparticles are very different from those of the bulk materials and these properties are often strongly dependent on the particle size, shape and morphology.

The major focus of the following chapter is to discuss the results of the experimental investigation of nanoparticle synthesis. The process parameters usually have influence on the particles' size and morphology.

7.1 Iron oxide nanoparticles synthesis

Fe_3O_4 magnetic nanoparticles have been synthesized by the wet-chemical method described in Chapter 5.3, which is quite a simple and efficient synthesis route. The main process involved a stoichiometric mixture of ferrous and ferric salts in aqueous medium, and the chemical reaction may be written:

$$Fe^{2+} + 2\ Fe^{3+} + 8OH^- \rightarrow Fe_3O_4 + 4\ H_2O \qquad (7.1)$$

The reaction is completed under nitrogen atmosphere to replace the air and prevent oxidation of ferrous ions in the water based solution. The constant nitrogen flow is important because if there is any oxygen involved in the reaction the next equation will occur:

$$Fe_3O_4 + 0.25\ O_2 + 4.5\ H_2O \rightarrow 3\ Fe(OH)_3 \qquad (7.2)$$

If this reaction (Eq. 7.2) occurs it will change the physical and chemical properties of the synthesised nanoparticles. The easiest proof is that the colour of the product changes. The partially oxidized product is reddish-brownish in colour but the pure Fe_3O_4 is dark brown. Iron oxide is sensitive to oxidation, and so the non-oxidizing environment is important.

Iron oxide nanoparticles are prepared in a water-based system i.e. on the surface of the particles are hydroxyl groups. Oleic acid has the formula $C_{18}H_{34}O_2$ or $CH_3(CH_2)_7CH{=}CH(CH_2)_7COOH$ and it has a carboxyl group in the end. During the synthesis the added oleic acid molecules with their carboxylic acid head groups reacted with the hydroxyl groups. The oleic acid layer on the surface of the nanoparticles forms a hydrophobic shell. The end of the synthesis of Fe_3O_4

nanoparticles the addition of ammonium solution has changed the outer oleic acid layer. The oleic acid layer reacts with NH_4OH and forms an ammonium salt of oleic acid. This means that the nanoparticles' surface changed to hydrophilic and they keep distance from each other and so become monodispersed.

The control over the size of the synthesised nanoparticles is dependent on:

-pH of the solution,

-reaction temperature,

-the ratio between Fe(III) and Fe(II),

-the type of the iron salt (chlorides, nitrates),

-stirring rate of mixing and the reaction time.

The influence of the pH

Regarding Eq. 7.1 the pH of the solution should be between 9 and 14 in order to precipitate Fe_3O_4. At high pH hydrolysis is the favoured reaction.

The influence of the temperature

Three different temperature settings were tried (60-65 ºC, 80-85 ºC and 90-95 ºC). The product yield showed at low temperature that the reaction could not be completed and resulted in a quite low yield. The middle temperature range (80-85 ºC) and the high temperature range (90-95 ºC) did not show any significant difference in the product yield so a temperature of 80 ºC was used.

The influence of the ratio of iron salts

According to the Eq. 7.1 at high pH the molar ratio of Fe(III) and Fe(II) has to be 2:1 in order to synthesise Fe_3O_4. If the balance of iron salts is not right this could produce a mixture of magnetite, hematite and iron-hydroxides.

The influence of the type of the iron salts

The type of the iron salt (chlorides, nitrates) used in the synthesis had influence on the particles' size. First both chloride salts were tried. $FeCl_2$ and $FeCl_3$ are both soluble in water at room temperature, but $FeCl_3$ solubility increases with temperature. Figure 7.1a shows the obtained iron oxide nanoparticles from both chloride salts and Fig. 7.1b shows it being obtained from nitrate salt. The use of nitrate salt in the synthesis slightly reduced the size of the final product. The difference between the nitrate and

the chloride iron salt is the solubility in water at room temperature. The $FeCl_3$ solubility is 0.3 mol/100g and the $Fe(NO)_3$ solubility is 0.19 mol/100g [Linke, W.F. et al. 1965]. The nitrate has lower solubility.

After a trial of different iron salts the result was quite close in terms of the size range. The chosen iron salt was the ferrous chloride and ferric chloride based on the price of the starting materials.

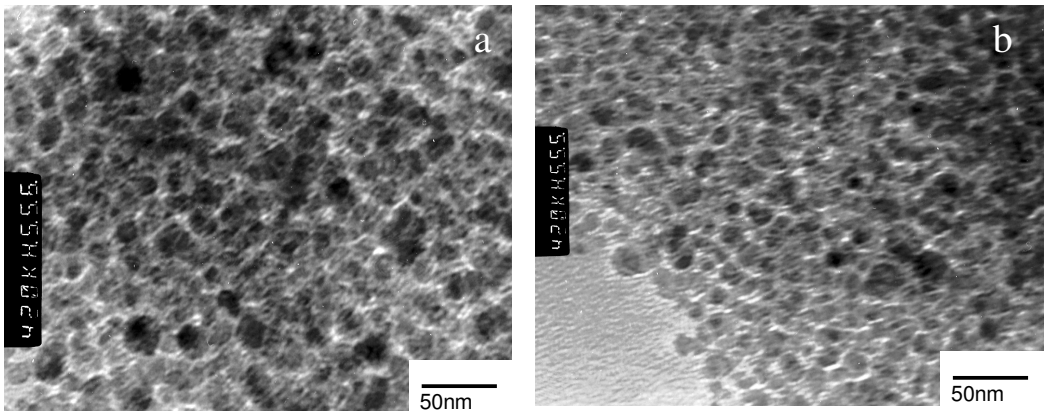

Figure 7.1 TEM images of iron oxide made from ferrous- and ferric-chloride salts (a), the average particle size 10-15 nm and from ferrous-nitrate and ferric-chloride salts (b), the average particle size 8-14 nm

The influence of stirring speed of mixing and reaction time

The stirring speed had influence on the product yield. It increased with the stirring speed rate up to a certain level and with the further incensement of the speed rate was not any significant change as Table 7.1 shows the product yield under the influence of the parameters.

Table 7.1 Influence of stirring speed on the product yield [%]

	reaction time 20 min	reaction time 30 min	reaction time 50 min
stirring speed			
500 rpm	51.4	52.5	53.8
800 rpm	63.1	**66.1**	65.9
1000 rpm	63.2	65.8	65.9

For any further synthesis the below optimised reaction parameters were used:

-reaction temperature was chosen 80-85 ºC,

-the molar ratio of $FeCl_2$ and $FeCl_3$ kept 2:1,

-stirring speed was 800 rpm and kept the reaction running for 30 minutes.

The size of the nanoparticles can be estimated by TEM and XRD. The TEM images of Fe_3O_4 nanoparticles (Fig. 7.1) show that the nanoparticles are predominantly spherical and the size of the nanoparticles varies from 10 to 15 nm, which is in a good agreement with the value estimated by X-ray diffraction measurements (Scherrer formula) [Chanda, S.C. et al. 2007] at 2θ of 35.5º (Fig. 7.2). The size of nanoparticles is determined by Scherrer formula:

$$t = (k\lambda)/ B \cos\theta \qquad (7.3)$$

where t is a crystal size, k is a shape factor (0.89) [Cullity, B.D. 1978], λ is 1.54Å (Cu K_α), θ is the peak position and B is the full width at half maximum of peak.

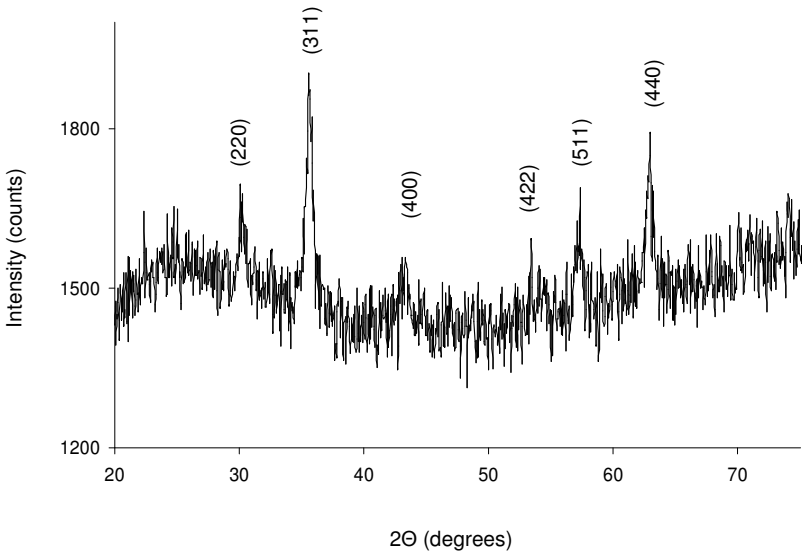

Figure 7.2 XRD pattern of iron oxide nanoparticles

The XRD peaks of Fe_3O_4 (Fig. 7.2) could be indexed by the cubic structure of Fe_3O_4 (JCPDS no. 19-629) indicating a high phase purity of Fe_3O_4 and the diffraction peaks are broad owing to small crystallite size. The XRD patent has some noise which is quite typical for samples containing iron, because the iron produces excessive fluorescence when Cu base is used in XRD [Cullity, B.D. 1978].

7.2 Nickel nanoparticles with variable morphology and size

Figure 5.3 shows a schematic illustration of the formation mechanism of Ni nanostructures. Through the reaction between Ni-acetate and hydrazine, various Ni-complexes could form such as $[Ni(NH_3)_6](CH_3COO)_2$ or $[Ni(N_2H_4)_3](CH_3COO)_2$ and then the complexes are decomposed by NaOH forming $Ni(OH)_2$. Subsequently the Ni^{2+} ion is dissolved from the $Ni(OH)_2$ that are further reduced to metal nickel. The detailed reaction steps are:

$$Ni^{2+} + 3N_2H_4 \leftrightarrow [Ni(N_2H_4)_3]^{2+} \quad (7.3)$$

$$2[Ni(N_2H_4)_3]^{2+} + 4OH^- \longrightarrow 2Ni\downarrow + N_2 + 4H_2O + 5N_2H_4 \quad (7.4)$$

The control over the size and morphology of the nickel nanoparticles is dependent on:

-the reaction temperature and time (including ageing time),

-and the precursors concentration.

The influence of the reaction temperature and time

It was found that the formation of the nickel nanoparticles was completed after 1 h at 55-60 ºC, and the variations of the molar ratio of $Ni(CH_3COO)_2/N_2H_4$ between 0.4 to 0.07 help to obtain various size of nickel nanoparticles between 80 nm to 400 nm (Fig. 7.3). Nickel particles precipitate fast at high pH (Eq. 7.4).

Increasing reaction temperature should be helpful in accelerating the formation of the nickel nuclei. At higher temperature (> 70 ºC), Ni^{2+} move faster, which makes the crystal growth slower. Therefore a longer time is needed to age the solution in order to obtain star- or flower-shaped crystals. With aging time and increased temperature, the morphology of spherical particles changes, and the nanoparticles develop into star structure and with further ageing (24 hrs) flowery nickel micro-crystals are obtained. Connection was found between the obtained particles morphology and the reaction temperature and ageing time. The formed Ni nanoparticles serve as seed sites for the further reduction of $Ni(N_2H_4)_3^{2+}$ (Eq. 7.4) and crystal growth as the reaction proceeds at high temperature with the longer ageing time. It is reasonable to think that the concentration of Ni^{2+}-ion in solution changes and the Ni nuclei sites gradually increase with the reaction proceeding, which results in the formation of Ni irregular nanoparticles when ageing.

The influence of precursor concentration

The concentrations of Ni-acetate and hydrazine affect the reduction rate and the distribution of ions (or atoms) in the system. When the reaction conditions (reaction time 1 hr and reaction temperature 55-60 ºC) stay constant the change in the obtained spherical nanoparticle size is purely due to the change in the molar ratio (concentration) of the precursors (Ni-acetate and hydrazine). The molar ratio of $Ni(CH_3COO)_2$ /N_2H_4 is kept between 0.4 to 0.07 and size of the produced spherical nickel nanoparticles is between 80 nm to 400 nm, which means the concentration of the precursors controlled the size of the obtained particles.

A minimum number of atoms are required to form nickel nucleus which means under certain precursor concentration and ratio, the reaction is incomplete. The obtained spherical nickel nanoparticles exhibit narrow particle size distribution which results from the fact that most nuclei are formed approximately at the same time and grow at the same rate.

The influence of NaOH concentration

The addition of NaOH leads to an increase of solution pH to 10-12. However, the production yield decreases if the NaOH concentration is >0.7 mol which raises the solution pH > 13. When the concentration of sodium-hydroxide solution is high (0.3 mol) the obtained morphology was the spherical nanoparticles, while the solution temperature was 55 ºC. The low concentration of NaOH solution (0.1 mol) and the high reaction temperature (≥ 70 ºC) can generate nano-size star-like Ni particles. Under the same conditions (NaOH concentration and reaction temperature) as obtaining star-like Ni nanoparticles with increased aging time up to 24 hrs, the formation of flower-like nickel micro-crystal can be produced. Ni^{2+}-ions in the solution with the supports of sodium-hydroxide solution, the crystals grow along a certain direction until all the Ni^{2+}-ions are consumed. Therefore to control the shape of Ni particles, it is important to monitor the concentration of nickel-ion source and sodium-hydroxide.

The morphology and the size of the samples were investigated by SEM. Images in Fig. 7.3 shows spherical Ni nanoparticles (a-f) with the average size between 80 and 400 nm. All the particles show a narrow particle size distribution. Figure 7.4 a-c shows the flower shape nickel structures, and Fig. 7.4 d-e shows the star shape nickel structure. In the form of a flower, the “petals” of the nickel micro-flower are short and

all the same length, while in the form of a star, the “segments” of the nickel nano-star are longer, but of slightly different lengths. Ni nanoparticles have a large surface to volume ratio and strong magnetic attraction forces, which means they tend to agglomerate in order to minimize the total surface energy of the system.

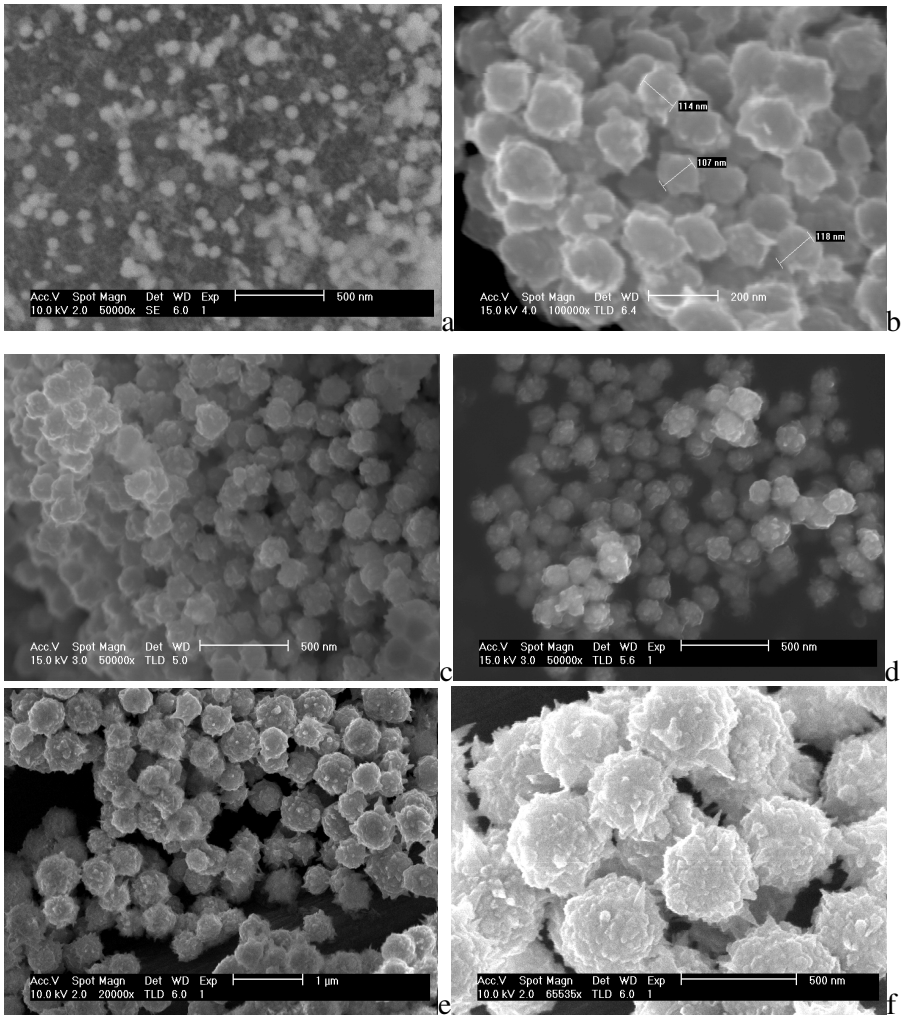

Figure 7.3 SEM images of spherical nickel nanoparticles, 80 nm (a), 100 nm (b), 120 nm (c), 150 nm (d), 300 nm (e) and 400 nm (f)

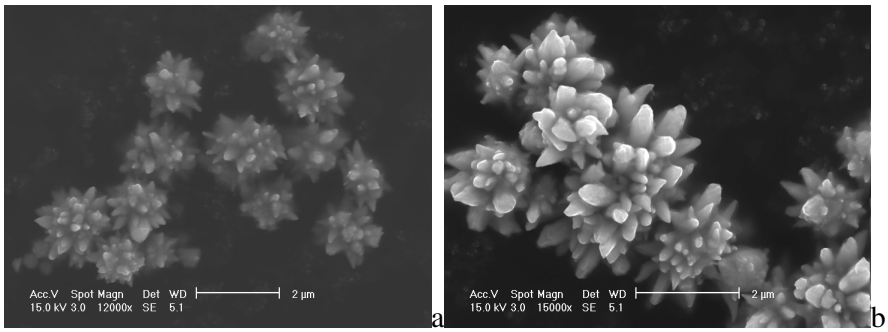

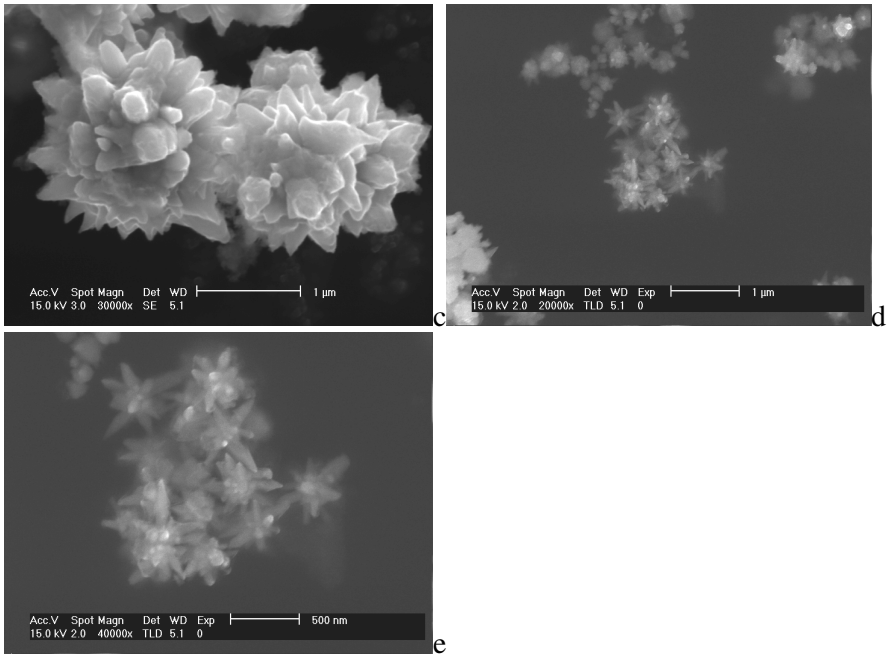

Figure 7.4 SEM images of microflower of Ni (a-c) and nanostars of Ni (d-e)

The XRD patterns of spherical Ni nanoparticles with size between 80-400 nm are shown in Fig. 7.5 (a). All of the three characteristic peaks for nickel (2θ = 44.5º, 51.8º, and 76.4º), corresponding to Miller indices (111), (200), and (222), are observed.

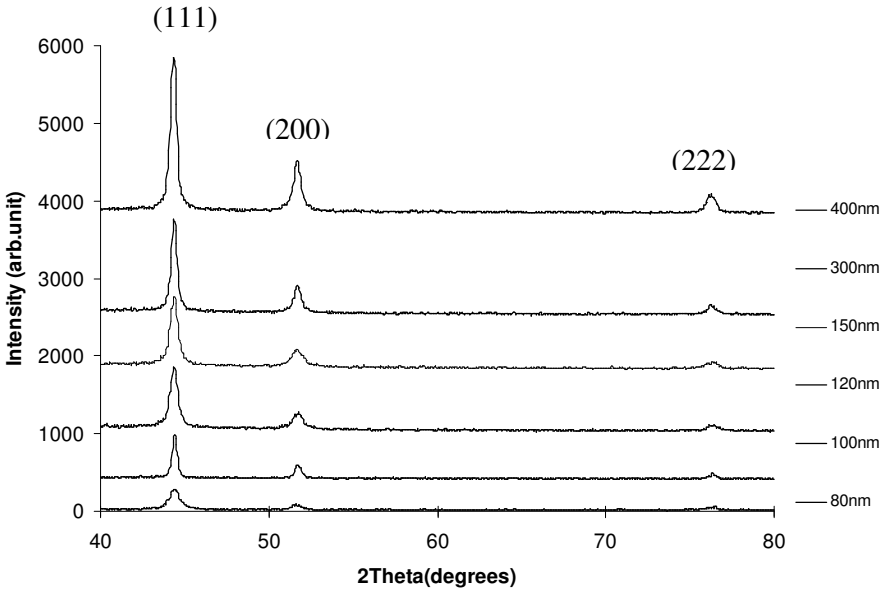

Figure 7.5 XRD patterns of spherical Ni nanoparticles

The decrease of Ni nanoparticle size results in the decrease in the intensity of these peaks. The appearance of those peaks reveals that the resultant particles are pure face-centred cubic (fcc) nickel (JCPDS, No. 04-0850).

It is worth noting that the experiments show that only nickel nanoparticles are obtained even without the use of an inert gas atmosphere. Nickel is easily oxidized to NiO or Ni_2O_3 but the XRD did not detect any impurity. This could be attributed to the fact that N_2 gas was produced during the reaction as shown in Eq. 7.4. The N_2 gas generated in the reaction might have created an inert atmosphere around the Ni particles and hence the input of inert gas was not necessary to prevent Ni nanoparticles from oxidation.

The calculated size values for all Ni samples by Scherrer formula [Chanda, S.C. 2007] at 2θ of 44.5º is in agreement with those observed by SEM (Fig. 7.3, 7.5).

7.3 Barium titanate nanoparticle synthesis

Hydrothermal synthesis might look simple and easy but it has some key parameters which have to be precisely calibrated during the synthesis. A systematic study of hydrothermal synthesis of $BaTiO_3$ (BT) was carried out to understand the effects of parameters such as temperature and time on the formation of $BaTiO_3$ under alkaline conditions because the morphologies of the nanoparticles depend on the temperature and time of the hydrothermal treatment. $BaTiO_3$ ferroelectric nanoparticles have been synthesized by the hydrothermal synthesis method described in Chapter 5.2.

The BT nanoparticles formed by four steps under hydrothermal synthesis at high pH (≥12) by a dissolution-precipitation mechanism:

-when the temperature reached ~50 ºC the $Ba(OH)_2$ octahydrate is dissolved to Ba^{2+} ions and OH^- ions and the water released,

-this released water and started the hydrolysis of Ti source,

-Ba^{2+} ions precipitate into BT nanoparticles,

-a thin layer of BT formed on the surface of TiO_2 and this layer inhibits the diffusion of Ba^{2+} ions and the reaction between the Ba^{2+} ions and TiO_2.

One of the key parameters of the $BaTiO_3$ hydrothermal synthesis is the low solubility of anatase (TiO_2) in highly alkaline (pH 12-13) solution which is necessary for this synthesis. Synthesis reactions [Gou, L. et al. 2006]:

$$Ba(OH)_2 \leftrightarrow Ba^{2+} + 2OH^- \quad (7.5)$$

$$TiO_2 + nH_2O + 2OH^- \leftrightarrow Ti(OH)_6^{2-} + (n-2)H_2O \quad (7.6)$$

$$Ba^{2+} + Ti(OH)_6^{2-} \rightarrow BaTiO_3 + 3H_2O \quad (7.7)$$

$$TiO_2 + 2\,H_2O \leftrightarrow Ti(OH)_4 \quad (7.8)$$

$$Ba^{2+} + Ti(OH)_4 \leftrightarrow BaTiO_3 + 2H^+ + H_2O \quad (7.9)$$

The CO_2 gas could come from the air and/or from the water:

$$CO_2 + 2OH^- \leftrightarrow CO_3^{2-} + H_2O \quad (7.10)$$

$$Ba^{2+} + CO_3^{2-} \leftrightarrow BaCO_3 \quad (7.11)$$

The crystal re-growth could occur due to Ostwald ripening phenomenon:

$$BT_{(small,\ cubic)} + H_2O + H^+ \rightarrow Ba^{2+} + Ti(OH)_4 \rightarrow BT_{(large,\ tetragonal)} + H^+ + H_2O \quad (7.12)$$

Stoichiometric reaction:

$$Ba(OH)_2 + TiO_2 \rightarrow BaTiO_3 + H_2O \quad (7.13)$$

The reaction has two steps from the reaction kinetics point of view:

-formation of titanium hydroxide gel which is a quick reaction,

-Ba^{2+} ions in the solution react with $Ti(OH)_4$ which is a slow reaction.

The reaction kinetics is controlled by the second reaction. The rate of the nucleation and growth is affected by parameters such as titania dissolution which has a connection with the starting Ti source and size. The Ba:Ti ratio was carefully chosen and it is 1.05:1. The reasons are:

-to avoid contamination of solid BT with the excess TiO_2 which was not needed for the formation of BT [Lencka, M.M. et al. 1993]

-high purity of BT synthesis,

-the hydroxyl ions from $Ba(OH)_2$ help the nucleation of BT from the thermodynamics point of view [Lencka, M.M. et al. 1993]

-the Ba excess needed for the $BaCO_3$ creation.

It is known from previous publications [Lencka, M.M. et al. 1993, Gou, L. et al. 2006] that the BT particles are negatively charged at the surface. Between the negative surface charge on the BT and OH^- ions there is a repulsive force acting on them which means there is less chance to form agglomerates. This means the average size of the particles decreases with the higher hydroxyl ion concentration.

Under the hydrothermal conditions the crystallization of BT nanoparticles is driven by kinetics or thermal equilibrium. The kinetics will dominate at low temperature and/or short time and the thermal equilibrium will dominate at high temperature and/or long time. At low temperature some lattice defects and/or the cation cavities form during the hydroxyl ion formation [Clark, I.J. et al. 1999, Chen, C.L. et al. 2008]. At higher temperature the crystal energy is minimised by the thermodynamic equilibrium and the result has less defects in the crystal and more stable structure.

The SEM micrographs (Fig. 7.6 a-d) of the $BaTiO_3$ obtained by the hydrothermal method show that powders contain agglomerated particles having uniform particles with size of 100 nm (a), 200 nm (b), 400 nm (c) and 500 nm (d).

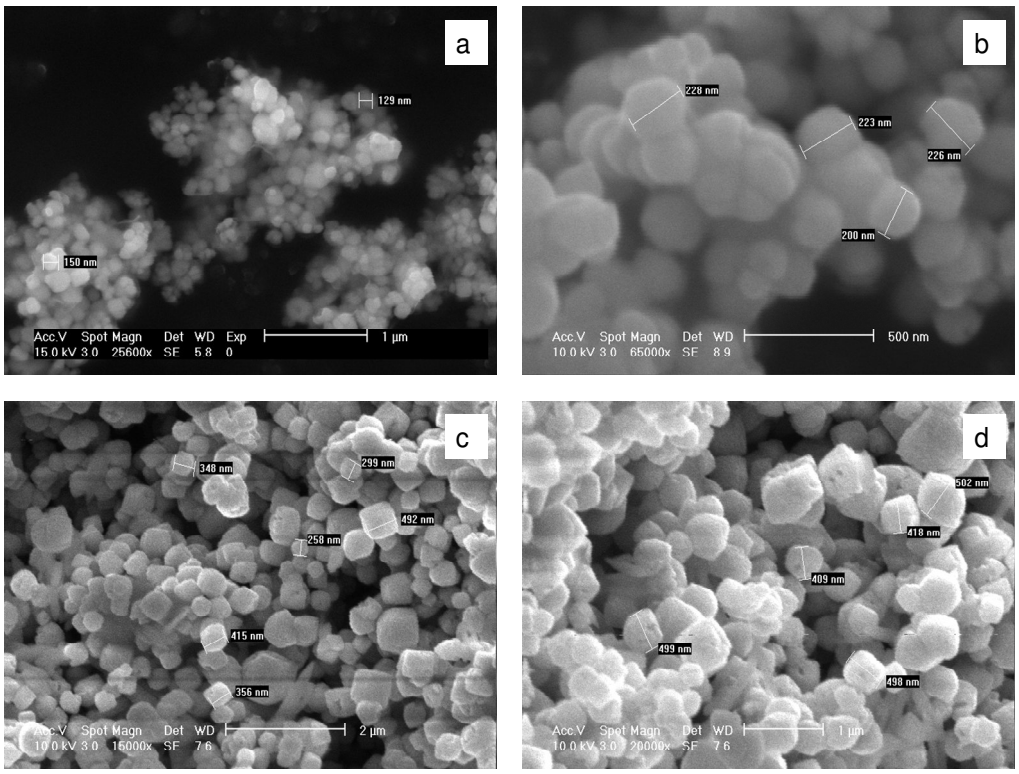

Figure 7.6 SEM images of $BaTiO_3$ nanoparticles, 100-150 nm (a), 200 nm (b), 400 nm (c) and 500 nm (d)

The average particle size obtained at 180 °C for 24 hrs is about 100-150 nm (Fig. 7.6a), at 100 °C for 52 hrs about 200 nm (Fig. 7.6b), at 85 °C for 72 hrs about 400 nm (Fig. 7.6c) and at 65 °C for 192 hrs about 500 nm (Fig. 7.6d). The Ba/Ti ratio remains 1.05:1 to achieve stoichiometric $BaTiO_3$ powder. The extra barium content is

necessary for the formation of $BaCO_3$ due to the reaction with atmospheric CO_2. The formed $BaCO_3$ was washed out with formic acid. The systematical study of the influence of the temperature showed that the reaction was incomplete (precursor was detectable) ≤ 60 ºC. $BaTiO_3$ nanoparticles (100 and 200 nm) are spherical but $BaTiO_3$ particles are more or less cubic especially at larger size (400-500 nm). All the nanoparticles have a quite narrow particle size distribution.

Figure 7.7 shows all the XRD patterns of the $BaTiO_3$ samples. The XRD patterns fit well to the peak positions of the standard cubic phase $BaTiO_3$ (JCPDS No.31-174). The peak at 2θ ~ 45º does not show any splitting in the peak which means that the BT powder stabilized in the cubic form. The cubic phase obtained by hydrothermal synthesis is meta-stable and active at high temperature but the phase transformation is possible with the calcination (≥ 1150 ºC) which eliminates OH^- vacancies and stabilize to tetragonal phase [Clark, I.J. et al. 1999].

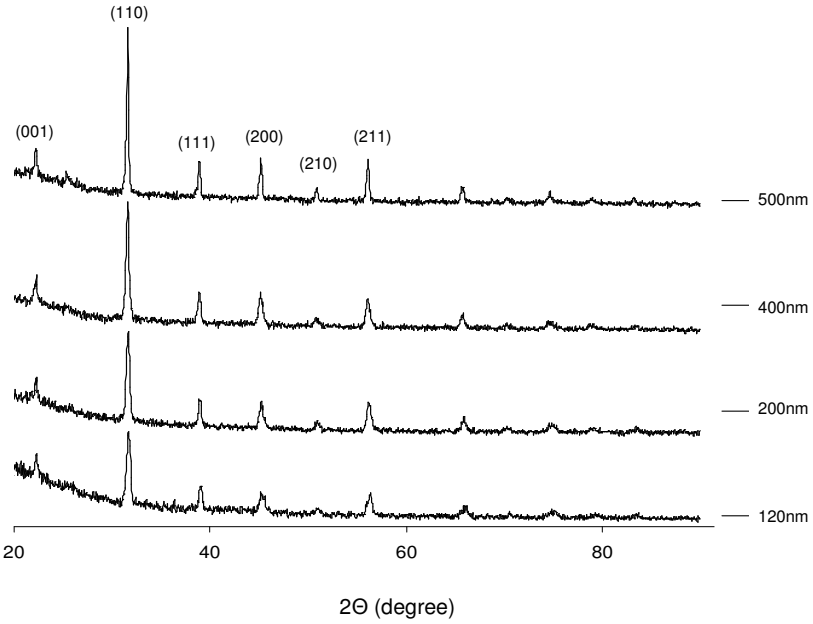

Figure 7.7 XRD patterns of BT with variable size from 120 nm to 500 nm

It is known that in the perovskite structure, the [100] planes have the lowest surface energy [Clark, I.J. et al. 1999]. The high-energy faceted edges of the cubic particles may be subject to preferential dissolution. In addition, the strain associated with the stabilization of the cubic structure tends to reduce the surface area of the growing particles. Therefore, the intermediate morphology consists of cubic particles with a spherical shape regained during the final stage of growth although some larger

particles still retain their cubic shape. The final particle morphology is probably a result of the competing effect between the growth rate and the edge effects. The structural defects of $BaTiO_3$ nanocrystals synthesized by hydrothermal method are primarily in the form of lattice OH^- ions, which are compensated by barium vacancies created on the surfaces of individual particles to maintain electro-neutrality [Clark, I.J. et al. 1999].

7.4 Lead zirconate titanate particles synthesis

Lead zirconate titanate (PZT) nanoparticles have been synthesized by a modified hydrothermal synthesis method described by Deng et al. (2003) and the optimised parameters are presented in Chapter 5.2. In the hydrothermal synthesis of PZT the parameters which play key roles are:

-the concentration of precursors,

-the reaction temperature and time.

At high KOH concentration the pH of the solution is high and the solubility of $Pb(OH)^{3-}$ is higher in these circumstances. PZT formation occurs when the dehydrating condensation takes place between $Pb(OH)^{3-}$ and Zr-hydroxide and Ti-hydroxide at high temperature under pressure. The formation of PZT involves nucleation and growth. With high concentration of monomers in the solution the nucleation is fast. The obtained particles' size and morphology depend on these steps.

The synthesis of PZT particles by hydrothermal reaction involves a dissolution-precipitation mechanism. Trainidis et al. (2000) explained the synthesis of PZT in a two step process when the Zr-Ti-co-precipate and Pb-ions diffuse and form aggregated particles with the beginning of the formation of cubic shape. In the second stage form the actual cubic shape of PZT. Harada (2008) concluded his research with that the PZT creation fully crystallised cubes represent without mid stage. We conclude our investigation with that the dissolution-precipitation mechanism present and PZT forming have an intermediate state with nearly cubic shape which leads to cubic PZT. The mechanism of our experiments could be the following:

-Zr-Ti co-precipitated particles with intermediate form, nearly cubic,

-Pb-ions diffusion and cubic form creation.

In our investigation of the hydrothermal synthesis of PZT the concentration of precursors is kept unchanged and the influence of the reaction temperature and time was studied.

The influence of time

Systematic studies of hydrothermal synthesis of PZT were carried out by studying the influence of the reaction time from 1hr to 4 hrs at 160 ºC (Fig. 7.8). When the reaction time was under two hours the reaction was incomplete, which was proven by XRD characterization (Fig. 7.9).

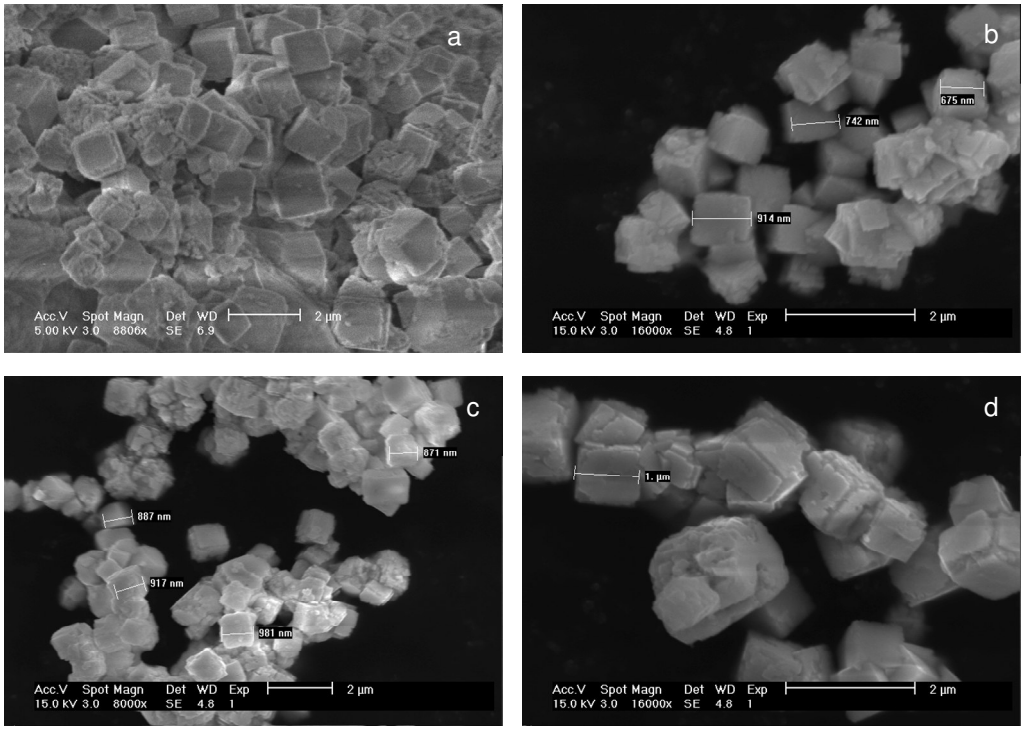

Figure 7.8 SEM images of PZT particles of 1.5 hrs (a), 2 hrs (b), 3 hrs (c) and 4 hrs (d) reaction time of hydrothermal treatment at 160 ºC

The XRD graphs show precursor materials peak with the final PZT. When the reaction time is > 2 hrs, no significant change in particle size estimated by XRD was found (Fig. 7.8 b-d) and the average size is between 800-1100 nm. This result of the effect of the reaction time on the size of particle suggested that the dissolution stage was the key step.

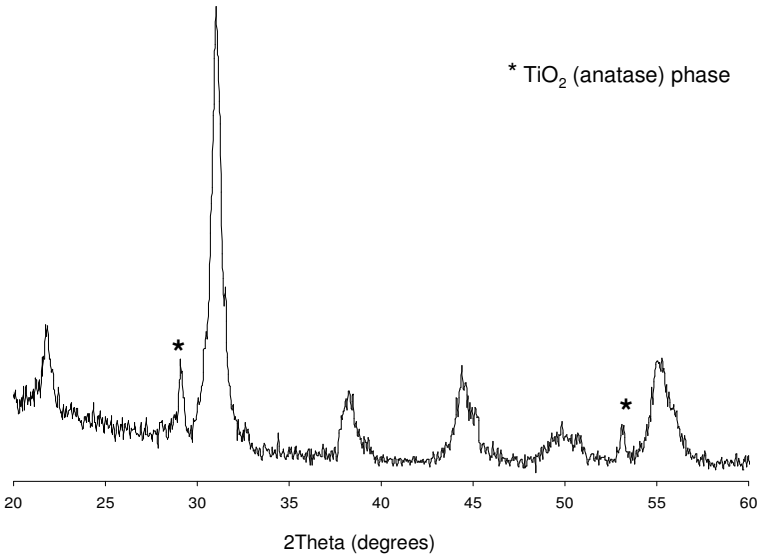

Figure 7.9 XRD patterns of PZT particles made by hydrothermal reaction at 160 ºC 1.5 hrs with some un-reacted precursor

The influence of temperature

In this part of the chapter the effect of the reaction temperature (from 160 ºC to 200 ºC) on the particles size was analysed. The changes of the reaction temperature had some effect on the size of the obtained PZT particles.

Deng et al. (2003) studied the influence of the temperature on the size of the PZT particles and they concluded the size increases with the increase of time and temperature. Meanwhile Harada (2008) and Dunn et al. (2008) found the reaction temperature between 140 ºC to 160 ºC did not make much influence on the particles' size. However, our investigation shows that the temperature has influence on the particle size and the morphology, and the latter changed from cubic to piled platelets via nearly-spherical.

Figure 7.10 shows the SEM images of PZT particles made by hydrothermal synthesis. The influence of the temperature was studied and the result shows that at lower temperature 160 ºC (Fig. 7.10a) the average obtained particles size is 800-900 nm. The size of the particles decreased when the temperature increased (170 ºC-200 ºC). At 170 ºC (Fig. 7.10b) the obtained particles size 700-800 nm. The size of particles is 100-200 nm at 190 ºC (Fig. 7.10c) and 80-100 nm at 200 ºC (Fig. 7.10d). The morphology of the PZT particles changed as well.

The XRD graphs (Fig. 7.11) shows that the indexed peaks of PZT powder matches up with the values for 52:48 PZT (PDF card 33-0784).

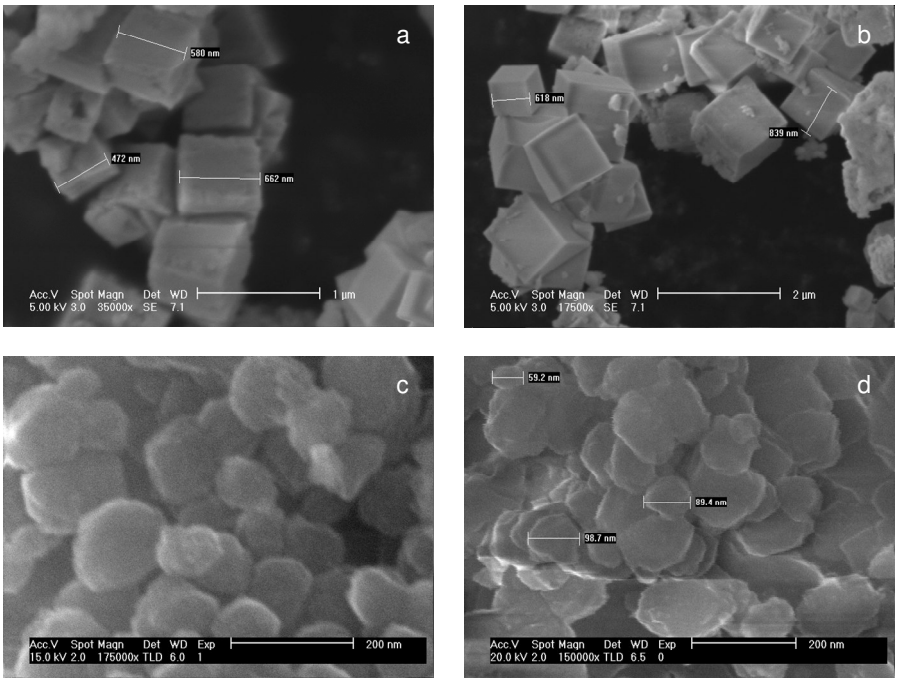

Figure 7.10 SEM images of PZT particles, produced at 160 ºC (a), 170 ºC (b), 190 ºC (c) and 200 ºC (d)

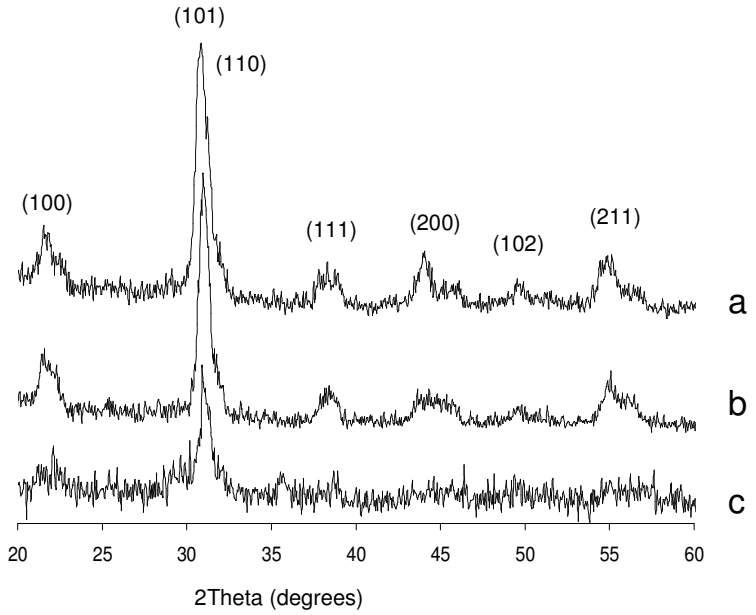

Figure 7.11 XRD patterns of PZT powder made by hydrothermal method at 160 ºC (a), 170 ºC (b) and 200 ºC (c)

7.5 Solid silicon dioxide nanoparticle synthesis

The main synthesis process of silicon dioxide nanoparticles is shown in Figure 5.1. The following reactions occur during the sol-gel process: hydrolysis, alcohol condensation, water condensation as seen in Equations 5.1-5.3. Overall reaction from TEOS (tetraethyl orthosilicate) into SiO_2 is:

$$Si(OC_2H_5)_4+2H_2O = SiO_2 + 4C_2H_5OH \quad (7.14)$$

The two main stages needed to form SiO_2 nanoparticles are nucleation and growth. The size of the final product depends on the reaction conditions. Key parameters of the silica nanoparticles by sol-gel synthesis are:

-precursor concentration (TEOS),

-base concentration and feed rate,

-reaction temperature,

-type of the mixing (ultrasonic or magnetic).

Effect of the precursor's concentration

The concentration of TEOS is important for the production of nuclei which in the meantime aggregate. The nuclei which did not aggregate dissolve in the solution and re-precipitate on the aggregated particles through Ostwald ripening. This reaction will be going on until the equilibrium condition is achieved.

Effect of the ammonium hydroxide concentration and feed rate

The second parameter is the added base concentration and feed rate because the base increases the hydrolysis of TEOS [Rahman, I.A. et al. 2007, 2008] and the condensation rate of hydrolysed monomers and this latest reaction results in the increased size of the SiO_2. The lower base concentration results in smaller particles size.

Hydrolysis is a slow reaction even when a base is used as a catalyst. Several studies [Matsoukas, T. et al. 1988, Park, S.K. et al. 2002] have already reported that the ammonium hydroxide concentration has an effect on the obtained particles' size. A short nucleation period results in nuclei with narrow size distribution. The creation of nuclei is followed by growth process until the equilibrium reaches. This is detected by the pH changes.

When the ammonium hydroxide feed rate was slow (0.03 ml/min) the kinetic energy produced by the reaction resulted in slow particle growth and small particle size (20 nm). The increase of the feeding rate of ammonium hydroxide and slightly reduced temperature have obtained bigger particles size (40 nm).

Effect of the temperature change on the reaction

It was found that the formation of the solid silica nanoparticles could be completed as low as 25 ºC. Increasing reaction temperature was helpful in accelerating the formation of the silica nuclei. A connection was found between the size of the particles obtained and the reaction temperature. A higher temperature resulted in a smaller particle size because the nucleation rate is higher.

Type of mixing (ultrasonic or magnetic)

Several studies [Park, S.K. et al. 2002, Rahman, I.A. et al. 2007] have shown that the type of the mixing makes different size and structure of final product. The use of ultrasonic mixing produced smaller particle size than the magnetic mixing. The higher temperature and the change of homogenising type (magnetic instead of ultrasonic) result in a radical increase of the particles size (300 nm). The obtained silica nanoparticles have a smooth surface, spherical shape and quite narrow size distribution. Figure 7.12 shows the size of obtained particles being in the range of 20 nm to 300 nm.

Table 7.2 summed up the effect of temperature and ammonium hydroxide feeding rate on the subsequent particle size while keeping the concentration of reactants ($EtOH/H_2O/TEOS/NH_4OH$) constant. The dramatic change in the size is caused by the change of the homogenising technique. In Table 7.2 the * means magnetic stirring and EtOH means ethanol.

Table 7.2 Parameters and results of the solid silica nanoparticles synthesis

	Concentration of reactants $EtOH/H_2O/TEOS/NH_4OH$ [ml]	NH_4OH feeding rate [ml/min]	Temperature [ºC]	Average Size [nm]
1	48 / 2.0 / 4.1 / 5.5	0.03	55	20±5
2	48 / 2.0 / 4.1 / 5.5	0.1	45	40±5
3	48 / 2.0 / 4.1 / 5.5	0.1	40	80±5
4	48 / 2.0 / 4.1 / 5.5	0.1	25	300*±5

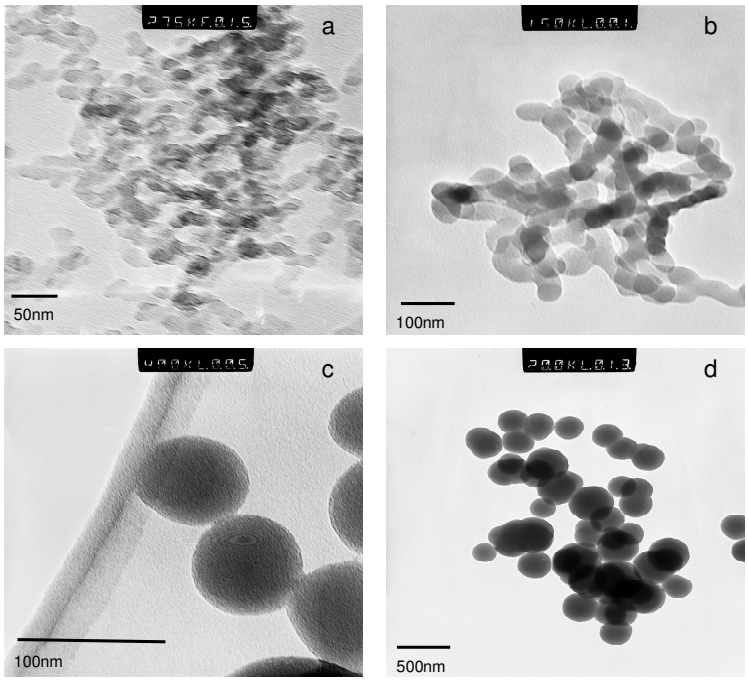

Figure 7.12 TEM images of silica nanoparticles with average size: 20 nm (a), 40 nm (b), 80 nm (c) and 300 nm (d)

7.6 Hollow silicon dioxide particles synthesis

The synthesis of hollow silicon dioxide particles was shown in Fig. 5.2, which is a two-step sol-gel-emulsion process. The following reactions occur: hydrolysis, alcohol condensation, water condensation as seen in Equations 5.1-5.3 and the overall reaction from TEOS into SiO_2 is shown in Eq. 7.14.

The morphology of the obtained silica particles depends on the kinetics of the TEOS during the hydrolysis and the condensation. The typical sol-gel method involves a hydrolysis of TEOS in polar solvent while using a base or acid as a catalyst. The chosen catalyst has an effect on the final product, because the acid as catalyst tends to promote network formation (like in our case the hollow form) and the base catalyst tends to promote the formation of solid nanoparticles (as seen in Chapter 7.5).

The first step is the pre-hydrolysis of TEOS and then the non-ionic surfactant (Span 80, $C_{24}H_{44}O_6$) and the silicon from TEOS bond together by hydrogen bonds and due to self-assembly the coated structure starts forming on the surface of the emulsion droplets and the core-shell structure is created. The hydrolysis of TEOS molecules

occurs when the TEOS molecules attack the interface of the water-in-oil emulsion where the polar $Si(OH)_xO(CH_2CH_3)_y$ (TEOS) molecules prefer to accumulate. During the hydrolysis a water molecule replaces one of the ethoxy groups of the TEOS, a hydroxyl group is forms. Two hydroxyl groups will then react and release a water molecule and simultaneously form a Si-O-Si bond, which is called polymerization and gellation starts. The preferred position of silica particles is at the water-oil interface. The whole synthetic method of obtaining hollow silica particles relies on the self-assembly of the surfactant on the droplet surface.

The surfactant has a double function in this synthesis. The functions are: facilitate emulsion formation and promote emulsion stability and form monolayer at the water-oil interface. The non-ionic surfactant (Span 80) is preferred due to its lower cost and has the advantage of varying the length of the hydrophilic and hydrophobic groups. Key parameters were studied in this investigation of the synthesis of hollow silica particles by sol-gel-emulsion method are:

-precursor concentration (TEOS),

-reaction temperature and time,

-type of mixing.

Effect of the reaction temperature and time

The time for the formation of viscous sol by pre-hydrolysis of water phase is tested to be a minimum of 40-45 min because if the time is shorter than this the reaction is unfinished as detected by an optical microscope. The dry product (before calcination) collapsed and could not keep the core-shell form, which means the reaction was not finished. The optimised reaction time of this stage was set for 60 min. The reaction temperature at this stage was set for 50 ºC. At lower temperature the reaction was unfinished and a higher temperature was not necessary to have as good a result for structure and as product yield.

Type of mixing (magnetic or mechanical) and the stirring rate

In the beginning of the experimental investigation a mechanical (rod) stirrer was used, but the equipment had a limited stirring rate (up to about 500 rpm) and to increase the stirring speed, magnetic stirring mode was used. Figure 7.13 shows the effect of the stirring rate on the particle size.

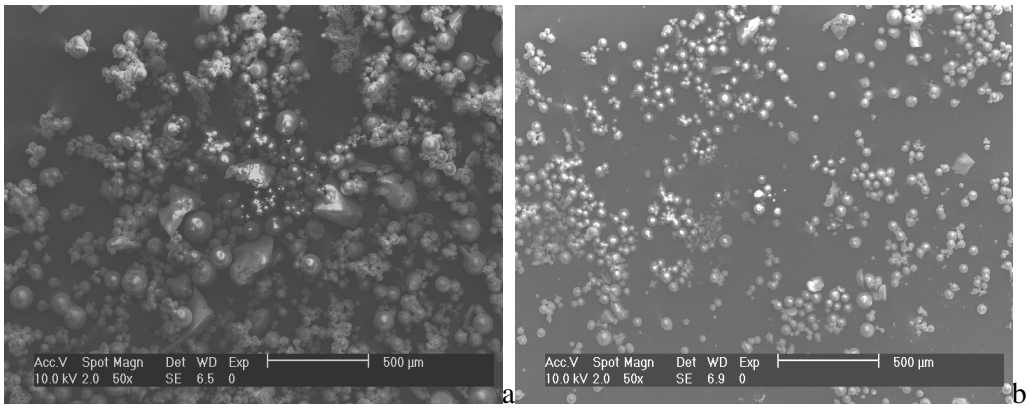

Figure 7.13 Hollow silica particles produced by mechanical (rod) stirring (a) and magnetic stirring (b)

The size distribution is quite wide in all batches of the synthesised hollow silica particles. Both stirring modes (mechanical and magnetic) could not provide homogeneous stirring effect, which leads to the broad size distribution in the final product.

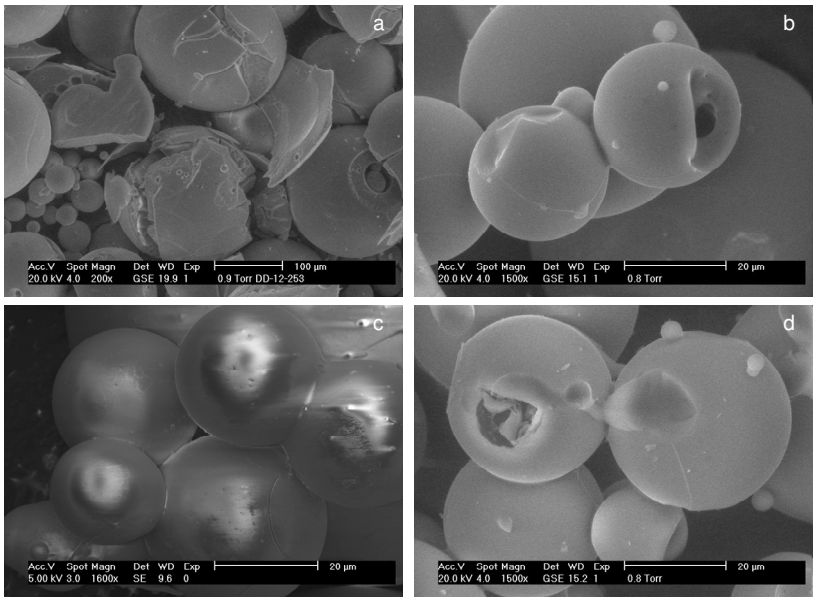

Figure 7.14 E-SEM images of hollow silica particles made by sol-gel-emulsion synthesis method, broken silica particles (a), hollow silica particle with a chip and a thick shell (b), images of silica by SEM (c) and silica particles (d)

The homogenisation step in the further batches was carried out in magnetic stirring mode. The final product of hollow silica before the calcination was whitish-pale-

yellow and after the calcination it was black. The resultant black colour could be carbon residues of the organic network. The surfactant in the reaction used for self-assembly (scaffolding) and to help the polymerisation. Fig 7.14 shows the obtained particle size and their structure.

7.7 Core-shell Ni- and Fe_3O_4 - coated SiO_2, BT, and PZT particles

The synthesis of the nanoparticles is described in Section 5.3.3. The synthesis route used to produce the coated particles is a quite simple and efficient. Figure 7.15 shows the SEM images of (a) SiO_2, (b) BT, (c) PZT (d) Ni and the TEM image of (e) Fe_3O_4. The average size of SiO_2, BT, PZT, Ni and Fe_3O_4 particles is about 15 μm, 130 nm, 1 μm, 90 ~100 nm and 10 nm, respectively. SiO_2, BT and Ni particles are spherical while PZT particles are more or less cubic. Except for SiO_2, all the particles showed a narrow particle distribution. Due to the large surface to volume ratio and strong magnetic attraction forces, the Ni and Fe_3O_4 nanoparticles tend to agglomerate in order to minimize the total surface energy of the system.

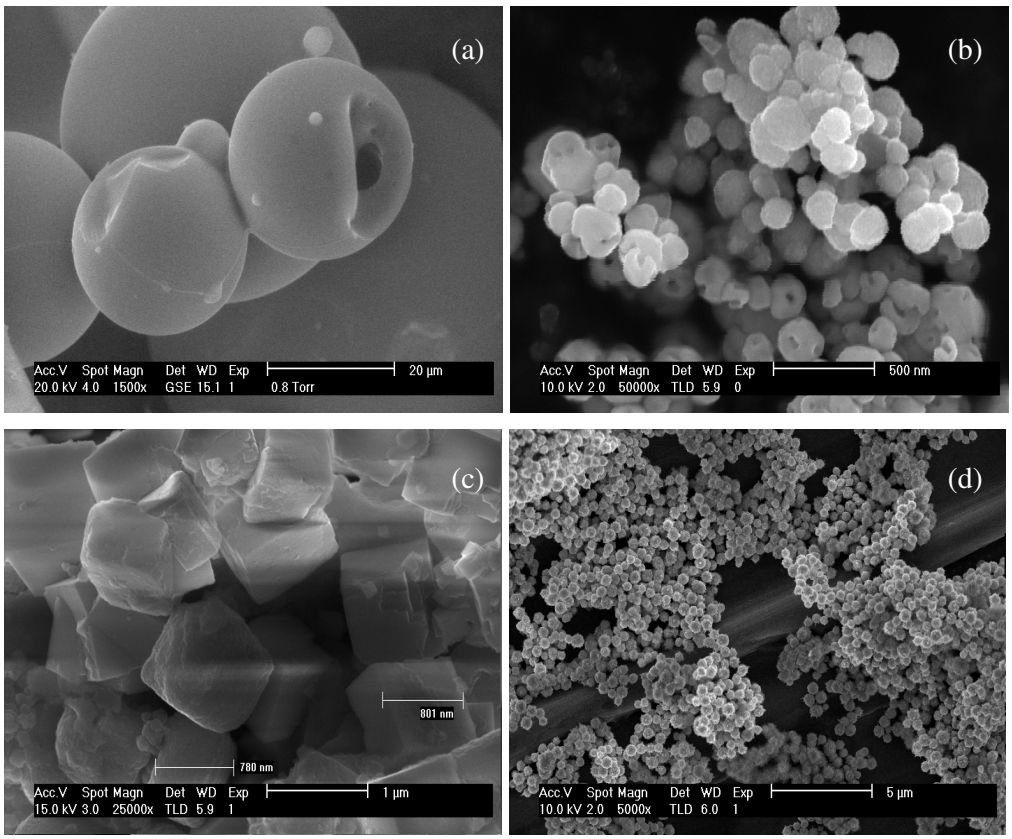

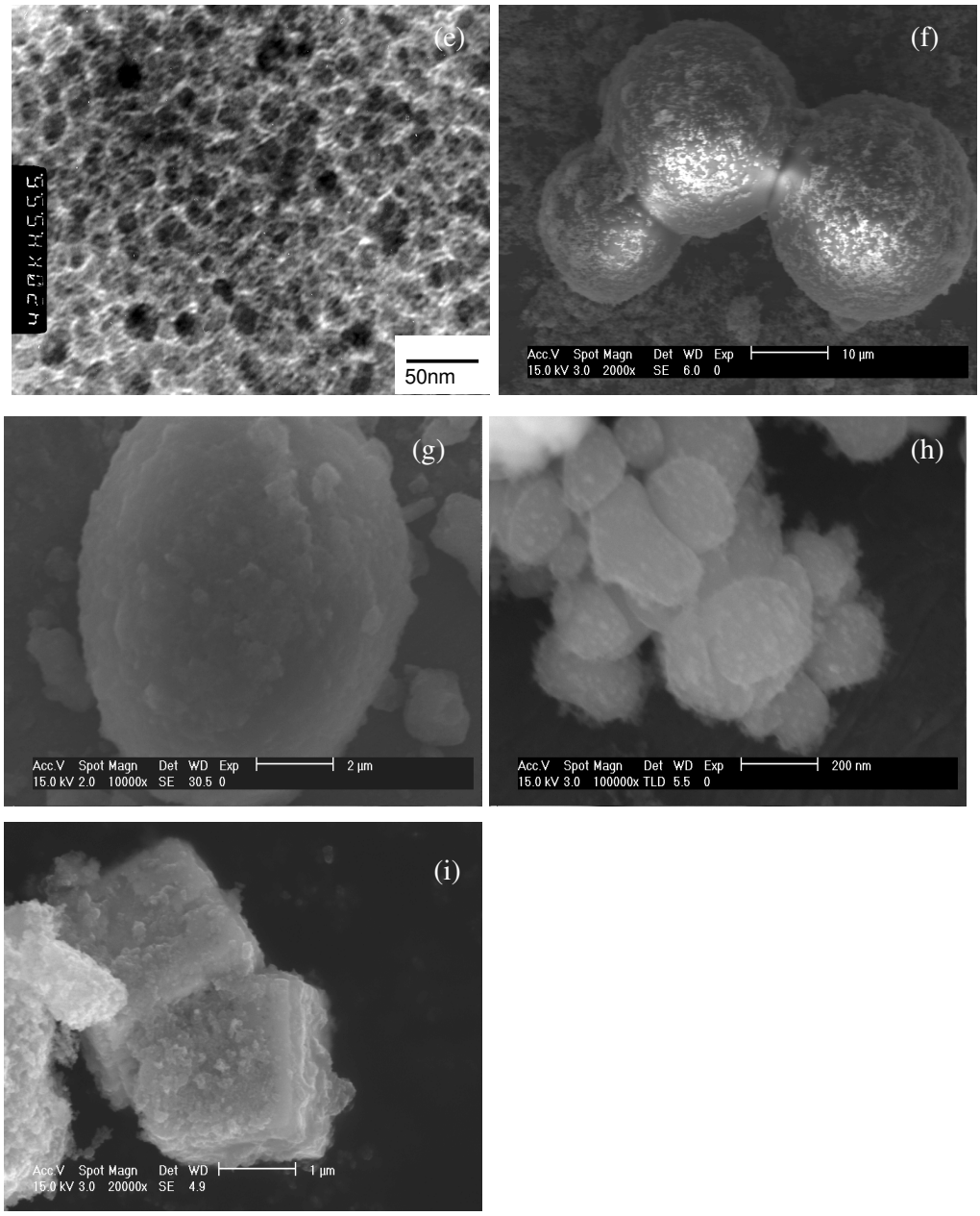

Figure 7.15 SEM and TEM images of particles (a-e) and core-shell particles (f-i). a: SiO_2; b: BT; c: PZT; d: Ni ; e: Fe_3O_4 (TEM); f: SiO_2/Ni; g: SiO_2/ Fe_3O_4; h:BT/Fe_3O_4; i: PZT/ Fe_3O_4

Fig. 7.16 shows the zeta potential values of the SiO_2, BT, PZT, Fe_3O_4 and Ni particles in water as a function of pH. Zeta potential measurement gives the information about the overall surface charge of the particles and how this is affected by the changes in the environment (e.g. pH). The measured colloid suspensions were prepared without adding any surfactant. Adjustment of the pH was carried out by adding HCl and

NaOH solutions. The results of the electrophoresis measurements revealed that the zeta potentials of core (SiO_2, BT and PZT) and shell (Ni and Fe_3O_4) particles have opposite signs in some pH regions, for example, at 4.3 <pH < 9.0, the zeta potential for SiO_2 particles was between 0 and -40 mV while the zeta potential of Fe_3O_4 particles was between +30 and 0 mV. This allowed for the easy attachment of the Fe_3O_4 particles on the surface of SiO_2 particles at this pH region, similarly, of the Ni particles on the surface of SiO_2 particles at 4.3 <pH < 10.7, of the Fe_3O_4 particles on the surface of BT and PZT particles at 4.2 <pH < 9.0 and 5.1 < pH < 9.0, respectively.

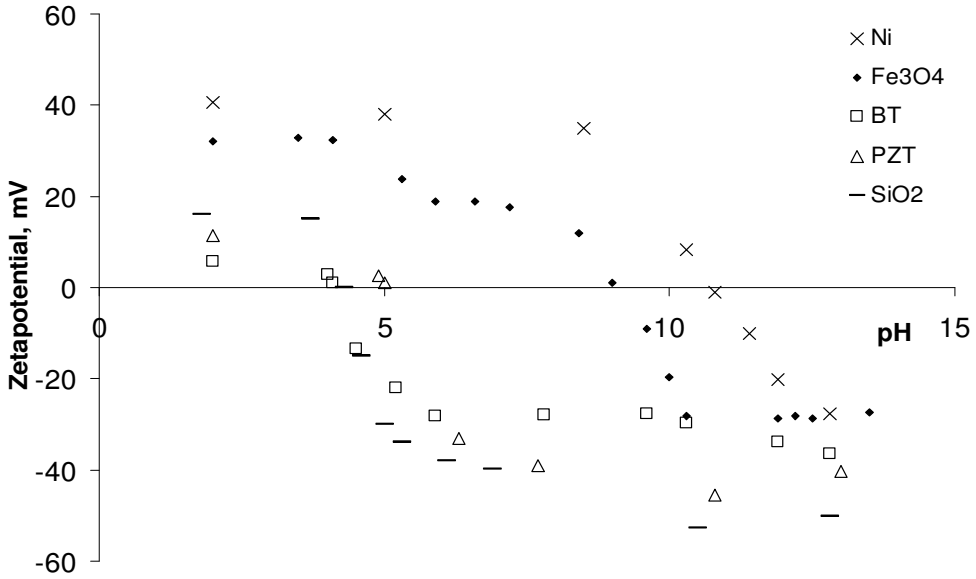

Figure 7.16 Zeta potentials of SiO_2, $BaTiO_3$, PZT, Fe_3O_4 and Ni particles in water as function of pH

SEM was also employed to examine the morphology of the coated particles (Fig. 7.15 f-i). In comparison with the un-coated particles (Fig. 7.15a-e), the coated particles have a rough surface. The ferrite coating is confirmed from the change in size, shape and the presence of Fe element in the particle determined from EDX (data shown Fig. 7.17). In the EDX analysis for core-shell structure, a suitable electron beam acceleration voltage needs to be selected in order to effectively identify the layers' elemental information.

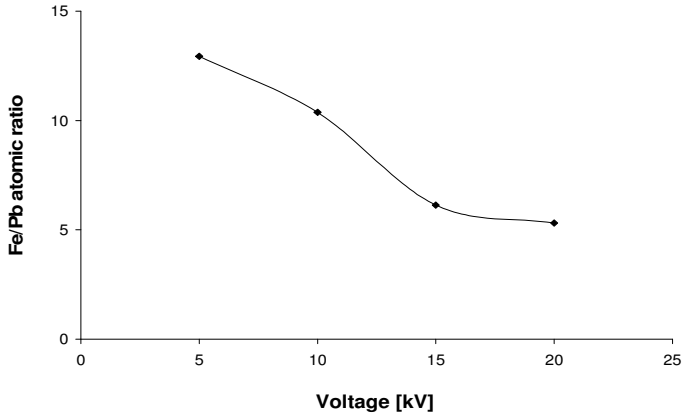

Figure 7.17 EDX results for PZT/Fe_3O_4 composite in different voltage

The SiO_2 particles remain spherical after they were coated with Ni (Fig. 7.15f) or Fe_3O_4 (Fig. 7.15g). The PZT crystals with cubic shape have a smooth edge after they were coated with Fe_3O_4 (Fig. 7.15i). The thickness of the shell can be controlled through the mediation of the ratio of core and shell particles and the reaction time. Fig. 7.18 shows the SEM images of Ni coated SiO_2 particles obtained at different molar ratios of core-shell particles. It is worth noting that the higher the shell particle concentration is, the rougher the coated surface is. This is understandable because the higher concentration of shell particles leads to multi-layer coating. Shell morphology is strongly dependent on the parameters, such as, pH values, suspension concentration and core-shell particle ratio. Fig. 7.18a and 7.18b show the core-shell particles obtained with the Ni particle concentration at 0.01 g/l and 1 g/l, respectively. Fig. 7.18b shows an obvious over-loaded surface coating.

Fig. 7.19 shows the XRD patterns of Fe_3O_4 particles and Fe_3O_4 coated SiO_2 particles. Because SiO_2 is amorphous (XRD pattern was not shown), all the peaks on the XRD pattern of core-shell SiO_2/Fe_3O_4 particles are the reflections from Fe_3O_4 particles. The XRD peaks correspond to the spinal structure in Fe_3O_4 particles and Fe_3O_4 coated SiO_2 sample. These peaks are broad due to the small particle size but did not shift after coating. Because the intensity of these peaks is very weak, it is difficult to estimate the crystallite size of these Fe_3O_4 particles using Scherrer formula. The XRD patterns of PZT/ Fe_3O_4 and BT/ Fe_3O_4 are not shown because the Fe_3O_4 peaks on these patterns are too weak compared to the peaks coming from PZT and BT reflections.

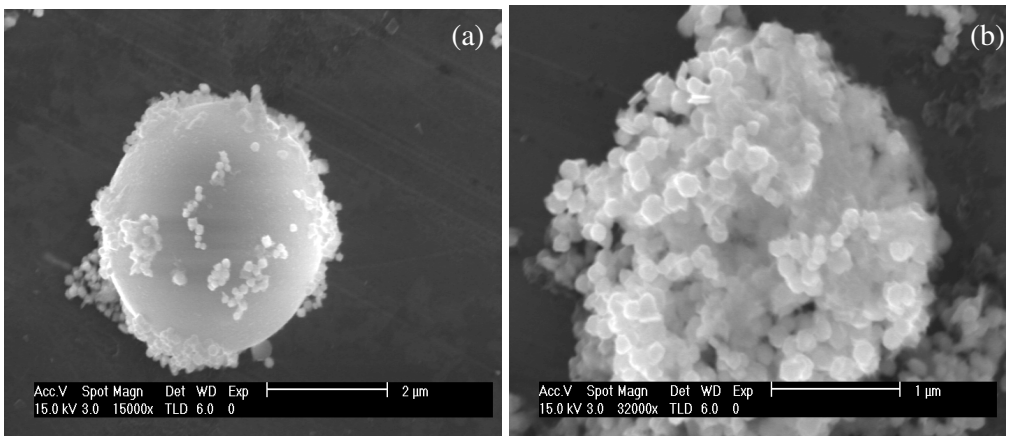

Figure 7.18 SEM of a single SiO_2 particle coated with nickel particles at different Ni concentration

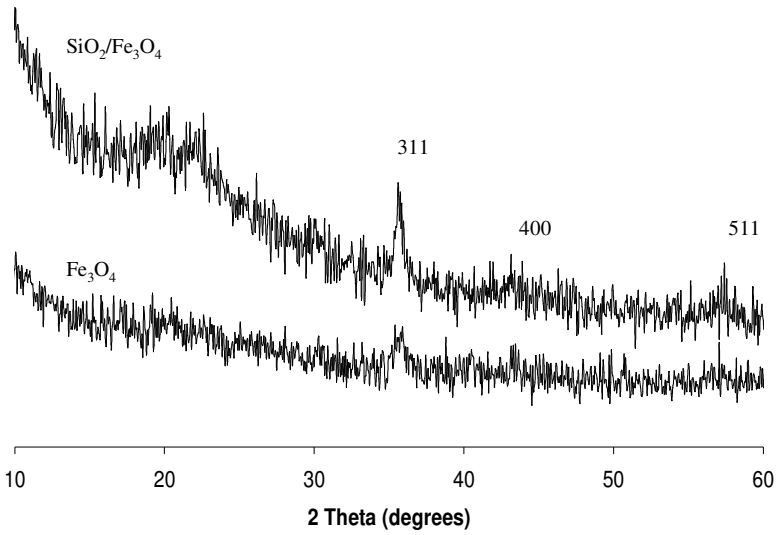

Figure 7.19 X-ray powder diffraction patterns of Fe_3O_4 particles and SiO_2/Fe_3O_4 core-shell composite at room temperature

Fig. 7.20 shows the XRD patterns of Ni particles and Ni coated SiO_2. Three characteristic peaks for nickel (2θ = 44.5º, 51.8º, and 76.4º), corresponding to Miller indices (111), (200), and (222), were observed. This revealed that the resultant particles were pure face-centred cubic (fcc) nickel at both samples (JCPDS, No. 04-0850). The XRD patterns reveal that only nickel is detected. Although it is known that nickel is easily oxidized to oxides, some possible oxides such as NiO, Ni_2O_3 are not observed in the XRD profiles. Because the core-shell samples have been exposed to

the air and water for a long time during the synthesis, the absence of nickel oxides also indicates that the current synthetic method for Ni coated core-shell structure is feasible in achieving metallic Ni coated core-shell structure. The calculated size values for both pure Ni and coated Ni by Scherrer formula at 2θ of 44.5º are general approximates to that of SEM observation (Fig. 7.15).

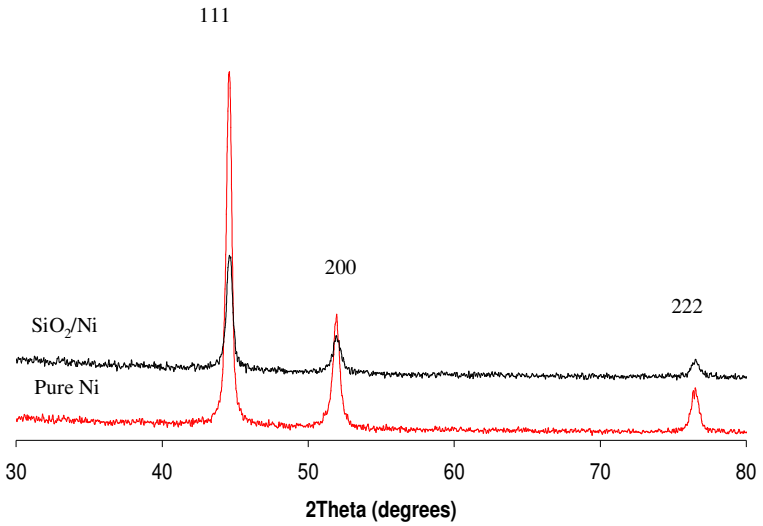

Figure 7.20 X-ray powder diffraction patterns of Ni particles and SiO_2/Ni core-shell composite at room temperature

The AFM is used to measure the surface topography of the samples in tapping mode. Fig. 7.21a shows the 3D image of the Fe_3O_4 coated PZT surface and Fig. 7.21b shows the 2D surface image of PZT/Fe_3O_4. The 3D image (Fig. 7.21a) shows a well coated PZT surface with a larger roughness in comparison with uncoated PZT surface (Fig. 7.21b).

The Fe_3O_4 coated particles were measured in the VSM at 300 K. Fig. 7.22 shows the magnetization versus field plots of the Fe_3O_4-coated particles. The magnetic curves of three samples exhibit ferromagnetic behaviour (hysteresis can be seen in the inset of Fig. 7.22). All of the samples possess a lower saturation magnetization M_s (Table 7.3) than bulk Fe_3O_4 (92 emu/g) [Zhang M, et al. 1994] due to the presence of the SiO_2, BT or PZT. After normalizing the M_s values of core-shell particles to emu per gram of bare 10 nm Fe_3O_4 nanoparticles (53.8 emu/g [Zhang, M. et al. 1994, Lee, J. et al. 1996, Huang, C.K. et al. 2008]), the weight percentage of shell can be crudely

estimated (Table 7.3). Under the same conditions, the content of Fe_3O_4 coated on the different surfaces is varied and this might be related to the relative size of core and shell particles. The magnetic properties of Ni coated SiO_2 particles were also measured at 300 K (Fig. 7.23) and M_s=7.8 emu/g is 14% of the bulk value was (55 emu/g) [Cullity, B.D. 1972] due to the presence of the SiO_2.

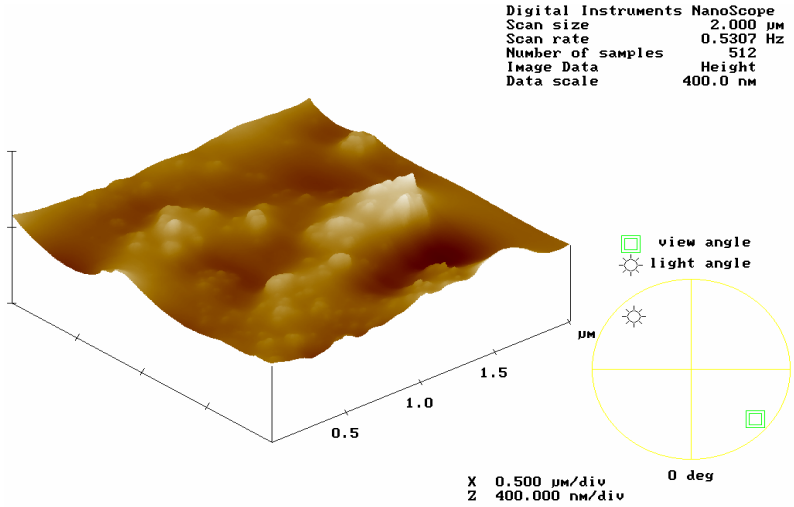

(a)

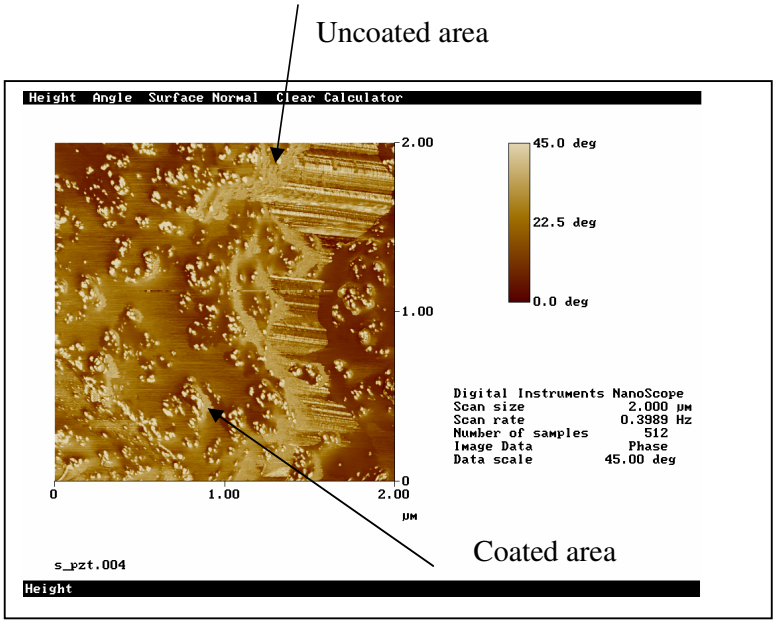

(b)

Figure 7.21 AFM images of the PZT surface coated with Fe_3O_4 particles. a: the 3D image of the Fe_3O_4 coated PZT surface; b: the surface of PZT/Fe_3O_4 obtained by the AFM in tapping mode

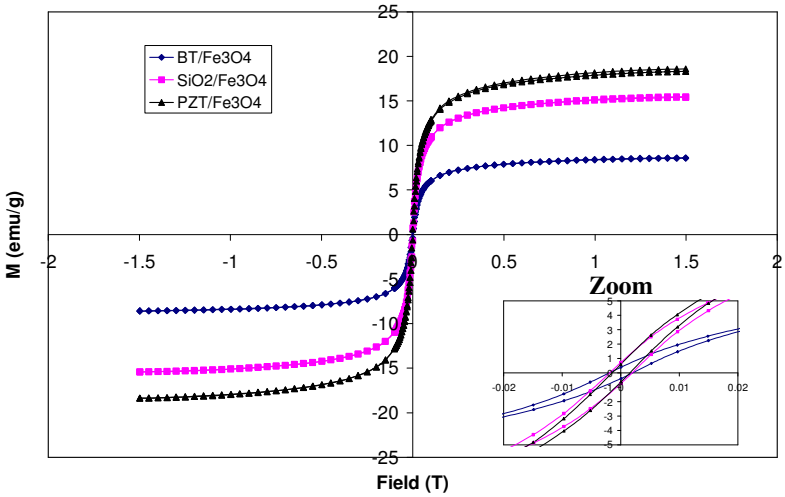

Figure 7.22 Magnetization as a function of applied magnetic field for Fe_3O_4 coated particles at room temperature. Inset: hysteresis is seen at low-fields

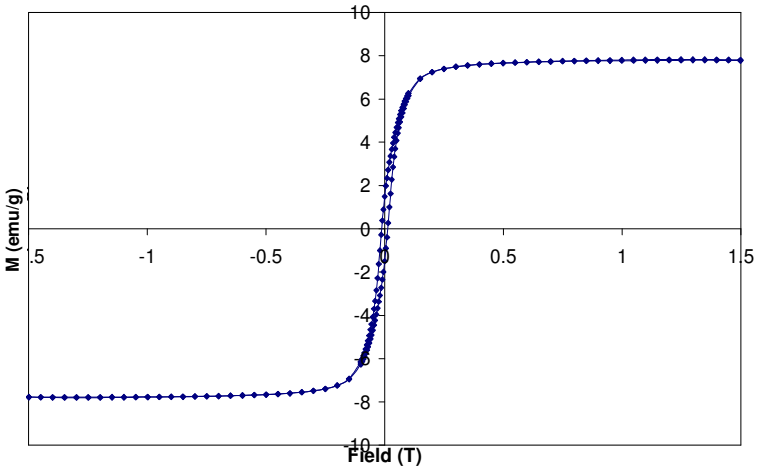

Figure 7.23 Magnetic hysteresis loop for SiO_2/Ni particles

Table 7.3 Magnetization data for various samples measured at room temperature

Sample	M_s (emu/g)	Content $_{shell}$ (%)
BT/Fe_3O_4	8.6	16
SiO_2/Fe_3O_4	15.4	29
PZT/Fe_3O_4	18.3	34
SiO_2/Ni	7.8	14

Chapter 8 Results and discussion of nanofluid characterization

This chapter presents the results and discussion of the experimental investigation on the rheological characterization, surface and interface tension results of nanofluids.

8.1 Sedimentation of nanoparticles in nanofluids

Our nanofluids have been made by a two-step method which first makes nanoparticles and then disperses them into the fluid as explained in Chapter 6. The nanofluids were found to be stable and there was no observable sedimentation over a period of three hours. The absence of surfactant gives an opportunity to use the "pure" nanofluid in further characterization without additional complexity.

The stability of nanofluids generally depends on the particles' surface properties, size and shape. Agglomeration of nanoparticles occurs readily in nanofluids, effectively increasing their size and their sedimentation rate.

The settling of small particles (<50 μm diameter) is described in the mid 19th century by George Gabriel Stokes. This assumes that the drag on a spherical particle is due to viscous forces. This is the case when particle velocity is insufficient to cause turbulence in the surrounding fluid [Wilson, S.A. 1999]. Therefore, a Stokes Law approximation was used to estimate the settling time for nanoparticles in the non-polar fluid:

$$\text{Settling time} = (18\mu s) / [gd^2 (D_s - D_f)] \quad (8.1)$$

where μ is the fluid viscosity; s is distance; d is the particle diameter; D_s and D_f are the densities of the solid and the fluid respectively.

Settling time is the time it takes for nanoparticles to settle through the same depth (1 mm) of nanofluid. This theoretical calculation (Table 8.1) can be used to estimate the sedimentation time of nanoparticles in nanofluid.

Table 8.1 Estimated settling times for nanoparticles in oils

Settling time [hours]					
BT [130 nm]		Ni [100 nm]		Fe_3O_4 [10 nm]	
Silicone oil	FC70	Silicone oil	FC70	Silicone oil	FC70
32.3	20.3	31.2	17.6	613	399

The experimental investigation of the settling of nanofluid gave the practical result and it is concluded that the sedimentation was not a significant factor during the time ranges of any our measurements (the longest took about 30 min).

The measured settling time of nanofluids shows that no sedimentation was visible in the iron oxide-silicone oil nanofluid after 8 hrs, in the nickel-silicone oil nanofluid the observable sedimentation started after 2.5 hrs, and the sedimentation of the BT-silicone oil nanofluid was observable after 3 hrs. The sedimentation has been started in different time due to the different size (iron oxide 10 nm, BT 130 nm and nickel 100 nm) and bulk density (iron oxide 5240 kg/m^3, BT 5850 kg/m^3, and nickel 8800 kg/m^3) of the suspended nanoparticles. The sedimentation occurred in all of the nanofluids after 2.5 hrs, due to aggregation of nanoparticles and a lack of any additives or surfactant.

The theoretical calculation of the settling time by Stokes law is not fully suitable for nanofluids and this caused the difference in the estimated and the measured settling times for nanofluids.

Our experimental results have good agreement with previous study [Donselaar, L.N. et al. 1997] which also shows that the sedimentation velocity has very little dependence on the particle concentration.

8.1.1 Sedimentation of mixed dispersion of nanoparticles in nanofluids

In our experiments mixtures of nanoparticles (Ni and Fe_3O_4) in fluid were studied. Nanofluids containing both Ni (100 nm) and Fe_3O_4 (10 nm) nanoparticles were made as explained in Chapter 6. The ratio of the size of the suspended particles is large enough (1:10 in this case) the mixed nanoparticles system was found to sediment more slowly than a mono-dispersion of the larger particles. It is believed that the smaller particles influence the “network” of larger particles. Even weak inter-particle attraction has an effect on the sedimentation result. The van der Waals attraction between the bigger particles is different when the system contains small sized particles as well. The small particles are thought to prevent the bigger particles touching each other and mixed-particle agglomerates are energetically unfavoured [Wilson, S.A. 1999].

Sedimentation was experimentally observable in the mixed nanoparticles system after 3.5 hrs which is 1 hour more than for the pure nickel nanofluid.

Our experimental result shows good agreement with the study by Thies-Weesie et al. (1996) which shows that the sedimentation velocity is reduced under gravity for mixed uncharged spherical particles.

8.2 Rheological characterization of nanofluids

This part of the work is an investigation into the rheological character of some non-polar fluids containing different types of nanoparticles. The nanoparticles (BT, nickel and iron oxide) were synthesised with controlled size distribution and morphology. Suspensions of particles in either silicone oil or FC70 oil with different solid loadings (10, 20 and 30 g/l) were measured over the shear-rate range of 0.10–10 s^{-1}.

8.2.1 Effect of solids concentration on viscosity

Fig. 8.1 shows the change in viscosity of the suspensions of silicone oil containing nanoparticles against shear rate in the range of 0.10-10 s^{-1}. The suspensions contain the particles of (a) Fe_3O_4, (b) nickel and (c) barium titanate with different solid concentrations (10, 20 and 30 g/l). All of the suspensions show shear-thinning flow behaviour over the whole examined shear rate range.

The viscosity of Fe_3O_4 nanofluids increases with increasing particle concentration, as shown in Fig. 8.1a. The rheological behaviour of the suspension containing nanoparticles is thought to depend mainly on the interaction of nanoparticles. When two colloidal particles approach each other, the double layer on each particle overlaps and thus they generate a repulsive force on each other. This repulsive force is partly affected by an attractive force due to the van der Waals interaction between the approaching particles and exhibits a power-law distance dependence whose strength depends on the dielectric properties of the interacting colloidal particles and intervening medium [Barnes, H.A. et al. 1993, Khastgir, D. et al. 2000].

The rheological behaviour of suspensions with different relative contents of nickel (Fig. 8.1b) is affected both by the volume fraction of solids and by agglomeration of nickel nanoparticles. The nickel nanoparticles are more or less spherical in shape and

tend to form agglomerates that in principle can induce local changes in the viscosity of the suspension.

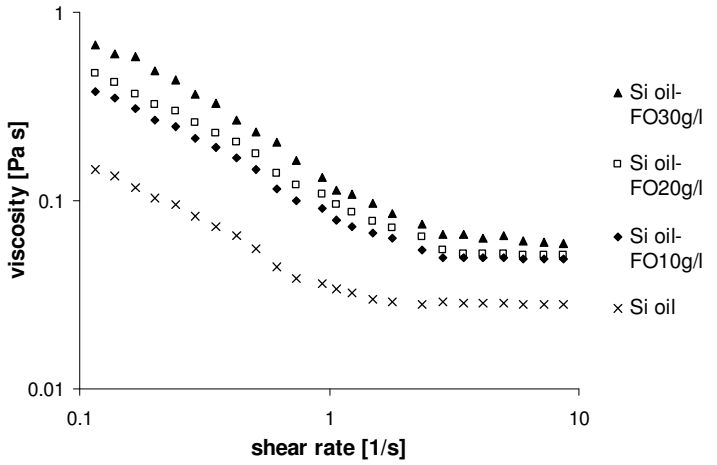

a;

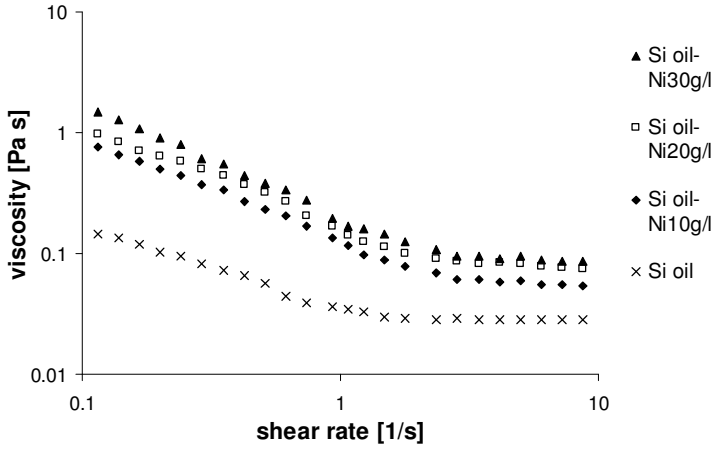

b;

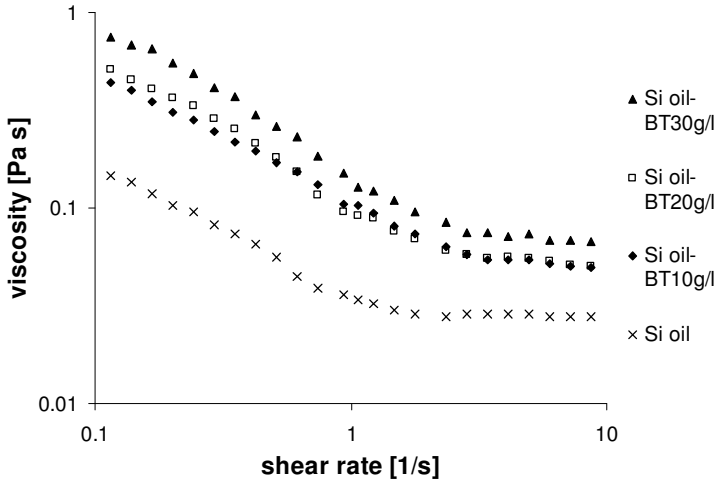

c;

Figure 8.1 a-c Iron oxide-silicone oil suspensions (a), nickel-silicone oil (b) and $BaTiO_3$ -silicone oil (c) suspensions viscosity vs. shear rate relationships

Figure 8.1b shows the highest increase of viscosity of base fluid amongst all of the tested fluids, is observed in the nickel nanoparticle suspensions in silicone oil. This is particularly interesting as it ties in with the findings of the later measurements on electrical conductivity described in Chapter 9.

Suspensions of $BaTiO_3$ in silicone oil (Fig. 8.1c) exhibit non-linear viscoelastic behaviour of shear thinning. This is agreement with the observations made by Khastgir et al. (2000), who attributed the viscoelastic behaviour to the shear rate dependence of the size and structure of aggregates of $BaTiO_3$ particles. If the system contained more than 10 vol% of solids, it shows signs of plasticity which was explained as the formation of networks of particles.

When the size of the particles decreases ($BaTiO_3$ 100-120 nm, Ni 90-100 nm and Fe_3O_4 10-15 nm), the specific surface area of the particles increases and there are larger numbers of nanoparticles in the suspension for a given weight loading. This clearly does have an influence on the macroscopic fluid properties.

The two fluid media used in this investigation have different chemical make-up, different viscosity and different density. Hence the inter-particle interaction in these media is expected to be different. Fig. 8.2 shows the change of viscosity of suspensions containing nanoparticles in FC70 against shear rate in the range of 0.10-10 s^{-1}: (a) Fe_3O_4, (b) Ni and (c) $BaTiO_3$. All of the suspensions show shear-thinning flow behaviour at the whole examined shear rate range. As before, the viscosity increases with the solid concentration of Fe_3O_4, Ni and $BaTiO_3$ indicating that the inter-particle interaction has an influence on the rheological behaviour of the suspensions.

Fig. 8.2a indicates that the rheological behaviour of the suspensions containing the particles of Fe_3O_4 depends mainly on the strength of nanoparticles interaction. The nickel-FC70 suspension (Fig. 8.2b) shows the greatest increase of viscosity with the increase of particle concentration. All the nickel suspensions show viscoelastic behaviour within the examined shear rate range. The $BaTiO_3$ -FC70 (Fig. 8.2c) suspensions with different solid additions are all viscoelastic in the 0.1-10 s^{-1} shear rate range.

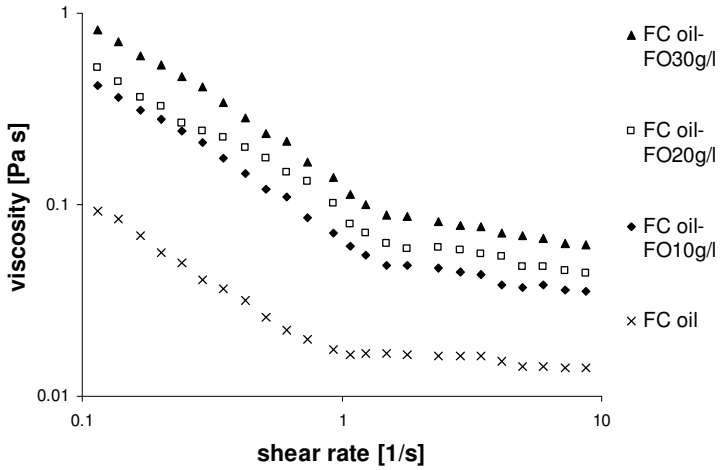

a;

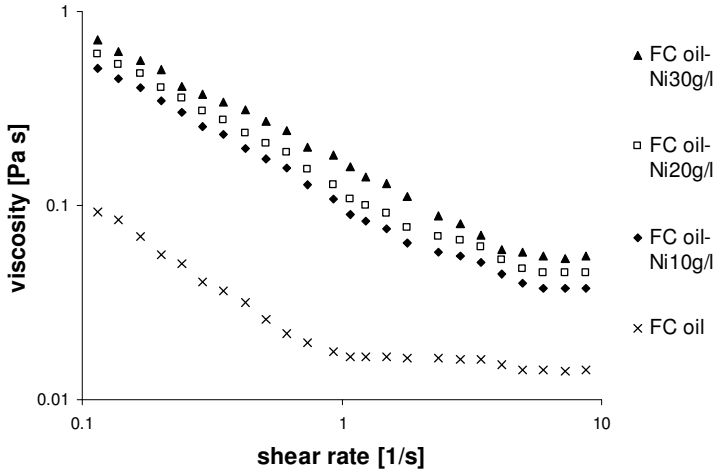

b;

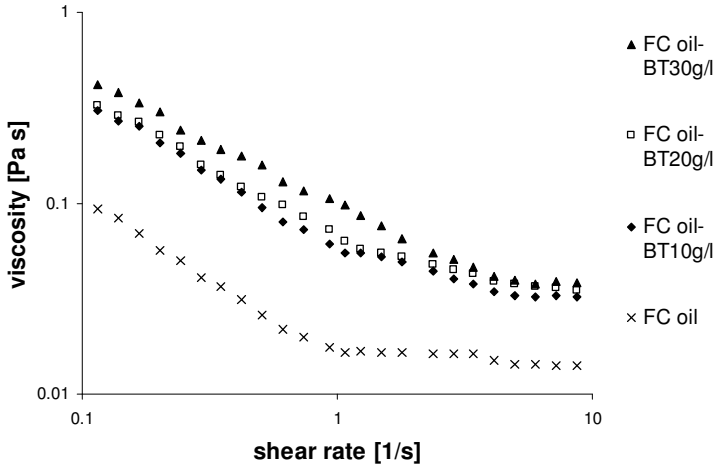

c;

Figure 8.2 Iron oxide-FC70 fluid suspensions (a) nickel-FC70 fluid (b) and $BaTiO_3$-FC70 fluid (c) suspensions viscosity vs. shear rate relationships

8.2.2 Effect of particle size on viscosity

In general, reducing the average size of the solid-phase while keeping the same solid-concentration brings particles much closer together. In this study the interparticle spacing varies typically within a notional, 3-10 particle diameters, given a uniform suspension. Fig. 8.3 shows the viscosity of suspensions against shear rate in the range of 0.10-10 s^{-1} for (a) silicone oil and for (b) FC70 fluid suspension with 20 g/l of solid concentrations of barium titanate particles (size 120 nm, 200 nm and 500 nm). The synthesis and characterization of different sizes of BT has been discussed in Section 7.3. All of the suspensions show shear-thinning flow character at the whole range of shear rate.

The viscosity both in silicone oil- and in FC70-based nanoparticles suspensions increases with decreasing size of the barium titanate particles. Fig. 8.3 shows that the size of the particles plays an important role in the silicone oil and in the FC70 fluid-based nanoparticles suspensions. The smaller particles (120 nm and 200 nm) cause bigger increase in the viscosity, which is in agreement with some previous studies [Yan, Y. et al. 1991, Chen, S. et al. 2005, Nguyen, C.T. et al. 2007]. The flow curves (Fig. 8.3) showed increasing shear thinning behaviour with decreasing particles size.

Overall it can be assumed that the rheological properties of nano-suspensions are influenced by many factors, such as the particle concentration, size and the interaction between the particles and the medium.

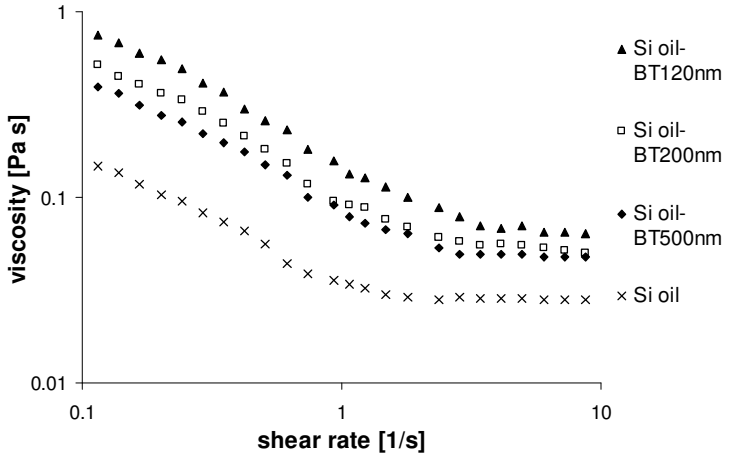

a;

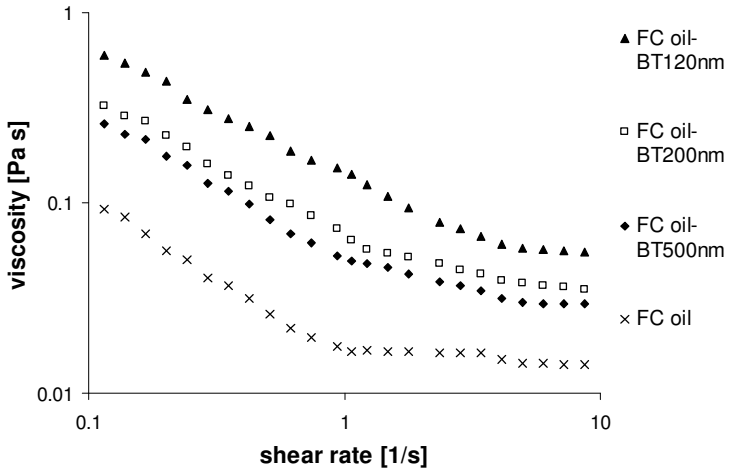

b;

Figure 8.3 The suspension viscosity-shear rate dependence of the $BaTiO_3$-silicone oil (a) and the $BaTiO_3$-FC70 fluid (b) suspension of different size of $BaTiO_3$ nanoparticles at 20 g/l concentration

One of the latest reviews [Murshed, S.M.S. et al. 2008a] shows a similar observation to those shown here, namely the viscosity increases with the volume fraction of nanoparticles and with the size reduction.

8.2.3 Effect of mixed dispersion of nanoparticles on the viscosity

Fig. 8.4 shows the viscosity of mixed-particle suspensions against shear rate in the range 0.10-10 s^{-1} for (a) silicone and (b) FC70 oils with 10 and 20 g/l.

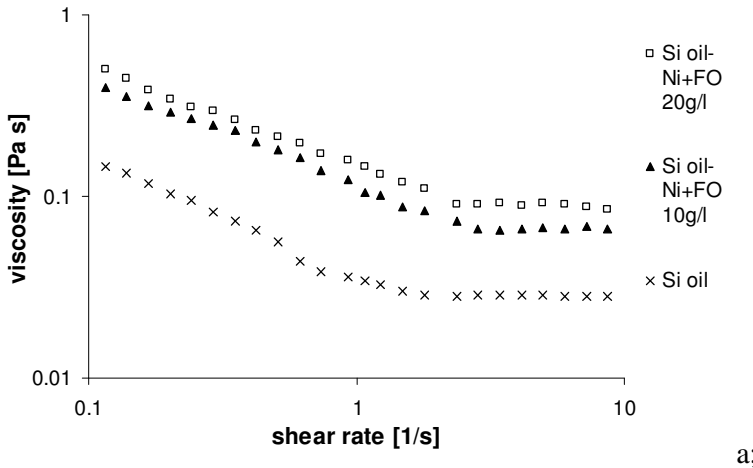

a;

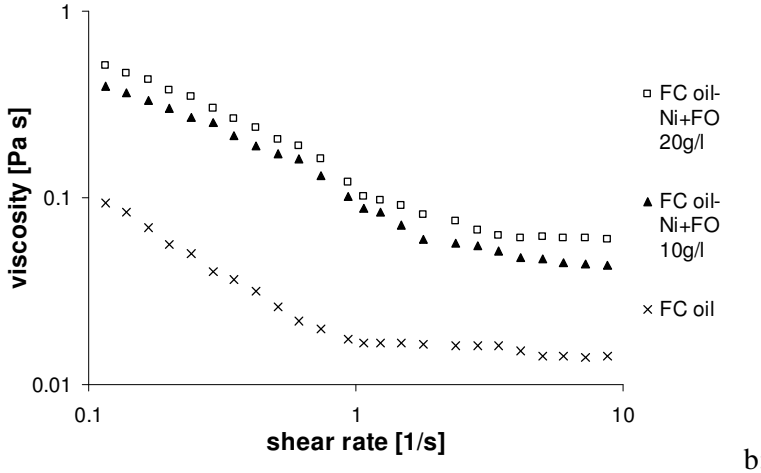

b;

Figure 8.4 The viscosity-shear rate dependence of the suspension containing both nickel and iron oxide in silicone oil (a) and nickel and iron oxide nanoparticles suspended in FC70 fluid (b) at 10 and 20 g/l concentration

The mixtures chosen were of nickel and iron oxide nanoparticles. The silicone oil-nickel suspension has shown the largest increase of viscosity in the all the examined monodispersed nanoparticles suspensions and the iron oxide particles were used to provide a bimodal size range. This leads to slightly reduced viscosity, when compared against the expected value at the same solid concentrations (Fig. 8.4).

Even through the models have been seen (Section 3.3), there is normally still inconsistency between the experimentally measured data and the prediction. The classical models which were used to predicting the viscosity of suspensions and nanofluids such as Einstein's (Eq. 3.8) and Krieger and Dougherty's (Eq. 3.9) could not be used to fully explain our observations. The classical models are not applicable for some of the nano-suspensions and this is a gap in current data. The existing models often under- or overestimate the viscosity of nanofluids.

8.3 Surface tension of nanofluids

The surface and interface tension play an important role in any droplet creation technique including micro-fluidic and dielectrophoretic systems. In droplet-based technologies the size of the droplet is related to the viscosity and the surface- and interface-tension of the fluid. This one of the reasons why the surface tension has been measured and the interface tension was estimated by models.

The following section addresses the surface- and interface tension of nanofluids. The surface tension has been measured by several different methods. The first part of this chapter (8.3.1) is explaining the sessile drop method, the next section (8.3.2) shows the result and discussion of the surface tension measured by Wilhelmy method, the 8.3.3 section shows the result of the pendant drop test and section 8.3.4 shows the interface tension calculation with different models.

8.3.1 Surface tension measured by sessile drop method

Scientists have been interested for a long time in the phenomena behind the droplet shape and the droplet contact angle with surfaces. One of the methods to measure the contact angle/surface tension of fluid on a surface is the sessile drop method. Many parameters affecting the surface tension measurements generally include drop size, temperature, time and contamination. The sessile drop method is affected by the roughness and non-homogeneity of surface as well. In the case of sessile drop method a drop of the fluid placed on a surface and the contact angle measured.

In the sessile drop measurement the type of the surface used to place the fluid droplet is special in the meaning of material, roughness and cleanliness. The water has special, very high surface tension 72 mN/m at 25 ºC. Figure 8.5 shows images of water drops on PZT (a), water-based iron oxide nanofluid on PZT (b), water on PTFE (c), and water-based iron oxide nanofluid on PTFE (d). The shapes of the drops are ideal for contact angle measurement by sessile drop method.

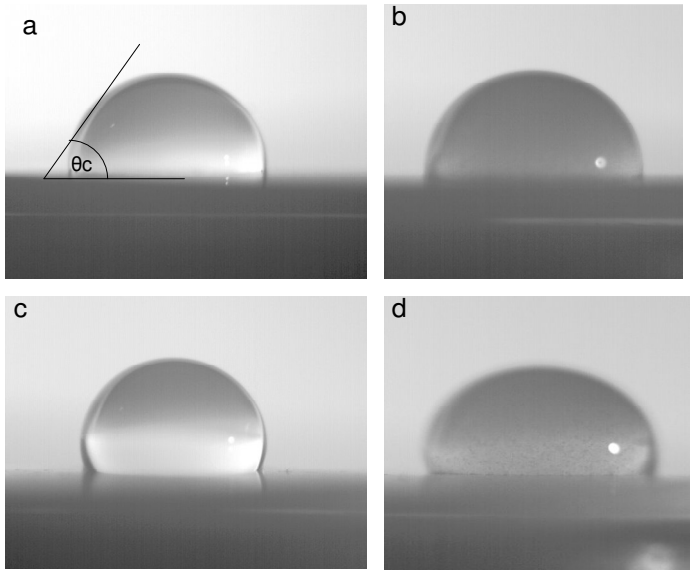

Figure 8.5 Ideal images of water on PZT (a), water-based iron oxide nanofluid on PZT (b), water on PTFE (c) and water-based iron oxide nanofluid on PTFE (d), θc means contact angle

Silicone oil and FC70 fluid have very low surface tensions 20.8 and 18 mN/m at 25 ºC respectively. Hence the surfaces used for the contact angle measurement for oil drops should be highly hydrophilic (or even super-hydrophilic) to be able to measure the contact angle. Otherwise the oil droplet will spread over the surface. Figure 8.6 shows images of FC70 oil on PZT (a), FC70-based BT nanofluid on PZT (b), silicone oil on gold coated glass (c), and silicone oil-based BT nanofluid on gold coated glass (d).

Unfortunately the contact angle of these oils could not been measured on common hydrophilic surfaces because the angle was too small. For this reason further experiments were carried out to produce a super-hydrophilic coating on a glass slide. Theoretically clean glass should be suitable for the oils contact angle measurement. For this reason different methods were used to deep clean the glass slide from chromo-sulphuric acid bath, acetone-isopropanol ultrasonic bath, and high temperature (150 ºC) heat treatment. Unfortunately none of the treatments produced a surface suitable for sessile drop measurements of these oils. Due to the very low surface tension, a super-hydrophilic surface would be necessary for use with the sessile drop method.

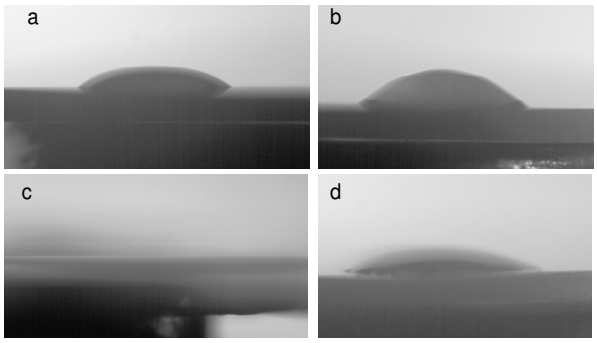

Figure 8.6 Images of FC70 oil on PZT (a), FC70-based BT nanofluid on PZT (b), silicone oil on gold coated glass (c), and silicone oil-based BT nanofluid on gold coated glass (d)

In the next step different sub-micro/nano coatings were produced on the glass surface to make it super-hydrophilic, by spin-coating, dip-coating or the nano-layer growth on the surface. In the literature [Greene, L.E. et al. 2005, Hosono, E. et al. 2007] TiO_2 and ZnO nano- and submicron-particles are used to create super-hydrophilic surfaces. The preferred surface should have nano-roughness which helps to keep the drop on the surface without spreading.

The original idea of the use of nano-scale roughness is from Nature. Lotus and some other plant leaves have a special water repellence due to nano-scale features on the leaves. This has inspired nano-scientists to create lab-made materials with nano-scale bumps on the surfaces that will be water and oil repellent.

Figure 8.7 shows SEM images of titanium dioxide plates (a) produced by hydrothermal method [Hosono, E. et al. 2007], ZnO nano-rods (b) produced by growing process on glass slide from solution [Greene, L.E. et al. 2005], TiO_2 nano-sheet (c) and ZnO nano-rods on glass (d) surface for super-hydrophilic surface. Unfortunately none of these surfaces was suitable for the contact angle measurement by sessile drop method of silicone and FC70 oils.

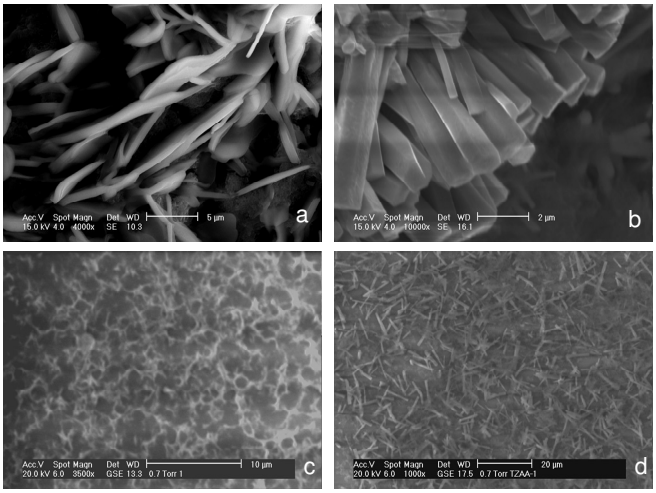

Figure 8.7 SEM images of titanium dioxide plates (a) and ZnO nano-rods (b), TiO_2 nano-sheet (c) and ZnO nano-rods on glass (d)

8.3.2 Surface tension measured by Wilhelmy plate method

The Wilhelmy plate method has been explained in Section 6.2. This method was used to measure the surface tension of silicone oil, FC70 oil and silicone oil-based and FC70 oil-based nanofluids. The result shows that added nanoparticles reduced the surface tension of base fluids (Fig. 8.8).

Figure 8.8a shows the surface tension of silicone oil-based iron oxide, BT and Ni nanofluids with nanoparticles concentration from 1 to 7.5 g/l. All sample behaved similarly which means that beyond a certain concentration (3 g/l) even added extra nanoparticles did not produce any further reduction on the surface tension. In the silicone oil based nanofluids the highest reduction occurred in the nickel nanofluid.

Figure 8.8b shows the surface tension of FC70 oil-based iron oxide, BT and Ni nanofluids with nanoparticles concentration from 1 to 7.5 g/l. The iron oxide nanofluid had the highest reduction in FC70 oil-based nanofluids.

The added nanoparticles reduced the surface tension of the base fluid even at very low concentrations.

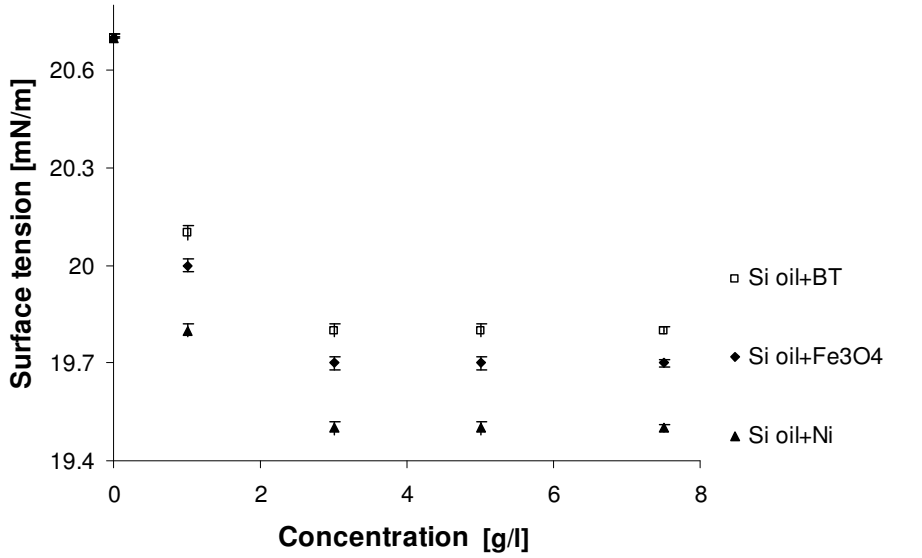

a

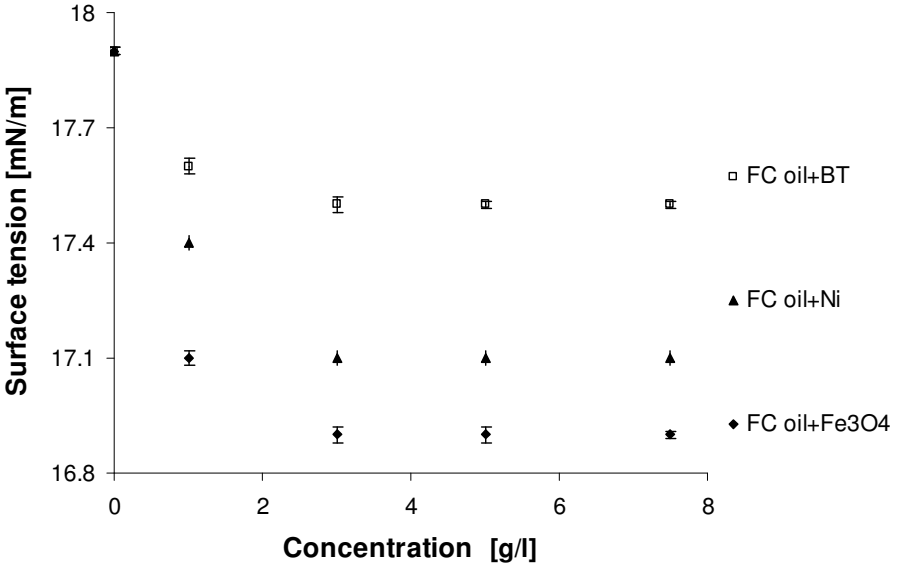

b

Figure 8.8 Surface tension of silicone oil-based (a) and FC70-based (b) iron oxide, BT and Ni nanofluids with various nanoparticle concentrations

8.3.3 Surface tension measured by the pendant drop method

The pendant drop method has been explained in Section 6.3. In this project it was used for surface tension measurements of silicone oil and silicone oil base SiO_2 nanofluid.

The first set of measurements was the check and calibration of our pendant drop system. The result of these tests showed in Table 8.2. The table shows the three tests on water, silicone and FC70 oils. The last line in the table shows the surface tension values from the literature. For each test ten consecutive frames near the dropping point were analysed.

Table 8.2 Pendant drop calibration tests result for water, silicone oil and FC70

Water [mN/m]	Silicone oil [mN/m]	FC70 [mN/m]
70.2	20.5	18.6
71.8	20.8	17.9
70.4	20.2	18.4
average:70.8±0.7	average:20.6±0.3	average:18.3±0.3
value in literature	value in literature	value in literature
72	20.8	18

The measured values indicate that our pendant drop set-up and calculation is quite correct and precise because the measured surface tension values were close enough to the literature values and the standard deviation is low. Tests on silicone oil based nanofluid were performed with different sizes of (20, 40 and 300 nm) SiO_2 nanoparticles, Table 8.3 shows the results. The presence of nanoparticles in the silicone oil gives a slightly higher density and this was compensated for in the code. The results indicate that the added nanoparticles slightly changed the surface tension of the silicone oil.

Table 8.3 Surface tension of SiO_2-silicone oil nanofluid by pendant drop test

SiO_2 nanoparticles [nm]	Concentration [g/l]	Surface tension [mN/m]
20	10	20.7±0.2
40	9.6	20.7±0.3
40	20	20.5±0.3
300	10.8	20.4±0.5

The influence of the hydrophobicity/lipophilicity of the particle has an affect on the surface tension of the fluid in that it is suspended. Generally, a moderate hydrophobicity is required to give particles sufficient interfacial detachment energy to remain at interfaces. Hydrophilic nanoparticles are more difficult to assemble into ordered film than hydrophobic nanoparticles.

Our result of surface tension reduction by silica nanoparticles is in good agreement with Ravera's et al. (2006) who used silica (15 nm) in water and reported reduced surface tension.

8.3.4 Interface tension calculation of nanofluids by different methods

Liquid-liquid interface tension is an important property and its estimated value is required for many fields such as colloid and environmental science. The estimation and calculation of interface tension has a long history which started in the late 19th century by Berthelot's rules Eq. (8.2) and Antonow's rule Eq. (8.3) [Tavana, H. et al. 2007]. The interface tension occurs from an imbalance of forces acting on molecules at the interface. The magnitude of the interface tension is depending on the difference between the intermolecular forces within the fluid and the intermolecular forces between the fluids [Tavana, H. et al. 2007]. When the interface tension is low the two fluids have comparable intra-phase molecular interactions and when it is high they have very different interactions.

Berthelot's: $$\gamma_{ab} = \gamma_a + \gamma_b - 2(\gamma_a + \gamma_b)^{1/2} \quad (8.2)$$

Antonow's: $$\gamma_{ab} = \gamma_a - \gamma_b \quad (8.3)$$

To modify Berthelot's rules Girifalco and Good (1957) developed a model for estimated the interfacial tension which including a modifying factor (Φ):

$$\gamma_{ab} = \gamma_a + \gamma_b - 2\Phi(\gamma_a \gamma_b)^{1/2} \quad (8.4)$$

where γ_a and γ_b are the surface tension of liquid *a* and *b* respectively and Φ is a constant which is equal to the ration of energies of adhesion and cohesion for two phases [Murshed, S.M.S. et al. 2008b].

The value of Φ varies from 0.31 (water/mercury) through 0.5-0.7 (water/hydrocarbons) to 1.15 (water/isobutyl-alcohol) [Girifalco, L.A. et al. 1957]. The closest system for us is the hydrocarbon/fluorocarbon system with Φ=0.8-0.9 [Girifalco, L.A. et al. 1957] and the value of Φ=0.8 of polymethylsiloxane/

polytetrafluoroethylene system. Figure 8.9 shows the chemical formulae of silicone oil (a), Fluorinert liquid (b) and polytetrafluoroethylene (c). The sequence of fully fluorinated carbons repeated in both Fluorinert and polytetrafluoroethylene.

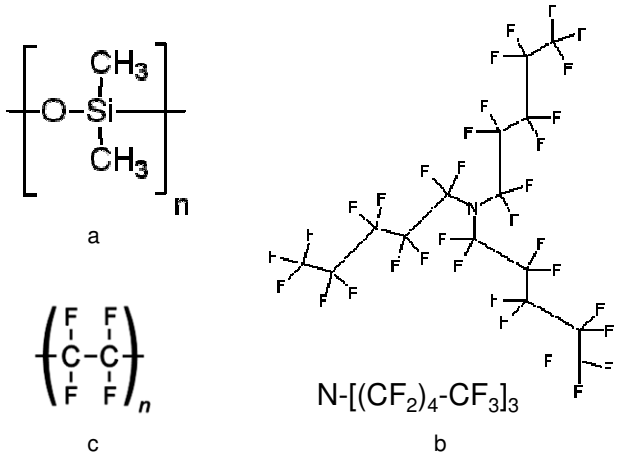

Figure 8.9 Chemical structures of silicone oil (a), Fluorinert (b) and polytetrafluoroethylene (c)

The interface tension data of silicone oil/Fluorinert reported by Someya (2005) and they used image processing with fitting a drop shape method (pendant drop method with they own image processing and calculating method). The calculated value for silicone oil KF96-20St/Fluorinert FC70 is 7.726 mN/m.

Table 8.4 shows the value of interface tension of silicone oil (200/50cS) / Fluorinert FC70 fluid calculated by different models. The first model used to calculate interface tension is by Berthelot's model (Eq. 8.2) the second one is the Antonow's model (Eq. 8.3) and the last is Girifalco and Good model (Eq. 8.4). The result compared to the published value of silicone oil/Fluorinert system and the calculated value clearly shows that the Berthelot's model overestimates, the Antonow's model underestimates and the Girifalco model has quite good agreement with the published value. In the further calculation of interface tension the Girifalco model (Φ=0.8) was used.

Table 8.4 Values of interface tension calculated by different models

Interface tension by Berthelot's model	26.3 mN/m
Interface tension Antonow's model	2.8 mN/m
Interface tension Girifalco's model*	7.8 mN/m

Table 8.5 shows the measured value of surface tensions by different methods and the calculated value of interface tension by Girifalco model. The first column of Table 8.5 shows the calculated value of the literature value of surface tension of fluids, the second column shows the surface tension of fluids measured by Wilhelmy plate method, the third column shows the surface tension of fluids measured by the pendant drop method and the last line shows the interface tension of silicone oil/ FC70. Our results both the Wilhelmy and the pendant drop as well show good agreement with published data (silicone oil KF96-20St/ FC70 is 7.726 mN/m) [Someya, S. et al. 2005].

Table 8.5 Calculated interface tension of by Girifalco model

	Value in literature	Wilhelmy method	Pendant drop method
Surface tension of silicone oil	20.8 mN/m	20.7 mN/m	20.6 mN/m
Surface tension of Fluorinert FC70	18.0 mN/m	17.9 mN/m	18.3 mN/m
Interface tension* Φ=0.8	7.8 mN/m	7.8 mN/m	7.9 mN/m

Literature on the interface tension calculation of nanofluids has a limited number of publications. In all of them Φ has increased by 4.2-19.4% [Murshed, S.M.S. et al. 2008b] and it depends on the type and concentration of nanoparticles and the base fluid. None of the published papers used the same system as ours (SiO_2, Ni, BT and Fe_3O_4 nanoparticulate suspension in silicone oil 200/50 / FC70 fluid) and the increase of Φ is generally calculated from literature and this means about 10% increase compared to the base fluid due to the change in the inter- and intra- molecular structure and forces. Table 8.6 shows the result of interface tension of nanofluids calculated by Girifalco model (Φ=0.88).

Table 8.6 Calculated interface tension of silicone oil based nanofluid/FC70

	Concentration [g/l]	Surface tension [mN/m]	Interface tension of silicone oil nanofluid / FC70 [mN/m]
Silicone oil + Fe_3O_4	1	20	4.6
	3	19.7	4.5
	5	19.7	4.5
	7.5	19.7	4.5
Silicone oil + BT	1	20.1	4.6
	3	19.8	4.6
	5	19.8	4.6
	7.5	19.8	4.6
Silicone oil + Ni	1	19.8	4.6
	3	19.5	4.5
	5	19.5	4.5
	7.5	19.5	4.5
Silicone oil + SiO_2			
20 nm	10	20.7	4.7
40 nm	9.6	20.7	4.7
40 nm	20	20.5	4.7
300 nm	10.8	20.4	4.7

Chapter 9 Results and discussion of nanofluids electrical characterization

This chapter will present the results and the discussion of the experimental investigation on the electrical characterization of non-polar fluid based nanofluids such as dc electrical conductivity and dielectric permittivity.

Relatively stable suspensions of nanoparticles are important for their electrical characterization. This chapter will show how the electrical properties of nanofluids depend on the properties of the base fluid and the dispersed particles properties such as concentration and size.

9.1 Electrical conductivity of nanofluids

Figure 9.1 shows DC conductivities for the six different nanofluids measured at different particle concentrations under moderate electric field conditions. The dc electrical conductivity of two base fluids and the prepared six nanofluids were measured as explained for the set-up and the nanofluid preparation in Section 6.4. The physical properties of the base fluids and the nanoparticles were shown in Table 6.1. Some interesting relationships could be found between the properties of the two base fluids:

-silicone oil and FC70 fluid have nearly same, very low electrical conductivity,

-the dielectric permittivity of FC70 is slightly lower than the permittivity of silicone oil,

-FC70 has got lower viscosity than the silicone oil,

-the specific gravity of FC70 is double that of the silicone oil.

Physical quantities for the nanoparticles are also shown in Table 6.1. Some interesting relationships could be found between the properties of the nanoparticles:

-the two magnetic nanoparticles the iron oxide and the nickel have different sizes and bulk densities,

-iron oxide nanoparticles have a similar bulk density as barium titanate nanoparticles, but the size of barium titanate nanoparticles is more than ten times bigger than the size of the iron oxide nanoparticles

-nickel nanoparticles and barium titanate nanoparticles have similar masses due to the large size of barium titanate nanoparticles and the high density of nickel

-for all nanoparticles used in these measurements it could be said that their effective electrical conductivities at the nano-scale are uncertain.

Figure 9.1 shows the conductivity of the 10 nm diameter iron oxide nanoparticles (FO) (row A); the 130 nm diameter barium titanate nanoparticles (BT) (row B) and the 90 nm diameter nickel nanoparticles (Ni) (row C) suspended in silicone oil (left side) and in FC70 fluid (right side).

The figure shows that the silicone oil based nanofluid has some field-dependent character over the examined range, shown as an increase in measured conductivity as the applied voltage is increased; but this is not the only effect observed. The base fluids conductivity hugely increased with the added nanoparticles especially in Ni-silicone oil suspension.

The conductivity of iron oxide-FC70 nanofluid is higher than it is in the silicone oil based nanofluid. In the silicone oil based nanofluid the field-induced conductivity enhancements were observable in all samples especially when the concentration of nanoparticles >10 g/l.

In the silicone oil based barium titanate nanofluids the observed DC conductivities were higher than in the FC70 based nanofluids. This tendency is opposite in comparison to the iron oxide nanofluids. The DC conductivities of FC70 based nickel and barium titanate nanofluids show small increases. Note that the 20 g/l BT and 30 g/l Ni have similar volume fractions of particles.

The DC conductivity of the silicone oil based nickel nanofluid shows an especially high increase even at very low concentration (4 g/l). In the higher concentration of nickel (30 g/l) the value of the dc conductivity result is 1E-1 S/m which is a huge increase of the conductivity of the silicone oil.

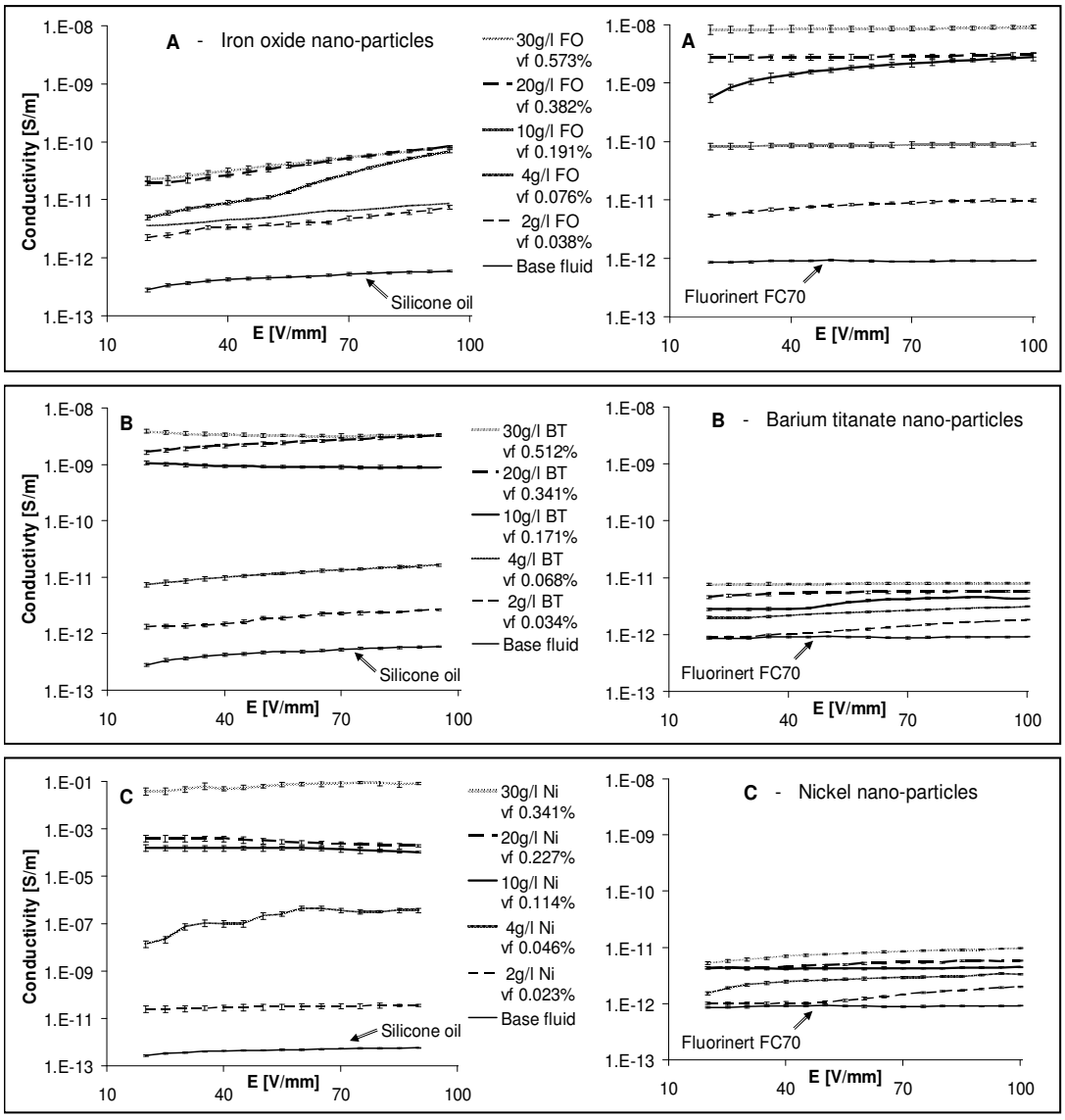

Figure 9.1 DC conductivities of three types of nanoparticles in two different dielectric fluids: silicone oil (left side) and FC70 (right side)

The increases of conductivity by nanoparticles in our measurements follow a relationship: $\ln J \propto \sqrt{E}$ (where J is the current density, E the applied electric field and the current density = electrical conductivity × electric field strength). This indicates an energy-activated Poole-Frenkel behaviour [Zielinski, M. et al. 1977, Ongaro, R. et al. 1991]. For example, Fig. 9.2 shows the relationship between $\ln J$ and $\sqrt{E}$ in the silicone oil based iron oxide nanofluids.

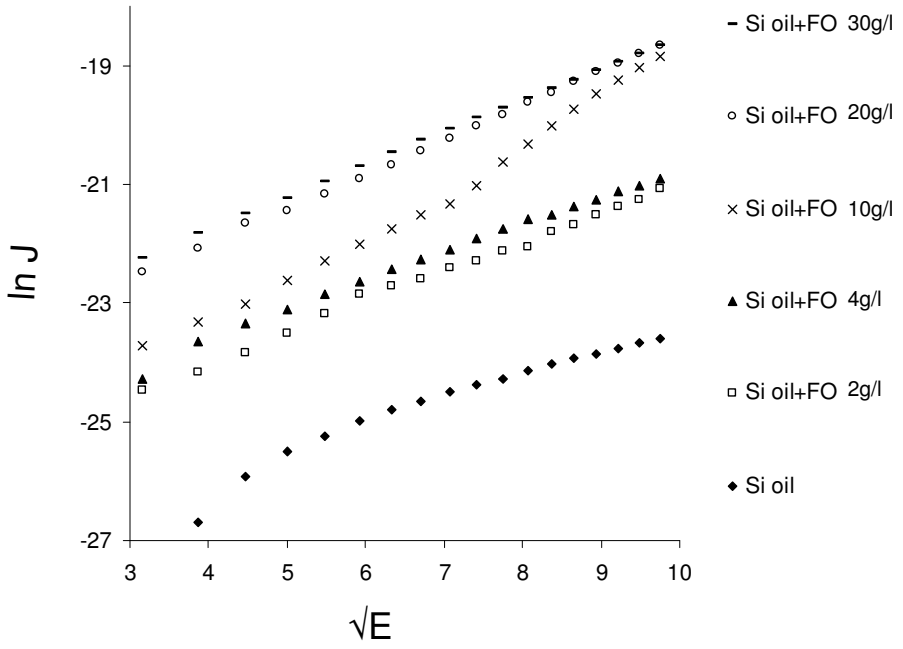

Figure 9.2 The ln *J* vs. $\sqrt{E}$ graphs of silicone oil-iron oxide nanofluids

In Figure 9.3 the DC conductivities of mixed nickel and iron oxide nanoparticles in the nanofluids are shown in different volume fractions. The particle combinations are nickel:iron oxide - top row in the ratio 1:1 by weight, middle row 3:1 by weight, bottom row 9:1 by weight.

The result shows that in silicone oil based nanofluids the nickel particles plays a dominant role which have a good agreement with the result obtained from the single particles type measurements. In FC70 oil based nanofluids the measured conductivities hardly varied at all with the different volume fraction of mixed nanoparticles (Fig. 9.3). The presence of nickel and iron oxide nanoparticles together enhance the electrical conductivity of the base fluid more than iron oxide nanoparticles on their own. There could be synergistic effects between the different types of particles as well as between the fluid-particles.

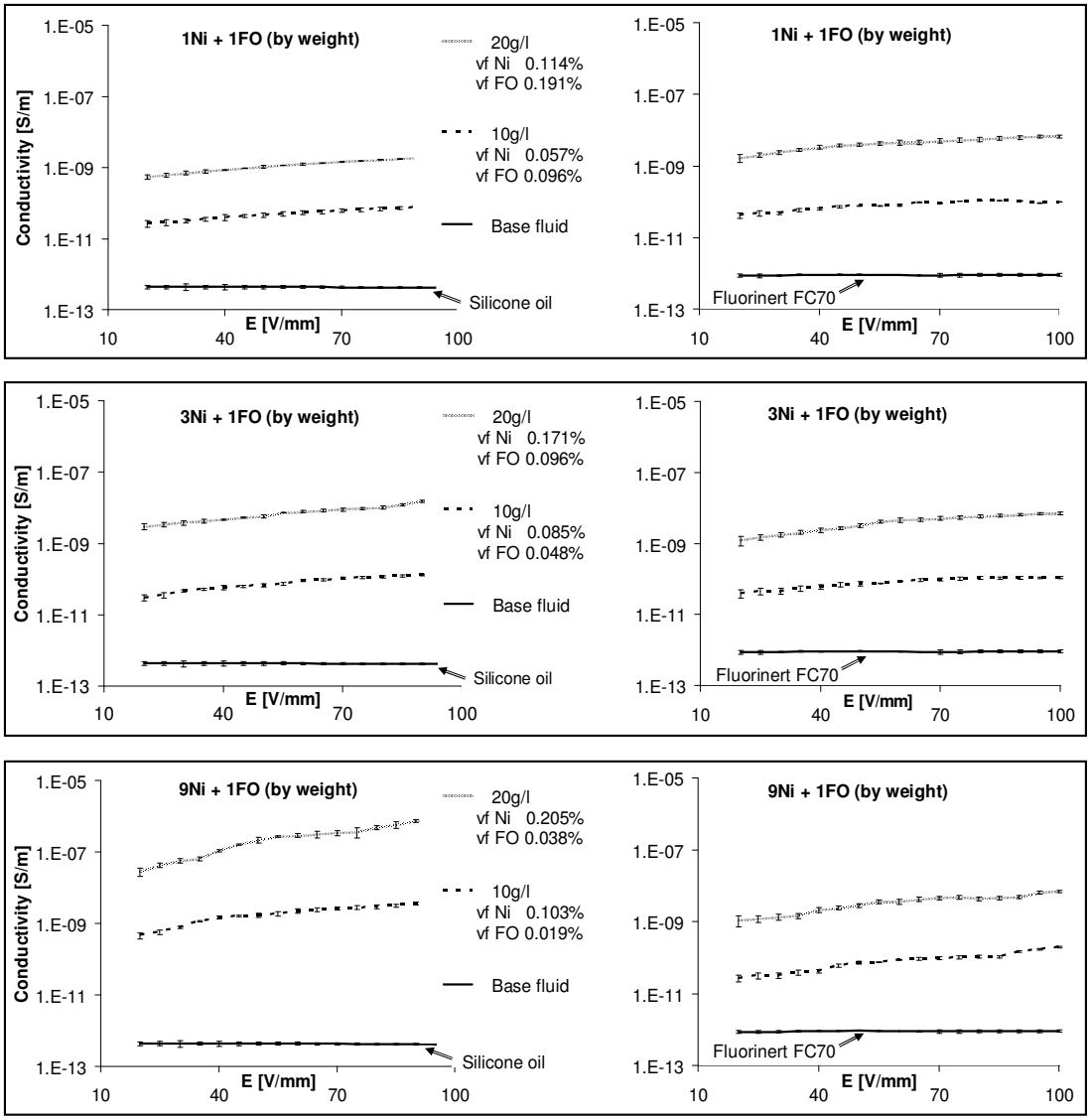

Figure 9.3 DC conductivities of nanofluids containing both nickel and iron oxide nanoparticles - silicone oil (left side) and FC70 (right side)

9.2 Dielectric permittivity of nanofluids

The dielectric permittivity of low volume-fraction (< 0.6 vol %) nanofluids in silicone and FC70 oils was studied experimentally at moderately high frequencies (100 Hz to 1 MHz). The dielectric permittivity of six different nanofluid systems, (representing combinations of three different nanoparticle types – Ni, Fe_3O_4, BT - and two base fluids – silicone and FC70 oils), was measured as explained the set-up and the nanofluid preparation were carried out in accordance with Chapter 6.4. The two base fluids (silicone oil and FC70) have similar relative permittivities as shown in Table 9.1. The measured permittivity data have a quite good agreement with the manufacturer's data of both oils.

Table 9.1 Permittivity of base fluids

Materials	Relative permittivity [Measured]	Relative permittivity [Manufacturer's Data]
200/50cS silicone oil	2.45	2.60
3M™ Fluorinert FC70	1.85	1.98

The permittivity of silicone oil-based (Fig. 9.4a) and FC70-based nanofluids (Fig. 9.4b) showed little change with variable (10 g/l and 30 g/l) concentration at 100 Hz to 1 MHz frequency range with 5V applied voltage.

Figure 9.4a shows the permittivity of silicone oil-based nanofluids. In all of the examined low concentration (≤ 20 g/l) of silicone oil-based nanofluid in this moderately low frequency range the permittivity was same value as the base fluid, which means on the graph they overlap each other. At high concentration (≥ 30 g/l) of nanoparticles the permittivity of nanofluid dropped to low value. The highest change obtained in the high concentration (≥ 30 g/l) nickel-silicone oil nanofluid which contains the conductive metal nanoparticles (average size 90 nm). Moderate change has been obtained in the iron oxide- and barium titanate- silicone oil nanofluids in ≥ 30 g/l concentration.

Figure 9.4b shows the permittivity of FC70 oil-based nanofluids. In all of the examined low concentration (≤ 20 g/l) of FC70 oil-based nanofluid in this moderately low frequency range the permittivity was same value as the base fluid, which means on the graph they overlap each other. At high concentration (≥ 30g/l) of nanoparticles

the permittivity of nanofluid has been dropped to low value. The highest change obtained in the high concentration iron oxide-FC70 oil nanofluid which contains the semi-conductive iron oxide nanoparticles (average size 10 nm). Moderate change has been obtained in the nickel- and barium titanate- FC70 oil nanofluids.

The permittivity change with the increase in frequency at room temperature could be explained by the dielectric polarization mechanism. Interfacial and dipolar polarizations are active in the low frequency range.

The type of the nanoparticles in the nanofluid had effect in the value of the measured permittivity. The metal nickel nanoparticles in silicone oil showed the highest change of permittivity.

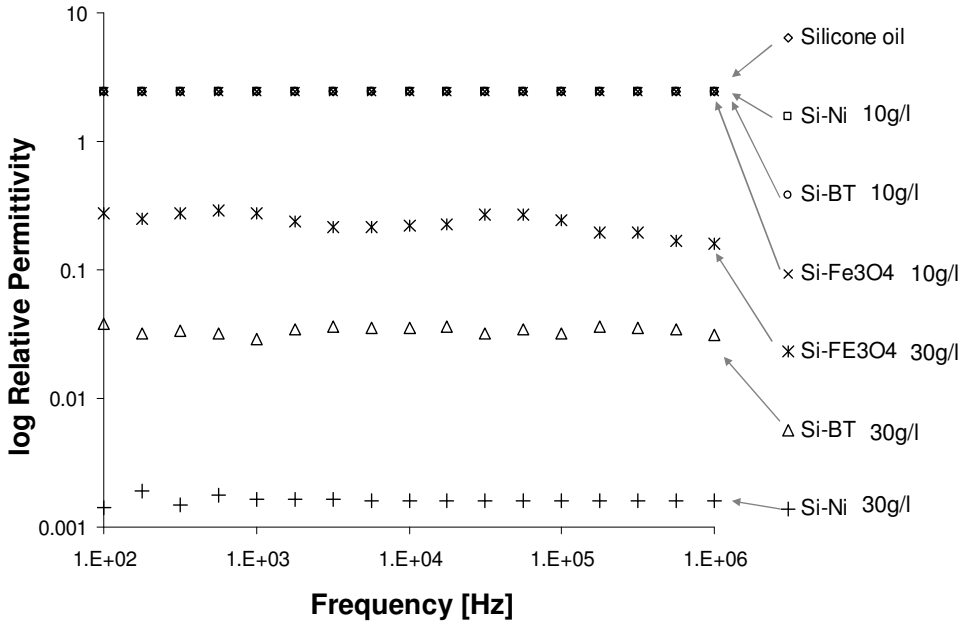

a;

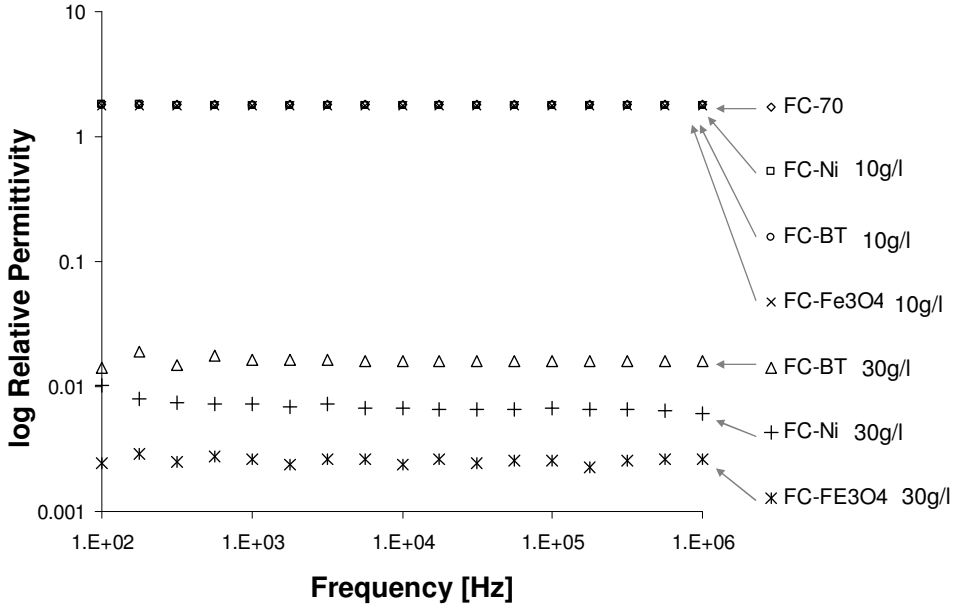

b;

Figure 9.4 Permittivity vs. frequency graphs of silicone oil-based nanofluids (a) and FC70-based nanofluids (b)

Chapter 10 Results and discussion of the dielectrophoretic manipulation technique

This chapter describes a relatively simple electrohydrodynamic technique that can be used for uniformly sized droplet creation and manipulation, oil-in-water emulsion creation and to remove nanoparticles from oils. No moving parts and no small diameter tubes are involved. In simple experiments the power consumption is quite low, typically in the low milliwatt range.

The advantages of using dielectrophoretic forces are to create droplets with uniform droplet size distribution and controllable droplet size. The disadvantage of the dielectrophoretic droplet manipulation technique is that the electrical and rheological properties of the two liquids have to match. The properties of pure oils (silicone and FC70 oils) such as permittivity and viscosity make them suitable for the use in the electrohydrodynamic technique. Whilst the physical (viscosity and surface tension) and electrical properties (conductivity and permittivity) of silicone and FC70 oils based nanoparticles suspensions (nanofluids) has been investigated, and previous chapters (Chapter 8 and 9) explained their properties.

10.1 Dielectrophoretic manipulation of fluids

The experimental system (explained in Section 6.6) used for studying the dielectrophoretic structuring is composed of a transparent dielectric cell (Fig. 10.1), which contains a needle electrode, the two immiscible dielectric fluids, and a plate which forms to earth connected electrode. Droplets of the dielectric fluid 1 (silicone oil) are generated at the tip of a needle electrode in point-plane configuration. Both micron- and nano-litre droplets of silicone oil are achievable using this method and they acquire an electrical charge, due to the injection from the needle tip. This is relatively slow to decay, as they pass through the lower fluid (dielectric fluid 2). FC70 is a very low conductivity, strongly-insulating perfluorinated oil.

Dielectrophoretic droplet generation is achievable using the Fig. 10.1 configuration with no externally applied pressure when three key conditions are in place:

-the upper fluid (silicone oil) must have a higher dielectric permittivity than the lower fluid (FC70 oil);

-the intensity of the electric field adjacent to the needle along its length must have sufficient intensity to generate a dielectrophoretic body force on the fluid;

-charge injection must take place at the needle tip. In practical terms, thinner needles are preferred as they provide the process with more controllability.

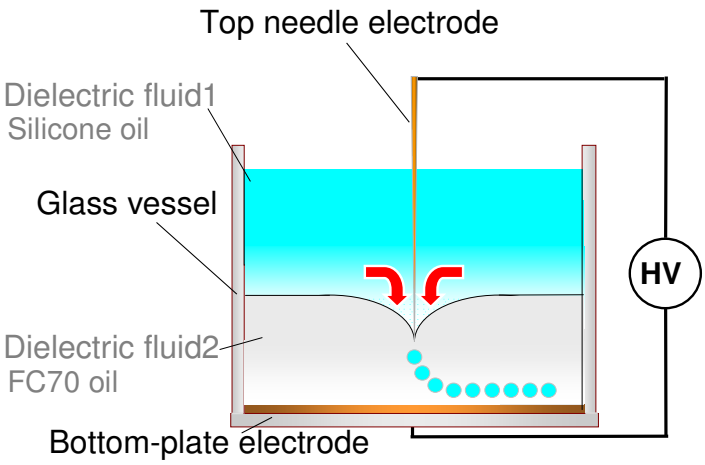

Figure 10.1 Schematic diagram of the dielectrophoretic vessel

Different phenomena were observed in the above explained system. Figure 10.2 shows the steps of the droplet generation by dielectrophoresis. Figure 10.2a shows the silicone oil and FC70 oil system without an applied electric field. Figure 10.2b-d and 10.3 shows images of the silicone oil sheath (cone) around the needle electrode. The field exerts a positive dielectrophoretic force on the fluid and there is a net flow of silicone oil towards the tip of the needle. Figure 10.3 represents a particular case where the electric-field-induced (dielectrophoretic) force is counter-balanced by the restoring (buoyancy) force exerted by FC70 fluid, preventing further fluid flow. Hence there is a detectable electric field threshold for droplet generation to occur. This is relatively insensitive to the sign of applied voltage.

Under electric field the generated charges in the fluid are repelled from the electrode (by Coulomb force) and injected into the bulk fluid. When the applied electric field strength reaches a threshold voltage level in the needle and a plane electrode configuration charge injection occurs through the tip of the needle.

At the threshold voltage, the highest electric field existing at the tip of the needle was capable of forming charged droplets from the silicone oil (Fig. 10.2e-f). When

buoyancy was dominated by the electric forces and the voltage was higher droplet creation was replaced by a continuous jet of silicone oil.

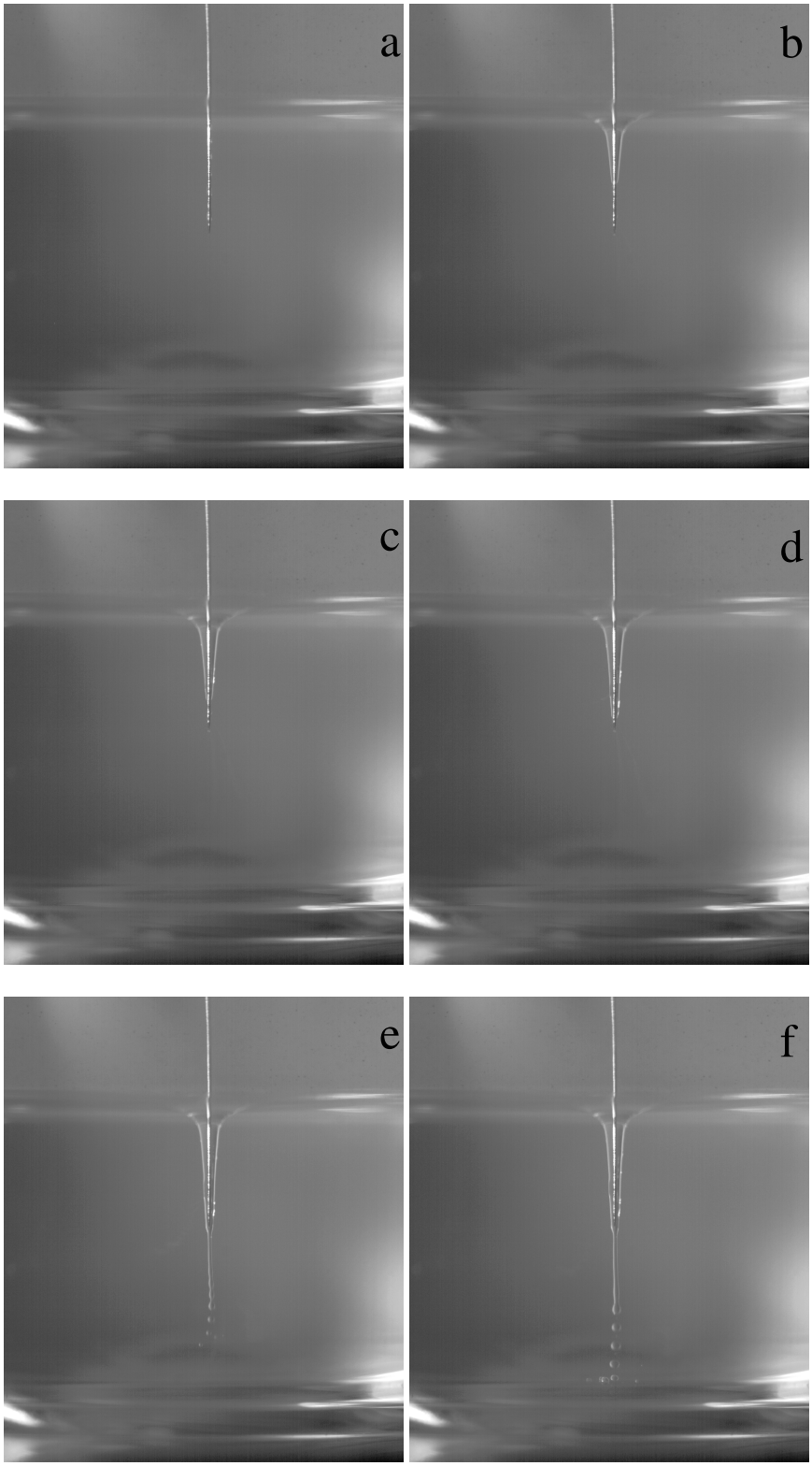

Figure 10.2 Filmstrip of the droplet generation by dielectrophoresis

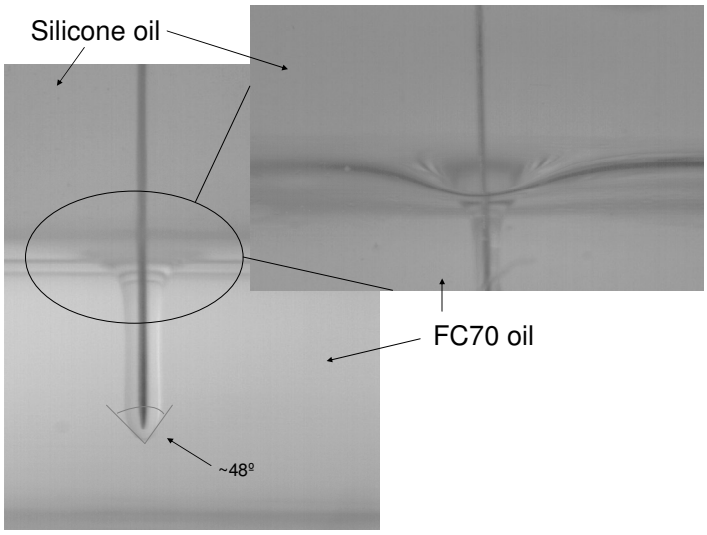

Figure 10.3 Cone generation of silicone oil around the needle into the FC70 oil

Note that the fluid at the tip assumes a conical shape with a swept angle of ~48º. This is very close to the Taylor angle (49.3º), characteristic of electrospray systems [Taylor, G.I. 1964].

In this needle-and-plate electrode configuration of dielectrophoretic system the size of the generated droplet could be controlled by:

-the rheological properties of silicone oil (Fig. 10.4),

-distance between the two electrodes (Fig. 10.5).

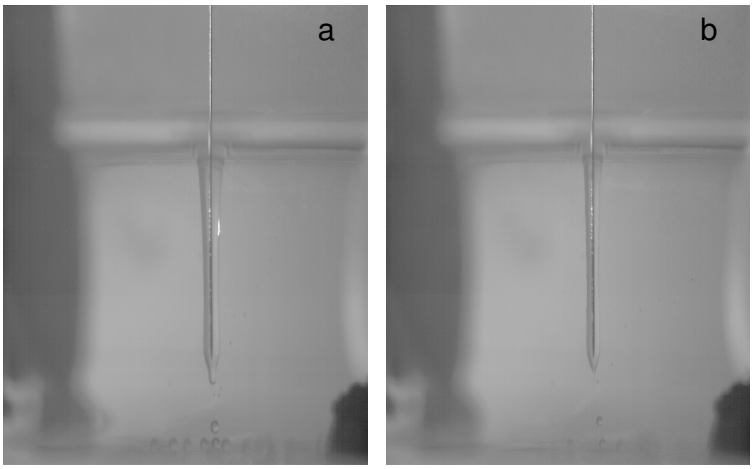

Figure 10.4 Generation of different size of droplets by DEP technique with variable silicone oil viscosity, 100 cSt (a) and 50 cSt (b)

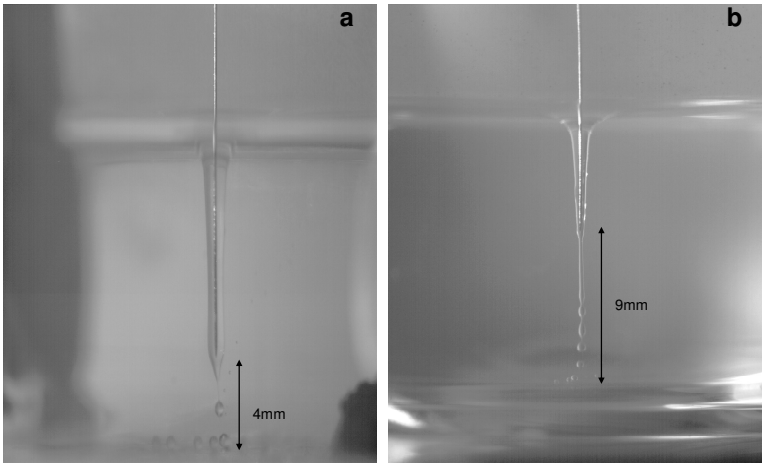

Figure 10.5 Drop size changes with the distance between the two electrodes. The distance between the two electrodes 4 mm (a) and 9 mm (b)

10.2 Dielectrophoretic manipulation of nanofluids

In previous experiments (for pure silicone oil and FC70 fluid) a glass or polycarbonate vessel was equally suitable for the dielectrophoretic droplet manipulation, but when the top fluid was changed from pure silicone oil to silicone oil based nanofluid the nanoparticles started to sediment on the side of the vessel by the interface of the two oils (silicone oil/FC70), due to the surface charge of the polycarbonate vessel. For this reason in any further experiments glass cell was used. The glass cell is filled with two immiscible dielectric liquids. Figure 10.6 shows the schematic graph of DEP vessel with silicone oil based nanofluid. In electric field, the permittivity of dielectric fluid 1 (silicone oil-based nanofluid) is higher than that permittivity of dielectric fluid 2 (FC70 oil).

Three different nanofluids (Ni, Fe_3O_4 and BT nanoparticles in silicone oil) were tested with variable concentration (1 g/l-30 g/l) to discover the effect of the nanoparticles in the dielectrophoretic droplet generation.

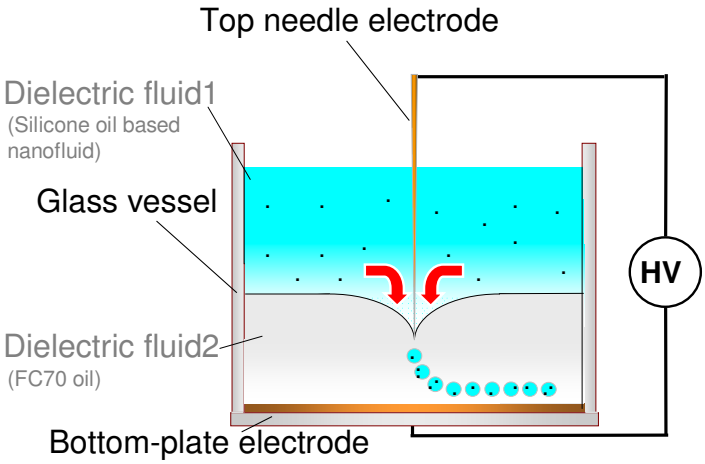

Figure 10.6 Schematic diagram of the dielectrophoretic vessel for nanofluid droplet generation

Figure 10.7, 10.8 and 10.9 shows the effect of the different concentration of nanoparticles on the created droplet size and the size of the cone around the top needle electrode also changed.

Figure 10.7 shows FC70 as lower fluid and silicone oil-based nickel nanofluid as upper fluid with low concentration (< 10 g/l) of nickel (a) and the high concentration (> 20g/l) of nickel (b) nanofluid systems. The size of the cone of the fluid around the needle is reducing when the concentration of nanoparticles is increasing due to the change in the electrical and surface tension properties.

Figure 10.8 shows FC70 as lower fluid and silicone oil-based iron oxide nanofluid as upper fluid, with low concentration < 10 g/l (a) and high concentration > 20g/l (b) of iron oxide nanoparticles respectively. The droplet size and cone size is decrease with the increase of the nanoparticles concentration. It is worth nothing that the iron oxide nanoparticles tend to separate at the interface at high concentration (Fig. 10.8b).

Figure 10.9a, b shows FC70 fluid and low (< 5 g/l) and high (10 g/l) concentration of BT nanofluid as upper fluid, respectively. The droplet size and cone size decrease with the increase of the nanoparticles' concentration till the concentration is <10 g/l. Our results have a good agreement with Tan et al. (2008) who showed that in micro-fluidic flow focusing device the size of the generated droplet is reduced by 20% in diameter when the base fluid changed to nanofluid. The observed difference is due to

the change of the interfacial tension and viscosity of nanofluid compare to the pure base fluid.

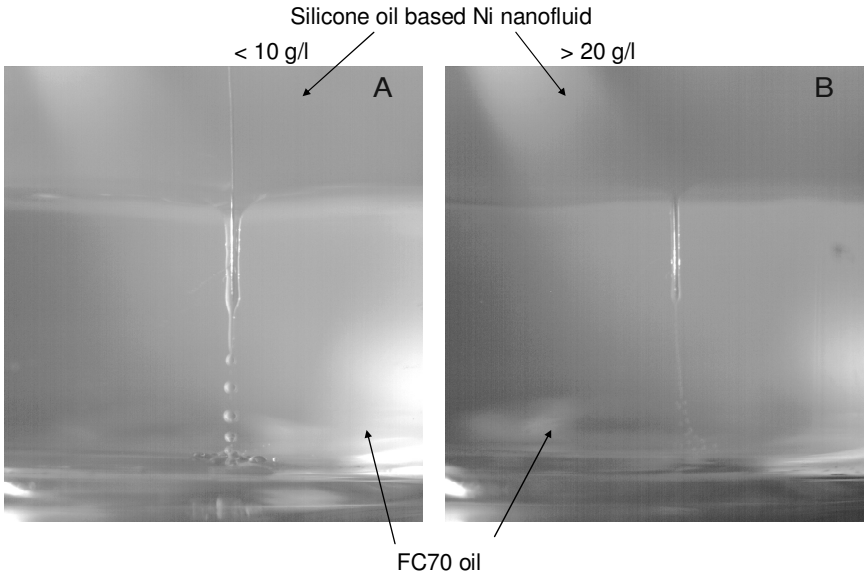

Figure 10.7 FC70 oil and silicone oil-based nickel nanofluid system, change of the droplet and cone size with the nanoparticle concentration

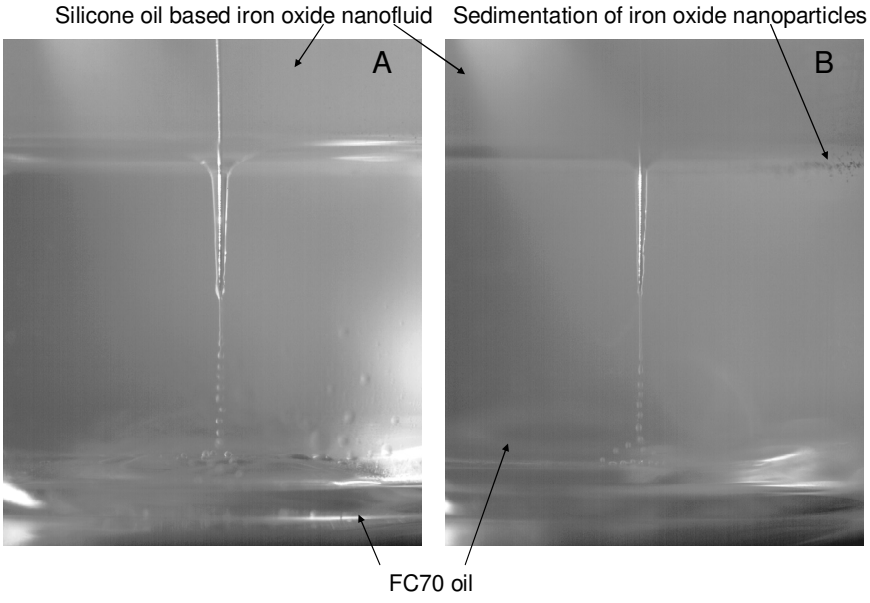

Figure 10.8 FC70 and silicone oil-based iron oxide nanofluid system, change of the droplet and cone size with the nanoparticle concentration

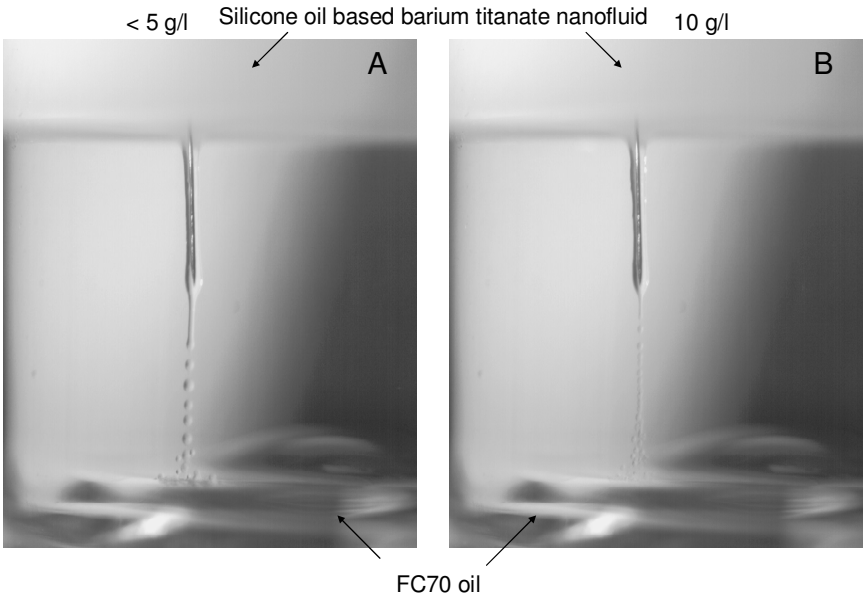

Figure 10.9 FC70 and silicone oil-based barium titanate nanofluid system, change of the droplet and cone size with the nanoparticle concentration

With the droplet and cone size changes the threshold voltages are changed as well. Table 10.1 shows the variable concentration of nanoparticles in the silicone oil-based nanofluid and the required applied voltages to produce droplet from the dielectrophoretic system. The threshold voltages increased with the increase of the nanoparticles concentration in the nanofluid.

Table 10.1 Threshold voltage of nanofluids for droplet generation

	Threshold [kV]		
Concentration[g/l]	Fe_3O_4	Ni	BT
0	2.90	2.90	2.90
1	2.50	2.70	2.82
5	3.10	3.30	3.50
10	4.04	3.50	4.70
20	7.00	4.30	-
30	7.96	4.44	-

The different types of nanoparticles in various concentrations have changed the electrical properties and the viscosity of the base oil (silicone oil) as previously

measured (Chapter 9). The surface and interface tensions of silicone oil also changed with the added nanoparticles. The changes of these properties of the silicone oil have an impact on the dielectrophoretic system as whole, which means had been changes in the threshold voltage and the generated droplet size.

10.3 Sedimentation of nanofluids under electric field

Sedimentation could occur under the influence of external field. Our nanofluids have been made by a two-step method (explained in Section 6) and created a well-mixed and uniformly dispersed nanofluid. Sedimentation of nanoparticles at the oil-oil interface has been evaluated.

Particles with induced dipole-moment could become sediment faster under electric field. The settling rate of suspensions in 1 g/l to 20 g/l concentrations at the oil-oil interface are enhanced by a non-uniform DC electric field and the settling rate increased with higher electric field intensity. Our result has a good agreement with previously published results [Yi, W.D. et al. 1995, Kim, S.S. et al. 2008]. Suspension of magnetic nanoparticles had shown agglomeration and sedimentation under DC electric field, which has good agreement with Peterson et al. (1977).

Due to a formation of aggregates the sedimentation velocity could be increased under the influence of an external field. Figure 10.6 shows a two phase fluid system of silicone oil with iron oxide nanoparticles formed a nanofluid (upper fluid) and FC70 oil (lower fluid).

The FC 70 oil (lower fluid) was placed into a glass vessel and topped up with silicone oil based nanofluid (upper fluid), then a non-uniform DC electric field was applied in a needle and plate electrode configuration. Figure 10.10 shows the system after the applied non-uniform electric field (dielectrophoresis). The settling of nanoparticles can be seen in the interface of the two oils (Fig. 10.10b). The sedimentation was observable after the dielectrophoresis in the high concentration (>20 g/l) of silicone oil based iron oxide nanofluid system.

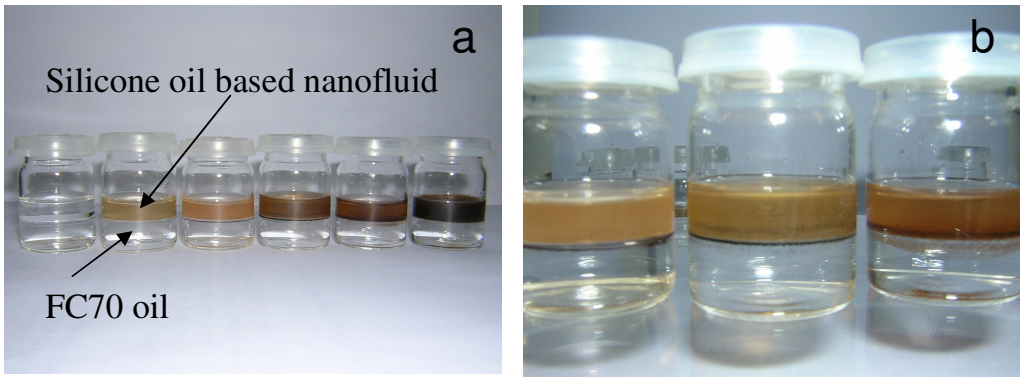

Figure 10.10 Sedimentation of iron oxide-silicone oil nanofluid after an applied electric field (a) and higher magnification (b)

10.4 Emulsion formation by dielectrophoretic manipulation of fluids

A particular application for the dielectrophoretic manipulation technique is for silicone oil-in-water emulsion preparation. The applications for oil-in-water emulsion are versatile from food industries through pharmaceutical to cosmetics.

This method is electrically controllable (by Nanomotion piezoelectric motor) to a fine degree, enabling precise quantities of droplets to be delivered to the aqueous phase. Both micron- and nano-litre droplets of silicone oil are achievable using this method and they acquire an electrical charge, due to injection from the needle tip, which is relatively slow to decay as they pass through the lower fluid (FC70 oil).

The experimental set up (Fig. 10.11) is fundamentally same as before (Chapter 10.1) but now has been extended with a new part which is semi separated from the main vessel.

A barrier effectively divides the container into two separate compartments. As the silicone oil droplets pass under the barrier, the buoyancy force allows them to rise up to the aqueous phase. The aqueous phase is containing surfactant which is reduces the high surface tension of the water and the droplet could cross the interface and keep the spherical shape in the aqueous phase to produce oil-in-water emulsion.

Figure 10.11 shows the system which has been used to create a silicone oil-in-water emulsion by DEP manipulation. The lower part of the vessel is filled with FC70 oil, and on the dielectrophoretic side (right side on the figure) topped up with silicone oil.

In the emulsion producing side (left side on Fig.10.11) the top liquid is distillate water with sodium dodecyl sulphate (SDS) surfactant.

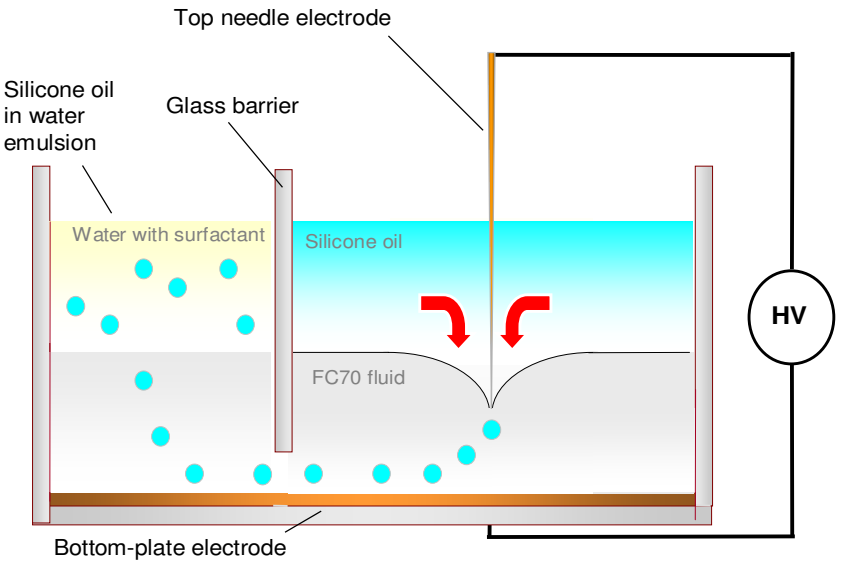

Figure 10.11 Schematic diagram of phenomenon to produce emulsion by DEP

Figure 10.12 shows transportation of oil droplets between chambers in a set-up similar to the Fig. 10.11 configuration. Using the non-uniform electric field, the droplets would travel under the barrier to the opposite side of the vessel but when the buoyancy was the predominant effect, they would ascend bursting at the interface between FC70 and the water phase. If the water phase contained surfactant which hugely reduced the interfacial tension of the water the silicone oil droplet (or nanofluid) could cross the interface and keep their spherical shape inside the water phase to create a silicone oil-in-water emulsion. Figure 10.13a, b shows optical microscope images of silicone oil-in-water emulsion, produced by DEP manipulation which is creating homogeneous emulsion with the controllable silicone oil droplet size.

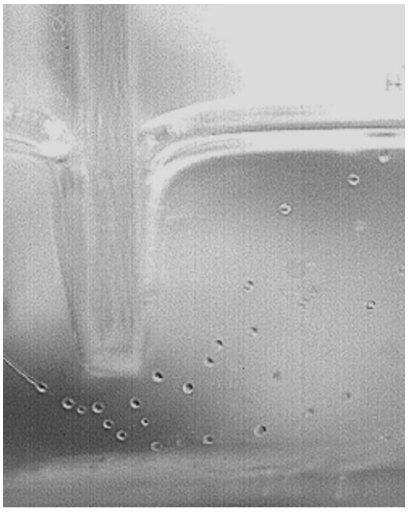

Figure 10.12 Silicone oil droplets travel under the barrier in the DEP system

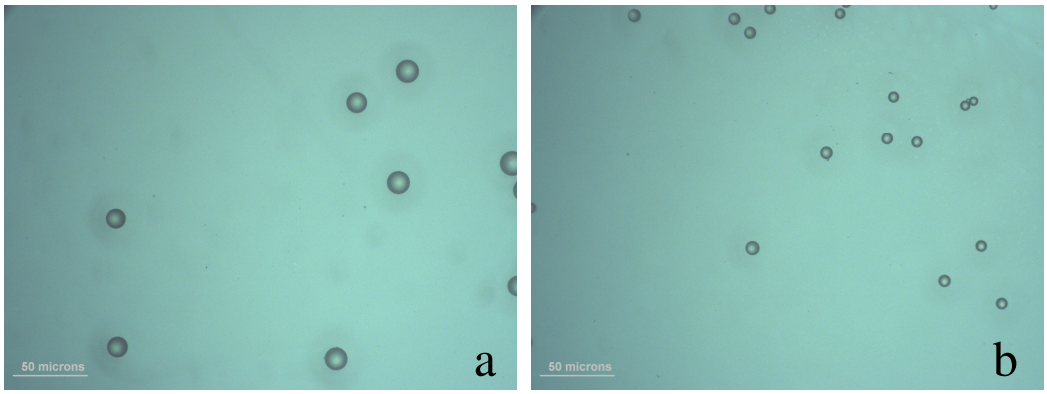

Figure 10.13 Silicone oil-in-water emulsions by dielectrophoretic manipulation

The choice of the surfactant is important and the function of the surfactant is to reduce the surface tension of the water and stabilize the emulsion. Surfactants are stabilizing emulsions by two main mechanisms: steric and electrostatic stabilization. When the SDS dissolved in the water it breaks into two main parts: the anionic surfactant part and the cationic counter ion (sodium). When the silicone oil drop hit the water from the DEP manipulation the hydrophobic tails of the anionic part gets close to the oil drop and the head (cationic part) moves to the drop surface because it is oppositely charged. The hydrophobic tail encapsulates the oil drop and the hydrophilic heads face the water phase.

10.4.1 Emulsion formation by dielectrophoretic manipulation of nanofluids

During the dielectrophoretic manipulation of silicone oil based nanofluid the generated droplet carried the nanoparticles inside the droplets into the aqueous phase to create silicone oil based nanofluid-in-water emulsion. The nanoparticles in the oil phase of oil-in-water emulsion are used in food, cosmetic and pharmaceutical industries. The experimental system (Fig. 10.11) shows the system which used to create the emulsion.

The influence of the concentration of the surfactant has been studied. In our system neither the added low concentration of surfactant nor the transferred very low concentration of nanoparticles from the silicone oil-based nanofluid could stabilize the oil-in-water emulsion on their own. The combination of the two made the oil-in-water emulsion stable. At the interface of oil and water both surfactant molecules and nanoparticles are adsorbed. The nanoparticles used in these experiments are hydrophilic nanoparticles and hydrophilic particles are tending to stabilize oil-in-water emulsions [Binks, B.P. 2002].

Table 10.2 shows the concentration of the added surfactant in the aqueous phase of silicone oil-in-water emulsion. The critical micelle concentration (CMC) of sodium dodecyl sulphate (SDS) is 8.2E-3 M in water at 25 °C [Mukerjee, P. et al. 1971]. The concentration of surfactant has been changed with the type of the nanoparticles.

The smallest amount of surfactant is needed in the iron oxide nanofluid to stabilize the emulsion. The size of the Fe_3O_4 nanoparticles (10 nm) is significantly smaller than the two other types of nanoparticles (Ni and BT). This means with the same nanoparticles concentration (g/l) the particles number density is a highest in the iron oxide suspension 1.91E24 m^{-3}.

The small different between the concentration of the surfactant was necessary to stabilize the BT- and Ni-nanofluids due to the different surface characteristics and the different particle number density of the two types of nanoparticles. The sizes of the particles are similar (Ni 100 nm and BT 130 nm) but the shape and the surface roughness (studied by SEM and AFM) are different. The particles number density of Ni and BT particles are 2.62E21 m^{-3} and 8.69E20 m^{-3}, respectively.

After an experimental study the minimum amount of surfactant was used in the pure silicone oil-in-water emulsion. The changes of the nanoparticles concentration in the

nanofluid before the dielectrophoresis of the nanofluid did not produce any detectable difference in the final silicone based nanofluid-water emulsion. The nanoparticles are positioned in the three phase interface (oil-water, oil-nanoparticle, and water-nanoparticle). Between the nanoparticles are strong inter-particle capillary forces. When the nanofluid drop hit the water-FC70 fluid interface the drop could cross it because the surface tension of water is lowered by the surfactant, and the bouncy is overcome after the drop has lost its acquired charge.

Table 10.2 Surfactant concentration in the silicone oil-in-water emulsion and in silicone oil- nanofluid-in-water emulsion

Nanofluid	**SDS concentration [M]**
Silicone oil	6.50E-05
Fe_3O_4- silicone oil	2.50E-06
Ni- silicone oil	7.50E-06
BT- silicone oil	9.00E-06

The drop enters into the aqueous phase and the surfactant molecules adsorb on the drop surface. The nanoparticles inside of the drop are already placed at the drop surface by the electrical forces. The nanoparticles spontaneously form a layer at the oil-water interface because the thermal energy is lower than the energy need to detach them from the interface as previously shown in silica stabilized emulsion [Horozov, T.S. et al. 2006]. It is worth nothing that those emulsions stabilized with nanoparticles and surfactant remain stable for a long time (months) without coalescence. This indicates that a complete adsorption layer of surfactant–nanoparticles has been formed on the drop surface to prevent it from coalescence.

The size different between the nanoparticles (10 nm to 100 nm) and the typical surfactant molecule (0.4-1 nm) [Tcholakova, S. et al. 2008] is significant for stabilizing the emulsions. Due to the size differences other effects occur [Tcholakova, S. et al. 2008]:

-nanoparticles have slower kinetics of adsorption,

-higher desorption energy.

The adsorption time increases with increasing particle size. The nanoparticle stabilized emulsion needs a higher concentration of nanoparticles than for the surfactant stabilized one, because the larger demand of material needed to adsorb onto

the drop surface to cover it. Several publications show [Taisne, L. et al. 1996, Tcholakova, S. et al. 2008] that the concentration of surfactant can be as low as 0.01 wt% but the nanoparticles concentration is varied as few weight percent. In our case the nanoparticle concentration in the silicone oil drop is very low, and could not stabilize the oil-in-water system.

The self-aggregation of surfactant molecules onto a drop surface is known but the effect on this process of the already existing nanoparticles on the drop surface is not yet clear. The surface cover of the droplet by nanoparticles could be as low as 5 % [Vignati, E. et al. 2003] and could be inhomogeneous and the emulsion is still stable, which should mean that the surface covered by nanoparticles in our system might be lower than 5 % because the emulsion was not stabilised by nanoparticles alone.

The believed mechanism in the case of the DEP formed oil-in water emulsion is that the molecules of low-molecular-weight surfactant adsorb at "vacant places" in the interfacial nanoparticle network. The surfactant could disconnect the nanoparticle network and cause patches (aggregates) of nanoparticles on the surface of the drop.

The excess amount of surfactant could not replace the nanoparticles place on the drop surface because once they adsorbed to the interface is should involve high energy to desorb the nanoparticles; otherwise the surfactant molecule could adsorb and desorb in shorter time and energy scale.

10.5 Nanoparticles recycling from nanofluid by dielectrophoretic manipulation

Part of this project demonstrates the successful clean up of nanoparticles from non-polar nanofluids by dielectrophoretic manipulation technique (Fig. 10.14).

The droplets created from the silicone oil-base nanofluid (upper fluid) transporting the nanoparticles through the Fluorinert FC70 (lower fluid) and captured at the interface between the top and bottom fluids in the opposite side of the vessel. When the nanofluid droplets burst at the interface, nanoparticles remain trapped at the interface between the two immiscible fluids. Filtration ideally takes place at this point and it occurs when it is energetically favourable for the nanoparticles to remain at the interface. Subsequent collection of the particles can be achieved, for example, by causing them to migrate along the interface towards a negatively charged surface.

Clearly the tendency for the nanoparticles to remain at a particular fluid-fluid interface, for deployment or collection, is dependent on the energetics of the particle-fluid interaction. For particles in the low nanometre size range the thermal energy of the system can be of the same order as the interfacial desorption energy, hence in addition to physicochemical factors there is also important size dependence [Böker, A. et al. 2007, Kutuzov, S. et al. 2007].

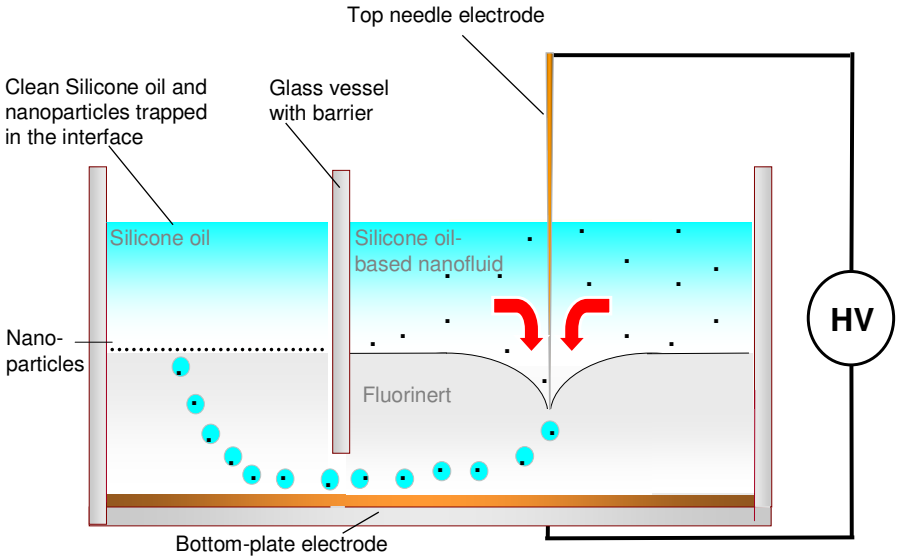

Figure 10.14 Schematic graph of nanofluid recycling system by dielectrophoretic manipulation

The technique used to shows no nanoparticles exist in the top fluid is quite simple, which involves shining a low power laser through the fluid of interest. Viewing the oil vertically to the laser beam, the beam itself is not visible, but in the presence of nanoparticles, the beam is scattered, and becomes visible, appearing as small motes of light in the fluid. Qualitative analysis of the upper fluid (silicone oil) with a laser showed it clean of nanoparticles (Fig. 10.15) and nanoparticles were present only at the interface between the two immiscible fluids. This was confirmed by using the same analysis through the top and bottom fluids, where no laser beam was observed.

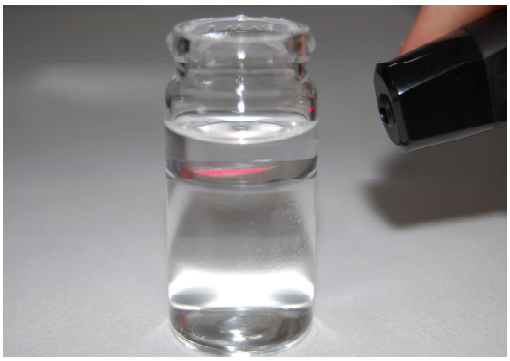

Figure 10.15 Laser beam scattering by nanoparticles at the interface

Currently there is no well known technique for the removing or recycling of nanoparticles or base fluid from nanofluid on an industrial scale. The future application of this process could be the recycling of engine oils. Recycling of nanoparticles will be environmentally favoured and could reduce cost for manufacturers.

10.6 Core-shell structure formation by dielectrophoretic technique

The synthesis and application of core-shell structures is constantly growing because of the wide variation of applications from biological, biomedical application to catalytic application. Part of this project demonstrates the successful preparation of core-shell structures from silicone oil based nanofluids by dielectrophoretic manipulation technique.

The experimental set up (Fig. 10.11) is the same as used to create silicone oil-in-water emulsion but the aqueous phase contains a polymer. The droplets created from the silicone oil (upper fluid) or silicone oil-based nanofluid which transporting the nanoparticles through the lower fluid (FC70 oil) and captured at the aqueous polymer solution in the opposite side of the vessel. When the nanofluid droplets reach the aqueous phase the polymers capture the droplet and create a silicone oil core with polymer shell. A spray drying method was used to isolate these fragile structures and make it possible to take images of the final product.

The zeta potential measurement of oil-in-water emulsion was carried out. Similarly, in another volumetric flask, PVP (poly vinylpyrrolidone) and PVA (poly vinylalcohol) shell materials were suspended in deionised water and at this point, the pH of the solution was adjusted by adding HCl or NaOH to the value given by the measurement of zeta potential. Based on the measurements of the zeta potential of silicone oil in water, core (oil droplets could be containing nanoparticles) and shell materials (aqueous polymer solution) would produce opposite surface charges at the certain pH regions. The electrostatic force on the surfaces of the core and the shell materials would make the attraction of different charged particles to each other and thus form a core-shell structure. Figure 10.16 shows the zeta potential values of the O/W emulsion and polymer solutions in water as a function of pH.

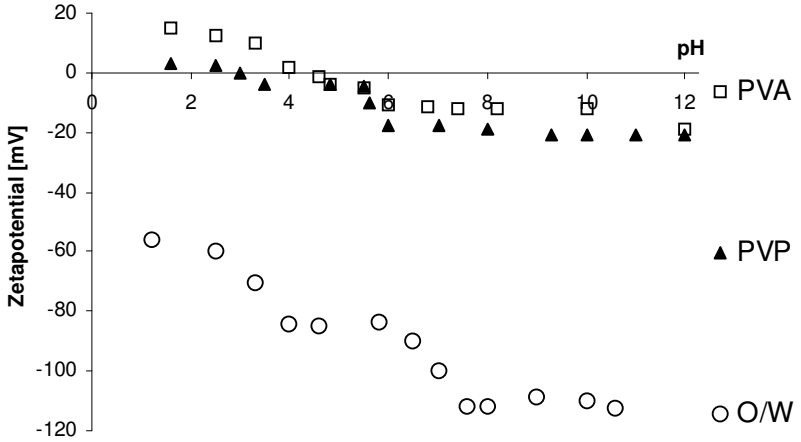

Figure 10.16 Zeta potentials of oil-in-water and polymer solutions as function of pH.

Zeta potential measurement gives the information about the overall surface charge of the particles and how this is affected by the changes in the environment (e.g. pH). The results of the electrophoresis measurements revealed that the zeta potentials of core (oil) and shell (PVP and PVA polymers) have opposite signs in some pH regions, for example, at 1 <pH < 4.0, the zeta potential for O/W emulsion was between -58 and -120 mV while the zeta potential of PVA solution was between +20 and 0 mV. This allowed for the easy attachment of the polymer on the surface of the oil droplets at

this pH region, similarly, of the PVP solution on the surface of O/W emulsion at 1 <pH < 2.4 respectively.

Environmental SEM was employed to examine the morphology of the spray dried core-shell structure. Figure 10.17 shows the PVA coated silicone oil drops and Fig. 10.18 shows the PVP coated silicone oil drops.

Figure 10.17 shows the silicone oil core-PVA polymer shell with various sizes (3-13 μm). The oil droplets with different sizes created by DEP technique and coated with a PVA shell. During the drying process some of the droplets had a higher temperature in certain places in the spray dryer chamber and the surface of these shells become wrinkled (Fig. 10.17 a, b and c). Most of the PVA shells have a smooth surface (Fig. 10.17a and c). Figure 10.17c shows a broken core-shell formation. Figure 10.17d shows a nice, smooth surfaced PVA coated silicone oil droplet and the wires on the surface come from an excess PVA. During the experiments different concentration of PVA solution was tried, and Fig. 10.17d shows a high concentration one. At high concentration of the polymer the excess of polymer dried in a wire formation.

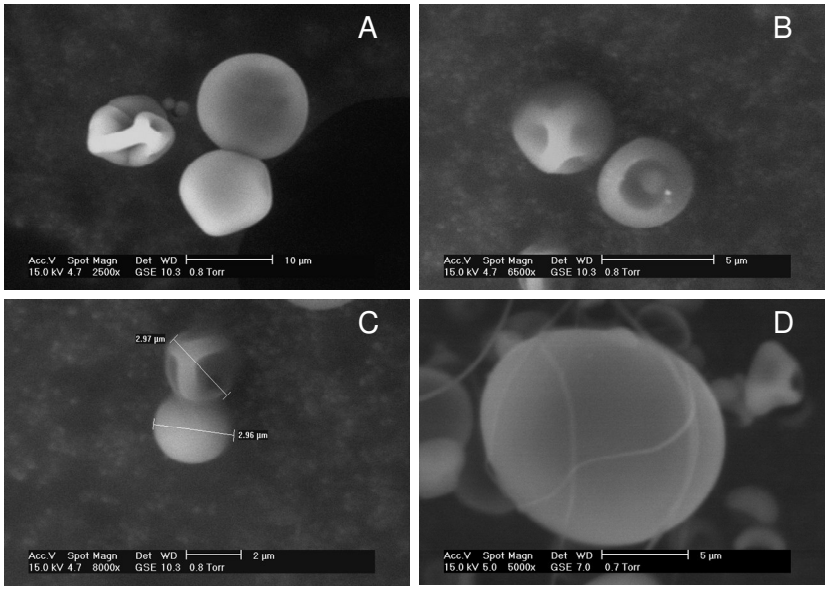

Figure 10.17 Silicone oil droplets coated with PVA produced by DEP manipulation

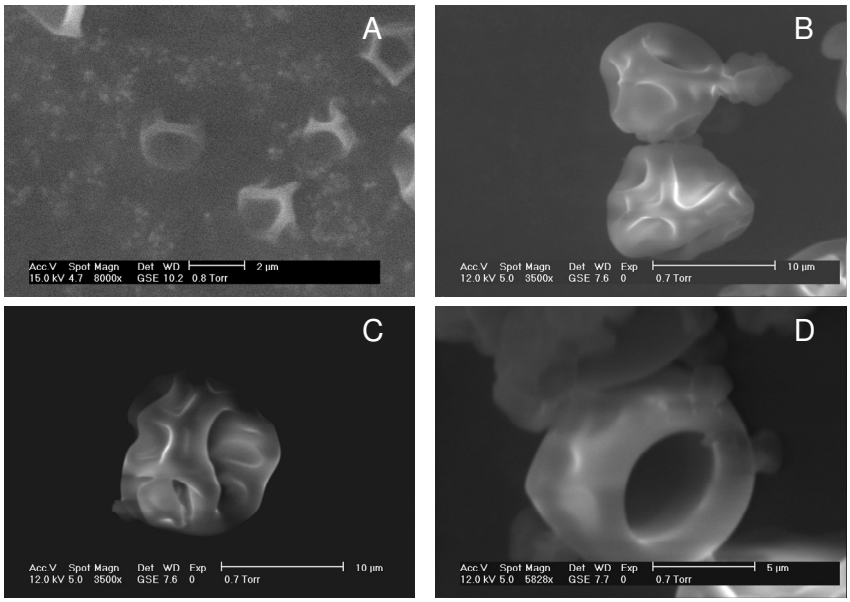

Figure 10.18 Silicone oil droplets coated with PVP produced by DEP manipulation

Figure 10.18 shows the silicone oil core-PVP polymer shell with various sizes (3-12 μm). The different sizes of oil droplets are created by DEP technique and coated with PVP. The surfaces of most of the PVP shells are wrinkled (Fig. 10.18 a, b and c), due to the difficulty of the precise control of the temperature and the nature of the polymer. Figure 10.18d shows a broken core-shell formation.

The polymer coating is confirmed by EDX analysis and the analysis also detected a small amount of nanoparticles form the silicone oil based nanofluid (Fig. 10.19). Table 10.3 shows the result of the EDX analysis. It is worth nothing that the iron component of the droplet of silicone oil base iron oxide nanofluid is very low. Components conformed by the analysis are: carbon (C) is from the polymer shell and the carbon tape, aluminium (Al) is from the aluminium sample holder, silicon (Si) is from the silicone oil and the very small amount of iron (Fe) is from the iron oxide nanoparticles. Fig.10.19a shows the spectrum of the analysed elements (excluding Fe peak due to its very low content). Fig. 10.19b shows the core-shell structure with the analysed area marked as Spectrum 1.

Another way of identifying the iron nanoparticles in the silicone oil droplets was to burn the sample at high temperature and analyse the ashes by EDX. The result had a good agreement with the EDX analysis of silicone oil based iron oxide nanofluid

core-PVP/PVA polymer shell structure and it has been confirmed to have a very low concentration of iron.

Table 10.3 EDX analysis report of silicone oil based iron oxide nanofluid core and PVP shell structure

Element	Weight%	Atomic%
C	70.25	77.95
O	22.67	18.88
Al	1.15	0.57
Si	5.03	2.38
Fe	0.90	0.22
Totals	100.00	100.00

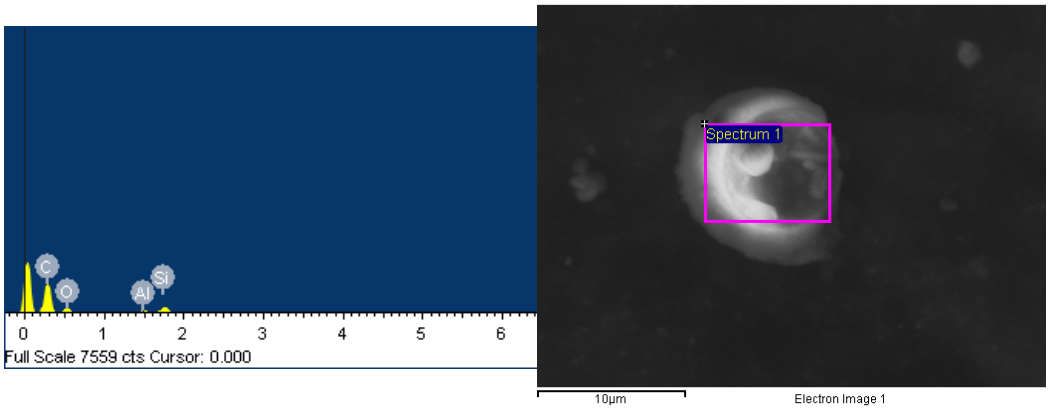

(a) (b)

Figure 10.19 Spectrum of the resulted elements of the core-shell structure analysed by EDX (a) and analysed area of iron oxide-silicone oil core and PVP shell structure (b)

Chapter 11 Overall discussion

The investigation presented in this thesis indicates an evaluation of electrical and physical properties of nanofluid in the optimised work of a new dielectrophoretic droplet generation and manipulation technique. This investigation consisted of experimental synthesis of nano-materials and the characterization of nanofluids.

11.1 Nanoparticle synthesis and characterization

New nanoparticles synthesis routes were required to provide a known size and morphology, which was essential to test the effect of particle size in the new dielectrophoretic droplet generation and manipulation technique. Experiments to date indicate that it is relatively easy to obtain nanoparticles but to have control over the size and morphology has proven to be difficult.

Fe_3O_4 nanoparticles

The type of the iron salt used had an influence on the obtained nanoparticles size due to their different solubilities. Ferric nitrate has the lowest solubility and provided smaller size nanoparticles. The product yield has been improved by the optimised reaction time and reaction temperature

Nickel nanoparticles

A new chemical solution synthesis method was used to produce nickel nanostructures with variable morphologies. The synthesis is described in a paper – see Appendix. Nano-sized spherical Ni nanoparticles, star-shaped Ni nano-crystals and flower-shaped Ni micro-particles were successfully prepared by using a new wet chemical solution route. Ni nanoparticles were prepared by reducing a Ni-complex formed between nickel-acetate and hydrazine solution at high pH in a solution. Then through the control of the precursor concentration, reaction temperature and ageing time, nano-sized Ni particles with different sizes and new morphologies could be formed.

Barium titanate nanoparticles

A systematic study of hydrothermal synthesis of $BaTiO_3$ was carried out to control and understand the effects of parameters such as reaction temperature and time on the formation of BT under alkaline conditions. The BT nanoparticles were formed by a dissolution-precipitation mechanism. The systematic study showed that the increasing the temperature (65 °C-180 °C) and decreasing the time (192 hrs-24 hrs) led to reduced size nanoparticles (<120 nm).

Lead zirconate titanate nanoparticles

The synthesis of PZT particles involves a dissolution-precipitation mechanism which involved Zr-Ti co-precipitated particles with intermediate form, nearly cubic, Pb-ion diffusion and cubic form creation.

The reaction temperature had the main influence on the obtained particle size and increasing the temperature (160 ºC-200 ºC) produced smaller size particles (<200 nm) and new morphology (from cubic to nearly-spherical nanoparticles). The morphology was affected by the reaction temperature and at high temperature the particle growth is faster in 2D dimension than in 3D, resulting in a novel nearly-spherical morphology.

Solid silicon dioxide nanoparticles

The two main stages to form SiO_2 nanoparticles are nucleation and growth. The feed rate and the concentration of NH_4OH has been studied and when the ammonium hydroxide feed rate was slow (0.03 ml/min) the kinetic energy produced by the reaction resulted in slow particle growth and small particle size (20±5 nm). Increasing the feed rate of ammonium hydroxide at slightly reduced temperature produces larger particle sizes (> 40 nm).

The mixing method of precursors has an effect on particle size. The magnetic mixing method leads to larger particle sizes than the use of ultrasonic bath as mixing.

Hollow silicon dioxide particles

Sol-gel method with water-in-oil emulsion synthesis process was used to produce hollow silicon dioxide particles with mesoporous shells. The catalyst has an effect on

the final product. The non-ionic surfactant (Span 80, $C_{24}H_{44}O_6$) tends to promote network formation which leads to hollow form. The surfactant has a double function in this synthesis and the functions are: facilitate emulsion formation and promote emulsion stability and form monolayer at the water-oil interface.

Core-shell Ni- and Fe_3O_4 - coated SiO_2, BT, and PZT particles

New synthesis route developed to produce coated particles which used the electrophoretic measurement of the water-based nanofluids.

Zeta potential measurement gives the information about the overall surface charge of the particles and how this is affected by the changes in the environment (e.g. pH). The measured colloid suspensions were prepared without adding any surfactant to avoid the change of the double layer around the particles. The results of the electrophoresis measurements revealed that the zeta potentials of core (SiO_2, BT and PZT) and shell (Ni and Fe_3O_4) particles have opposite signs in some pH regions, which allowed for the easy attachment of oppositely charged nanoparticles on the surface of other particles at certain pH region.

Core-shell structure of Ni- and Fe_3O_4 - coated SiO_2, BT, and PZT particles successfully synthesised by this novel electrostatic synthesis route with the control of the thickness of the shell through the ratio of core and shell particles.

11.2 Preparation and characterization of nanofluids

The nanofluids have been made without surfactant during this project. The absence of surfactant gives an opportunity to use the “pure” nanofluid in further characterization without additional complexity. If surfactant is added to the nanofluid system the nanoparticle has an interaction with the surfactant and furthermore an interface between the nanoparticles and the stabilizer is created. The surfactant layer could conceivably act as an insulating layer around the nanoparticles and at minimum introduces uncertainty to the effective particle size and interparticle spacing.

Through the characterization of nanofluids it was demonstrated that the nanoparticles have an effect on all kinds of measured properties. The properties of nanofluids depend on the properties of the base-fluid and the properties of the dispersed

nanoparticles, such as concentration, size and morphology. Importantly they are also shown to be dependent on fluid-particle interaction.

Sedimentation of nanofluids

The nanofluids show observable sedimentation over a long time period (> 24 hrs) due to aggregation of nanoparticles through gravity and the lack of any stabilizer or surfactant. The stability of nanofluids generally depends on the particle surface properties, size and shape. Experimental investigation showed that all of the nanofluids used in this project were stable for at least 2.5 hours and the measurement periods were under half an hour. The fluid that was stable for the longest time was the iron oxide-silicone oil base nanofluid, due to the small size (average 10 nm) and the high viscosity of the base fluid.

Viscosity of nanofluids

The viscosity change of base fluids (silicone and FC70 oils) was investigated when different types of nanoparticles were added in various concentrations over a shear-rate range of 0.10–10 s^{-1}. All of the suspension viscosities increased with increasing nanoparticle concentration. The viscosity vs. shear rate curves for all of the samples showed shear-thinning behaviour over the whole shear rate range. This means increasing the shear rate decreases the viscosity due to deaggregation of particles in the base fluid.

The influence of nanoparticle size on the viscosity of the medium was studied. The viscosity both in silicone oil- and in FC70 fluid-based nanoparticle suspensions increases with decreasing size of the BT particles.

Surface tension of nanofluids

In any droplet creation technique (including dielectrophoretic droplet generation technique) the size of the created droplet is directly related to the surface tension and the rheological properties of the fluid.

In the silicone oil based nanofluids at low nanoparticle concentration (1-3 g/l) the reduction of surface tension was observed. At higher nanoparticle concentrations (>3 g/l) no further reduction of surface tension was observed and the value remained at

the same level. In the silicone oil based nanofluids the highest reduction (6 %) of the surface tension of the pure oil occurred in the nickel nanofluid.

In the FC70 based nanofluids the observed trend was the same as in silicone oil based nanofluids and the highest reduction occurred in the iron oxide nanofluid.

It is quite likely that until the nanoparticle concentration reaches certain level (about 3 g/l in these cases) the nanoparticle network at the surface is not completed. Above this concentration any additional nanoparticles would stay inside the solution. This may be the result of the network of nanoparticles at the surface becoming saturated. This was indicated by the surface tension remaining constant, despite a further increase in concentration.

The interface tension of silicone oil/FC70 oil and silicone oil-based nanofluids/FC70 oil was calculated by different models such as Berthelot, Antonow, and Girifalco [Tavana, H. et al. 2007]. The interface tension occurs from an imbalance of forces acting on molecules at the interface. The value of interface tension depends on the interactions between the two fluids and the molecular interaction in the individual fluids. The result shows that the interface tension of silicone oil/Fluorinert oil (7.8 mN/m) is reduced (4.5-4.7 mN/m) by the addition of the nanoparticles.

DC conductivity of nanofluids

The electrical properties of the fluids play an important role in dielectrophoretic droplet generation and manipulation technique, specifically the conductivity and permittivity of the base fluid and the nanofluids.

DC electrical conductivity has been measured for low nanoparticle concentrations in silicone and FC70 oils at moderate electric field strengths [Appendix]. The results showed that, the silicone oil base nanofluids have some field-dependent character over the observed range, shown as an increase in measured conductivity as the applied voltage is increased. The DC conductivity of the silicone oil based nickel nanofluid shows an especially high increase even at very low concentration (4 g/l) and at the higher concentration of nickel (30 g/l) the value of the DC conductivity of the silicone oil increased by eight orders of magnitude.

There is evidence of field-induced behaviour in silicone oil based nanofluids and analysis shows that the observed increases follow the relationship: $\ln J \propto \sqrt{E}$ (where

J is the current density and E the applied electric field) characteristic of energy-activated (Poole-Frenkel type) behaviour.

Enhanced DC conductivity through interaction between the particles and the fluid has been demonstrated even at moderate fields and different types of nanoparticles have been shown to exhibit different behavioural trends. Whilst the DC enhancement is partly related to the spatial arrangement of the particles as expected, there is clear evidence that energy-activated (electric-field activated) processes also play a major role. Synergies clearly exist between nanoparticles and carrier fluids that can have a major influence on the conductivity of nanofluids.

Dielectric permittivity of nanofluids

The dielectric permittivity of low concentrations (< 30 g/l) of nanofluids was studied. All of the examined fluids with low concentrations (≤ 20 g/l) of nanoparticles had the same permittivity value as the base fluid (silicone oil 2.45 and FC70 1.85). At higher concentrations (≥ 30 g/l) of nanoparticles the permittivity of nanofluid dropped to a lower value. The permittivity change with the increase in frequency at room temperature could be explained by the dielectric polarization mechanism. Interfacial and intermolecular polarizations are active in the low frequency range (< 1 MHz).

11.3 Dielectrophoretic droplet manipulation techniques

All of the previously investigated physical and electrical properties of non-polar fluid based nanofluids have a great influence on the new dielectrophoretic droplet generation and manipulation technique. For potential use of the dielectrophoretic technique in further applications deeper understanding is needed of its physical limits. The new electrohydrodynamic technique produces very uniform droplet size distribution and controllable droplet size. This new technique is unique and has a bright future both economically and environmentally. Characteristically:

-no small tubes involved in the droplet creation, which means no clogging,

-it can produce droplets in submicron size or even smaller size, depending on the fluid properties,

-droplet generation occurs without externally applied pressure,

-the energy consumption is very low, usually in the milliwatt range.

Dielectrophoretic droplet generation is achievable using the Fig. 10.1 configuration with no externally applied pressure when three key conditions are in place:

-the upper fluid (silicone oil) must have a higher dielectric permittivity than the lower fluid (FC70);

-the intensity of the electric field adjacent to the needle along its length must have sufficient intensity to generate a dielectrophoretic body force on the fluid;

-charge injection must take place at the needle tip.

Under non-uniform electric fields different phenomena were observed. With an applied electric field the silicone oil sheath (cone) around the needle electrode was observed (Fig. 11.1 a).

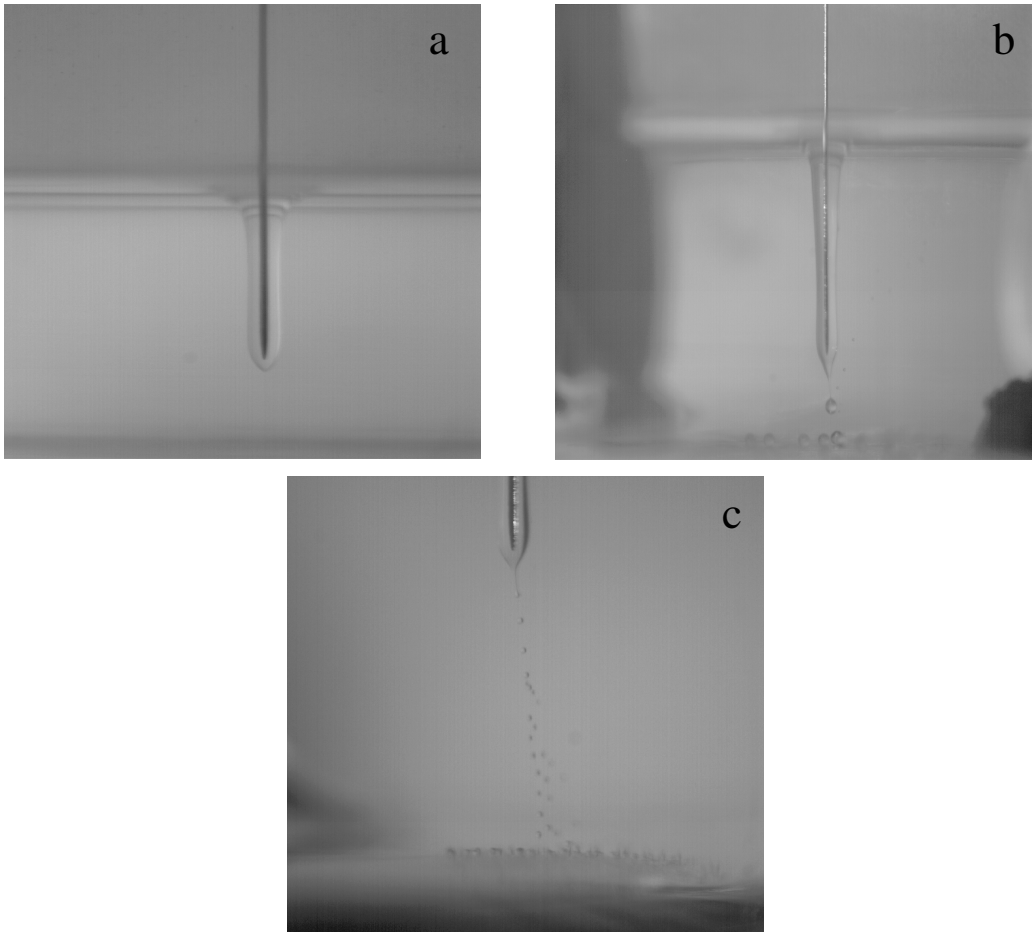

Figure 11.1 Two-phase fluid systems of silicone and FC70 oils, left: a static image shows control of the phenomenon (a), droplet generation (b) and creation of small droplets (c)

The field exerts a positive dielectrophoretic force on the fluid and there is a net flow of silicone oil towards the tip of the needle. In this case, where the electric-field-induced (dielectrophoretic) force is counter-balanced by the restoring (buoyancy) force exerted by FC70 fluid, preventing further fluid flow. Hence there is a detectable electric field threshold for droplet generation to occur (Fig.11.1 b and c). When buoyancy was dominated by the electric forces and the voltage was higher droplet creation was replaced by a continuous jet of silicone oil.

In this needle-and-plate electrodes configuration of dielectrophoretic system the size of the generated droplet could be controlled by the rheological properties of silicone oil and with the distance between the two electrodes (Fig. 11.1).

Emulsion creation by DEP manipulation technique

The new electrohydrodynamic technique was used for preparation of silicone oil-in-water emulsion (Fig. 10.11). The aqueous phase contains surfactant which reduces the surface tension of the water and then the droplet could cross the interface and retain its spherical shape in the aqueous phase. The oil-in-water emulsion produced by DEP manipulation creates a homogeneous emulsion with controllable oil drop size which is significant.

Adding nanoparticles to the silicone oil created a non-polar nanofluid and during the dielectrophoretic droplet manipulation the nanoparticles were carried inside the formed droplets.

In our system neither the very low concentration of surfactant nor the transferred nanoparticles could stabilize the oil-in-water emulsion on their own. The combination of the two made the oil-in-water emulsion stable. The added surfactant concentration could be reduced with an increased number of nanoparticles from the nanofluid.

It is worth noting that emulsions stabilized with nanoparticles and surfactant remain stable for a long time without coalescence. This indicates that a complete adsorption layer of surfactant–nanoparticles should be formed on the drop surface for preventing coalescence.

Recycling of nanoparticles from nanofluids by DEP manipulation technique

The successful recycling of silica nanoparticles from a silicone oil based nanofluid system has been demonstrated, using the new dielectrophoretic technique (Fig. 10.14). The droplets created from the silicone oil-base nanofluid transporting the nanoparticles through the FC70 fluid. When the nanofluid droplets burst at the interface between FC70 and silicone oil, nanoparticles remain trapped at the interface between the two immiscible fluids. Pure silicone oil could be reused and nanoparticles could be recycled which is important from the environmental and financial point of view as well.

Core-shell structure creation by DEP

Part of this project demonstrated the successful preparation of silicone oil core-polymer shell structures by the dielectrophoretic technique and by a spray drying technique. This could be significant as the synthesis and application of the core-shell structures is constantly growing particularly for biological and medical applications.

The droplets created from the silicone oil or silicone oil-based nanofluid were transported through the FC70 fluid and captured in the aqueous polymer (PVA or PVP) solution. When the nanofluid droplets reach the aqueous phase a silicone oil core with polymer shell is created. By controlling the zeta potential of silicone oil core and shell materials (aqueous polymer solution) it is possible to produce opposite surface charges which attract each other.

Chapter 12 Conclusions

The main conclusions drawn from this study are the following:

-New nanoparticles synthesis methods have been created that enable:

-nickel (Ni) nanoparticles to be made spherical, star and flower shape with size range from 80 nm-400 nm,

-lead zirconate titanate (PZT) particles to be made with variable size from 200 nm-1200 nm with cubic, pellet and nearly spherical shapes,

-spherical solid silicon dioxide (SiO_2) nanoparticles to be made in the size range from 20 nm-300 nm,

-core-shell Ni- and Fe_3O_4 - coated SiO_2, BT, and PZT particles to be made.

-In order to achieve accurate control over droplet generation and manipulation by a new dielectrophoretic technique the measurements of physical and electrical properties of nanofluids were required. All of the measurements (stability, viscosity, surface tension, DC conductivity and dielectric permittivity) showed that the addition of a small volume fraction of nanoparticles into the base fluids changes the properties such as:

-the viscosity of base fluid is directly proportional to the concentration of nanoparticles and inversely proportional to the size of the nanoparticles,

-the DC conductivity is enhanced through interaction between the particles and fluid at moderate electric fields with different types of nanoparticles,

-the surface and interface tensions are reduced.

-Results from previous measurements indicated that the novel dielectrophoretic droplet generation and manipulation technique is able to produce droplets with a uniform size distribution and showed the control over the size even with addition of small volume fraction of nanoparticles. This new electrohydrodynamic structuring technique was also used for:

-nanofluid cleaning for recycling the base fluid,

-oil-in-water emulsion formation,

-the creation of core-shell structures, silicone oil core-polymer shell.

Chapter 13 Suggested further work

Further work aimed at improving and scaling up the systems is listed below:

-In doing this work it has become apparent that the volume fraction, morphology and size of nanoparticles have a strong influence on the physical and electrical properties of nanofluids. In order to shed some further light on how the surface charge of nanoparticles affects the properties of non-polar fluids, it will be necessary to add hydrophobic and hydrophilic nanoparticles to the base fluids. The properties of these nanofluids can then be measured and the results compared.

- In order to find out the effect of surfactant on the properties of surfactant stabilized nanofluids and the effect of the surfactant on the dielectrophoretic manipulation system the following experiments would need to be performed: (a) the use of ionic, non-ionic surfactants and polymer as surface–active agents to stabilize nanofluids, (b) the measurements of physical and electrical properties.

-Testing out motor oil and other kind of oils used in different industries in order to find out their suitability for the dielectrophoretic manipulation system. A wide variety of oils with nano-contamination is commercially available, but it is unlikely that a large number of material combinations will be possible.

-Future development of the recycling of nanofluids project for environmental application, including the scale up of the equipment with the use of parallel needles.

References

Abdel-Aal, E.A., Malekzadeh, S.M., Rashad, M.M., El-Midany, A.A., El-Shall, H., (2007) Effect of synthesis conditions on preparation of nickel metal nanopowders via hydrothermal reduction technique, *Powder Technology*, 171, 63-68

Adamson, A.W., (1967) *Physical Chemistry of surfaces*, Wiley, New York

Alam, K., (1999) *Surface and interfacial tension measurements of polymer melts with pendant drop apparatus*, PhD Thesis, Department of Chemical Engineering, McGill University, Montreal, Quebec, Canada, p. 3-5

Arruebo, M., Fernandez-Pacheco, R., Ibarra, M.R., Santamaria, J., (2007) Magnetic nanoparticles for drug delivery, *Nanotoday*, 12, 2, 3, 22-32

Badr, Y., Mahmoud, M.A., (2006) Size-dependent spectroscopic, optical, and electrical properties of PbSe nanoparticles, *Cryst. Res. Technol*., 41, 7, 658 – 663

Barnes, H.A., Hutton, J.F., Walters, K., (1993) Rheology Series 3, *An Introduction of Rheology*, Elsevier, Amsterdam

Barrero, A., Lopez-Herrera, J.M., Boucard, A., Loscertales, I.G., Marquez, M., (2004) Steady cone-jet electrosprays in liquid insulator baths, *Journal of Colloid Interface Science*, 272, 104-108

Barrero, A., Loscertales, I.G., (2007) Micro- and Nanoparticles via Capillary Flows, *Annual Review of Fluid Mechanics*, 39:89-106

Bateni, A., Langhton, S., Tavana, H., Susuar, S.S., Amirfazli, A., Neumann, A.W., (2005) Effect of Electric Fields on Contact Angle and Surface Tension of Drops, *Journal of Colloid and Interface Science*, 283, 215-222

Becher, P., (1983) *Encyclopedia of Emulsion Technology*, Dekker, New York

Beecroft, L.L., Ober, C.K., (1997) Nanocomposite Materials for Optical Applications, *Chem. Mater.* 9, 1302-1317

Bettge, M., Chatterjee, J., Haik, Y., (2004) Physically synthesized Ni-Cu nanoparticles for magnetic hyperthermia, *BioMagnetic Research and Technology*, 2:4

Binks, B.P., Desforges, A., Duff, D.G., (2007) Synergistic Stabilization of Emulsions by a Mixture of Surface-Active Nanoparticles and Surfactant, *Langmuir,* 23, 1098-1106

Binks, B.P., (2002) Particles as surfactants-similarities and differences, *Current Opinion in Colloid & Interface Science*, 7, 21-41

Bohlin CVO Rheometer Handbook (1990), http://www.malvern.co.uk, (accessed 10th May 2007)

Böker, A., He, J., Emrick, T., Russell, T.P., (2007) Self-assembly of nanoparticles at interfaces, *Soft Matter*, 3, 1231-1248

Bresme, F., Oettel, M., (2007) Nanoparticles at fluid interfaces, *J. Phys., Condensed Matter.*, 19, 413101, 1-33

Buchi 190 Spray Dryer Manual and Handbook (2006), http://www.buchi.com, (accessed 14th January 2009)

Buscaglia, M.T., Bassoli, M., Buscaglia, V., (2008) Solid-state synthesis of nanocrystalline $BaTiO_3$: reaction kinetics and powder properties, *J. Am. Ceram. Soc.*, 91, 9, 2862-2869

Butt, H.J., Graf, K., Kappl, M., (2006) *Physics and Chemistry of Interfaces*, Wiley-VCH, Second Edition, ISBN: 3-527-40629-8

Cameron, N., Darve, C., Freyman, C., Sun, L., (2004) *Manipulation of microbeads and nanoparticles by dielectrophoresis*, ME 395, 1-30

Capria, E., (2007) *Electrostatic manipulation of piezoelectric fibres using a sharp probe electrode in a dielectric liquid: Analysis of the electrohydrodynamic phenomena*, PhD Thesis, Cranfield

Caruso, F., Caruso, R.A., Mohwald, H., (1998) Nanoengineering of Inorganic and hybrid hollow spheres by colloidal templating, *Science*, 282, 6, 1111-1113

Chakraborty, S., Padhy, S., (2008) Anomalous Electrical Conductivity of Nanoscale Colloidal Suspensions, *ACS Nano*, 2, 10, 2029-2036

Challis, R.E., Povey, M.J.W., Mather, M.L., Holmes, A.K., (2005) Ultrasound techniques for characterizing colloidal dispersions, *Reports on Progress Physics*, 68:1541-1637

Chanda, S.C., Manna, A., Vijayan, V., Nayak, P.K., Ashok, M., Acharya, H.N., (2007) PIXE & XRD analysis of nanocrystals of Fe, Ni and Fe_2O_3, *Materials Letters*, 61 5059-5062

Chartier, T., Jorge, E., Boch, P., (1993) Dispersion properties of $BaTiO_3$ tape-casting slurries, *Journal of European Ceramic Society*, 11, 387-393

Chen, C.L., Wei, Y.L., Jiao, X.L., Chen, D., (2008) Hydrothermal synthesis of $BaTiO_3$: Crystal phase and the Ba^{2+} ions leaching behaviour in aqueous medium, *Materials Chemistry and Physics*, 110, 186-191

Chen, D.H., Wu, S.H., (2000) Synthesis of nickel nanoparticles in water-in-oil microemulsions, *Chem. Mater.*, 12, 1354-1360

Chen, H., Ding, Y., Tan, C., (2007) Rheological behaviour of nanofluids, *New Journal of Physics*, 9, 367

Chen, S., Oye, G., Sjoblom, J., (2005) Rheological Properties of Silica Particle Suspensions in Mineral Oil, *Journal of Dispersion Science and Technology*, 26, 791-798

Chen, S., (2006) *Rheological properties of water in oil emulsions and particulate suspensions*, Norwegian University of Science and Technology, PhD Thesis, 176, pp 23

Chen, Y., Peng, D.-L., Lin, D., Luo, X., (2007) Preparation and magnetic properties of nickel nanoparticles via the thermal decomposition of nickel organometallic precursor in alkylamines, *Nanotechnology,* 18, 505703

Choi, J.Y., Lee, K.Y., Yoon, S.M., Lee, S.L., Kim, B.K., Kim, J.M., (2005) A Chemical Route to Large-Scale Preparation of Spherical and Monodisperse Ni Powders, *J. Am. Ceram. Soc*., 88, 11, 3020-3023

Choi, S.U.S., (2009) Nanofluids: From Vision to Reality through Research, *Journal of Heat Transfer*, 131, 033106

Christopher, G.F., Anna, S.L., (2007) Microfluidic methods for generating continuous droplet streams, *J. Phys. D Appl. Phys.*, 40, R319-R336

Clark, I.J., Takeuchi, T., Ohtori, N., Sinclair, D.C., (1999) Hydrothermal synthesis and characterization of $BaTiO_3$ fine powders: precursors, polymorphism and properties, *J. Mater. Chem.*, 9, 83-91

Clegg, P.S., (2008) Fluid-bicontinuous gels stabilized by interfacial colloids: low and high molecular weight fluids, *J. Phys. Condensed Matter*, 20, 113101

Cohen, I., Li, H., Hongland, J.L., Mrksish, M., Nagel, S.R., (2001) Using Selective Withdrawal to Coat Microparticles, *Science*, 292, 265-267

Cornell, R.M. Schwertmann, U., (1996) *The Iron Oxides, Structure, Properties, Occurrences and Uses*, Wiley-VCH, Second, Completely Revised and Extended Edition, New York

Cuenot, S., Fretigny, C., Demoustier-Champagne, S., Nysten, B., (2004) Surface tension effect on the mechanical properties of nanomaterials measured by atomic force microscopy, *Phys. Rev. B*., 69, 165 410-1–165 410-5

Cullity, B.D., (1978) *Elements of X-ray diffraction*, Second Edition, Addision-Wesley Publisher, London

Cullity, B.D., (1972) *Introduction to Magnetic Materials*, Addison Wesley, New York, p. 129

Danov, K.D., Kralchevsky, P.A., Ananthapadmanabhan, K.P., Lips, A., (2006) Particle-Interface Interaction across a Nonpolar Medium in Relation to the Production of Particle-Stabilized Emulsions, *Langmuir*, 22, 106-115

Demiere, N., (2008) *Continuous-Flow Separation of Cells in a Lab-on-a-Chip using "Liquid Electrodes" and Multiple-Frequency Dielectrophoresis*, PhD Thesis No 4099, EPFL, France

Deng, Y., Liu, L., Cheng, Y., Nan, C.W., Zhao, S.J., (2003) Hydrothermal synthesis and characterization of nanocrystalline PZT powders, *Materials Letters*, 57, 1675-1678

Dinsmore, A.D., Hsu, M.F., Nicolaides, M.G., Marques, M., Bausch, A.R., Weitz, D.A., (2002) Colloidosomes: Selectively Permeable Capsules Composed of Colloidal Particles, *Science*, 298, 1006-1009

Dogan, A., Gunkaya, G., Suvaci, E., (2006) Electrophoretic deposition of nano sized $BaTiO_3$, *J. Mater. Sci.*, 41, 8196-8201

Donselaar, L.N., Philips, A.P., Suurmond, J., (1997) Concentration-dependent sedimentation of dilute magnetic fluids and magnetic silica dispersions, *Langmuir*, 13, 6018-6025

Dunn, S., Harada, S., (2008) Hydrothermal deposition of heteroepitaxial lead-zirconate-titanate nanostructures and thin films, *Journal of the European Ceram. Soc.*, 28, 2747-2753

Espin, M.J., Delgado, A.V., Plocharski, J., (2006) Effect of additives and measurement procedure on the electrorheology of hematite/silicone oil suspensions, *Rheol. Acta*, 45, 865-867

Farook, U., Edirisinghe, M.J., Stride, E., Colombo, P., (2008) Novel co-axial electrohydrodynamic in-situ preparation of liquid-filled polymer-shell microspheres for biomedical applications, *Journal of Microencapsulation*, 25(4), 241-247

Feng, X., Jiang, L., (2006) Design and creation of superwetting/antiwetting surfaces, *Adv. Mater.*, 18, 3063-3078

Flores-Rodriguez, N. Markx, G.H., (2006) Anomalous dielectrophoretic behaviour of barium titanate microparticles in concentrated solutions of ampholytes, *J. Phys. D: Appl. Phys*., 39, 3356–3361

Foygel, M., Morris, R.D., Anez, D., French, S., Sobolev, V.L., (2005) Theoretical and computational studies of carbon nanotube composites and suspensions: Electrical and thermal conductivity, *Phys. Rev. B*, 71, 104201

Frenandez de la Mora, J., (2007) The Fluid Dynamics of Taylor Cones, *Annual Review of Fluid Mechanics*, 39:217-43

Ganan-Calvo, A.M., (1998) Generation of steady liquid microthreads and micron-sized monodisperse sprays in gas streams, *Phys. Rev. Lett.,* 80:285-288

Garg, J., Pondel, B., Chiesa, M., Gordon, J.B., Ma, J.J., Wang, J.B., Ren, Z.F., Kang, Y.T., Ohtani Nanda, H., McKinley, G.H., Chen, G., (2008) Enhanced thermal

conductivity and viscosity of copper nanoparticles in ethylene glycol nanofluid, *Journal of Applied Physics*, 103, 074301

Ghasemi, E., Mirhabibi , A., Edrissi, M., (2008) Synthesis and rheological properties of an iron oxide ferrofluid, *Journal of Magnetism and Magnetic Materials*, 320, 21, 2635-2639

Ghasemifard, M., Hosseini, S.M., Khorsand Zak, A., Khorrani, Gh.H., (2009) Microstructural and optical characterization of PZT nanopowder prepared at low temperature, *Physica E*, 41, 418-423

Girifalco, L.A., Good, R.J., (1957) A Theory for the Estimation of Surface and Interfacial Energies. I. Derivation and Application to Interfacial Tension, *J. Phys. Chem.,* 61, 904-909

Gong, X., Wu, J., Huang, X., Wen, W., Sheng, P., (2008) Influence of Liquid Phase on Nanoparticle-based Giant Electrorheological Fluid, *Nanotechnology*, 19 165602

Greene, L.E., Law, M., Tan, D.H., Montano, M., Goldberg, J., Somorjai, G., Yang, P., (2005) General route to vertical ZnO nanowire arrays using textured ZnO seeds, *Nano Letters*, 5, 7, 1231-1236

Guo, L., Luo, H., Gao, J., Guo, L., Yang, J., (2006) Microwave hydrothermal synthesis of barium titanate powder, *Materials Letters*, 60, 3011-3014

Hallouet, B., Wetzel, B., Pelster, R., (2007) On the Dielectric and Magnetic Properties of Nanocomposites, *Journal of Nanomaterials*, ID 34527, doi:10.1155/2007/34527, p11

Harada, S., (2008) *Issues related to the processing of ferroelectric nanostructures via ex situ and in situ methods*, PhD Thesis, Cranfield University, Cranfield

Hayati, I., Bailey, A.I., Tadros, T.F., (1986) Mechanism of Stable Jet Formation in Electrohydrodynamic Atomization, *Nature*, 319, 41-43

Heeren, A., Luo, C.P., Henschel, W., Fleischer, M., Kern, D.P., (2007) Manipulation of micro- and nano-particles by electro-osmosis and dielectrophoresis, *Microelectronic Eng*., 84, 1706-1709

Hench, L.L., West, J.K., (1990) The Sol-Gel Process, *Chemistry Reviews*, 90, 33-72

Higuera, F.J., (2003) Flow rate and electric current emitted by a Taylor cone, *Journal of Fluid Mechanics*, 484: 303-327

Hong, R.Y., Ren, Z.Q., Han, Y.P., Li, H.Z., Zeng, Y., Ding, J., (2007) Rheological properties of water-based Fe_3O_4 ferrofluids, *Chemical Eng. Sci*., 62, 5912-5924

Horozov, T.S., Aveyard, R., Binks, B.P., Clint, J.H., (2005) Structure and Stability of Silica Particle Monolayers at Horizontal and Vertical Octane-Water Interface, *Langmuir*, 21, 7407-7412

Horozov, T.S., Aveyard, R., Clint, J.H., (2005) Particle Zips: Vertical Emulsion Films with Particle Monolayers at their Surfaces, *Langmuir*, 21, 2330-2341

Horozov, T.S., Binks, B.P., (2006) Particle-Stabilised Emulsions: A Bilayer or a Bridging Monolayer? *Angew. Chem. Int. Ed.*, 45, 773-776

Hosono, E., Matsuda, H., Honma, I., Ichihara, M., Zhou, H., (2007) Synthesis of a Perpendicular TiO_2 Nanosheet Film with the Superhydrophilic Property without UV Irradiation, *Langmuir*, 23, 7447-7450

Huang, C.K., Hou, C.H., Chen, C.C., Tsai, Y.L., Chang, L.M., Wei, H.S., Hsieh, K.H., Chan, C.H., (2008) Magnetic SiO_2/Fe_3O_4 colloidal crystals, *Nanotechnology*, 19, 055701

Hunter, T.N., Pugh, R.J., Franks, G.V., Jameson, G.J., (2008) The role of particles in stabilizing foams and emulsions, *Advances in Colloid and Interface Science*, 137, 57-81

Hwang, J.S., Lee, J., Chang, Y.H., (2005) Surface Properties of Silane-Treated Titania Nanoparticles and Their Rheological Behaviour in Silicone Oil, *Macromolecular Research*, 13, 5, 409-417

Jordan, A., Wurst, P., Fahling, H., John, W., Hinz, A., Felix, R., (1993) Inductive heating of ferrimagnetic particles and magnetic fluids: Physical evaluation of their potential for hyperthermia, *International Journal of Hyperthermia*, 9, 1, 51-68

Joscelyne, S.M., Tragardh, G., (2000) Membrane emulsification-a literature review, *Journal of Membrane Science*, 169, 107-117

Keblinski, P., Prasher, R., Eapen, J., (2008) Thermal conductance of nanofluids: is the controversy over? *J. Nanopart. Res*., 10, 1089-1097

Khastgir, D., Adachi, K., (2000) Rheological and dielectric studies of aggregation of barium titanate particles suspended in polydimethylsiloxane, *Polymer*, 41, 6403-6413

Kim, J., Wilhelm, O., Pratsinis, S.E., (2002) Nanoparticle packaging, *Adv. Eng. Mater.*, 4(7), 494-496

Kim, S.H., Kim, M.J., Choa, Y.H., (2007) Fabrication and estimation of Au-coated Fe_3O_4 nanocomposite powders for the separation and purification of biomolecules, *Materials Science and Engineering A*, 449-451, 386-388

Kim, S.S., Lee, M., Kim, D.H., (2008) Electrokinetic settling and sedimentation behaviour of cohesive soils in dilute suspension, *Journal of Environmental Science and Health Part A*, 43, 975-984

Koo, J., Kleinstreuer, C., (2004) A new thermal conductivity model for nanofluids, *J. Nanopart. Res.*, 6, 577–588

Krupke, R., Hennrich, F., Lohneysen, H., Kappes, M., (2003) Separation of Metallic from Semiconducting Single-Walled Carbon Nanotubes, *Science*, 301, 344-347

Kudlash, A.N., Vorobyova, S.A., Lesnikovich, A.I., (2008) Interphase synthesis and some characterization of aqueous nickel dispersions, *Journal of Physics and Chemistry of Solids*, 69, 1652-1656

Kurihara, L.K., Chow, G.M., Schoen, P.E., (1995) Nanocrystalline metallic powders and films produced by the polyol method, *Nanostruct. Mater*., 5, 6, 607-613

Kutuzov, S., He, J., Tangirala, R., Emrick, T., Russell, T.P., Böker, A., (2007) On the kinetics of nanoparticle self-assembly at liquid/liquid interfaces, *Physical Chemistry Chemical Physics*, 9, 6351-6358

Kwon, S.W., Yoon, D.H., (2007) Tetragonality of nano sized barium titanate powder prepared with growth inhibitors upon heat treatment, *Journal of European Ceramic Society*, 27, 247-252

Landfester, K., (2001) The generation of nanoparticles in miniemulsion, *Adv. Mater*., 13(10), 765-768

Laurent, S., Forge, D., Port, M., Roch, A., Robic, C., Vander Elst, L., Muller, R.N., (2008) Magnetic iron oxide nanoparticles: synthesis, stabilisation, vectorization, physicochemical characterizations and biological applications, *Chem. Review*, 108, 2064-2110

Lee, J., T. Isobe and M. Senna, (1996) Preparation of Ultrafine Fe_3O_4 particles by Precipitation in the Presence of PVA at High pH, *J. Colloid Interface Sci*., 177, 490-494

Lee, J.J., Park, K.J., Hur, K.H., Yi, S.C., Koo, S.M., (2006) Synthesis of ultrafine and spherical barium titanate powders using a titania nano-sol, *J. Am. Ceram. Soc*., 89, 10, 3299-3301

Lee, K.R., Kim, S.J., Song, J.S., Lee, J.H., Chung, Y.J. and Park, S., (2002) Photocatalytic characteristics of nanometer-sized titania powders fabricated by a homogeneous-precipitation process, *J. Am. Ceram. Soc*., 85(2), 341-345

Lee, T., Aksay, A., (2001) Hieralchical structure ferroelectricity relationships of barium titanate particles, *Crystal Growth & Design*, 1, 5, 401-409

Lencka, M.M., Riman, E., (1993) Thermodynamic modeling of hydrothermal synthesis of ceramic powders, *Chem. Mater*., 5, 61-70

Leunissen, M.E., Blaaderen, van A., Hollingsworth, A.D., Sullivan, M.T., Chaikin, P.M., (2007) Electrostatics at the oil-water interface, stability, and order in emulsions and colloids, *PNAS*, 104, 8, 2585-2590

Li W.J., Sha X., Dong W., Wang Z., (2002) Synthesis of stable hollow silica microspheres with mesoporous shell in nonionic W/O emulsion, *Chem. Commun*., 2434-2435

Libor, Z., Zhang, Q., (2009) The synthesis of nickel nanoparticles with controlled morphology and SiO_2/Ni core-shell structures, *Materials Chemistry and Physics*, 114, 2-3, 902-907

Linke, W.F., (1965) *Solubilities, Inorganic and Metal-organic compounds; a compilation of solubility data from the periodical literature*, Fourth edition, Princeton, Van Nostrand

Liu, Z., Li, S., Yang, Y., Peng, S., Hu, Z., Qian, Y., (2003) Complex-Surfactant-Assisted Hydrothermal Route to Ferromagnetic Nickel Nanobelts, *Adv. Mater*., 22, 1946-1948

Lopez H.J.O., (2004) *Synthesis of stable hollow silica microspheres with mesoporous shells in W/O emulsion*, MSc Thesis, Cranfield University, Cranfield

Lopez-Esteban, S., Diaz, M., Moya, J.S., (2007) Rheology of zirconia/nickel particulate system and microstructure of composites, *Composites Science and Techn*., 67, 2303-2310

Loscertales, I.G., Barrero, A., Guerrero, I., Cortijo, R., Marquez, M., (2002) Micro/nano encapsulation via electrified coaxial liquid jets, *Science*, 295, 1695-1698

Lou, X.W., Yuan, C., Archer, L.A., (2007) Shell by shell synthesis of tin oxide hollow colloids with nanoarchitectured walls: Cavity size tuning and functionalization, *Small*, 3, 2, 261-265

Lou, X.W.D., Archer, L.A., Yang, Z., (2008) Hollow micro/nanostructures: synthesis and applications, *Adv. Mater.*, 20, 3987-4019

Lu, A.H., Salabas, E.L., Schuth, F., (2007) Magnetic nanoparticles: synthesis, protection, functionalization and application, *Angew. Chem. Int. Ed*., 46, 1222-1244

Ma, F., Li, Q., Huang, J., Li, J., (2008) Morphology control and characterizations of nickel sea-urchin-like and chain-like nanostructures, *Journal of Crystal Growth*, 310, 3522-3527

Maex, K., Baklanov, M.R., Shamiryan, D., Iacopi, F., Brongersma, S.H., Yanovitskaya, Z.S., (2003) Low dielectric constant materials for microelectronics, *J. Appl. Phys.*, 93, 11, 8793-8836

Malvern Instrument Technical Note MRK 654-01, Malvern Handbook http://www.malvern.co.uk, (accessed 20th June 2009)

Mandal, S.K., Lequeux, N., Rotengerg, B., Tramier, M., Fattaccioli, J., Bibette, J., Dubertret, B., (2005) Encapsulation of Magnetic and Fluorescent Nanoparticles in Emulsion Droplets, *Langmuir*, 21, 4175-4179

Matijevic, E., (1993) Preparation and properties of uniform size colloids, *Chem. Mater.*, 5, 412-426

Matsoukas, T., Gulari, E., (1988) Dynamics of growth of silica particles from ammonia-catalyzed hydrolysis of tetraethyl orthosilicate, *J. Colloid Surfaces Sci.*, 124, 252

Millman, J.R., Bhatt, K.H., Prevo, B.G., Velev, O.D., Anisotropic Particle Synthesis in Dielectrophoretically Controlled Microdroplet Reactors, *Nature Materials*, 4, 98-102, 2005

Moreau, L., Kim, H.J., Decker, E.A., McClements, D.J., (2003) Production and characterization of oil-in-water emulsions containing droplets stabilized by beta-lactoglobulin–pectin membranes, *J. Agric. Food Chem.*, 51, 6612-6617

Morgan, H., Green, N.G., (2003) *AC Electrokinetics: colloids and nanoparticles*, Research Studies Press

Moulson, A.J., Herbert, J.M., (2003) *Electroceramics*, John Wiley and Sons Publisher, Second Edition, ISBN 0471497479, p. 339

Mukerjee, P., Mysels, K.J., (1971) *Critical Micelle Concentrations of Aqueous Surfactant Systems*, NSRDS-NBS 36, US. Government Printing Office, Washington,.D.C.

Murshed, S.M.S., Leong, K.C., Yang, C., (2008) Thermophysical and electrokinetic properties of nanofluids – a critical review, *Applied Thermal Engineering*, 28, 2109-2125

Murshed, S.M.S., Tan, S.H., Nguyen, N.T., (2008) Temperature dependence of interfacial properties and viscosity of nanofluids form droplet-based microfluidics, *J. Phys.D:Appl. Phys*., 41, 085502

Nguyen, C.T., Desgranges, F., Roy, G., Galanis, N., Mare, T., Boucher, S., Angue Mintsa, H., (2007) Temperature and Particle-Size Dependent Viscosity Data for Water-Based Nanofluids –Hysteresis Phenomenon, *International Journal of Heat and Fluid Flow*, 28, 1492-1506

Ni, X., Zhao, Q., Zheng, H., Li, B., Song, J., Zhang, D., Zhang, X., (2005) A Novel Chemical Reduction Route towards the Synthesis of Crystalline Nickel Nanoflowers from a Mixed Source, *European Journal of Inorganic Chemistry*, 23, 4788-4793

Nikolaides, M.G., Bausch, A.R., Hsu, M.F., Dinsmore, A.D., Brenner, M.P., Guy, C., Weitz, D.A., (2002) Electric-field-induced capillary attraction between like-charged particles at liquid interfaces, *Nature*, 420, 299-301

Nima Technology Ltd, Set up and Operational Guide (2006)

Ongaro, R., Pillonnet, A., (1991) Synthetic theory of Poole and Poole-Frenkel (PF) Effects, *IEEE Proceedings-A*, 138 No.2, 127-130

Paik, U., Hackley, V.A., Choi, S., Jung, T., (1998) The effect of electrostatic repulsive forces on the stability of $BaTiO_3$ particles suspended in nonaqueous media, *Colloids Surf. A Physicochemical Eng. Aspects*, 135, 77-88

Pankhrust, Q.A., Connolly, J. Jones, S.K. and Dobson, J., (2003) Applications of magnetic nanoparticles in biomedicine, *J. Phys. D; Appl. Phys*., 36, R167-R183

Park, S.K., Kim, K.D., Kim, H.T., (2002) Preparation of silica nanoparticles: determination of the optimal synthesis conditions for small and uniform particles, *Colloids and Surfaces A: Physiochemical and Engineering Aspects*, 197, 7-17

Patel, H.E., Sundararajan, T., Pradeep, T., Dasgupta, A., Dasgupta, N., Das, S.K., (2005) A micro-convection model for thermal conductivity of nanofluid, *Pramana, J. Phys.*, 65, 863–869

Peterson, E.D., Krueger, D.A., (1977) Reversible, field induced agglomeration in magnetic colloids, *J. Colloid and Interface Sci*., 62, 1, 24-34

Pethig, R., Markx, G.H., (1997) Applications of dielectrophoresis in biotechnology, *TIBTECH*, 15, 426-432

Pickering, S.U.S., (1907) Emulsions, *J. Chem. Soc*., 91, 2001-2021

Pieranski, P, (1980) Two-dimensional interfacial colloidal crystals, *Phys. Rev. Lett*., 45, 569-572

Pohl, H.A., Pethig, R., (1977) Dielectric measurements using non-uniform electric field (dielectrophoretic) effects, *Journal of Phys E: Scientific Instruments*, 10, 190-193

Polla, D.L., Francis, L.F., (1996) Ferroelectric thin films in microelectromechanical systems applications, *MRS Bulletin,* 21, 7, 59-65

Preining, O., (1998) The physical nature of very, very small particles and its impacts on their behaviours, *Journal of Aerosol Science*, 5/6, 481-495

Puntes, VF, Krishnan, K.M., Alivisatos, A.P., (2001) Colloidal nanocrystal shape and size control: The case of cobalt, *Science*, 291, 2115-2117

Rahaman, M.N., (2006) *Ceramic processing*, CRC, Taylor & Francis, ISBN 9780849372858, p. 179

Rahman, I.A., Vejayakumaran, P., Sipant, S., Ismail, J., Abu Bakar, M., Adnan, R., Chee, C.K., (2007) An optimized sol-gel synthesis of stable primary equivalent silica particles, *Colloid and Surfaces A Physichem. Eng. Aspects*, 194, 102-110

Rahman, I.A., Vejayakumaran, P., Sipaut, C.S., (2008) Effect of the Drying Techniques on the Morphology of Silica Nanoparticles Synthesized via Sol-Gel Process, *Ceramics International*, 34, 8, 2059-2066

Ravera, F., Santini, E., Loglio, G., Ferrari, M., Liggieri, L., (2006) Effect of nanoparticles on the interfacial properties of liquid/liquid and liquid/air surface layers, *J. Phys. Chem. B*, 110, 19543-19551

Saimoto, Y., Satoh, T., Konno, M., (1999) Correlation between Generated Shear Stress and Generated Permittivity for the Electrorheological Response of Colloidal Silica Suspensions, *Journal of Colloid and Interface Science*, 219, 135-143

Sakabe, Y., Yamashita, Y., Yamamoto, H., (2005) Dielectric properties of nanocrystalline $BaTiO_3$ synthesized by micro emulsion method, *Journal of European Ceramic Society*, 25, 2739-2742

Sato, M., Hatori, T., Saito, M., (1997) Experimental investigation of droplet formation mechanisms by electrostatic dispersion in a liquid-liquid system, *IEEE, Transactions on Industry Applications*, 33, 6, 15271534

Sato, M., Kudo, N., Saito, M., (1998) Surface tension reduction of liquid by applied electric field using vibrating jet method, *IEEE Transactions on Industry Applications*, 34, 2, 294-300

Scholten, P.C., Felius, J.A.P., (1990) The magnetical and rheological behaviour of aggregating magnetic suspensions, *Journal of Magnetism and Magnetic Materials*, 85, 107-113

Sedighi, S. Murad, S. Aggarwal, (2008) *Size Effect on Nano-Droplet Spreading on Solid Surface, Nanotechnology*, Boston, June 1-5, NSTI Nanotech, The Nanotechnology Conference and Trade Show, Boston, Mass., 71.8083/N186ns:2008(3)

Shan, G.B., Xing, J.M., Zhang, H.Y., Liu, H.Z., (2005) Biodesulfurization of Dibenzothiophene by Microbial Cells Coated with Magnetite Nanoparticles, *Applied and Environmental Microbiology*, 71, 8, 4497-4502

Shaw, D.J., (1999) *Introduction to colloid and surface chemistry*, Butterworth-Heinemann a division of Reed Educational and Professional Publishing Ltd, Oxford

Sherman, P., (1968) *Emulsion science*, Academic Press, 541.182.41, London

Simovic, S., Prestidge, C.A., (2003) Hydrophilic Silica Nanoparticles at the PDMS Droplet−Water Interface, *Langmuir*, 19, 3785-3792

Someya, S., Munakata, T., (2005) Measurement of the interface tension of immiscible liquids Interface, *Journal of Crystal Growth*, 275, e343-e348

Stöber, W., Fink, E., Bohn, E., (1968) Controlled growth of monodisperse silica spheres in the micro size range, *J. Colloid Interface Sci*., 26, 62-69

Suehiro, J., Pethig, R., (1998) The dielectrophoretic movement and positioning of a biological cell using a three-dimensional grid electrode system, *J. Phys. D Appl. Phys.*, 31, 3298-3305

Sugimoto, T., Zhou, X., Muramatsu, A., (2003) Synthesis of uniform anatase TiO_2 nanoparticles by gel–sol method 3, Formation process and size control, *J. Colloid. Interface Sci.*, 259(1), 43-52

Sun, D., Rocks, S.A., Edirisinghe, M.J., Dorey, R.A., Wang, Y., (2005) Electrohydrodynamic deposition of nanostructured lead zirconate titanate, *J. Nanosci. Nanotechnology*, 5, 1846–1851

Taisne, L., Walstra, P., Cabane, B., (1996) Transfer of oil between emulsion droplets, *J. Colloid Interface Sci.*, 184, 378-390

Tan, S.H., Sohel Murshed, S.M., Nguyen, N.T., Wong, T.N., Yobas, L., (2008) Thermally controlled droplet formation in flow focusing geometry: formation regimes and effect of nanoparticle suspension, *J. Phys. D: Appl. Phys*., 41, 165501

Tavana, H., Neumann, A.W., (2007) Recent progress in the determination of solid surface tensions from contact angles, *Advances in Colloid and Interface Science*, 132, 1-32

Taylor, G.I., (1964) Disintegration of water drops in electric field, *Proc. Roy. Soc. Ser. A*, 280, 383-397

Tcholakova, S., Denkov, N.D., Lips, A., (2008) Comparison of Solid Particles, Globular Proteins and Surfactants as Emulsifiers, *Phys. Chem. Chem. Phys*., 10, 1608-1627

Testino, A., Buscaglia, M.T., Viviani, M., Buscaglia, V., Nanni, P., (2004) Synthesis of $BaTiO_3$ particles with tailored size by precipitation from aqueous solution, *Journal of American Ceramic Society*, 87, 1, 79-83

The Royal Society and The Royal Academy of Engineering, (2004) *Nanoscience and Nanotechnologies: opportunities and uncertainties*, Chapter 2, London, UK

Thies-Weesie, D.M.E., Philipse, A.P., Lekkerkerker, H.N.W., (1996) Sedimentation of Bidisperse, Uncharged Colloidal Sphere Suspensions: Influence of Viscosity and Irregular Surfaces, *J. of Colloid and Interface Sci*., 177, 427-438

Thwar, P.K., Linderman, J.J., Burns, M.A., (2007) Electrodeless direct current dielectrophoresis using reconfigurable field-shaping oil barriers, *Electrophoresis*, 28, 4572-4581

Traianidis, M., Courtois, C., Leriche, A., (2000) Mechanism of PZT crystallisation under hydrothermal conditions, Development of a new synthesis route, *J. European Ceram. Soc.*, 20, 2713-2720

Trisaksri, V., Wongwises, X., (2007) Critical Review of Heat Transfer Characteristics of Nanofluids, *Renewable & Sustainable Energy Reviews*, 11, 3, 512-523

Tripathy, S.S., Raichur, A.M., (2008) Dispersibility of barium titanate suspension in the presence of polyelectrolytes: A Review, *J. of Dispersion Science and Technology*, 29:230-239

Tseng, W.J., Chun-Nan Chen, (2006) Dispersion and rheology of nickel nanoparticle inks, *J. Mater. Sci*., 41, 1213-1219

Vafaei, S., Borca-Tascine, T., Podowski, M.Z., Purkayastha, A., Ramanath, G., Ajayan, P.M., (2006) Effect of nanoparticles on sessile droplet contact angle, *Nanotechnology*, 17, 2523-2527

Velev, O.D., Kaler, E.W., (1999) In situ assembly of colloidal particles into miniaturised biosensors, *Langmuir*, 15, 3693-2698

Vignati, E., Piazza, R., (2003) Pickering Emulsions: Interfacial Tension, Colloidal Layer Morphology and Trapped-Particle Motion, *Langmuir*, 19, 6650-6656

Villegas, M., Sirerra, T., Caballero, A.C., Fernandez, F., (2007) Ti-based nanocoatings on Al_2O_3 powders, *J. Ceramics International*, 33, 875-878

Vinothini, V., Singh, P., Balasubramanian, M., (2006) Synthesis of barium titanate nanopowder using polymetric precursor method, *Ceramics International*, 32, 99-103

Wang, J., Duan, H.L., Huang, Z.P., Karihaloo, B.L., (2006) A scaling law for properties of nano-structured materials, *Proc. R. Soc. A*., 462, 1355–1363

Watanabe, A., Higashitsuji, K., Nishizawa, K., (1978) Studies on electrocapillary emulsification, *Journal of Colloid and Interface Science*, 64, 2, 278-289

Wen, W., Huang, X., Sheng, P., (2008) Electrorheological fluids: structures and mechanisms, *Soft Matter*, 4, 200-210

Wen, W., Huang, X., Yang, S., Hu, K., Sheng, P., (2003) The giant electrorheological effect in suspensions of nanoparticles, *Nature Materials*, 2, 727-730

Whitby, C.P., Djerdjev, A.M., Beattie, J.K., Warr, G.G., (2006) Nanoparticle adsorption and stabilisation of surfactant-free emulsions, *Journal of Colloid and Interface Science*, 301, 342-345

Wilson, S.A., (1999) *Electric-field structuring of piezoelectric composite materials*, PhD Thesis, Cranfield University, Cranfield

Wilson, S.A., Libor, Z., Skordos, A.A., Zhang, Q., (2009) Enhanced DC conductivity of low volume-fraction nano-particulate suspensions in silicone and perfluorinated oils, *J. Phys. D: Appl. Phys*., 42, 062003

Xuan, Y., Li, Q., Zhang, X., Fujii, M., (2006) Stochastic thermal transport of nanoparticle suspensions, *J. Appl. Phys.*, 100, 043507

Yan, Y., Pal, R., Masliyah, J., (1991) Rheology of Oil in Water Emulsions with Added Solids, *Chemical Engineering Science*, 46, 985-994

Yang, J., Mei, S., Ferreira, J.M., (2001) Hydrothermal synthesis of nanosized titania powders: influence of tetraalkyl ammonium hydroxides on particle characteristics, *J. Am. Ceram. Soc*., 84(8), 1696-1702

Yi, W.D., Iwata, M., (1995) Analysis of an electro forced sedimentation of highly concentrated clay slurry in consolidation region, *Korean Journal of Chemical Engineering*, 12, 5, 576-581

Yin, W., Yates, M.Z., (2008) Effect of Interfacial Free Energy on the Formation of Polymer Microcapsules by Emulsification/Freeze Drying, *Langmuir*, 24, 701-708

Yu, H.G., Zoub, L., Deng, K., Wolf, R., Tadigadapa, S., Trolier-McKinstry, S., (2003) Lead zirconate titanate MEMS accelerometer using interdigitated electrodes, *Sensors and Actuators A*, 107, 26-35

Yu, W., Choi, S.U.S., (2003) The role of interfacial layers in the enhanced thermal conductivity of nanofluids: a renovated Maxwell model, *J. Nanopart. Res*., 5, 167–171

Zhang, H,T., Wu, G., Chen, X.H., Qiu, X.G., (2006) Synthesis and magnetic properties of nickel nanocrystals, *Materials Research Bulletin*, 41, 495-501

Zhang, M., Zhang, Q., Itoh, T., Abe, M., (1994) Ferrite plating on porous silica microspheres for ultrasonic contrast agents, *IEEE Trans. Magn*., 30, 4692

Zielinski, M., Samoc, M., (1977) An investigation of the Poole-Frenkel effect by the thermally stimulated current technique, *Journal of Physics D: Applied Physics*, 10 L105

Zoldesi, C.I., Imhof, A., (2005) Synthesis of Monodisperse Colloidal Spheres, Capsules, and Microballoons by Emulsion Templating, *Adv. Mater*., 17, 924-928

Appendices

Libor, Z. and Zhang, Q., The synthesis of nickel nanoparticles with controlled morphology and SiO_2/Ni core-shell structures, *Materials Chemistry and Physics*, 114, 2-3 (2009) 902-907

Wilson, S.A., **Libor, Z.**, Skordos, A.A. and Zhang, Q., Enhanced DC conductivity of low volume-fraction nano-particulate suspensions in silicone and perfluorinated oils, J. *Phys. D: Appl. Phys*. 42 (2009) 062003

Ansari, F., Grigoriev, P., **Libor, Z.**, Tothill, I.F. and Ramsden, J.J., DBT Degradation Enhancement by Decorating Rhodococcus erythropolis IGST8 with magnetic Fe_3O_4 nanoparticles, *Biotechnology and Bioengineering,* 102, 5 (2009) 1505-1512

Materials Chemistry and Physics 114 (2009) 902–907

Contents lists available at ScienceDirect

Materials Chemistry and Physics

journal homepage: www.elsevier.com/locate/matchemphys

The synthesis of nickel nanoparticles with controlled morphology and SiO_2/Ni core-shell structures

Z. Libor, Q. Zhang*

Department of Advanced Materials, Cranfield University, Cranfield, Bedfordshire MK43 0AL, UK

ARTICLE INFO

Article history:
Received 26 August 2008
Received in revised form 1 October 2008
Accepted 27 October 2008

Keywords:
Spherical nickel nanoparticles
Star-shape nickel
Flower shape nickel
Magnetic materials
Zetapotential
Core-shell structure
SiO_2/Ni composite

ABSTRACT

The magnetic nanopowders can be potentially applied in wide range of fields such as magnetic storage, magnetic fluid, medical diagnosis, conducting paints, rechargeable batteries, optoelectronics, magnetic recording media, drug delivery system and catalysis. They have attracted interest in the past decade and have also been studied extensively because of their size- and shape-dependent physical-chemical and magnetic properties for applications in various useful technologies. In this work, we present our experimental results on the preparation of nanosized Ni nanoparticles with different shapes by using a wet chemical solution route. Ni nanoparticles were prepared by reducing a Ni-complex formed between nickel-acetate and hydrazine solution under basic condition. Then through the control of reaction temperature and ageing time, nanosized Ni particles with different morphologies could be formed. The morphology and sizes of synthesized nanostructures were studied by scanning electron microscopy (SEM). Structural properties of nanoparticles were examined by X-ray diffraction. We also report the core-shell structures of micro-composites of silica-nickel (SiO_2/Ni). The composite core-shell structures were formed by the control of the surface charges of particles in aqueous solutions. A specific composite (SiO_2/Ni) can be produced by controlling the surface charge, the pH and the molar ratio of the components. Core-shell structures are stable at room temperature.

1. Introduction

Nanomaterials have attracted interest in the past decade and have been studied extensively because of their size- and shape-dependent physical-chemical and magnetic properties for applications in various useful technologies. In recent years, with growing interest in building advanced materials using nanoscale particles, there is a need for general approaches to controlling the size and shape of nanocrystals [1,2]. Nanoscale metal materials have attracted much attention owing to their promising potential in magnetic storage, magnetic fluid, medical diagnosis and catalysis. Small metal particle arrays have been used to build single-electron devices [2–4]. More attention has been attracted on nanoscale magnetic transition metal-based materials, including Ni, Co and Fe duo to their magnetic properties and application potential. For such crystallites, the physical and chemical properties depend sensitively on particle size and shape [2–11]. In the last few years, nickel nanomaterials with the following shapes have been synthesized: nanotubes, nanorods, hollow spheres, nanobelts, nanoprisms, and hexagonal flakes [2–6]. Magnetic nanoparticles are being widely used in rechargeable batteries [7], optoelectronics [8], chemical catalysts [9], conducting paints [10], magnetic recording media, ferro-fluids, magnetic resonance imaging contrast enhancement, drug delivery [11] and magnetic hyperthermia [12,13]. Several methods have been developed to synthesize particles with controlled size and shape. These methods include photolytic reduction [14], radiolytic reduction [15], sonochemical method [16], solvent extraction reduction [17], microemulsion technique [18], polyol process [19], and chemical route [20]. Chemical control over the size and shape of nanocrystals presents a challenge to this field. Li et al. [21] have reported the synthesis of pure black powder Ni through reduction of aqueous $NiSO_4$ with hydrazine. Ni et al. [22] have synthesized distinct flowery shapes of Ni nanocrystals using a hydrothermal chemical reduction containing a mixture of $Ni(N_2H_4)_3^{2+}$ and $Ni(dmg)_2$ (nickel dimethylglyoximate) as the nickel source. In this paper, we report our experimental results on the preparation of nanosized Ni nanoparticles with different shapes by using a modified version of the wet chemical solution route used by Li et al. [21]. Through the control of reaction temperature and ageing time, nanosized Ni particles with different morphologies were prepared. We also report a core-shell structure of SiO_2/Ni composite synthesized by an electrophoretic method.

* Corresponding author. Fax: +44 1234751346.
E-mail address: q.zhang@cranfield.ac.uk (Q. Zhang).

0254-0584/$ – see front matter © 2008 Elsevier B.V. All rights reserved.
doi:10.1016/j.matchemphys.2008.10.068

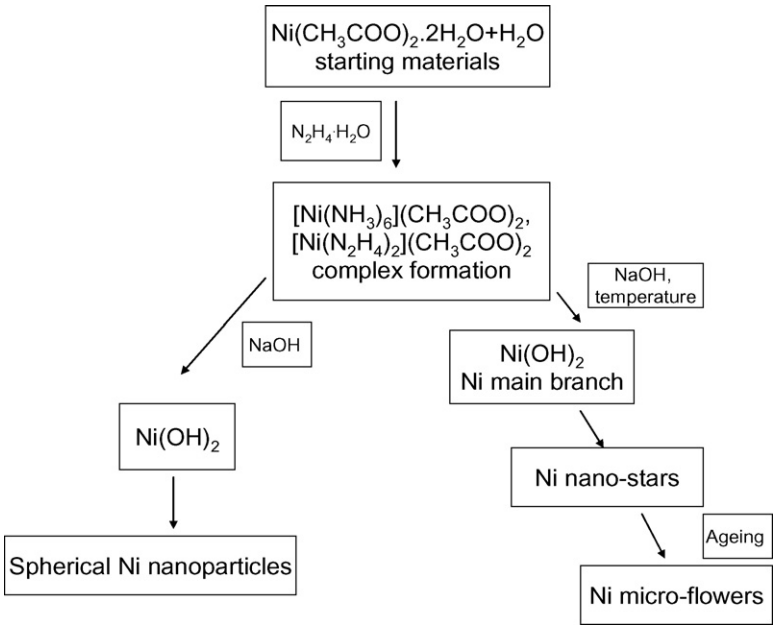

Fig. 1. Schematic illustration of the possible formation process of the spherical nickel nanoparticles and Ni nanostars- and microflower-structures.

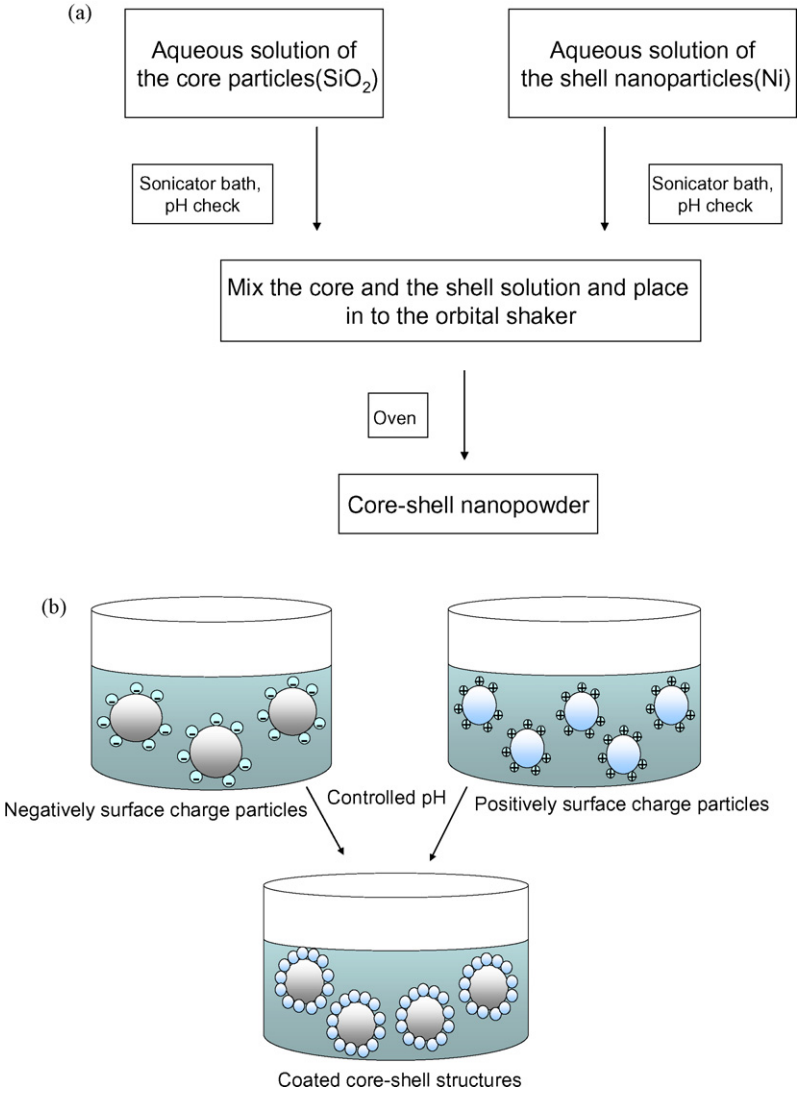

Fig. 2. (a) Synthesis route of core-shell particles; (b) schematic diagram of the formation of core-shell particles.

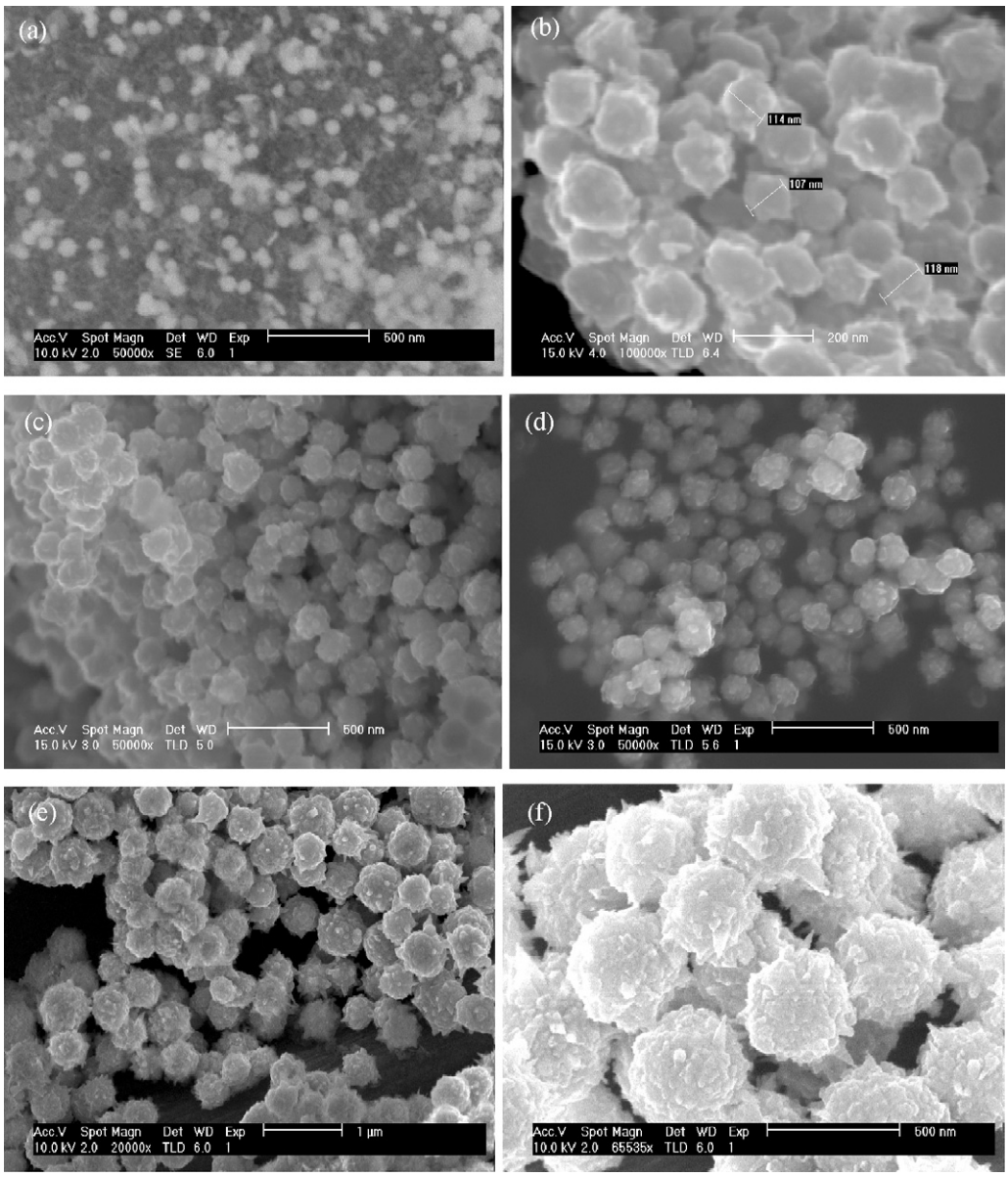

Fig. 3. SEM images of spherical nickel nanoparticles. (a) 80 nm, (b) 100 nm, (c) 120 nm, (d) 150 nm, (e) 300 nm, and (f) 400 nm.

2. Experimental procedure

Chemicals used in this paper are: tetra-ethyl ortho-silicate (TEOS), isopropanol, nitric acid (HNO_3), kerosene, sorbitan monooleate (Span 80), $Ni(CH_3COO)_2{\cdot}2H_2O$, $N_2H_4{\cdot}2H_2O$, HCl and NaOH. All the chemicals and solvents used in the synthesis of particles were purchased from Aldrich (UK) and used without further purification.

2.1. Preparation of spherical nickel nanoparticles, star-like nanoparticles and flower-like micro-particles

The current synthetic procedure is a modified version of the method developed by Choi et al. [20]. Fig. 1 shows a flow chart of the synthesis procedure of spherical nickel nanoparticles, nanostars and microflowers. In the synthesis, spherical nickel-metal nanoparticles were prepared by the thermal decomposition of Ni-hydrazine complexes and subsequent reduction of Ni ions. The following procedure describes the synthesis of nickel nanoparticles. First, nickel-acetate (0.1 mol) aqueous solution was heated to 50 °C and then hydrazine ($N_2H_4{\cdot}H_2O$, 0.25 mol) was added to the solution with vigorous stirring. The solution was then heated to 65 °C, which results in light violet precipitate. When the solution was cooled to 50 °C, an aqueous solution of sodium-hydroxide (0.3 mol) was added to it. To obtain the spherical nanoparticles, the solution was again heated to 55 °C and remained for 1 h. To obtain nanosize nickel stars, to the N-hydrazine complex added an aqueous solution of sodium-hydroxide (0.1 mol) and then the solution was heated to 70 °C and remained for 3 h. When the solution was aged for 24 h at 70 °C, the product was microsized nickel flower. The precipitated particles were retrieved by centrifugation. The yield of the overall synthesis was 60% based on the amount of Ni acetate. The formed black Ni precipitate was finally washed five times with distilled water and dried at 40 °C in oven overnight.

2.2. Preparation of hollow silica particles

The process is a combination of sol–gel process and water-in-oil (W/O) emulsion based on the work described in [23]. For the water phase: TEOS, H_2O, isopropanol and nitric acid (HNO_3) were mixed at the molar ratio of 1:4:3:0.01. The solution was vigorously stirred at 50 °C for 60 min. For the oil phase, kerosene and sorbitan monooleate were mixed at 3:1 molar ratio. The water phase and oil phase were then mixed in a Teflon beaker and stirred at 80 °C for 60 min. The obtained precipitates (SiO_2) were washed with acetone, isopropanol and water to remove any impurity and dried in vacuum oven at 100 °C for 10 h, and finally the powders were calcined at 700 °C for 8 h in a furnace.

2.3. Preparation of Ni coated SiO_2 particles

The principle of synthesis for core-shell structure used in this study is based on the electrostatic attraction between particles having opposite surface charges. The surface charge of particles in solution can be determined by the measurement of

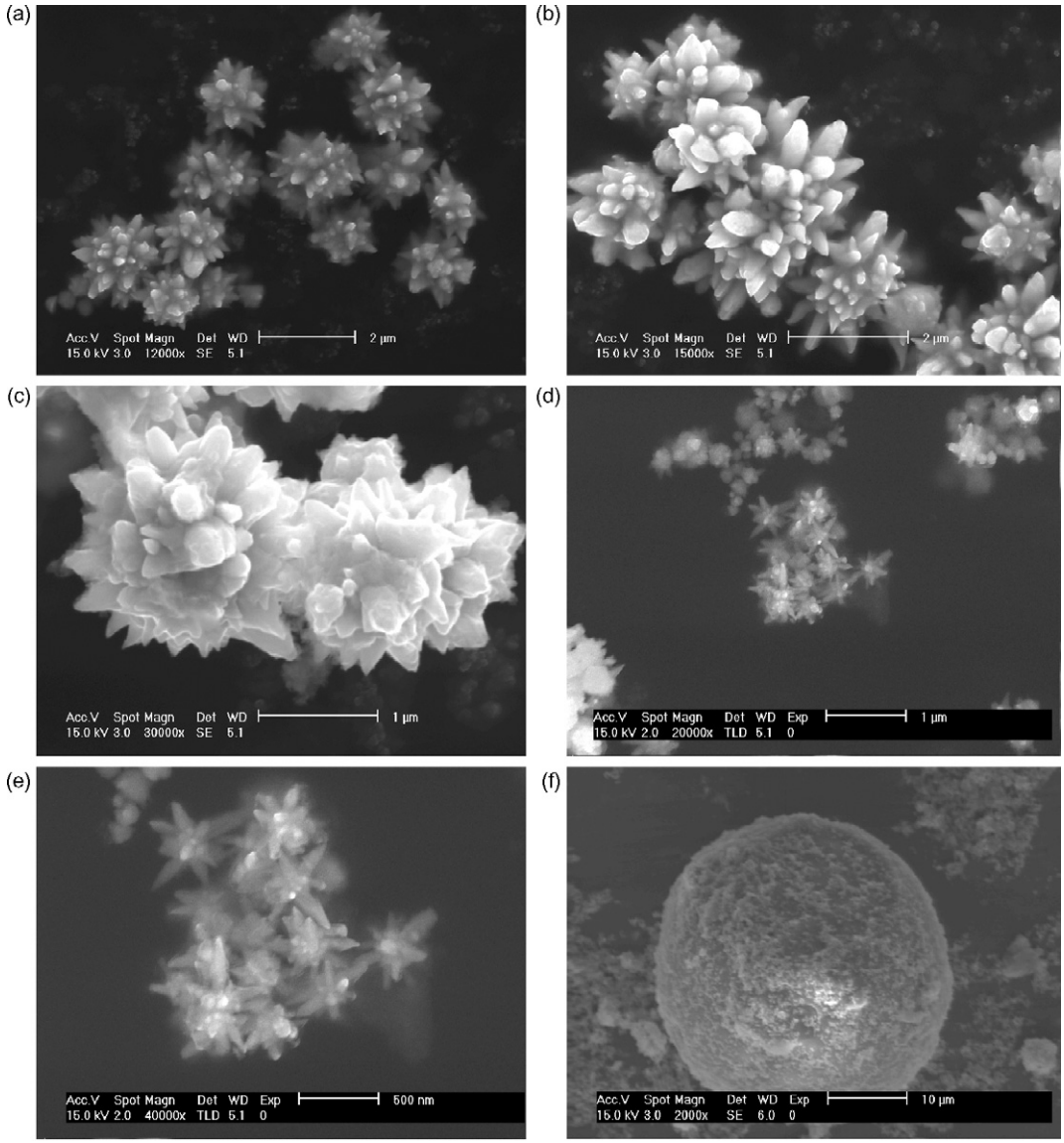

Fig. 4. SEM images of microflower of nickel (a–c) and nanostars of nickel (d and e) and SEM of a single SiO_2 particle coated with nickel particles (f).

zeta potential. Because the zeta potential of the particles is a function of pH value of the solution, it is possible to control the sign of the zeta potential by adjusting the pH of the solution through adding either HCl or NaOH. Fig. 2a shows a flow chart of the synthesis procedure of core-shell structures. SiO_2 core and Ni shell particles were suspended in deionised water, respectively, in a volumetric flask and the particle concentration of SiO_2 core particles in solution was 0.1 g L^{-1} and the particle concentration of Ni varies depending on the requirement of coating thickness. Higher Ni concentration leads to thicker coated layer. The SiO_2 and Ni suspensions were then placed in an ultrasonic bath for 30 min. At this stage, HCl or NaOH was added to the SiO_2 and Ni suspensions to adjust the pH value. Based on the results of zeta potential measurements of particle colloids in water, core and shell particles would produce opposite surface charges at the certain pH regions. The core and shell particle colloids with such pH values were then mixed and placed to the orbital shaker for 30 min. The electrostatic force on the surfaces of the core and shell particles would make the attraction of different charged particles to each other and thus form a core-shell structure (Fig. 2b). The core-shell particles were then dried in the oven at 40 °C overnight.

2.4. Characterization

Scanning electron microscopy (S-FEG SEM) was performed on a Philips XL30. X-ray diffraction studies used a standard XRD θ-2θ measurement in the range $2\theta = 20$–60° on a Siemens D5005 diffractometer with Cu Kα radiation and a Goebel mirror. The crystallite size is determined from the X-ray line broadening using Scherrer formula given by $D = 0.9\lambda/\beta\cos\theta$, where D is the average crystallite size, λ is the X-ray wavelength used (1.5406 Å), β is the angular line width of half maximum intensity and θ is the Bragg's angle in degree. The pH values of particles in water were measured using a Jenway 3540 pH meter. Electrophoresis measurements were performed using a Malvern Zetasizer 3000.

3. Results and discussion

A schematic illustration of the formation mechanism of Ni nanostructures is shown in Fig. 1. Ni-complex such as $[Ni(NH_3)_6](CH_3COO)_2$ or $[Ni(N_2H_4)_3](CH_3COO)_2$ is decomposed by NaOH forming $Ni(OH)_2$. Subsequently the Ni^{2+} ion was reduced to nickel nanoparticles.

Previous publications [22,24,25] on the synthesis of nickel nanocrystals by hydrothermal reduction from different complexes described the possible mechanisms of formation of the nickel nanoflowers. For example, Ni et al. [22] used two complexes, $Ni(N_2H_4)_3^{2+}$ and $Ni(dmg)_2$ as the nickel source in hydrothermal synthesis and they think that the reaction process involves two steps: firstly, $Ni(N_2H_4)_3^{2+}$ is reduced, and the resulting spherical nanocrystals serve as the flower centers. Then $Ni(dmg)_2$ yields swordlike nanocrystals which grow radially on the existing spheri-

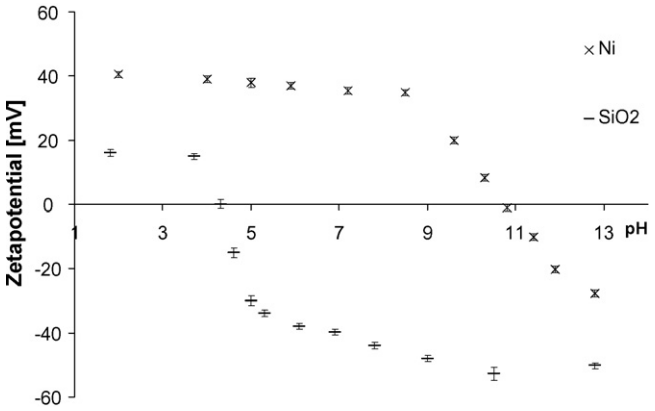

Fig. 5. Zetapotentials of SiO_2 and Ni particles in water as function of pH. Adjustment of the pH was carried out by adding standard HCl and NH_4OH solutions.

cal centers as petals [22]. In our case, a chemical solution synthesis method is used. The formation mechanism of the nickel nanocrystals is possibly similar to the ones described in [6,21]: hydrazine reacts with nickel ions in aqueous media to form hydrazine complex [26,27].

$$Ni^{2+} + 3N_2H_4 \leftrightarrow [Ni(N_2H_4)_3]^{2+} \quad (1)$$

Then $[Ni(N_2H_4)_3]^{2+}$ reacts with OH^- in alkali system as following:

$$2[Ni(N_2H_4)_3]^{2+} + 4OH^- \rightarrow 2Ni\downarrow + N_2 + 4H_2O + 5N_2H_4 \quad (2)$$

Hydrazine is a powerful reducing agent. Temperature and time of the reaction influence the products. Between 50 and 70 °C and under the basic condition, the reaction (2) proceeds fast and leads to spherical Ni particles. If the temperature of the reaction (2) is higher (70–85 °C), crystals grow fast on the spherical Ni particles. Therefore, star-like Ni particles would yield. The pH value of the solution also influences the products. At 50–70 °C, NaOH is necessary for the formation of pure spherical powder of metal nickel. If temperature rises to 85–95 °C, Na_2CO_3 can be used to obtain pure powder of metal nickel. pH value in both NaOH and Na_2CO_3 situations should be adjusted to 10–12 in order to keep the reaction speed and products under control.

The low concentration of NaOH solution (≤0.1 mol) and the high reaction temperature (≥70 °C) can generate nanosize star-like Ni particles and longer reaction time (aging time 24 h) can lead to the formation of flower-like nickel crystal with microsize. $Ni(N_2H_4)_3{}^{2+}$ was first reduced and yielded spherical nickel particles, which were dispersed in the system. The newly formed Ni nanoparticles serve as seed sites for the further reduction of $Ni(N_2H_4)_3{}^{2+}$ and crystal growth as the reaction proceeds at high temperature.

It is reasonable to think that the concentration of Ni^{2+}-ion in solution changes and the Ni nuclei sites gradually increase with the reaction proceeding, which result in the formation of Ni irregular nanoparticles when ageing. Ni^{2+}-ion concentration in the solution with high pH (≥13) supports the crystals growth along a certain direction until all the Ni^{2+}-ions are consumed. Therefore to control the shape of Ni particles, it is important to monitor the pH. The other factors that need to be considered are the temperature of the solution and the ageing time.

At higher temperature (>85 °C) and shorter time it will produce nanoparticles. Because, at higher temperature, Ni^{2+}-ions move faster, which makes the crystal growth slower and therefore it needs longer time to age the solution in order to obtain star or flower shape crystals.

The morphology of the samples was investigated by field emission scanning electron microscopy (FE-SEM). Fig. 3 shows the SEM images of spherical shape Ni nanoparticles (Fig. 3a–f) with the average size between 80 and 400 nm. Ni particles are spherical (Fig. 3a–f) while particles are more or less flower shape in Fig. 4a–c and stars shape in Fig. 4d and e. All the particles showed a narrow particle size distribution. Due to the large surface to volume ratio and strong magnetic attraction forces, the Ni nanoparticles tend to agglomerate in order to minimize the total surface energy of the system. The produced nanoparticles are spherical with the size between 80 and 400 nm depending on the molar ratio of $Ni(CH_3COO)_2/N_2H_4$ between 0.4 and 0.07.

Fig. 4f shows the SEM images of SiO_2 particles coated with nickel nanoparticles (the average size of SiO_2 particles is about 15 μm and the average size of nickel nanoparticles 100 nm). The SiO_2 particles remain spherical after they were coated with Ni. The thickness of the shell can be controlled through the mediation of the ratio of core and shell particles and the reaction time.

Fig. 5 shows the zeta potential values of the SiO_2 and Ni particles in water as a function of pH. Zeta potential measurement gives the information about the overall surface charge of the particles and how this is affected by the changes in the environment (e.g. pH). The measured colloid suspensions were prepared without adding any surfactant. The results of the electrophoresis measurements revealed that the zeta potentials of core (SiO_2) and shell (Ni) particles in their solution have opposite signs at $4.3 < pH < 10.7$. The zeta potential for SiO_2 particles was between 0 and −50 mV while the zeta potential of Ni particles was between +40 and 0 mV. This

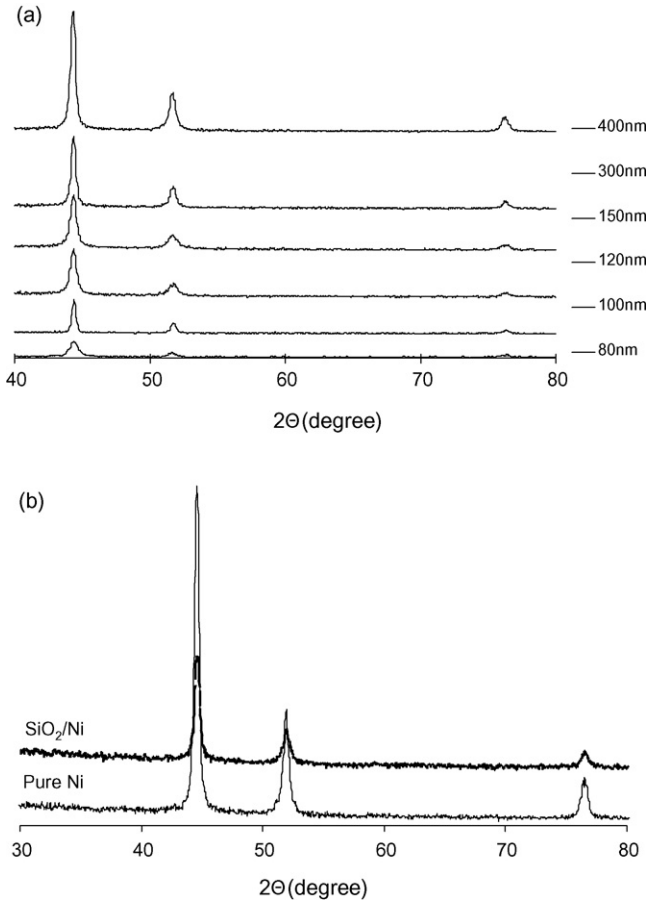

Fig. 6. X-ray powder diffraction patterns of spherical Ni nanoparticles (a) and SiO_2/Ni core-shell composite at room temperature (b).

allowed for the easy attachment of the nickel nanoparticles on the surface of SiO_2 particles in this pH region.

Fig. 6a shows the XRD patterns of spherical Ni nanoparticles with size between 80 and 400 nm and Fig. 6b shows the XRD patterns of the core/shell SiO_2/Ni. Three characteristic peaks for nickel ($2\theta = 44.5^\circ$, 51.8°, and 76.4°), corresponding to Miller indices (1 1 1), (2 0 0), and (2 2 2), were observed. The intensity of these peaks increases with the increase of Ni nanoparticles size. The appearance of those peaks reveal that the resultant particles are pure face-centred cubic (fcc) nickel at these samples (JCPDS, No. 04-0850). The XRD patterns revealed only nickel. The calculated size values for all Ni samples by Scherrer formula [28] at 2θ of 44.5° are general approximates to those of SEM observation (Figs. 3 and 6).

4. Conclusions

Spherical Ni nanoparticles, star-shaped Ni nanocrystals and flower-shaped Ni micro-particles were successfully prepared by using a wet chemical solution method. All these products were synthesised by reduction of the complex of $[Ni(N_2H_4)_3]^{2+}$ in alkaline solution with hydrazine hydrate. The present work realized the control of the crystal shape through controlling various Ni-ions reduction reaction parameters to adjust the crystal nucleation and growth processes. Also, through adjusting the solution pH values of core and shell particles, Ni nanoparticles were successfully coated onto the SiO_2 particles in an aqueous solution forming core-shell nanostructure. The resultant nickel nanoparticles, nanostar and microflower and the core-shell particles have been confirmed by XRD, SEM analysis.

References

[1] C.M. Lieber, Solid State Commun. 107 (1998) 607.
[2] V.F. Puntes, K.M. Krishnan, A.P. Alivisatos, Science 291 (2001) 2115.
[3] Y. Hou, S. Gao, J. Mater. Chem. 13 (2003) 1510.
[4] S. Sun, C.B. Murray, D. Weller, L. Folks, A. Moser, Science 287 (2000) 1989.
[5] C.C. Chen, A.B. Herhold, C.S. Johnson, A.P. Alivisatos, Science 276 (1997) 398.
[6] Z. Liu, S. Li, Y. Yang, S. Peng, Z. Hu, Y. Qian, Adv. Mater. 22 (2003 1946).
[7] E. Antolini, M. Ferretti, S. Gemme, J. Mater. Sci. 31 (1996) 2187.
[8] L.L. Beecroft, C.K. Ober, Chem. Mater. 9 (1997) 1302.
[9] L.N. Lewis, Chem. Rev. 93 (1993) 2693.
[10] H. Eisazadeh, G. Spinks, G.G. Wallace, Mater. Forum 17 (3) (1993) 241.
[11] H.T. Zhang, G. Wu, X.H. Chen, X.G. Qiu, Mater. Res. Bull. 41 (2006) 495.
[12] M. Bettge, J. Chatterjee, Y. Haik, BioMagn. Res. Technol. 2 (2004) 4.
[13] K. Okawa, M. Sekine, M. Maeda, M. Tada, M. Abe, N. Matsushita, K. Nishio, H. Handa, J. Appl. Phys. 99 (2006), 08H102.
[14] S. Remita, M. Mostafavi, M.O. Delcourt, Radiat. Phys. Chem. 47 (1996) 275.
[15] J.H. Hodak, A. Henglein, M. Giersig, G.V. Hartland, J. Phys. Chem. B 104 (2000) 11708.
[16] Y. Mizukoshi, K. Okitsu, Y. Maeda, T.A. Yamamoto, R. Oshima, Y. Nagata, J. Phys. Chem. B 101 (1997) 7033.
[17] M. Brust, M. Walker, D. Bethell, D.J. Schiffrin, R. Whyman, J. Chem. Soc., Chem. Commun. 7 (1994) 801.
[18] D.H. Chen, S.H. Wu, Chem. Mater. 12 (2000) 1354.
[19] L.K. Kurihara, G.M. Chow, P.E. Schoen, Nanostruct. Mater. 5 (1995) 607.
[20] J.Y. Choi, K.Y. Lee, B.K. Kim, J.M. Kim, J. Am. Ceram. Soc. 88 (11) (2005) 3020.
[21] Y.D. Li, C.W. Li, H.R. Wang, L.Q. Li, Y.T. Qian, Mater. Chem. Phys. 59 (1999) 88.
[22] X. Ni, Q. Zhao, H. Zheng, B. Li, J. Song, D. Zhang, X. Zhang, Eur. J. Inorg. Chem. 23 (2005) 4788.
[23] W. Li, X. Sha, W. Dong, Z. Wang, Chem. Commun. (2002) 2434.
[24] X.M. Liu, S.Y. Fu, J. Cryst. Growth 9 (2007) 428.
[25] Z.A. Peng, X.G. Peng, J. Am. Chem. Soc. 123 (2001) 1389.
[26] H. Tominaga, S. Ito, M. Yoshihara, J. ShiiokawaShikizai Kyokaishi 64 (6) (1991) 373 (in Japanese).
[27] R.S. Sapieszko, E. Matijevic, Corrosion 36 (10) (1980) 204.
[28] S.C. Chanda, A. Manna, V. Vijayan, P.K. Nayak, M. Ashok, H.N. Acharya, Mater. Lett. 61 (28) (2007) 5059.

IOP PUBLISHING
IOP FTC
JOURNAL OF PHYSICS D: APPLIED PHYSICS
J. Phys. D: Appl. Phys. **42** (2009) 062003 (5pp)
doi:10.1088/0022-3727/42/6/062003

FAST TRACK COMMUNICATION

Enhanced dc conductivity of low volume-fraction nano-particulate suspensions in silicone and perfluorinated oils

S A Wilson[1], **Z Libor, A A Skordos and Q Zhang**

Materials Department, Cranfield University, Bedfordshire, MK43 0AL, UK

E-mail: s.a.wilson@cranfield.ac.uk

Received 5 January 2009, in final form 11 February 2009
Published 3 March 2009
Online at stacks.iop.org/JPhysD/42/062003

Abstract
The dc conductivities of several different types of nanoparticles (nickel, barium titanate and magnetite) suspended in both silicone and perfluorinated oils have been measured and contrasted. Enhanced dc conductivity through interaction between the particles and the fluid has been demonstrated, even at quite moderate fields, and different types of nanoparticles have been shown to exhibit different behavioural trends. Whilst the dc enhancement is partly related to the concentration (or spatial arrangement) of the particles as expected, there is clear evidence that energy-activated (electric field activated) processes also play a major role. It can be said that effective-medium theories based solely on the electrical properties and volume fractions of the component materials have limited applicability when assessing the dc conductivities of these nanoparticle–fluid combinations at low volume fractions.

1. Introduction

Nano-particulate suspensions or 'nanofluids' illustrate a classical conundrum whereby the continuum properties are often readily measurable (in terms of the across and through variables) and hence macroscopic behaviour can be modelled adequately for engineering purposes, but afterwards there remains a doubt that part of the story remains untold and a real technological breakthrough is only one step away. Researchers have sometimes found that very small volume fractions of nanoparticles suspended in a carrier fluid can produce quite remarkable increases in macroscopic properties, such as thermal conductivity. This cannot be easily dismissed. If these improvements could be stabilized at the higher end of expectations then the technological benefits could indeed be huge. However, when the experiments are repeated under ostensibly the same conditions, the results can sometimes be less encouraging than previously observed. One explanation could be that nanofluids are inherently unstable. Generally speaking, nanoparticles tend to cluster and agglomerate if they are not prevented from doing so. This leads to uncertainties in the effective particle size, particle shape, particle numbers and inter-particle spacing. For thermo-fluids, it is easy to conceive that synergies existing between the particles and the carrier fluid can be overshadowed when particle agglomeration occurs; causing the system to change its characteristics and, in effect, reverting to one with fewer, larger particles. In this scenario the macroscopic fluid properties can be described broadly by effective-medium theories [1–5]. However, this does not mean that synergistic effects between the particles and fluid do not exist, rather that they may be length-scale sensitive and they can become obscured by randomization. For the case of fluids that exhibit the giant electro-rheological effect, mathematical models based only on the volume fractions and the physical properties of the individual phases do not

[1] Author to whom any correspondence should be addressed.

Table 1. Physical quantities of the nanoparticles (nickel—Ni, barium titanate—BT and magnetite—FO) and two base fluids.

	Mean particle diameter (nm)	Bulk density ($kg\,m^{-3}$)	Particle number density (m^{-3})	Inter-particle spacing (notional) (nm) at volume fraction (%)				
				0.05	0.1	0.2	0.4	0.6
Ni	90	8800	2.62×10^{21}	824	635	486	367	309
BT	130	5850	8.69×10^{20}	1190	918	702	530	447
FO	10	5240	1.91×10^{24}	92	71	54	41	34
Manufacturer's data	Viscosity (mPas)	Relative permittivity	Specific gravity	Conductivity at $1\,kV\,m^{-1}$ ($S\,m^{-1}$)				
200/50cS silicone oil	50	2.60	0.973	10×10^{-12}				
3M™ Fluorinert FC70	14	1.98	1.940	10×10^{-12}				

adequately describe the overall behaviour [6–9]. Here the free energy of the system has an electrical component, due to the applied electric field, that dominates over the randomizing effects of thermal motion and there is a true synergistic effect. However, the physical explanation for this is not complete and the influence of the imaginary component of the dielectric permittivity is at present unclear. In the following study we demonstrate that the dc electrical conductivity of low volume-fraction nano-particulate suspensions in silicone and perfluorinated oils is enhanced even at very moderate electric field strengths and this effect is related intrinsically to the fluid-particle combinations. The experiments are designed to reveal trends by comparison and the findings do not rely on knowledge of the nanoparticles electrical properties.

2. Experimental procedure

The dc electrical conductivities of six different nanofluid systems (representing combinations of three different nano-particle types and two different carrier fluids) were measured experimentally. The nanoparticles were an electrical conductor (nickel—Ni), an electro-active ceramic (barium titanate—BT) and iron oxide (magnetite—which is one part wüstite FeO and one part haematite Fe_2O_3—FO). All of these were synthesized in our laboratory, BT by hydrothermal synthesis, Ni and FO by wet chemical synthesis [10]. In all cases a narrow particle size distribution was achieved. The base fluids were silicone oil (Dow Corning 200/50cS) and a perfluorinated oil (3M™ Fluorinert FC70) which have almost the same electrical conductivity and similar relative permittivity, but which differ both in viscosity and specific gravity. Physical quantities for the fluids are listed in table 1. Figures given in table 1 for the nanoparticles are based on the mean particle size, which is the only measured quantity (derived from SEM image analysis). Hence the inter-particle spacing of particles is a notional figure. It assumes a perfect dispersion in the fluid and it is provided only as an aid to visualization of the scale of inter-particle spacing at different volume fractions. Note that the chosen range is from around 9 to 3.5 particle diameters. Theory suggests that the inter-particle distances in these suspensions may be too large for multi-polar interactions to dominate the electrical behaviour [11]. However, in a practical context it is assumed that this may be a factor.

Particles were dispersed in an ultrasonic bath for 30 min. The concentration sets were 2, 4, 10, 20 and $30\,g\,l^{-1}$. The systematic weighing error in all cases was <0.001%. Volume fractions are calculated for each suspension using the bulk densities of the materials. Dc current measurements were carried out using a Keithley 6517 electrometer for different applied voltages between 20 and 100 V. The fluidic conductivity cell consisted of a 1 mm gap between concentric copper electrodes and the effective electrode area was $21.88\,cm^2$. The systematic error due to the measurement system was 0.05% at 20 V and 0.01% at 100 V. The current versus time profile showed a transient peak, due to capacitance, between 1 and 2 s after the application of the voltage. Readings were therefore taken after 20 s representing the steady-state values. Measurements were carried out at 295 K and the cell was dried scrupulously in nitrogen between measurements to exclude moisture. All of the experiments were subsequently duplicated in order to confirm that the measurements represented a true record of systematic behaviour.

3. Results and discussion

Figure 1 shows dc conductivities for the six different nanoparticle-fluid combinations measured for different particle loadings and under moderate electric field conditions. When considering the results it is useful to take the following correlations into account: (i) The barium titanate particles and the iron oxide particles have quite similar bulk densities, but their sizes are very different and their effective electrical conductivities at the nano-scale are uncertain; (ii) the nickel particles and the barium titanate particles have very similar masses (BT larger particles, Ni higher density), but the materials have very different electrical properties (high dielectric permittivities, but contrasting electrical conductivities); (iii) the iron oxide and the nickel particles both have some magnetic character, but they are very different in size and mass; (iv) the two fluids have almost the same (very low) electrical conductivity; (v) the viscosity of the silicone oil is higher than that of the FC70 and its specific gravity is around half; (vi) the dielectric permittivity of the

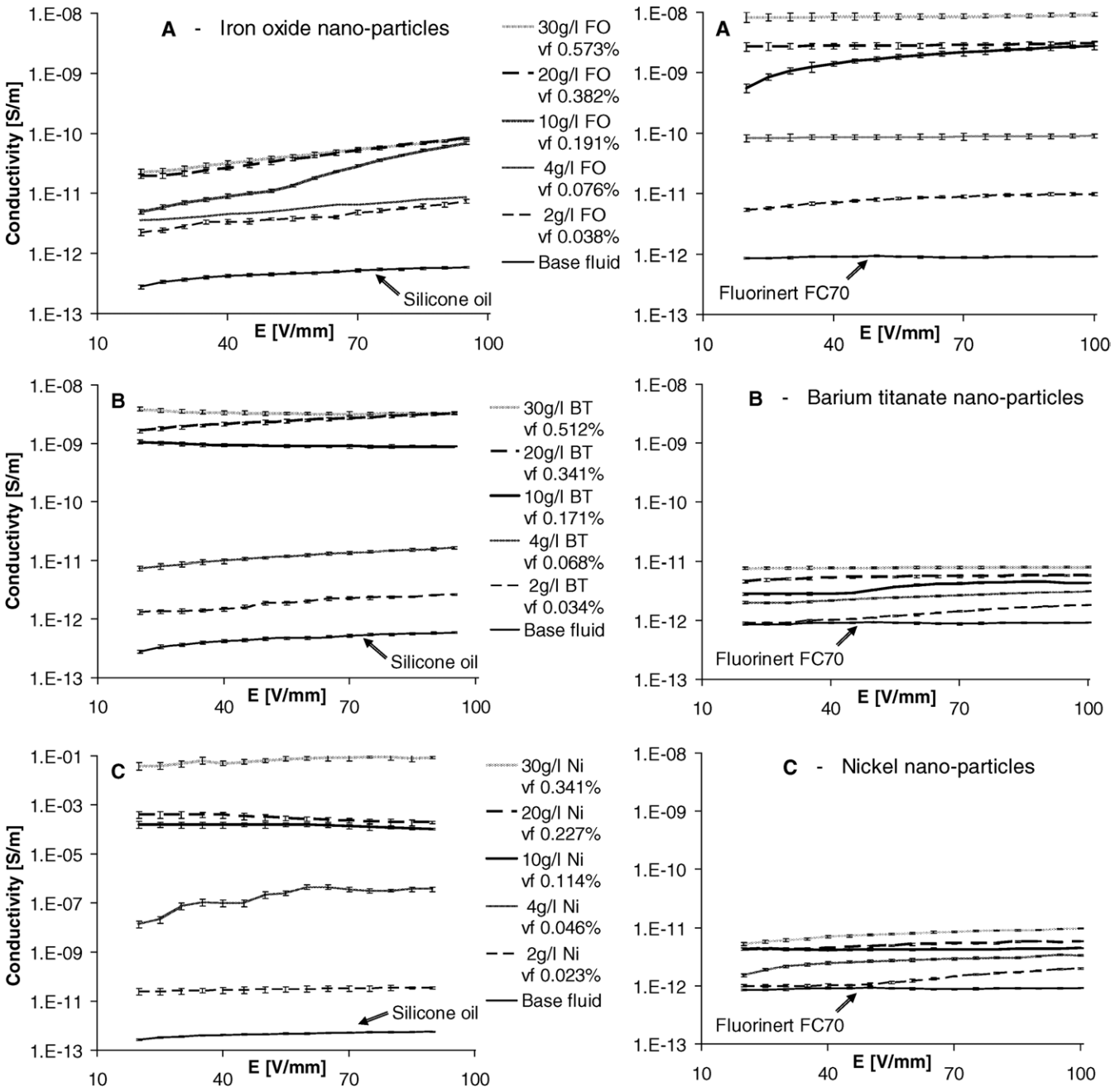

Figure 1. Dc conductivities of three types of nanoparticles in two different insulating fluids: silicone oil (left side) and 3M™ Fluorinert FC70 (right side). Row A—10 nm diameter iron oxide nanoparticles (FO); Row B—130 nm diameter barium titanate nanoparticles (BT); Row C—90 nm diameter nickel nanoparticles (Ni).

silicone oil is a little higher than that of the Fluorinert FC70; for particles of the same type, the effect this has on the real part of the complex Clausius–Mossotti value is therefore estimated in the ratio of ∼11 : 10 [1, 12]. By consideration of the applied electric field threshold for particle agglomeration [13] and using the 'non-equilibrium phase diagram of structures' approach adopted by Melrose [14], it can be said that, in all cases, the inter-particle forces due to polarization are estimated by calculation to be much too small for any polarization-induced aggregation of particles to occur.

In figure 1 (top row) it can be seen that the silicone oil base fluid has some field-dependent character over the observed range, shown as an increase in measured conductivity as the applied voltage is increased; but this is not the only effect observed. The conductivity of iron oxide particles in FC70 is higher than it is in the silicone oil. There is evidence of field-induced behaviour in silicone oil at all concentrations and particularly at $10\,\mathrm{g\,l^{-1}}$. At $10\,\mathrm{g\,l^{-1}}$ in FC70 an increase is also observed and this occurs at a lower applied field; repeated experiments have confirmed that this is a consistent occurrence. More detailed analysis shows that the observed increases follow the relationship: $\ln J \propto \sqrt{E}$ (where J is the current density and E the applied electric field) characteristic of energy-activated, Poole–Frenkel type behaviour [15, 16].

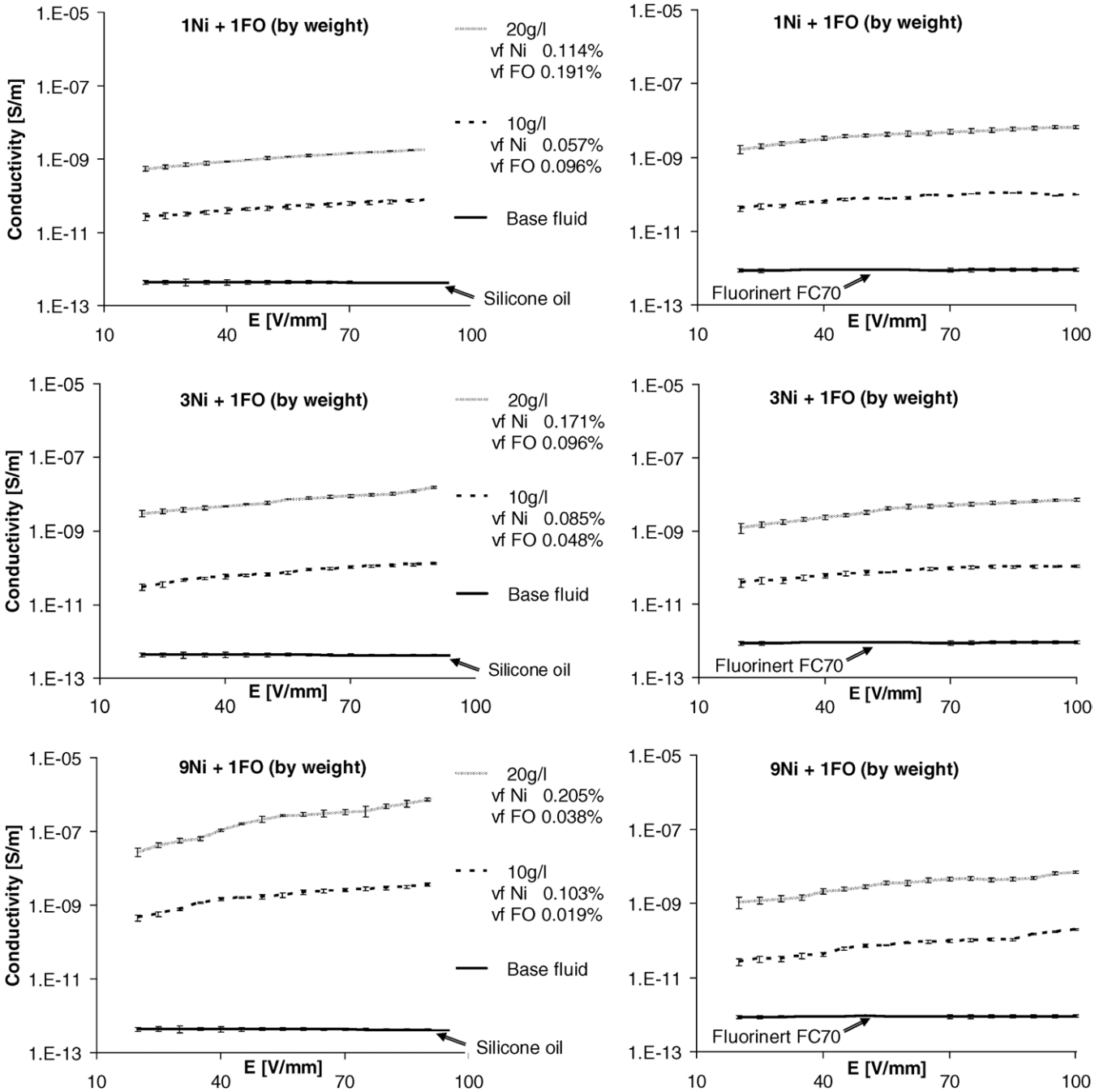

Figure 2. Dc conductivities of suspensions containing both nickel (90 nm diameter) and iron oxide (10 nm diameter) nanoparticles: silicone oil (left side) and 3M™ Fluorinert FC70 (right side). The particle combinations are nickel : iron oxide—top row in the ratio 1 : 1 by weight, middle row 3 : 1 by weight, bottom row 9 : 1 by weight.

The barium titanate suspensions, in contrast, exhibit an opposite tendency; they have higher conductivities in silicone oil than in FC70. In FC70 both nickel and barium titanate show very modest increases with increasing particle concentration. Note that $20\,\mathrm{g\,l^{-1}}$ BT and $30\,\mathrm{g\,l^{-1}}$ Ni have similar volume fractions of particles. Some small increases are observable at low concentrations for both materials; however, the overall flat response would suggest that there is no significant Hall-effect contribution, although this may have been expected.

The dc conductivity of the nickel nanoparticles in silicone oil shows an exceptionally high increase even at very low volume fractions (∼0.05%). Note that the peak conductivity measured here is more than six orders of magnitude greater than for the iron oxide and barium titanate suspensions. When this nanoparticle-fluid combination was repeated the trends remained the same; however, the measured values are not consistent. Under the same experimental conditions the dc conductivity value at $30\,\mathrm{g\,l^{-1}}$ nickel in silicone oil has also been measured at $1 \times 10^{-4}\,\mathrm{S\,m^{-1}}$ ($20\,\mathrm{g\,l^{-1}}$, $8 \times 10^{-6}\,\mathrm{S\,m^{-1}}$, $10\,\mathrm{g\,l^{-1}}$, $8 \times 10^{-8}\,\mathrm{S\,m^{-1}}$). This range of variability is not present in any of the other particle–fluid combinations; the nickel-FC70 combination provides consistent repeatable values at all concentrations. Given the experimental conditions it is concluded that the observed instability is a consequence of a

difference in the spatial distribution of the particles. It is known that particle chains are able to grow from asperities [17–19] with concomitant changes to the local electric field distribution. Electrohydrodynamic forces also pertain [20–22].

In figure 2 the dc conductivities of suspensions containing both nickel nanoparticles and iron oxide nanoparticles are shown over a range of volume fractions. The main features to note are that in silicone oil the measurements correspond to what might be expected from particle mixtures given the earlier results, with the nickel particles assuming a dominant role. In FC70, however, the findings are more surprising, in that the dc conductivity of the suspension varies very little when the proportions of nickel and iron oxide are varied over quite a wide range. For all combinations some field-activated character has been introduced that was absent in the single particle-type suspensions. Conductivities are higher than could be expected from either particle-type acting alone and overall behaviour is, therefore, dependent on the particle–fluid interaction. Note that both types of particle have some magnetic character which may promote a Hall effect contribution.

4. Conclusion

Effective-medium theories based solely on the electrical properties and volume fractions of the component materials have limited applicability when assessing the dc conductivity of the above nanoparticle-fluid combinations at low volume fractions. Enhanced dc conductivity through interaction between the particles and the fluid has been demonstrated even at quite moderate fields and different types of nanoparticles have been shown to exhibit different behavioural trends. Whilst the dc enhancement is partly related to the spatial arrangement of the particles as expected, there is clear evidence that energy-activated (electric field activated) processes also play a major role. The dc conductivity of a perfluorinated oil, 3M™ Fluorinert FC70, is increased in the presence of 10 nm diameter iron oxide nanoparticles. Combinations of different species of nanoparticles appear to influence percolation, sometimes enhancing and sometimes moderating the observed systems' behaviour. Synergies clearly do exist between nanoparticles and carrier fluids that can have a major influence on their systems' properties, hence they may be exploitable in the future development of engineering nanofluids.

Acknowledgment

Zsuzsanna Libor would like to acknowledge the financial support of the UK Engineering and Physical Sciences Research Council (EPSRC) under Platform Grant No EP/D506638/1 Nanoscale Multifunctional Ferroic Materials and Devices

References

[1] Felderhof B U 1982 *J. Phys. C: Solid State Phys.* **15** 3953
[2] Wilson S A, Maistros G M and Whatmore R W 2005 *J. Phys. D: Appl. Phys.* **38** 175
[3] Keblinski P, Prasher R and Eapen J 2008 *J. Nanoparticle Res.* **10** 1089
[4] Starke T K H, Johnson C, Hill S, Dobson P and Grant P S 2006 *J. Phys. D: Appl. Phys.* **39** 1305
[5] Tomer V and Randall C A 2008 *J. Appl. Phys.* **104** 074106
[6] Wen W, Huang X and Sheng P 2008 *Soft Matter* **4** 200
[7] Wen W, Huang X, Yang S, Lu K and Sheng P 2003 *Nature Mater.* **2** 727
[8] Gong X, Wu J, Huang X, Wen W and Sheng P 2008 *Nanotechnology* **19** 165602
[9] Wang B-X, Zhao Y and Zhao X-P 2007 *Colloids Surf.* A **295** 27
[10] Libor Z and Zhang Q 2009 *Mater. Chem. Phys.* **114** 902
[11] Jones T B 1985 *IEEE Trans. Indust. Appl.* **1A-21** 930
[12] Pethig R, Huang Y, Wang X-B and Burt J P H 1992 *J. Phys. D: Appl. Phys.* **25** 881
[13] Tao R 1993 *Phys. Rev.* E **47** 423
[14] Melrose J R 1992 *Mol. Phys.* **76** 635
[15] Zielinski M and Samoc M 1977 *J. Phys. D: Appl. Phys.* **10** L105
[16] Ongaro R and Pillonnet A 1991 *IEE Proc.* A **138** 127–37
[17] Rattray P 1994 *PhD Thesis* Cranfield University, UK
[18] Green N G and Jones T B 2007 *J. Phys. D: Appl. Phys.* **40** 78
[19] Capria E and Wilson S A 2006 *Proc. ICPADM 2006 8th Int. Conf. on Properties and Applications of Dielectric Materials (IEEE, 26–30 June 2006)* vol 1–2, p 865
[20] Pohl H 1978 *Dielectrophoresis* (Cambridge: Cambridge University Press)
[21] Landau L D and Lifshitz E M 1984 *Electrodynamics of Continuous Media* 2nd edn (New York: Pergamon)
[22] Ramos A, Morgan H, Green N G and Castellanos A 1998 *J. Phys. D: Appl. Phys.* **31** 2338

ARTICLE

BIOTECHNOLOGY and BIOENGINEERING

DBT Degradation Enhancement by Decorating *Rhodococcus erythropolis* IGST8 With Magnetic Fe_3O_4 Nanoparticles

F. Ansari,[1] P. Grigoriev,[2] S. Libor,[1] I.E. Tothill,[3] J.J. Ramsden[1]

[1]Microsystems & Nanotechnology Centre, Cranfield University, Bedfordshire MK43 0AL, UK; telephone: 44-1234-750111 ext 2465; fax: 44-751346; e-mail: f.ansari@cranfield.ac.uk

[2]Institute of Cell Biophysics, Russian Academy of Science, Pushchino, Moscow Region, Russia

[3]Cranfield Health, Cranfield University, Bedfordshire, UK

Received 9 May 2008; revision received 19 September 2008; accepted 29 September 2008

Published online 3 October 2008 in Wiley InterScience (www.interscience.wiley.com). DOI 10.1002/bit.22161

ABSTRACT: Biodesulfurization (BDS) of dibenzothiophene (DBT) was carried out by *Rhodococcus erythropolis* IGST8 decorated with magnetic Fe_3O_4 nanoparticles, synthesized in-house by a chemical method, with an average size of 45–50 nm, in order to facilitate the post-reaction separation of the bacteria from the reaction mixture. Scanning electron microscopy (SEM) showed that the magnetic nanoparticles substantially coated the surfaces of the bacteria. It was found that the decorated cells had a 56% higher DBT desulfurization activity in basic salt medium (BSM) compared to the nondecorated cells. We propose that this is due to permeabilization of the bacterial membrane, facilitating the entry and exit of reactant and product, respectively. Model experiments with black lipid membranes (BLM) demonstrated that the nanoparticles indeed enhance membrane permeability.

Biotechnol. Bioeng. 2008;xxx: xxx–xxx.

KEYWORDS: biodesulfurization; dibenzothiophene; *Rhodococcus erythropolis*; magnetic Fe_3O_4; nanoparticles; black lipid membrane

Introduction

In any industrial process using freely dispersed microorganisms as catalysts, they need to be separated from the products after catalysis has taken place and the reaction has reached its conclusion. Typically, the separation is carried out either by filtration or centrifugation (Luo and Sirkar, 2000). This is the first step of the downstream processes required to purify the product.

Correspondence to: F. Ansari

Although the free dispersal of microorganisms in a fluid reaction volume optimizes mass transport, it is sometimes difficult to carry out the necessary separation afterwards, and usually the separation procedure compromises viability; that is, the organisms die. Therefore, efforts have been made to immobilize bacteria, typically in the form of biofilms coating reaction vessels with high surface to volume ratios.[1] The starting materials must then simply be made to flow over the biofilm, and no separation is subsequently required (Naito et al., 2001). Furthermore, biofilms offer protection to the cells against adverse environmental conditions, and to some extent at least they are self-renewing and may therefore be used for many production cycles, or even for continuous rather than batch processes. On the other hand, mass transport is much slower than with freely dispersed microorganisms.

Some dibenzothiophene (DBT) biodesulfurization (BDS) results have been reported using immobilized *Rhodococcus erythropolis*. Naito et al. (2001) immobilized the bacteria by entrapping them with calcium alginate, agar and resin polymers; and Prieto et al. (2002) used Biolite beads to support an adsorbed network of bacteria on their external surface. Naito et al. (2001) found out that using immobilized cells made it easy to recover desulfurized oil

[1]Three major techniques are used for immobilizing bacteria: entrapment, adsorption, and coupling (Corcoran, 1985). To achieve entrapment, the microbial cells are mixed with a gel-forming polymer, yielding pores smaller than the size of the cells. This ensures retention of the cells, but permits movement of nutrients, starting reagents and products. Adsorption means allowing the bacteria to form weak chemical bonds to the substrate; electrostatic interactions between a charged support and charged cells have been made use of (Yang and Albayrak, 2007). However, the forces involved in cell attachment are then so weak that cells are readily lost from the adsorbent (Shan et al., 2005). To overcome this problem, cells can be covalently bonded (coupled) to an activated support (Hulst and Tramper, 1989).

and to use the biocatalyst repeatedly for long periods with reactivation. Immobilization of bacteria by traditional entrapment methods has major downsides, however. Mass transfer problems reduce cell access to the substrate and usually lead to a disappointingly low biotransformation activity (Xu et al., 2006).[2]

In order to combine the advantages of immobilization; that is, ease of separation and microbial longevity—with those of free diffusion; that is, good mass transport—another approach is possible, namely to decorate the bacterial cells with magnetic nanoparticles (Shan et al., 2005). After completion of the reaction, the bacterial cells can be separated from the products using a magnetic field. This is a much milder and more cost-effective process than centrifugation, and allows the bacteria to be reused many times (Gupta and Hung, 1989).

In the present work we have made use of a widely studied Gram-positive desulfurizing bacterial strain, *R. erythropolis* IGTS8, in order to investigate the effects of decorating the bacteria with magnetic nanoparticles. *R. erythropolis* is known to be able to utilize a wide variety of sulfur compounds as sulfur sources (Kayser et al., 1993) and this microorganism has been investigated in some detail (Ansari et al., 2007; Gray et al., 1996; Li et al., 1996). We suspended *R. erythropolis* in basic salt medium (BSM) containing DBT as the sole source of sulfur, and the DBT degradation ability of *R. erythropolis* was measured with the help of high-performance liquid chromatography (HPLC). DBT was chosen in this study as a model compound for the forms of thiophenic sulfur found in fossil fuels; up to 70% of the sulfur in petroleum is found as DBT and substituted DBTs (methylated DBTs); these compounds are however particularly recalcitrant to hydrodesulfurization (HDS), the current standard industrial method (Yang and Marison, 2005). We have used Fe_3O_4 as the nanoparticulate material; it is chemically stable in the working environment and nontoxic to the bacterium. Previous work by Yang and Albayrak (2007) has moreover suggested that bacteria can be decorated with them by simple adsorption.

Experimental

Chemicals

Dibenzothiophene (99%), dimethyl sulfoxide, 2-hydroxybiphenyl (HBP), ferrous chloride tetrahydrate ($FeCl_2 \cdot 4H_2O$), ferric chloride hexahydrate ($FeCl_3 \cdot 6H_2O$), glycine, Ringer's solution and all other chemicals were from Fisher Scientific (Loughborough, UK), Lipids were from Sigma (St. Louis, MO), Water was purified by ion exchange and reverse osmosis (ELGA-option3B, Elga Water Ltd, Marlow, UK).

[2]As an exception to the general rule, Díaz et al. (2002) reported that by immobilization of bacterial cells the biodegradation rate of crude oil was significantly enhanced compared to free-living cells.

Bacterial Strain and Medium

R. erythropolis IGTS8 (ATCC 53968) was from American Type Culture Collections. The bacteria were grown in basic salt medium (BSM), a sulfur-free medium containing 2.44 g KH_2PO_4, 5.47 g Na_2HPO_4, 2.00 g NH_4Cl, 0.2 g $MgCl_2 \cdot 6H_2O$, 0.001 g $CaCl_2 \cdot 2H_2O$, 0.001 g $FeCl_3 \cdot 6H_2O$, 0.004 g $MnCl_2 \cdot 4H_2O$ and 1.84 g glycerol in 1 L of deionized water. DBT dissolved in ethanol was added to give a final concentration of 0.5 mM as the sole sulfur source.

Nanoparticle Synthesis

Magnetic nanoparticles were synthesized using the procedure described by Yeh et al. (2005) to obtain Fe_3O_4 nanoparticles: briefly 25 mL of 0.2 M ferrous chloride ($FeCl_2$) was mixed with 100 mL of 0.1 M ferric chloride ($FeCl_3$) solution in a flask at room temperature and then 3 mL of 2 M HCl solution was added to make the solution slightly acidic. Then 1 g of glycine was added, and 11 mL 5 M NaOH solution was slowly dripped into the mixture to increase its pH to over 10, to provide an alkaline environment for Fe_3O_4 to precipitate; next, an additional 3 g of glycine was added, and the mixture agitated with an FB15024 vortexer (Fisher Scientific) for 10–15 min and then sonicated for 30 min; subsequently 5 mL acetone was added and agitated. The resulting precipitate (Fe_3O_4) was isolated with a permanent magnet and the supernatant discarded by decantation. The precipitate was washed twice with ultrapure water followed by centrifugation at 2,500*g* for 5 min to remove excess ions in the suspension and obtain water-dispersible nanoparticles. Finally, the washed precipitate was dispersed in ultrapure water for further investigation. The magnetic nanoparticle concentration is expressed as dry weight per volume of suspension medium.

A particle diameter of 50 nm was chosen, because if the particles are large, their Brownian energy overwhelms the relatively weak attachment forces. Preliminary experiments using iron oxide particles with a diameter of 1 μm (Dynabeads, Dynal Biotech, Bramborough, UK) showed that they did not attach to the bacteria. Furthermore, the particles should be small enough to be superparamagnetic, that is, smaller than the critical magnetic domain size (Morrish and Yu, 1956; Schmidt 2001; Zhang et al., 2006). This critical diameter is around 50 nm for our material.

Nanoparticle Characterization

Transmission electron microscopy (TEM) and scanning electron microscopy (SEM) were used to characterize the particles (Fig. 1). In order to prepare TEM samples, the final nanoparticle slurry was sonicated for approximately 5 min to better disperse the nanoparticles. A drop was placed on a carbon-coated copper TEM grid (200–300 mesh) and then left to dry in air. The particle diameters were determined directly from the TEM images to be in the range of 45–55 nm

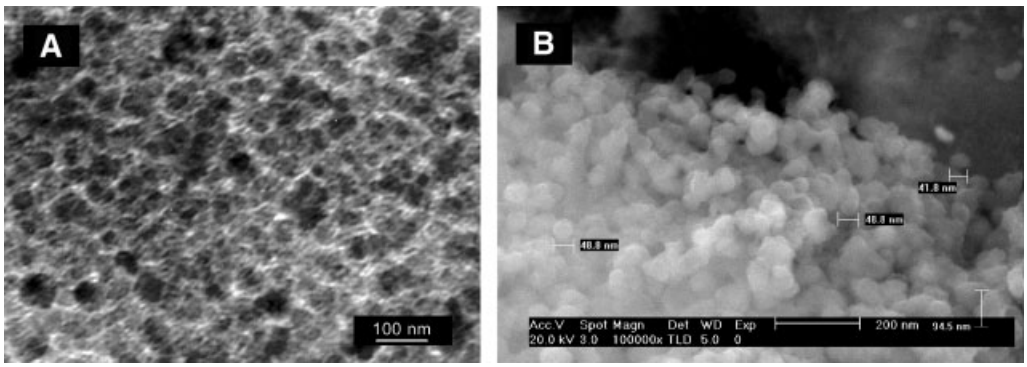

Figure 1. **A**: TEM image of the Fe_3O_4 nanoparticles. Capillary forces during drying of the suspension on the grid result in the aggregation visible on the micrographs. **B**: SEM image of the synthesized Fe_3O_4 nanoparticles.

(Fig. 1A). Figure 2 shows a bar chart of the sizes. Further characterization of the synthesized Fe_3O_4 nanoparticles was obtained using a FEI XL30 field emission SEM (Fig. 1B). In order to prepare SEM samples, the particle suspension was washed several times in deionized water to remove any salt residue, then diluted using deionized water, and finally using a pipette a drop was placed on an Al-stub and left to dry overnight, before mounting the stub on the SEM sample holder. The operating voltage was in the range of 10–20 kV to minimize charging of the sample. The SEM images were not subjected to quantitative analysis, but merely served to gain a visual impression.

Magnetic hysteresis loops of the samples were measured using a Magnetic Measurements (Petersen Instruments, Berlin, Germany) variable field translation balance (MMVFTB). Saturation magnetization (9.9 emu/g) was obtained from the hysteresis loop resulting from applying a magnetic field from -8 to $+8$ kOe (Fig. 3). The paramagnetic component was removed by assessing the gradient of the magnetization curve (B vs. H) once saturation had been reached. It should be emphasized that the residual magnetization is almost negligible for these particles, which is very likely important for achieving good dispersibility of the nanoparticles in a fluid.

Powder X-ray diffraction (XRD) studies were performed between 10° and 85° with a copper X-ray source (Siemens, Karlsruhe, Germany). The XRD pattern of the nanoparticles indicates the presence of predominantly Fe_3O_4 crystals (Fig. 4).

The zeta potentials of the prepared nanoparticles suspended in deionized water (100 μg/mL) were measured using a 3000HS Zetasizer (Malvern Instruments Ltd, Malvern, UK). The pH of the as-prepared particles in suspension was 7.0 ± 0.2. The variation of the zeta potential with pH (Fig. 5) revealed that the isoelectric point of the particles is 9.0. Hence at pH 7, at which the bacteria are negatively charged, they will electrostatically attract the nanoparticles.

Cell Growth and Decoration

The bacteria were grown in BSM until the mid-exponential growth phase and harvested by centrifugation at 1,400*g* for

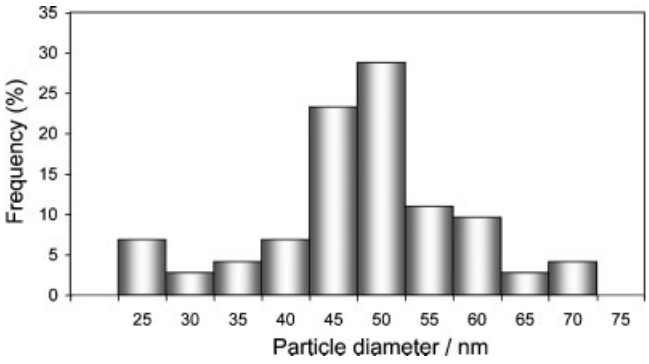

Figure 2. Bar chart of the particle sizes from a typical preparation determined from TEM images (a total of 100 particles were measured). Mean size is 47.22 ± 0.96 nm (SD).

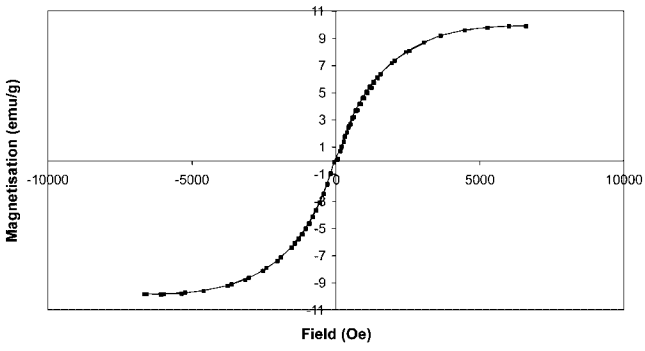

Figure 3. Magnetic hysteresis loop of Fe_3O_4 nanoparticles measured at room temperature. The paramagnetic component of the magnetization has been removed according to a standard procedure (see text).

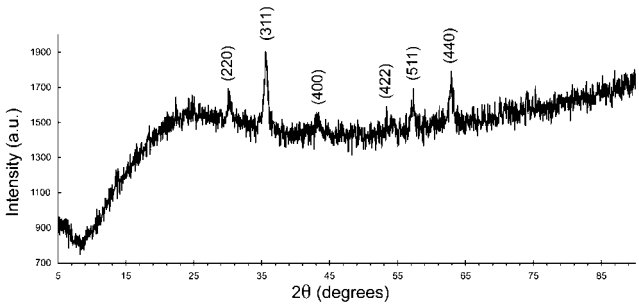

Figure 4. X-ray diffraction pattern of the nanoparticles. The numbers in parenthesis give the Miller indices of pure Fe_3O_4 (JCPDS19-0629) assigned to the observed peaks.

10 min. The cell pellets were washed twice with Ringer's solution and resuspended back in BSM at a concentration of 5.6 mg dry cells/L. The cells were then decorated with magnetic nanoparticles as follows: 10 mL of a suspension containing 100 μg/mL Fe_3O_4 nanoparticles per mL of water were mixed with 100 mL of the cell suspension in BSM at a final concentration of 0.5 mM. The ratio of nanoparticle mass to biomass is 1.78 (w/w). We estimated that this ratio makes sufficient particles available per bacterium to yield a suitable level of decoration. The resulting successful separation (Fig. 6) did not require subsequent optimization.

Batch Biodesulfurization of DBT

BDS was carried out using the cells in 100 mL of BSM containing DBT at a final concentration of 0.5 mM, in a 250 mL flask incubated on a rotary shaker at 120 rpm and 30°C (0.5 mM of DBT are equivalent to 0.092 g DBT/L). For analysis of the supernatant by HPLC, it should not contain any contamination (like free bacteria or other nonmagnetic contamination) that could damage the HPLC column. Therefore, prior to analyzing the supernatant, the cells were

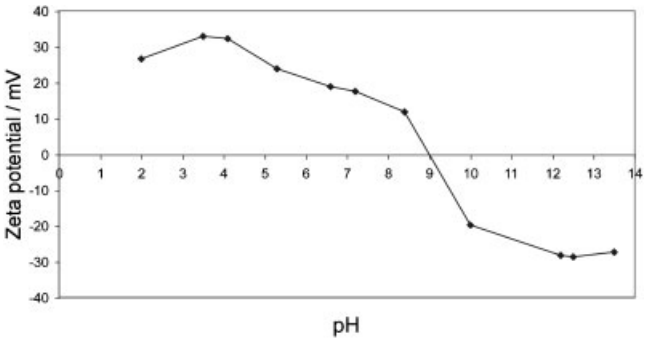

Figure 5. Surface charges of the Fe_3O_4 magnetic nanoparticles suspended in water at 25°C as a function of pH, achieved by appropriate additions of 2 M HCl or NaOH.

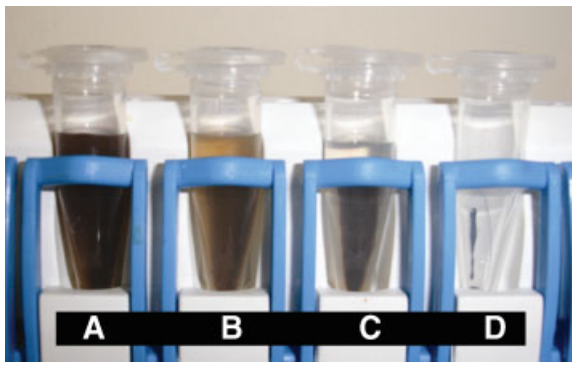

Figure 6. Photograph of nanoparticle-coated cells (*Rhodococcus erythropolis* IGTS8) in Eppendorf tubes showing, successively: (**A**) dispersed cells coated with magnetic nanoparticles; (**B** and **C**) coated cells were gradually concentrated and collected towards the rear of the tube by an external permanent magnet (within the white housing behind the tubes); (**D**) liquid medium free of suspended nanoparticles, which are visible as a thin dark stripe at the back of the tube. [Color figure can be seen in the online version of this article, available at www.interscience.wiley.com.]

separated from the reaction mixture by centrifugation at 6,600*g* for 10 min, so that the same procedure could be used for both decorated and nondecorated controls.

Product Analysis

The concentrations of DBT and HBP were analyzed by HPLC using a HPLC Model LC-10AD VP (Shimadzu, Kyoto, Japan) equipped with a Nova Pak phenyl column (3.9 mm × 150 mm) with a guard column. Isocratic elution with 60% acetonitrile and 40% water at 1.5 mL min^{-1} was carried out and detection was realized with a 117 UV detector fixed at a wavelength of 233 nm. The mobile phase, a mixture of HPLC grade water and acetonitrile, was sonicated for 10 min, and further deaerated with helium before use.

Nanoparticle-Induced Membrane Permeability Assay

Lipid bilayer membranes were formed by the method of Mueller et al. (1962) from a cardiolipids:phosphatidylcholine 5:95 mixture mimicking the bacterial outer membrane. The membrane current was measured by an OPA 129 operational amplifier (Burr-Brown, Phoenix, AZ) used as a current-to-voltage converter.

Results

Visualization of Decoration

Scanning electron micrographs of the surfaces of cells decorated with Fe_3O_4 nanoparticles are shown in Figure 7, which clearly shows that the Fe_3O_4 nanoparticles were adsorbed on the surface of the bacteria.

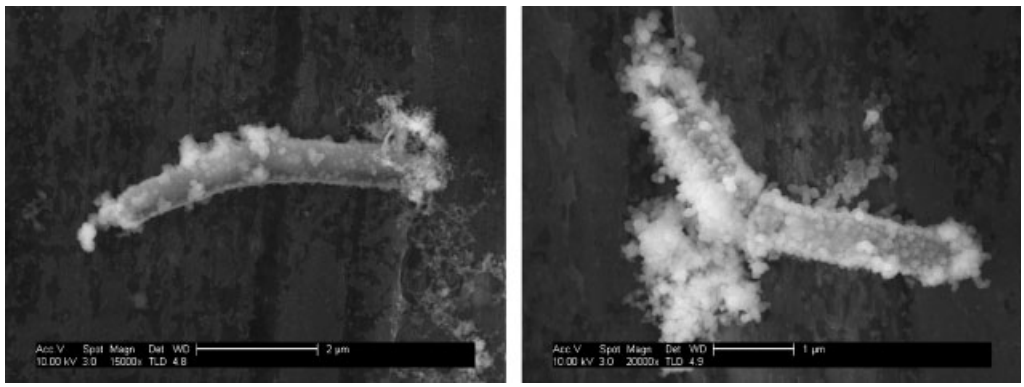

Figure 7. SEM images of two different *Rhodococcus erythropolis* IGTS8 bacteria decorated with magnetic nanoparticles. The bacterium shown on the right-hand panel is about to undergo division.

Magnetic Separation

Figure 6 shows a suspension of bacteria coated by nanoparticles in a holder equipped with a removable slide-out magnet: the decorated cells in the liquid culture medium could easily be separated by bringing an external magnet into their vicinity.

Biodesulfurization

Figure 8 compares the degradation of DBT with non-decorated and nanoparticle-coated cells. The results show that the production of HBP was significantly higher in the latter. It can be seen that whereas the production rate of the nondecorated cells falls off to almost zero after about 70 h, the decorated bacteria continue producing more vigorously until at least 100 h, with a concomitant increase in DBT HBP conversion.

Discussion

The main discovery emerging from these experiments is that the decorated bacteria are significantly more active in desulfurization. Here we discuss possible reasons, starting with the open issue whether the BDS takes place within the cytoplasm or at the bacterial surface.

Degradation Pathway

The first and rate-limiting step in the oxidative desulfurization of DBT and other sulfur compounds in living organisms is apparently transfer of DBT from the oil to the cell (Setti et al., 1999). In support of this, Folsom et al. (1999) found that the overall rate kinetics were affected by the concentration and distribution of the DBT. It is then oxidized to HBP in several steps by desulfurizing (Dsz) enzymes as illustrated in Scheme 1. These enzymes are

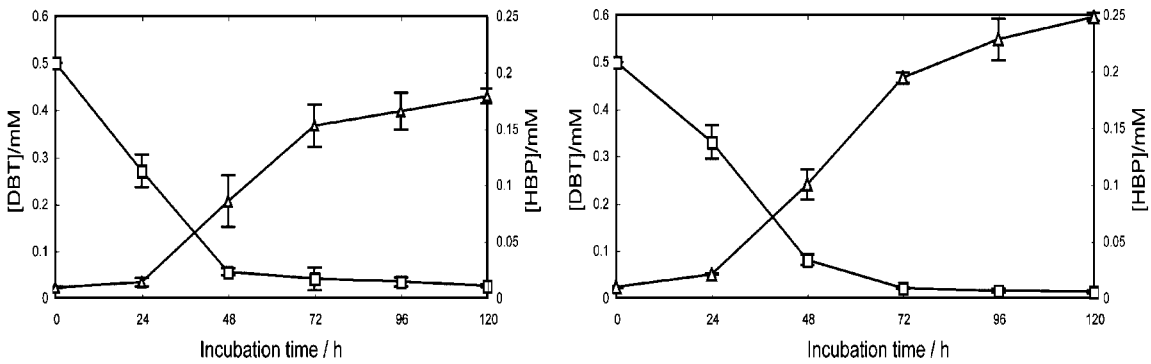

Figure 8. Degradation of DBT by *R. erythropolis* IGTS8 without (left) and with (right) decoration by nanoparticles, in BSM with DBT at the initial ($t = 0$) concentration of 0.5 mM as the sole sulfur source. (–□–) concentration of DBT, (–△–) concentration of HBP. The bacteria were present at a concentration of 4×10^7 cm^{-3}.

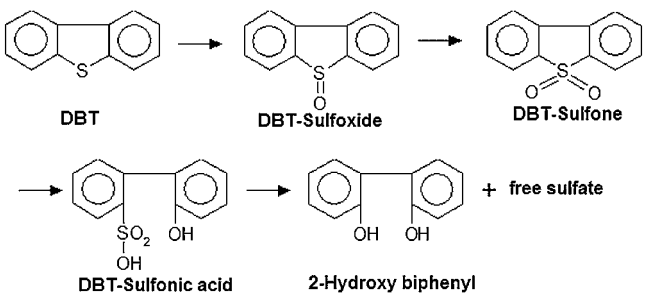

Scheme 1. Proposed (so-called 4S) pathway for DBT desulfurization by *R. erythropolis*. The DBT desulfurization pathway results in the formation of 2-hydroxybiphenyl (HBP) and sulfate, via the Dsz enzymes (cf. Van Hamme et al., 2003).

soluble and presumably found in the cytoplasm (Marcelis, 2003). On the other hand, there is no evidence that the DBT molecules are actively transported into the cell (Monticello, 2000). Patel et al. (1997) attributed the mass transfer of the very hydrophobic DBT to the hydrophobic nature of the *R. erythropolis* IGTS8 surface, because of their finding that desulfurization activity is correlated to the external surface hydrophobicity of the IGTS8 wall/membrane. It might therefore be supposed that at least some of the enzymes are located in the wall/membrane region.[3]

It is not presently known how the product, HBP, leaves the cells (Monticello, 2000)—assuming it is produced in the cytoplasm, not on the bacterial surface. At any rate the HBP released into the oil maintains fuel value (Gray et al., 1996). However, this compound is toxic to bacterial cells; hence growth and BDS activity become inhibited by its accumulation (Zhang et al., 2005). The sulfate formed during the 4S pathway remains in the aqueous phase and will combine with any ions—for example, sodium, ammonium, calcium—that are present in the medium (McFarland et al., 1998), and might be assimilated by other microorganisms (Kilbane and Bielaga, 1990).

Membrane Permeabilization

The observation of significantly increased HBP production in the decorated cells suggests that the magnetic nanoparticles might facilitate transport of HBP out of the cells—assuming that it is produced in the cytoplasm. A possible mechanism for the enhancement is that the nanoparticles bound to the bacteria make their membranes more permeable. In order to investigate this hypothesis, the possible effect of nanoparticles on membrane permeability was assessed in a model membrane system mimicking the outer bacterial membrane (Grigoriev, 2002). Figure 9 shows typical results. They provide evidence for nanoparticle-induced permeabilization, supporting the proposed enhanced ingress of DBT into the decorated bacterial cells.

In the model experiments, the added nanoparticles diffuse to the surface of the membrane and are presumably adsorbed and diffuse within the membrane. We infer they self-assemble into a conducting transmembrane system, resulting in an increased transmembrane current. Step by step the membrane conductance is increased: it is a dynamic, reversible process, the pore-forming substance can also leave the membrane and the conductance then decreases. The step-like fluctuations of the membrane current at the start of the trace probably correspond to the formation of discrete ion-conducting 20 pS pores.

Analysis of the Biodesulfurization Kinetics

The overall biodesulfurization reaction is:

$$\mathrm{DBT} \rightarrow \mathrm{HBP}$$

Writing D and H for the concentrations of DBT and HBP, respectively, the corresponding kinetic equation is

$$\frac{\mathrm{d}H}{\mathrm{d}t} = kDB \tag{1}$$

where B is the concentration of the bacteria and k the rate coefficient. The integrated form is

$$\ln\left(1 - \frac{H}{D_0}\right) = -kBt \tag{2}$$

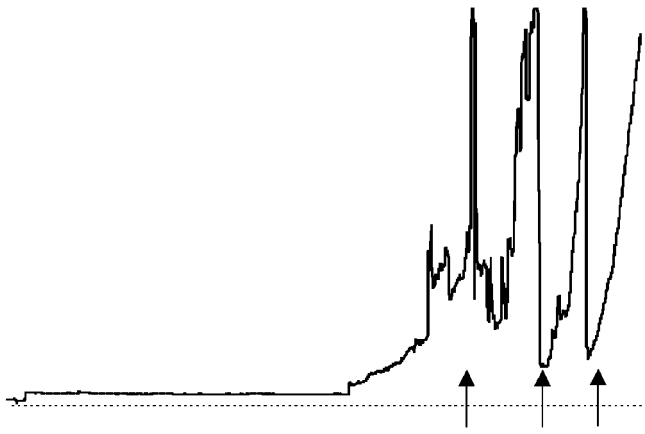

Figure 9. Temporal change of membrane current (ordinate), in the presence of nanoparticles. The sensitivity of the current recording device was changed during the recording (at the moments marked by arrows) from 1 nA/V at the start of the trace to 1 μA/V at the end. Conditions: nanoparticle concentration 300 μg/mL, 200 mM KCl, pH 6, transmembrane voltage 60 mV. The plane of the lipid bilayer was vertical and it was situated about 10 mm above the floor of the glass chamber. The entire trace shown lasted 33 s, and the initial vertical scale was 1 pA mm^{-1}.

[3]This suggests that some of the desulfurization enzymes should function in nonaqueous solvents, which consequently would facilitate contact with the oil phase and enhance mass transfer during biodesulfurization. In other words, the *Rhodococcus* strains should be able to access to DBT directly from the oil (Monticello, 2000). This is consistent with the large body of work reporting growth of *R. erythropolis* IGTS8 on hydrocarbons such as hexadecane (Solano et al., 1999).

Table I. Rate coefficient for biodesulfurization (Eq. 1).

	k $cm^3 s^{-1}$ (means ± SD)
Nondecorated	$1.01 \times 10^{-10} \pm 5.92 \times 10^{-12}$
Decorated	$1.58 \times 10^{-10} \pm 6.85 \times 10^{-12}$

where D_0 is the initial DBT concentration (0.5 mM). Linear regression of the data from Figure 8 according to Equation (2) yields k (Table I). It can be seen that decoration increases the biodesulfurization activity by 56%.

Conclusions

We decorated bacteria with Fe_3O_4 nanoparticles to facilitate cell separation at the end of the desulfurization process; decoration is facilitated by electrostatic attraction between the nanoparticles and the bacteria. The synthesized nanoparticles are dispersible in water and biological media. Magnetic separation is compatible with any automated platform that can be equipped with a magnet.

We found that we could thereby achieve a 56% higher rate of desulfurization. We favour the view that the rate limiting step of the process is transport of DBT into the cell, where it undergoes desulfurization. We show that the nanoparticles increase the permeability of a model black lipid membrane, and infer that they thereby enhance ingress of the DBT into the cell or egress of the HBP.

Magnetic nanoparticle-decorated *Rhodococcus* also facilitates its recovery and reuse; hence it offers a number of advantages for industrial applications compared to non-decorated cells. The nanoparticles are easy to prepare from rather cheap precursor materials, and are therefore suitable for large scale industrial applications. The generation of these stable, inexpensive and nontoxic adjunct materials for use with the microbial cells greatly facilitates the separation of the cells from the products during bioreactor process development, and the removal of the cells from the medium at any time via magnetic decantation.

We thank Mimi Hill for the magnetization measurements carried out at Liverpool University and Qi Zhang & Matthew Kershaw (Cranfield University) for help with the zeta potential measurements and XRD, respectively.

References

Ansari F, Prayuenyong P, Tothill I. 2007. Biodesulfurization of dibenzothiophene by *Shewanella putrefaciens* NCIMB 8768. J Biol Phys Chem 7:75–78.

Corcoran JA. 1985. The production and use of immobilized living microbial cells. In: Wiseman A, editor. Topics in enzyme and fermentation biotechnology. Chichester: Ellis Horwood. 10: p 12–50.

Díaz MP, Boyd KG, Grigson SJW, Burgess JG. 2002. Biodegradation of crude oil across a wide range of salinities by an extremely halotolerant bacterial consortium MPD-M, immobilized onto polypropylene fibers. Biotechnol Bioeng 79:145–153.

Folsom BR, Schieche DR, Digrazia PM, Werner J, Palmer S. 1999. Microbial desulfurization of alkylated dibenzothiophenes from a hydrodesulfurized middle distillate by *Rhodococcus erythropolis* I-19. Appl Environ Microbiol 65:4967–9972.

Gray KA, Pogrebinsky OS, Mrachko GT, Xi L, Monticello DJ, Squires CH. 1996. Molecular mechanisms of biocatalytic desulfurization of fossil fuels. Nat Biotechnol 14:1705–1709.

Grigoriev P. 2002. Unified carrier-channel model of ion transfer across lipid bilayer membranes. J Biol Phys Chem 2:77–79.

Gupta PK, Hung CT. 1989. Magnetically controlled targeted micro-carrier systems. Life Sci 44:175–186.

Hulst AC, Tramper J. 1989. A new technique for the production of immobilized biocatalyst in large quantities. Enzyme Microb Technol 11:546–556.

Kayser KJ, Bielaga-Jones BA, Jackowski K, Odusan O, Kilbane JJ. 1993. Utilization of organosulphur compounds by axenic and mixed cultures of Rhodococcus rhodochrous strain IGTS8. J Gen Microbiol 139:3123–3129.

Kilbane JJ, Bielaga BA. 1990. Toward sulfur-free fuels. Chemtech 20:747–751.

Li MZ, Squires CH, Monticello DJ, Childs JD. 1996. Genetic analysis of the dsz promoter and associated regulatory regions of *Rhodococcus erythropolis* IGTS8. Bacteriol J 178:6409–6418.

Luo RG, Sirkar KK. 2000. Method and apparatus for isolation purification of biomolecules. US Patent 6,022,477.

Marcelis CLM. 2003. Anaerobic biodesulfurization of thiophenes. PhD Thesis, University of Wageningen.

McFarland BL, Boron DJ, Deever W, Meyer JA, Johnson AR, Atlas RM. 1998. Biocatalytic sulfur removal from fuels: Applicability for producing low sulfur gasoline. Crit Rev Microbiol 24:99–147.

Monticello DJ. 2000. Biodesulfurization and the upgrading of petroleum distillates. Curr Opin Biotechnol 11:540–546.

Morrish AH, Yu SP. 1956. Magnetic measurements on individual microscopic ferrite particles near the single-domain. Phys Rev 102:670–673.

Mueller P, Rudin DO, Tien H, Wescott W. 1962. Reconstitution of cell membrane structure in vitro and its transformation into an excitable system. Nature 194:979–980.

Naito M, Kawamoto T, Fujino K, Kobayashi M, Maruhashi K, Tanaka A. 2001. Long-term repeated biodesulfurization by immobilized *Rhodococcus erythropolis* KA2-5-1 cells. Appl Microbiol Biotechnol 55:374–378.

Patel SB, KilbaneII JJ, Webster DA. 1997. Biodesulphurisation of dibenzothiophene in hydrophobic media by Rhodococcus sp strain IGTS8. J Chem Technol Biotechnol 69:100–106.

Prieto MB, Hidalgo A, Serra JL, Llama MJ. 2002. Degradation of phenol by *Rhodococcus erythropolis* UPV-1 immobilized in Biolite in a packed-bed reactor. J Biotechnol 97:1–11.

Schmidt H. 2001. Nanoparticles by chemical synthesis, processing to materials and innovative applications. Appl Organomet Chem 15: 331–343.

Setti L, Farinelli P, Di Martino S, Frassinetti S, Lanzarini G, Pifferi P. 1999. Developments in destructive and non-destructive pathways for selective desulfurizations in oil biorefining processes. Appl Microbiol Biotechnol 52:111–117.

Shan G, Xing J, Zhang H, Liu H. 2005. Biodesulfurization of dibenzothiophene by microbial cells coated with magnetic nanoparticles. Appl Environ Microbiol 71:4497–4502.

Solano SF, Marchal R, Ropars M, Lebeault J, Vandecasteele J. 1999. Biodegradation of gasoline: Kinetics, mass balance and fate of individual hydrocarbons. J Appl Microbiol 86:1008–1016.

Van Hamme JD, Singh A, Ward OP. 2003. Recent advances in petroleum microbiology. Microbiol Mol Biol Rev 67:503–549.

Xu P, Yu B, Li FL, Cai XF, Ma CQ. 2006. Microbial degradation of sulfur, nitrogen and oxygen heterocycles. Trends Microbiol 14:398–405.

Yang S, Albayrak N. 2007. Immobilization of enzyme on a fibrous matrix. US Patent 7,166,451.

Yang J, Marison WI. 2005. Two-stage process design for the biodesulfurization of a model diesel by a newly isolated *Rhodococcus globerulus* DAQ3. Biochem Eng 27:77–82.

Yeh CS, Cheng FY, Shieh DB, Wu CL. 2005. Method for preparation of water-soluble and dispersed iron oxide nanoparticles and application thereof. US Patent Application 0271593 A1.

Zhang L, Dong Y, Wang M, Shi S. 2005. Biodesulfurization of dibenzothiophene and other organic sulfur compound by newly isolated *Micobacterium* strain ZD-M2. FEMS Microbiol Lett 247:45–50.

Zhang XY, Chen YJ, Fan LN, Li ZY. 2006. Enhancement of low-field magnetoresistance in Fe_3O_4 particles induced by ball milling. Solid State Commun 137:673–677.